

Kaon Fragmentation Functions From Semi-Inclusive Deep Inelastic Scattering of Muons on an Isoscalar Target

**Dissertation
zur
Erlangung des Doktorgrades (Dr. rer. nat.)
der
Mathematisch-Naturwissenschaftlichen Fakultät
der
Rheinischen Friedrich-Wilhelms-Universität
Bonn**

**vorgelegt von
Daniel Hahne
aus
Aachen**

Bonn, Juli 2016

Angefertigt mit Genehmigung der Mathematisch-Naturwissenschaftlichen Fakultät
der Rheinischen Friedrich-Wilhelm-Universität Bonn

1. Gutachter: Prof. Hartmut Schmieden
2. Gutachter: Prof. Jörg Pretz

Tag der Promotion: 16.12.2016
Erscheinungsjahr: 2017

Abstract

This thesis presents the analysis of K_S^0 multiplicities from COMPASS 2006 data, and the extraction of kaon fragmentation functions (FFs) including fits to K^+ and K^- multiplicities available from previous analyses and the K_S^0 multiplicities from this thesis.

The K_S^0 multiplicities, analyzed in the kinematical region of $0.004 < x < 0.4$, $Q^2 > 1 \text{ (GeV/c)}^2$, and $0.2 < z < 0.85$, are complementary to the K^+ and K^- multiplicities. The K_S^0 are identified by their decay into $\pi^+\pi^-$ pairs, in contrast to the charged kaons which rely on the RICH detector for particle identification. This yields a larger coverage of z and different systematic uncertainties. Furthermore the FFs have a different weight on the multiplicities of charged and neutral kaons.

The FFs are extracted from the multiplicities using a LO pQCD fit. Isospin and charge invariance allow for a simultaneous fit of K^+ , K^- , and K_S^0 multiplicities. To perform the fit, good knowledge of the parton distribution functions (PDFs) of the nucleon is necessary. The impact of the PDFs on the FFs is studied by performing the fits with different PDF sets. It is shown that the PDF sets have the largest contribution to the systematic uncertainties of the FFs.

Furthermore it is shown that fits with the K_S^0 multiplicities included are able to constrain the FFs with more accuracy. The largest impact is found for the FF of strange quarks. The strange FFs of fits with the K_S^0 included ranging between 0.456–1.265 are larger and better constrained than the ones of fits with the K_S^0 excluded, ranging between 0.195–0.563. A comparison of kaon multiplicities from COMPASS and HERMES shows large differences between the two, which, in LO, cannot be explained by the different kinematics of the experiments.

The K^+ and K^- multiplicities, together with the K_S^0 multiplicities of this thesis, provide a full set of kaon multiplicities for further analyses, especially for more sophisticated extractions of FFs by theory groups.

Contents

1. Introduction	1
2. Deep Inelastic Scattering	5
2.1. Kinematics of Deep Inelastic Scattering	5
2.2. The Quark Parton Model	7
2.3. Parton Distribution Functions	13
2.4. Semi-Inclusive Deep Inelastic Scattering	14
2.5. Fragmentation Functions	17
2.5.1. Kaon Fragmentation Functions	18
3. The COMPASS Experiment	25
3.1. Beamline	27
3.2. The Target System	28
3.3. Large and Small Angle Spectrometers	29
3.3.1. Tracking detectors	30
3.3.2. Particle Identification	34
3.3.3. Trigger System	36
3.4. Event Reconstruction	39
4. Extraction of K_S^0 Multiplicities	41
4.1. Event Selection	41
4.1.1. Binning	42
4.1.2. Selection of Deep Inelastic Scattering Events	42
4.1.3. Selection of Neutral Kaon Candidates	48
4.1.4. Radiative Corrections	54
4.2. K^0 Identification	58
4.3. Raw Multiplicities	61
4.4. Acceptance	61
4.4.1. Uncertainty Estimation	64
4.5. Vector Meson Correction	64
4.6. Systematic Uncertainties	67
4.6.1. From K_S^0 identification	67
4.6.2. From Acceptance	67
4.6.3. From Diffractive Vector Mesons	70
4.6.4. Stability over Time	72

Contents

4.6.5. Total Systematic Uncertainties	76
4.7. Final K_S^0 Multiplicities	76
5. Extraction of Fragmentation Functions	81
5.1. General Fit Method	81
5.1.1. FF Uncertainties	82
5.2. Pion Fragmentation Functions	83
5.3. Kaon Fragmentation Functions	87
5.3.1. Kaon Fragmentation Functions from K^\pm Multiplicities . . .	90
5.3.2. Kaon Fragmentation Functions from K^\pm and K_S^0 Multiplicities	101
5.3.3. Comparison with HERMES Multiplicities	110
5.3.4. Summary	116
6. Summary and Conclusions	119
Appendices	123
A. Multiplicity Equations	125
A.1. Pions	125
A.1.1. Pion Fragmentation Functions	125
A.1.2. Pion Multiplicities	126
A.2. Kaons	127
A.2.1. Relation between Charged and Neutral Kaon Fragmentation Functions	127
A.2.2. Charged Kaon Multiplicities	128
A.2.3. Neutral Kaon Multiplicities	128
B. Fragmentation Functions	131
B.1. Kaon FFs from Fits to K^+ and K^- Multiplicities	131
B.1.1. Residuals	131
B.1.2. Individual Quark Contributions to the Multiplicities	134
B.2. Kaon FFs from Fits to K^+ , K^- , and K_S^0 Multiplicities	144
B.2.1. Residuals	144
B.2.2. Individual Quark Contributions to the Multiplicities	147
Bibliography	157
List of Figures	163
List of Tables	171

1. Introduction

One goal of physics is to understand the structure of matter and its interactions. The idea that matter consists of elementary, no further divisible particles, called atoms, whose name is derived from the ancient Greek word for indivisible, is very old. The existence of atoms, however, was not proven experimentally until the beginning of the 19th century when Dalton applied the concept of atoms to explain that elements react in certain ratios with each other. With the discovery of the electron by Thompson in 1897 and the nucleus through the Rutherford experiment in the early 20th century, it was found that atoms are not the elementary particles one was looking for but that atoms themselves consist of smaller particles, namely a nucleus orbited by electrons. In 1919 the proton as the positive component of the nucleus was discovered, followed by the discovery of the neutron in 1932. The term nucleon was introduced as a generic name for the proton and the neutron. The nucleons inside the nuclei are bound by the strong force. Generally particles that interact via the strong force are named hadrons. In the years that followed, experiments with cosmic rays led to the discovery of a multitude of different hadrons besides the nucleon. In the 1960s the quark parton model (QPM) was developed with the purpose to order the hadrons. Its basic idea is that hadrons are composed of quarks, elementary spin- $\frac{1}{2}$ particles with an electric charge of $+\frac{2}{3}$ or $-\frac{1}{3}$ of the elementary charge. To the present day, six quark flavors are known: up, down, strange, charm, bottom, and top. The interactions between quarks are described by Quantum Chromodynamics (QCD) as the exchange of gluons. Gluons, whose existence was experimentally proven in 1979, are gauge bosons of spin 1 and the carrier of the strong force.

Hadrons consist of either three quarks, three antiquarks, or of a quark-antiquark pair. These so-called valence quarks give the hadrons their quantum numbers. For example, the valence quark configuration of the nucleon consists of combinations of up and down quarks. From QCD follows that gluons can decay into quark-antiquark pairs, the so-called sea quarks, which can annihilate back into gluons.

A common tool to study the nucleon structure is deep inelastic scattering (DIS) experiments, where highly energetic leptons are scattered off nucleons. During the scattering process a virtual photon transfers four-momentum from the lepton to the nucleon. The scattering gives access to the distributions of quarks and gluons inside the nucleon which are described by so-called parton distribution functions (PDFs), defined as the number density $q(x, Q^2)$ for finding a parton q with the fraction x of the nucleon's momentum at a given Q^2 . The four-momentum transfer

1. Introduction

squared, Q^2 , of the virtual photon of DIS is a measure for the spatial resolution power. For sufficiently large momenta, which correspond to small distances, the interaction between the quarks and gluons inside the nucleon diminishes and the quarks can be viewed as quasi-free particles. This property is called asymptotic freedom and at this range the quark and gluon interactions are calculable with perturbative QCD (pQCD).

To the present day no free quarks have been observed by experiments. This is the phenomenon of confinement: at large distances the strong force between the quarks does not diminish; instead the energy of the gluon field increases until the creation of a new quark-antiquark pair is energetically more favorable than adding more energy to the gluon field. In this process the newly created quarks recombine, together with the already existing quarks, into new hadrons. Thus no quark is released but a new hadron is produced. This process, called hadronization or fragmentation, is described by fragmentation functions (FFs), denoted as D_q^h , that give the number density for a quark q to fragment into a final state hadron h .

In many physics processes short and long distance, that is perturbative and non-perturbative, phenomena are combined. Often the cross sections can be factorized into perturbative and non-perturbative parts. The perturbative part is valid for the cross section at short distances, the non-perturbative part covers the long-distance functions, such as PDFs and FFs. The PDFs and FFs are considered universal, that is process independent. This property is usually exploited to perform global fits on combined experimental data of different processes. Unpolarized PDFs, for example, can be determined from data of both electron and muon DIS as well as proton-proton collisions.

An important research issue over the last decade was the nucleon spin. To better understand its origin it is mandatory to measure PDFs separated into quark flavors. This is particularly important for the determination of the strange quark contribution to the nucleon spin. The quark flavor can be tagged in semi-inclusive DIS (SIDIS) where a final state hadron is identified along with the scattered lepton, provided that the FFs of the corresponding hadrons are known. The FFs can be determined in unpolarized DIS by extracting them from fits to hadron multiplicities. The multiplicity of a hadron of type h is defined as the number of final state hadrons h per DIS event. Thus, in order to measure the multiplicity from DIS, the final state hadrons must be detected in addition to the scattered lepton. If strange or anti-strange quarks shall be involved then kaons need to be identified in SIDIS reactions.

This thesis has two main goals. The first is the extraction of K_S^0 multiplicities from data measured at the COMPASS experiment. Based on this, the second main goal is the extraction of kaon fragmentation functions.

The thesis is organized as follows. The next chapter introduces the basic theoretical concepts needed to understand the extraction of multiplicities and the

extraction of fragmentation functions from multiplicities. Chapter 3 introduces the COMPASS experiment with focus on the experimental setup. In chapter 4 the method to extract the K_S^0 multiplicities from data is explained followed by chapter 5 in which the FFs are extracted from the measured kaon multiplicities of the COMPASS collaboration. The FFs are extracted solely from K^+ and K^- multiplicities, known from previous analyses, as well as from a combined analysis of K^+ , K^- , and K_S^0 multiplicities, including the results of chapter 4. The results are summarized and the thesis is concluded in chapter 6.

2. Deep Inelastic Scattering

One way to probe the structure of nucleons is deep inelastic scattering (DIS). In DIS a highly energetic lepton l scatters off a nucleon N . The process is called inclusive if only the scattered lepton is measured. Inclusive DIS gives access to Parton Distribution Functions (PDFs) which describe the parton distribution inside the nucleon. If in addition to the scattered lepton parts of the final state hadrons are measured, the process is called semi-inclusive deep inelastic scattering (SIDIS). The hadronization of a struck parton into final state hadrons is described by Fragmentation Functions (FFs). Fragmentation functions cannot be measured directly but are extracted from hadron multiplicities, that is the number of final state hadrons per DIS event. In SIDIS the hadron multiplicity is defined as the number of final state hadrons normalized with the total number of DIS events. In leading order (LO) the multiplicity depends only on the quark charges, PDFs, and FFs. The existing parametrizations of PDFs are utilized to extract the FFs by performing a LO fit on the multiplicities.

This chapter gives the basic theoretical principles that are needed to extract FFs from hadron multiplicities. The first three sections 2.1, 2.2, and 2.3 describe the kinematics of (inclusive) DIS, the quark parton model, and PDFs, respectively. In section 2.4 SIDIS and FFs are addressed. The final section 2.5 introduces the charged and neutral kaons and gives an overview of the status of kaon FFs.

The material presented in this chapter can be found in text books such as Refs. [1, 2].

2.1. Kinematics of Deep Inelastic Scattering

Deep inelastic scattering (DIS) is the process of a highly energetic lepton scattering off a nucleon. It is illustrated in Fig. 2.1. The DIS process is described with Lorentz invariant variables listed in Tab. 2.1. The incoming leptons l and scattered leptons l' carry the four-momenta $k = (E, \vec{k})$ and $k' = (E', \vec{k}')$, respectively. The nucleon N has the four-momentum $P = (E_P, \vec{P}) \stackrel{\text{lab}}{=} (M, 0)$. A virtual photon carries the four-momentum transfer

$$Q^2 = -q^2 = -(k - k')^2 \stackrel{\text{lab}}{=} 2 \left(m^2 c^4 - EE' + |k||k'| \cos \theta \right) \quad (2.1)$$

from the lepton to the nucleon. The mass of the final state hadronic system is given by

2. Deep Inelastic Scattering

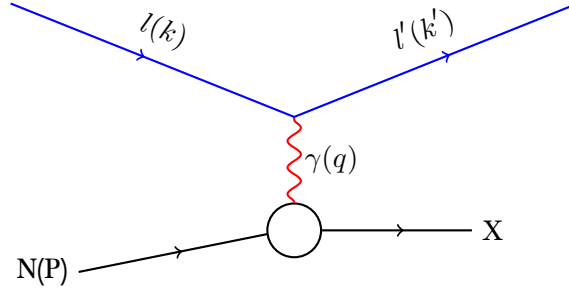


Figure 2.1.: DIS process $lN \rightarrow l'X$ of a lepton off a nucleon.

m	lepton mass
M	nucleon mass
$k(k')$	incoming (outgoing) lepton momentum four-vector
$E(E')$	incoming (outgoing) lepton energy
$q = k - k'$	four-momentum transfer
$Q^2 = -q^2$	four-momentum transfer squared
$\nu = \frac{p \cdot q}{M} \stackrel{\text{lab}}{=} E - E'$	energy transfer
P	nucleon momentum four-vector
$x = \frac{Q^2}{2Pq} \stackrel{\text{lab}}{=} \frac{Q^2}{2M\nu}$	Bjorken scaling variable
$y = \frac{E-E'}{E} \stackrel{\text{lab}}{=} \frac{\nu}{E}$	relative energy transfer
$W^2 = (P + q)^2$	hadronic final state energy

Table 2.1.: List of inclusive and semi-inclusive DIS variables.

$$W^2 c^2 = (P + q)^2 = M^2 c^2 + 2Pq + q^2 = M^2 c^2 + 2M\nu - Q^2 \quad (2.2)$$

with the energy transfer

$$\nu = \frac{Pq}{M} \stackrel{\text{lab}}{=} E - E'. \quad (2.3)$$

The Bjorken scaling variable

$$x = \frac{Q^2}{2Pq} \stackrel{\text{lab}}{=} \frac{Q^2}{2M\nu} \quad (2.4)$$

gives a measure of the inelasticity of the DIS process. The scattering is elastic if $x = 1$ and inelastic for $0 < x < 1$. The relative energy transfer is given by

$$y = \frac{p \cdot q}{p \cdot k} \stackrel{\text{lab}}{=} \frac{E - E'}{E} = \frac{\nu}{E}. \quad (2.5)$$

Of the five variables Q^2 , x , y , ν , and W^2 only two are required to fully describe the inclusive DIS scattering process. Here x and Q^2 are chosen.

Then the inclusive DIS cross section can be expressed as

$$\frac{d^2\sigma}{dx dQ^2} = \frac{4\pi\alpha^2}{xQ^4} \left[xy^2 F_1(x, Q^2) + \left(1 - y - \frac{x^2 y^2 M^2}{Q^2}\right) F_2(x, Q^2) \right] \quad (2.6)$$

where $F_1(x, Q^2)$ and $F_2(x, Q^2)$ are structure functions that describe the inner structure of the nucleon.

With the assumption that the constituents of the nucleon are spin- $\frac{1}{2}$ particles, the Callan-Gross relation [3] states that F_1 and F_2 are related by

$$2xF_1(x) = F_2(x). \quad (2.7)$$

Using the Callan-Gross relation the DIS cross section can be rewritten in terms of only one structure function, here F_2 :

$$\frac{d^2\sigma}{dx dQ^2} = \frac{2\pi\alpha^2}{xQ^4} \left[1 + (1 - y)^2 - 2\frac{x^2 y^2 M^2}{Q^2} \right] F_2(x, Q^2) \quad (2.8)$$

2.2. The Quark Parton Model

In the Quark Parton Model (QPM) the nucleon is considered to be composed of point-like objects, called partons. When first measuring the structure functions $F_1(x, Q^2)$ and $F_2(x, Q^2)$ no Q^2 dependence was found. This and the experimentally proven Callan-Gross relation (Eq. 2.7) led to the assumption that the nucleon

2. Deep Inelastic Scattering

consists of electromagnetically charged, point-like spin- $\frac{1}{2}$ partons: the quarks. Today six quarks u (up), d (down), s (strange), c (charm), b (bottom) and t (top) as well as their antiquarks are known and ordered in doublets:

$$\begin{pmatrix} u \\ d \end{pmatrix}, \begin{pmatrix} c \\ s \end{pmatrix}, \begin{pmatrix} t \\ b \end{pmatrix} \quad (2.9)$$

where the quarks in the top row have electric charge $+\frac{2}{3}e$ and those in the bottom row have electric charge $-\frac{1}{3}e$.

In the QPM the nucleon is composed of a combination of u and d quarks. Thus, they must give the nucleon its quantum numbers such as charge, spin and isospin. At least three quarks of spin- $\frac{1}{2}$ are needed to add up to the nucleon spin of $\frac{1}{2}$. The proton consists of two up quarks and one down quark, the neutron of one up quark and two down quarks.

Since the proton and neutron build an isospin doublet it is considered that up and down quarks build an isospin doublet too.

The quarks that give the hadrons their quantum numbers are called valence quarks. Besides the valence quarks an (almost) infinite number of (virtual) quark-antiquark pairs may exist. These are called sea quarks.

In the QPM, DIS can be interpreted as the sum over all quarks of incoherent scattering of leptons off quarks. If the nucleon is viewed in an infinite momentum frame (IMF), a frame where the nucleon has infinite momentum in longitudinal direction, the transverse momenta and interactions between partons can be neglected. The Breit-frame is a special IMF where the nucleon momentum is chosen such that no energy is transferred from the virtual photon to the nucleon, that is only the momentum of the struck parton changes sign. In the Breit-frame the struck parton carries the fraction ξ of the longitudinal momentum of the nucleon, which is identical to the Bjorken scaling variable x .

The structure functions have the probabilistic interpretation

$$\begin{aligned} F_1(x, Q^2) &= \frac{1}{2} \sum_q e_q^2 \left[q(x, Q^2) + \bar{q}(x, Q^2) \right] \\ F_2(x, Q^2) &= x \sum_q e_q^2 \left[q(x, Q^2) + \bar{q}(x, Q^2) \right] \end{aligned} \quad (2.10)$$

where e_q are the electrical quark charges. The unpolarized quark and antiquark distribution functions $q(x, Q^2)$ and $\bar{q}(x, Q^2)$ describe the momentum distributions in terms of x for a given Q^2 of quarks and antiquarks, respectively.

The sums in Eq. (2.10) are extended over the quark flavor q .

Integrating over all parton momenta $x \cdot q$ one would expect the integral to be equal to the total nucleon momentum. However, experimentally it is found that the quarks carry only about half of the nucleon's momentum:

$$\sum_q \int_0^1 x \cdot [q(x) + \bar{q}(x)] dx \approx 0.5 . \quad (2.11)$$

This indicates that parts of the nucleon momentum are carried by a parton that interacts non-electromagnetically. Today these partons are identified as gluons, massless spin-1 particles. They are the exchange particles of the strong force that binds quarks together. Their discovery led to the development of quantum chromodynamics (QCD), a quantum field theory with symmetry group SU(3). In QCD an additional quantum number – a color charge – is assigned. Color is an analogy to color theory where every color is made up of three primary colors. Quarks are assigned the colors red (R), green (G) and blue (B), while antiquarks are assigned the complementary colors or anticolors cyan (antired) (\bar{R}), magenta (antigreen) (\bar{G}) and yellow (antiblue) (\bar{B}).

The gluon, as interacting particle between two quarks with color, carries color and anticolor at the same time. Therefore, gluons not only couple to quarks but coupling of three or four gluons with themselves is possible too. Quarks can emit and absorb gluons and gluons can split into quark-antiquark pairs.

In QCD the strength of the interaction among the partons is described by the strong coupling constant α_s . The coupling depends strongly on Q^2 and increases for higher distances or smaller momentum transfers and decreases for shorter distances or higher momentum transfers. In leading order it is given by

$$\alpha_s(Q^2) = \frac{12\pi}{(33 - 2n_f) \cdot \ln(Q^2/\Lambda_{\text{QCD}}^2)}, \quad (2.12)$$

where n_f denotes the number of quark flavors at a given Q^2 and Λ_{QCD} is the QCD scale parameter. The numerical value of Λ_{QCD} depends on the energy scale of the inspected process. It is empirically determined and usually between 200–300 MeV/c².

The Q^2 dependence leads to confinement on the one hand and asymptotic freedom on the other hand. Confinement means that even for large distances the strong force between quarks does not diminish. Instead the energy of the gluon field increases until enough energy is available for the creation of a new quark-antiquark pair. Although it is not analytically proven that confinement follows from QCD, it explains the phenomenon that in nature no free quarks are observed. At short distances or large exchanges of momenta the interaction between quarks and gluons becomes feeble and they can be viewed as quasi-free particles. Thus, probing the nucleon with high momentum transfers renders the description of hard interactions with perturbation theory possible.

Fig. 2.2 shows $F_2(x, Q^2)$ as a function of Q^2 for different values of x . The first measurements of F_2 were made in the intermediate region around $x = 0.15$

2. Deep Inelastic Scattering

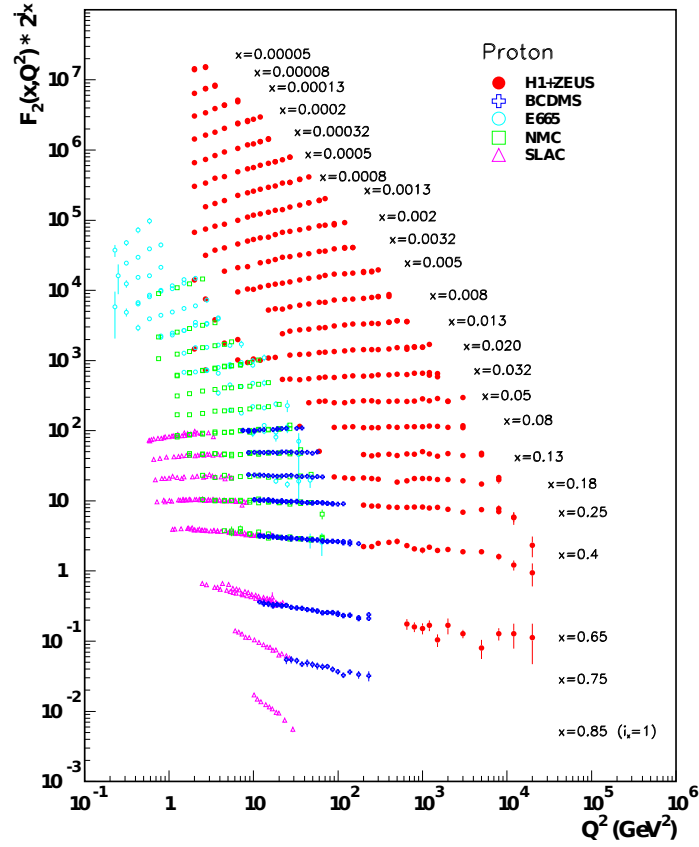


Figure 2.2.: The F_2 structure function for the proton. $F_2(x, Q^2)$ is plotted against Q^2 for different values of x . The F_2 for different x are staggered. The plot is taken from [10].

and did not show a Q^2 dependence. The term Bjorken scaling was introduced, meaning that the structure functions do not depend on the energy Q^2 but only on the dimensionless variable x . Moving away from the intermediate region towards smaller or larger values of x , F_2 rises or falls with increasing Q^2 . Consequently, this behavior was named scale breaking.

Bjorken scaling and scale breaking can be explained by QCD effects [5, 6]. In DIS, Q^2 refers to the spatial resolution of the virtual photon which can resolve distances up to $\hbar/\sqrt{Q^2}$. Scaling, in this context, means that the scattering does not depend on the resolution, thus, the scattering must occur on point-like objects. The principle of scale breaking is illustrated in Fig. 2.3. If Q^2 of the virtual photon is small, the quark-gluon structure cannot be resolved but is measured as one compound. With increasing Q^2 , partons with a lower momentum fraction x are

resolved.

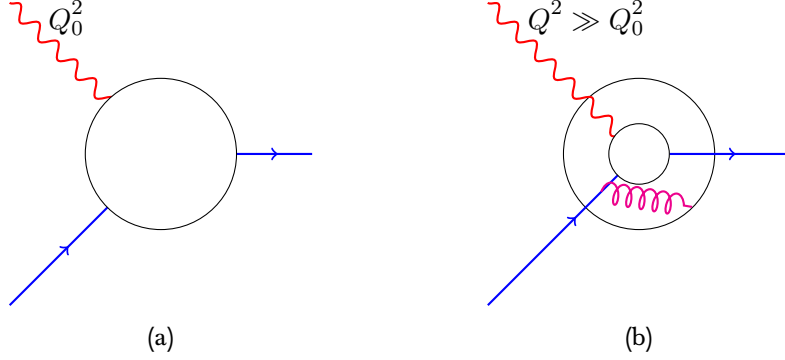


Figure 2.3.: Illustration of scale breaking due to resolution. At small values of $Q^2 = Q_0^2$ (left) the photon cannot resolve the quark-gluon structure and measures the compound as one unit. At Q^2 values larger than Q_0^2 (right) the resolution increases and the individual momenta of q and g are resolved. The quark is measured without the gluon.

Mathematically the fact that a quark with momentum fraction x originates from a parton with a larger momentum fraction x' , either a quark that radiates a gluon or a gluon splitting into a quark-antiquark pair, is expressed by the DGLAP (Dokshitzer–Gribov–Lipatov–Altarelli–Parisi) Q^2 evolution equations [7, 8, 9].

The DGLAP equation for non-singlet flavor combinations, such as $q^{NS} = q_i - q_j$, is given by

$$\frac{d}{d \ln Q^2} q^{NS}(x, Q^2) = \frac{\alpha_s(Q^2)}{2\pi} P_{qq}^{NS} \otimes q^{NS}. \quad (2.13)$$

The gluon distribution $g(x, Q^2)$ couples to the singlet flavor combination $\Sigma(x, Q^2) = u + d + s$ in the following way

$$\frac{d}{d \ln Q^2} \begin{pmatrix} \Sigma(x, Q^2) \\ g(x, Q^2) \end{pmatrix} = \frac{\alpha_s(Q^2)}{2\pi} \begin{pmatrix} P_{qq}^S & 2n_f P_{qg} \\ P_{gq} & P_{gg} \end{pmatrix} \otimes \begin{pmatrix} \Sigma(x, Q^2) \\ g(x, Q^2) \end{pmatrix}, \quad (2.14)$$

where n_f is the number of flavors for a given Q^2 . The splitting functions $P_{ab}(x/x', Q^2)$ in Eq. (2.13) and Eq. (2.14) describe the probability that a parton b with the momentum fraction x' radiates a parton a with the momentum fraction x , or splits into two partons of type a . They are illustrated in Fig. 2.4.

2. Deep Inelastic Scattering

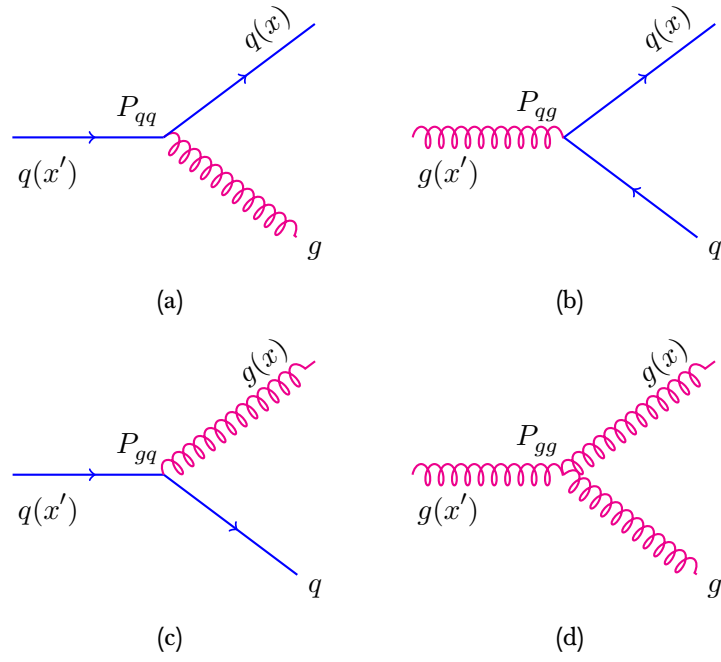


Figure 2.4.: The splitting functions describe the probability that (a) a quark radiates a gluon, (b) a gluon splits into two quarks, (c) a gluon originates from a quark, and (d) a gluon radiates a gluon.

2.3. Parton Distribution Functions

The distribution of quarks and gluons in the nucleon is given by Parton Distribution Functions (PDFs). PDFs describe the number density to find a quark or a gluon at a given x and Q^2 . The helicity of the parton can be either parallel (q_+) or anti-parallel (q_-) with respect to the helicity of the nucleon. The spin-averaged or unpolarized PDFs are given by

$$q = q_+ + q_-. \quad (2.15)$$

They can be extracted from the unpolarized structure functions F_1 and F_2 from Eq. (2.10).

The spin-dependent or polarized PDFs are given by

$$\Delta q = q_+ - q_-. \quad (2.16)$$

Similar to the unpolarized PDFs, they can be extracted from polarized structure functions. The polarized structure functions, denoted as g_1 and g_2 , are equivalent to the unpolarized structure functions but with the q replaced by Δq :

$$g_1 = \frac{1}{2} \sum_q e_q^2 \Delta q(x, Q^2), g_2(x, Q^2) = x \sum_q e_q^2 \Delta q(x, Q^2). \quad (2.17)$$

The PDFs are determined by analyzing data of DIS or hadron-hadron collisions. Factorization theorems [11] allow the DIS cross section to be separated into the product of perturbatively calculable subprocesses and non-perturbative PDFs, see (Eq. 2.8). The non-perturbative part is in the structure functions.

PDFs are considered to be universal, that is they are independent of the underlying physical process. This allows to determine PDFs from a global analysis over data sets from different experiments.

Unpolarized PDFs are parameterized up to next-to-next-to leading order (NNLO) from global data by several groups. For the purpose of this analysis, they can be categorized in two groups.

The first group corresponds to those that have tuned their PDFs to LHC data, amongst others ABM12 [12] and HERAPDF [13], usually at $Q^2 > 1000 \text{ (GeV/c)}^2$. Using their PDFs would need to extrapolate the PDFs to the Q^2 region of COMPASS with corresponding large uncertainties.

The other group includes data in the Q^2 region where COMPASS data are taken, that is for values of Q^2 below $\sim 35 \text{ (GeV/c)}^2$. The most recent available PDF sets are from MMHT, MSTW, NNPDF, and CTEQ. The ones used in this analysis are: MSTW08 [14], MMHT14 [15], NNPDF2.3 [16], NNPDF3.0 [17], and CT10 [18]. MMHT14 supersedes the data set of MSTW08 and NNPDF3.0 supersedes the data set of NNPDF2.3. In addition to the existing data sets, both have included recent LHC data into their fits.

2. Deep Inelastic Scattering

Since the analysis is performed in LO, only LO PDFs will be taken into account. The LO PDFs of the light quark flavors and the gluon of MSTW08, MMHT14, NNPDF2.3, NNPDF3.0, and CT10 are compared in Fig. 2.5.

The parametrizations have similar shape and size for the valence quarks, but vary for the sea quarks. The strange quark distribution is the least best determined light quark PDF. Not only it is affected by large uncertainties but its shape differs significantly between the different parametrizations.

Electrons and muons interact with the nucleon by exchanging photons. Since they are weighted by their squared charge, they give only access to the sum of quark and antiquark PDFs $q + \bar{q}$. To determine separate PDFs of quarks or antiquarks, data from experiments with deep inelastic neutrino scattering off nucleons is used. The neutrinos interact with quarks by exchanging W bosons, which are charge and helicity sensitive. Left handed neutrinos couple to left handed negatively charged quarks (d_L, s_L), while right handed anti-neutrinos couple to right handed positively charged antiquarks (\bar{u}_R, \bar{c}_R).

Due to the low cross section of neutrinos, this is experimentally not feasible for polarized DIS. In order to determine polarized PDFs, knowledge of the fragmentation process into final state hadrons from DIS scattering is necessary.

2.4. Semi-Inclusive Deep Inelastic Scattering

To obtain additional information of the quark and gluon substructure of the nucleon, information of the final state hadrons is needed. In semi-inclusive DIS (SIDIS) parts of the final state hadrons are detected in addition to the scattered lepton. A schematic representation of the SIDIS process is illustrated in Fig. 2.6. The incoming lepton scatters off a quark inside the nucleon. Thereby the virtual photon transfers the four-momentum q to the quark. The struck quark then fragments into final state hadrons. The fragmentation is described by fragmentation functions which are discussed in Sect. 2.5. To describe the SIDIS process for a fixed energy E , five independent variables are needed. Together with x and Q^2 , already used to describe the inclusive DIS cross section, it is common to use the azimuthal angle ϕ between the scattering plane of the lepton and the final state hadron, the transverse momentum p_t , and the fraction of the virtual photon energy carried by the final state hadron

$$z = \frac{P \cdot p_h}{P \cdot q} \stackrel{\text{lab}}{=} \frac{E_h}{\nu}, \quad 0 \leq z \leq 1, \quad (2.18)$$

with the final state hadron momentum and energy p_h and E_h , respectively.

The spin-averaged cross section of the one-photon-exchange contribution can be written with four independent hadronic structure functions $H_i(x, Q^2, z, p_t^2)$:

2.4. Semi-Inclusive Deep Inelastic Scattering

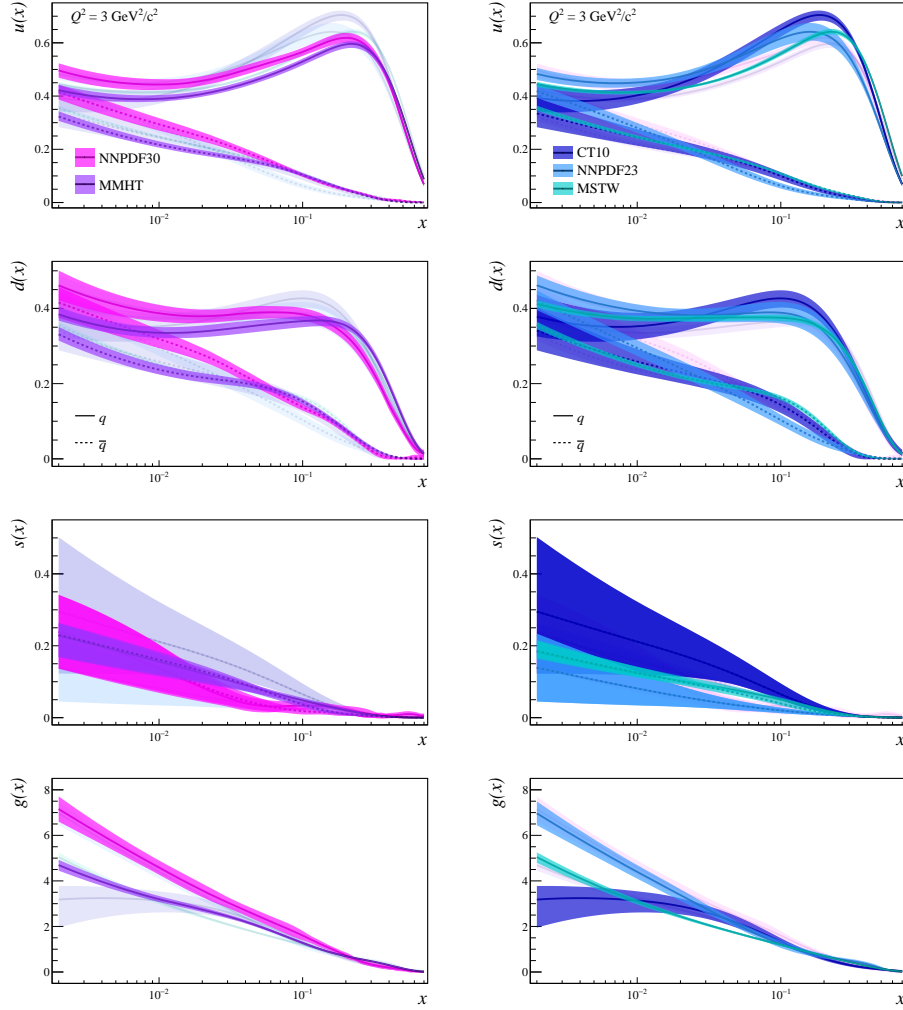


Figure 2.5.: Comparison of LO PDF parametrizations from MMHT14, MSTW08, and NNPDF2.3, NNPDF3.0, and CT10 for $Q^2 = 3 (\text{GeV}/c)^2$. The solid line represents the distribution of quarks and the dashed line the ones for anti-quarks. The plots on the left and on the right side show the same PDFs but the ones on the left highlight NNPDF3.0 and MMHT14, while the ones on the right highlight MSTW08, NNPDF2.3, and CT10. The PDF values are taken from [19].

2. Deep Inelastic Scattering

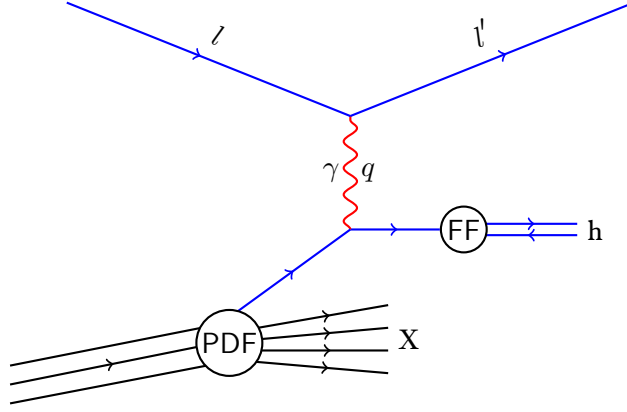


Figure 2.6.: Schematic representation of the SIDIS scattering process.

$$\begin{aligned} \frac{d\sigma^h}{dx dQ^2 dz dp_t^2 d\phi} = & \frac{4\pi\alpha^2}{xQ^4} \left[xy^2 H_1 + (1-y) H_2 \right. \\ & + \frac{2p_t}{Q} (2-y) (1-y)^{\frac{1}{2}} \cos\phi H_3 \\ & \left. + \frac{p_t^2}{Q^2} (1-y) \cos 2\phi H_4 \right]. \end{aligned} \quad (2.19)$$

Integrating over ϕ eliminates the dependencies on H_3 and H_4 . Integrating over p_t^2 allows to express the cross section in terms of only two independent and dimensionless hadronic structure functions $F_i^h(x, Q^2, z)$ similar to the DIS case:

$$\begin{aligned} \frac{d\sigma^h}{dx dQ^2 dz} = & \frac{4\pi\alpha^2}{xQ^4} \left[xy^2 F_1^h(x, Q^2, z) \right. \\ & \left. + \left(1 - y - \frac{x^2 y^2 M^2}{Q^2} \right) F_2^h(x, Q^2, z) \right]. \end{aligned} \quad (2.20)$$

Through the Callan-Gross relation $2xF_1^h = F_2^h$, Eq. (2.20) may be rewritten as:

$$\frac{d\sigma^h}{dx dQ^2 dz} = \frac{2\pi\alpha^2}{xQ^4} \left[1 + (1-y)^2 - 2\frac{x^2 y^2 M^2}{Q^2} \right] F_2^h(x, Q^2, z). \quad (2.21)$$

The SIDIS cross section is similar to the DIS cross section (Eq. (2.8)) but the structure function F_2^h depends on additional information of the final state hadron, that is on the kinematic variable z .

2.5. Fragmentation Functions

In SIDIS energy and momentum are transferred to the struck quark. For high enough values of Q^2 the momentum of the quark becomes large enough to escape the nucleon. Due to confinement new quark-antiquark pairs are created. Together with the struck quark or the spectator quarks (the not struck quarks in the nucleon), they recombine to new hadrons. The production of hadrons originating from the struck quark is called current or quark fragmentation. The fragmentation process of a quark of flavor q into a final state hadron of type h is described by fragmentation functions (FFs) denoted as $D_q^h(z, Q^2)$. Since all quarks eventually fragment into final state hadrons the following sum rule must hold:

$$\sum_h \int_0^1 z D_q^h(z, Q^2) dz = \sum_h \int_0^1 z D_{\bar{q}}^h(z, Q^2) dz = 1. \quad (2.22)$$

The fragmentation is independent of the physical process from which the fragmenting quark originates, amongst others SIDIS, semi-inclusive e^-e^+ annihilation (SIA), or hadron-hadron collisions. Thus, the FFs are universal, as well as the PDFs, which allows to factorize the scattering process into PDFs and FFs. In LO the hadronic structure function F_2^h has a form similar to its inelastic counterpart (Eq. (2.10)):

$$F_2^h = x \sum_q e_q^2 \left[q(x, Q^2) D_q^h(z, Q^2) + \bar{q}(x, Q^2) D_{\bar{q}}^h(z, Q^2) \right]. \quad (2.23)$$

If the hadrons originate from the spectator quarks one speaks of target fragmentation. In the rest frame of the target, the produced hadrons have relative low momenta and the fragmentation is described by more complex fracture functions [22].

The concept of factorization cannot be applied to the region of target fragmentation. To get a pure data sample for the extraction of FFs, the two regions must be separated. In the center-of-mass frame (CMS) it is expected that the current fragmentation happens in forward direction and the target fragmentation in backward direction [23]. The rapidity y_h is a useful variable to distinguish the two regions. For a final state hadron h the rapidity is defined as:

$$y_h = \frac{1}{2} \ln \left[\frac{E_h + p_{h,L}}{E_h - p_{h,L}} \right], \quad (2.24)$$

2. Deep Inelastic Scattering

being E_h the hadron energy and $p_{h,L}$ its momentum longitudinal to the momentum transfer q . In the CMS the rapidity is positive for hadrons moving in forward direction and negative for hadrons moving in backward direction. The maximum kinematically allowed rapidity is given by $Y = \ln W^2 = \ln [Q^2(1-x)/x]$.

To be distinguishable in experiment, the current and target fragmentation regions need to be separated by large enough momentum. It has been established experimentally that this is the case for $\Delta y_h > 2$. This is often referred as the Berger criterion [20].

Not only quarks but also gluons fragment into final state hadrons. Their FFs are denoted by $D_g^h(z, Q^2)$. However, the leptons in SIDIS do not interact directly with the gluons inside the nucleon. Instead after the energy transfer by the virtual photon, the gluons only enter through the DGLAP equations. This can also be seen from the equation for the LO structure function (Eq. 2.23), where the gluons have no direct contribution. For higher order equations the gluon FFs are convoluted with their PDF, see Ref. [28] as an example.

To determine the FFs from SIDIS data, a measurable quantity is needed. Combining Eqs. (2.10, 2.8, 2.21, and 2.23) one can define the hadron multiplicity:

$$\begin{aligned} M^h(x, Q^2, z) &= \frac{1}{\sigma_{\text{tot}}} \frac{d\sigma^h}{dz} = \frac{1}{\sigma_{\text{DIS}}} \frac{d\sigma^h}{dx dQ^2 dz} \\ &= \frac{\sum_q e_q^2 \left[q(x, Q^2) D_q^h(z, Q^2) + \bar{q}(x, Q^2) D_{\bar{q}}^h(z, Q^2) \right]}{\sum_q e_q^2 \left[q(x, Q^2) + \bar{q}(x, Q^2) \right]}. \end{aligned} \quad (2.25)$$

The hadron multiplicity can be determined experimentally by measuring the amount of produced final state hadrons of type h per DIS events. To extract the FFs from the multiplicities, the FFs are parameterized and Eq. (2.25) is fitted to the experimental multiplicities. More precisely the χ^2 sum

$$\chi^2 = \sum_j \frac{(T_j - M_j)^2}{\sigma_j^2}, \quad (2.26)$$

is minimized, where T_j and M_j are the theoretical and experimental multiplicities, respectively, weighted by the experimental uncertainties. The sum is extended over the number of measured data points j .

A detailed description of the fitting process is given in Sect. 5.1 as it is specific to this particular analysis.

2.5.1. Kaon Fragmentation Functions

The goal of this thesis is the extraction of kaon FFs. Kaons are mesons having a valence quark configuration of an up or down quark (antiquark) and a strange

antiquark (quark) pair. They are named as:

$$\begin{aligned} K^+ &= u\bar{s} \\ K^- &= \bar{u}s \\ K^0 &= d\bar{s} \\ \bar{K}^0 &= \bar{d}s \end{aligned}$$

The K^0 and \bar{K}^0 decay weakly into two and three pion states, that is into states of different parity. Thus, the decay of neutral kaons is a parity violating process. This can be understood with the introduction of intermediate pionic states

$$K^0 \longleftrightarrow \left\{ \begin{array}{c} 2\pi \\ 3\pi \end{array} \right\} \longleftrightarrow \bar{K}^0$$

that both the K^0 and the \bar{K}^0 can transform into [25].

In other words, the K^0 and \bar{K}^0 create mixed states through the weak interaction. If applied separately, the weak interaction violates parity (P) and charge conjugation (C). However, it stays invariant under the combined parity and charge conjugation (CP). Thus, it is possible to represent neutral kaons in a basis of CP eigenstates

$$\begin{aligned} |K_S^0\rangle &= \frac{1}{\sqrt{2}} (|K^0\rangle - |\bar{K}^0\rangle) \\ |K_L^0\rangle &= \frac{1}{\sqrt{2}} (|K^0\rangle + |\bar{K}^0\rangle) \end{aligned}$$

where K_S^0 and K_L^0 decay into two and three pions, respectively. Their names K-short and K-long are references to their lifetime. Due to the smaller available phase space for the decay into three pions, the lifetime of K_L^0 is longer than that of K_S^0 . The K^+ and K^- have leptonic and hadronic decay modes. A list with kaon properties and their main decay modes is given in Tab. 2.2.

For each kaon: K^+ , K^- , K^0 , and \bar{K}^0 , a set of FFs exists containing the FFs for all quark flavors. A FF is called favored if the struck quark is part of the valence quark configuration of the final state hadron, otherwise it is called unfavored. According to Eq. (2.25), the contribution of a quark of flavor q to the multiplicity is: $e_q^2 q(x, Q^2) D_q^h$, that is the quark's PDF times the FF weighted by its charge squared. In the nucleon, the heavier quark flavors charm and bottom only occur as sea quarks produced from gluons splitting into quark-antiquark pairs. For the production of heavier quark flavors a larger phase-space is needed. Thus, heavier quarks are less likely to be found inside the nucleon and they are neglected for the purpose of this work. Only the light quark flavors up, down, and strange are taken into account, adding six FFs to each kaon. Thus, the total number of independent

2. Deep Inelastic Scattering

Particle	quark composition	mass $[\text{MeV}/c^2]$	lifetime [s]	main decay modes	branching ratio
K^+	$u\bar{s}$	493.667 ± 0.013	$(1.2379 \pm 0.0021) \times 10^{-8}$	$\mu^+ + \nu_\mu$ $\pi^+ + \pi^0$	63.56 ± 0.11 20.67 ± 0.08
K^-	$\bar{u}s$			$\pi^+ + \pi^+ + \pi^-$	5.583 ± 0.024
K_S^0	$\frac{1}{\sqrt{2}}(d\bar{s} - s\bar{d})$	497.611 ± 0.016	$(8.954 \pm 0.004) \times 10^{-11}$	$\pi^+ + \pi^-$ $\pi^0 + \pi^0$	69.20 ± 0.05 30.69 ± 0.05
K_L^0	$\frac{1}{\sqrt{2}}(d\bar{s} + s\bar{d})$	497.611 ± 0.016	$(5.099 \pm 0.021) \times 10^{-8}$	$\pi^\pm + e^\mp + \nu_e$ $\pi^\pm + \mu^\mp + \nu_\mu$ $\pi^0 + \pi^0 + \pi^0$ $\pi^+ + \pi^- + \pi^0$	40.55 ± 0.11 27.04 ± 0.07 19.52 ± 0.12 12.54 ± 0.05

Table 2.2.: List of kaon properties and their most common decay channels taken from [10].

2.5. Fragmentation Functions

quark-to-kaon FFs is 24. This number can be reduced by applying isospin and charge invariance.

Applying charge invariance yields two favored FFs for both the charged and neutral kaons. For historic reasons the favored FFs of u , d , \bar{u} , and \bar{d} quarks are denoted as D_{fav}^h and the favored FFs of s and \bar{s} quarks as D_s^h :

$$\begin{aligned} D_{\text{fav}}^{K^+} &\equiv D_u^{K^+} = D_{\bar{u}}^{K^-} \\ D_s^{K^+} &\equiv D_s^{K^+} = D_{\bar{s}}^{K^-} \\ D_{\text{fav}}^{K^0} &\equiv D_d^{K^0} = D_{\bar{d}}^{\bar{K}^0} \\ D_s^{K^0} &\equiv D_s^{K^0} = D_{\bar{s}}^{\bar{K}^0} \end{aligned} \quad (2.27)$$

With the additional assumption that all unfavored FFs are equal the number of independent FFs is further reduced:

$$\begin{aligned} D_{\text{unf}}^{K^+} &\equiv D_d^{K^\pm} = D_{\bar{d}}^{K^\pm} = D_{\bar{u}}^{K^+} = D_u^{K^-} = D_s^{K^+} = D_{\bar{s}}^{K^-} \\ D_{\text{unf}}^{K^0} &\equiv D_u^{K^0/\bar{K}^0} = D_{\bar{u}}^{K^0/\bar{K}^0} = D_{\bar{d}}^{K^0} = D_d^{\bar{K}^0} = D_s^{K^0} = D_{\bar{s}}^{\bar{K}^0} \end{aligned} \quad (2.28)$$

Isospin symmetry and charge symmetry relates K^0 , \bar{K}^0 , and K^\pm fragmentation functions:

$$\begin{aligned} D_{\text{fav}}^K &\equiv D_{\text{fav}}^{K^0} = D_{\text{fav}}^{K^+} \\ D_s^K &\equiv D_s^{K^0} = D_s^{K^+} \\ D_{\text{unf}}^K &\equiv D_{\text{unf}}^{K^0} = D_{\text{unf}}^{K^+} \end{aligned} \quad (2.29)$$

These relations allow to extract the kaon FFs through a combined analysis of charged and neutral kaons. A more detailed derivation of the kaon FFs can be found in A.2.1.

The most recent attempts to extract kaon FFs are made by AKK [27], DSS[28], and HKNS [29]. They all use semi-inclusive e^+e^- annihilation (SIA) data from measurements of ALEPH [30], OPAL [31], and DELPHI [32] taken at CERN, and measurements of TPC [33] and SLD [34] taken at SLAC (Stanford Linear Accelerator Center). HKNS use in addition SIA data from HRS [35] and TOPAZ [36],

2. Deep Inelastic Scattering

also located at SLAC, and data from TASSO [37, 38, 39] at DESY (Deutsches Elektronen-Synchrotron). AKK and DSS use additional data of heavy ion collisions at RHIC (Relativistic Heavy Ion Collider) from measurements of PHENIX [40], STAR [41], and BRAHMS [42]. Furthermore DSS are using SIDIS preliminary proton data from the HERMES collaboration [43] at DESY.

Their results for LO and NLO are presented in Fig. 2.7. It is common to show the results for $zD_q^h(z, Q^2)$ because the integral of $\int zD_q^h(z, Q^2) dz$ is the average number of final state hadrons of type h , that are produced when a quark of type q is struck. The first two rows show the results for the two favored FFs: D_{fav}^K and D_s^K . The results of the unfavored FF D_{unf}^K and the gluon FF D_g^K are presented in the third and the bottom row, respectively. Thereby the left column shows results in NLO and the right column results in LO. AKK published only NLO FFs and no gluon FF. As expected both favored FFs D_{fav}^K and D_s^K are larger than the unfavored FF. Furthermore, the strange FF D_s^K is larger than the FF of favored u and d (anti)quarks D_{fav}^K . This can be explained due to the about three times larger energy that is needed to produce a $s\bar{s}$ pair from vacuum when starting with a struck u, \bar{u} , d, or \bar{d} quark compared to a $u\bar{u}$ or $d\bar{d}$ pair when starting with a struck s or \bar{s} quark. Thus, naively D_s^K is expected to be three times larger than D_{fav}^K .

The FFs from AKK and HKNS have a similar shape and size. This can be expected as they both rely mainly on the same set of SIA data.

In contrast, the parametrization of DSS is different in shape and size. The differences between DSS and the other parametrizations might occur because of the usage of additional SIDIS data. With this data the contribution of the strange quarks can be constrained. This shows the importance of new SIDIS data for the extraction of FFs.

2.5. Fragmentation Functions

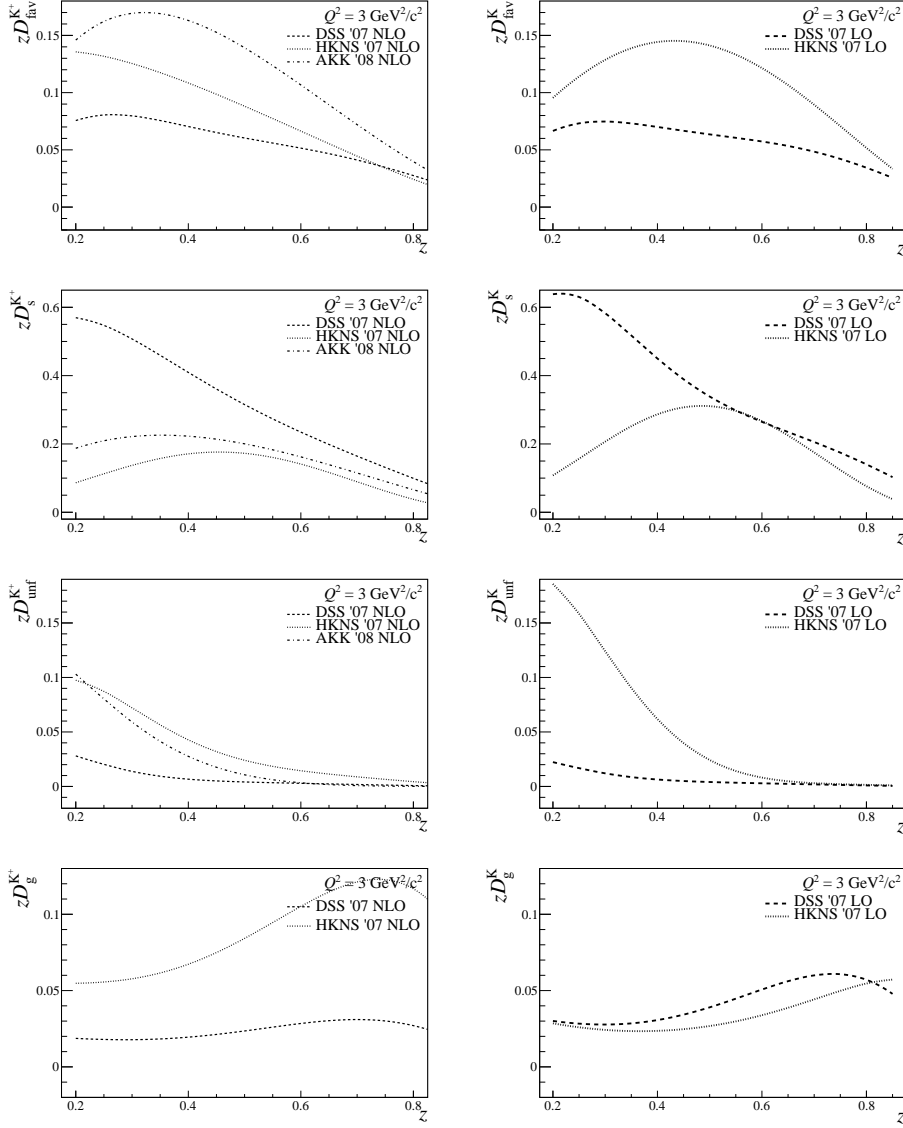


Figure 2.7.: Comparison of NLO (left) and LO (right) FFs extracted from DSS, AKK, and HKNS at $Q^2 = 3 \text{ GeV}^2/c^2$. The FF values are generated with [45].

3. The COMPASS Experiment

For the extraction of K_S^0 multiplicities from DIS, precise knowledge of the incoming and scattered leptons and the outgoing final state hadrons is necessary. Therefore a precise kinematic event reconstruction, including particle identification with good mass resolution, must be achieved. To achieve enough statistics in K_S^0 production, high luminosity and high trigger rates are needed. The COMPASS experiment located at CERN in Geneva meets these requirements and thus it is ideally suited for this task. It is a fixed target experiment with a two-stage spectrometer with a polar coverage of 180 mrad and a large momentum range. It has a versatile setup with two main physics programs: the hadron program and the muon program.

The hadron program is set to investigate the hadronic structure with hadron spectroscopy and search for exotic states. In Primakoff scattering ($\pi N \rightarrow \pi N \gamma$) the electric and magnetic polarisabilities of pions are measured. The Drell-Yan reaction [46] ($\pi N \rightarrow \mu^- \mu^+ X$) is utilized to measure the muon pair production from annihilation of quarks and antiquarks from beam and target particles. This process is practically reverse lepton scattering.

The muon program aims to investigate the subnuclear structure of the nucleon. Its main goals are to determine the composition of the longitudinal and transversal nucleon spin structure, with special interest in the helicity contribution from the gluon.

Fig. 3.1 shows the experimental setup for the muon program as it was used in 2006. The experimental setup can be divided into three parts: The first part are the beamline detectors and the target. The second and third parts are the Large Angle Spectrometer (LAS) and the Short Angle Spectrometer (SAS) located downstream from the target. The coordinate system used in the following is indicated in Fig. 3.1. The origin lies in the target center with the x and y -axes being horizontal and vertical, respectively, The z -axis is parallel to the beamline.

Both spectrometers have a similar layout with tracking detectors in front of and behind a dipole magnet, followed by electromagnetic and hadron calorimeters. They are completed by muon filter stations for muon identification. The LAS has an additional RICH detector for hadron identification. The specific experimental setup depends on the requirements given by the physics program. In the following sections the beamline, the Large Angle Spectrometer (LAS), the Small Angle Spectrometer (SAS), the particle identification, the trigger system, and event reconstruction for the muon setup in 2006 are described. A detailed description of

3. The COMPASS Experiment

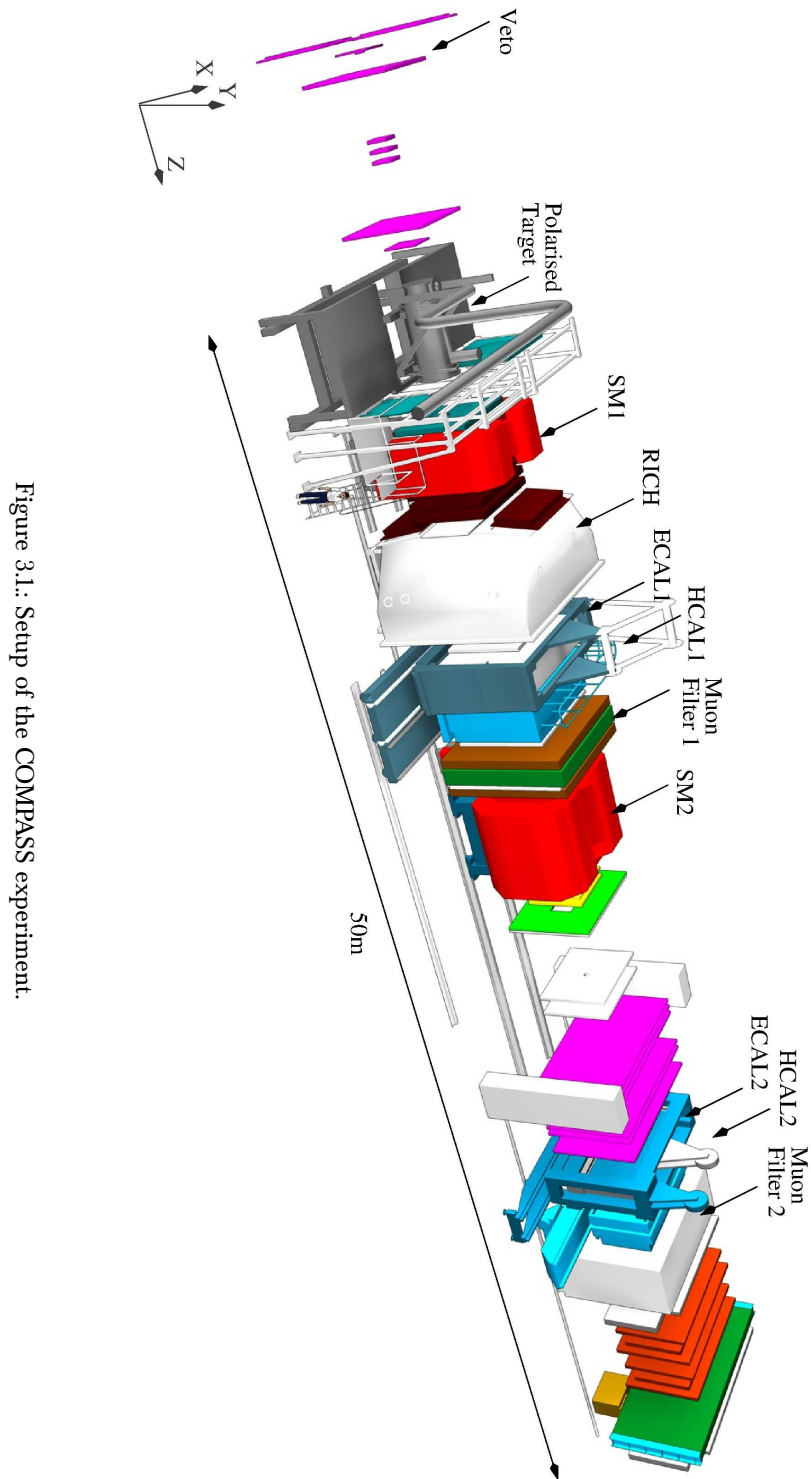


Figure 3.1.: Setup of the COMPASS experiment.

the COMPASS experiment can be found in [47].

3.1. Beamline

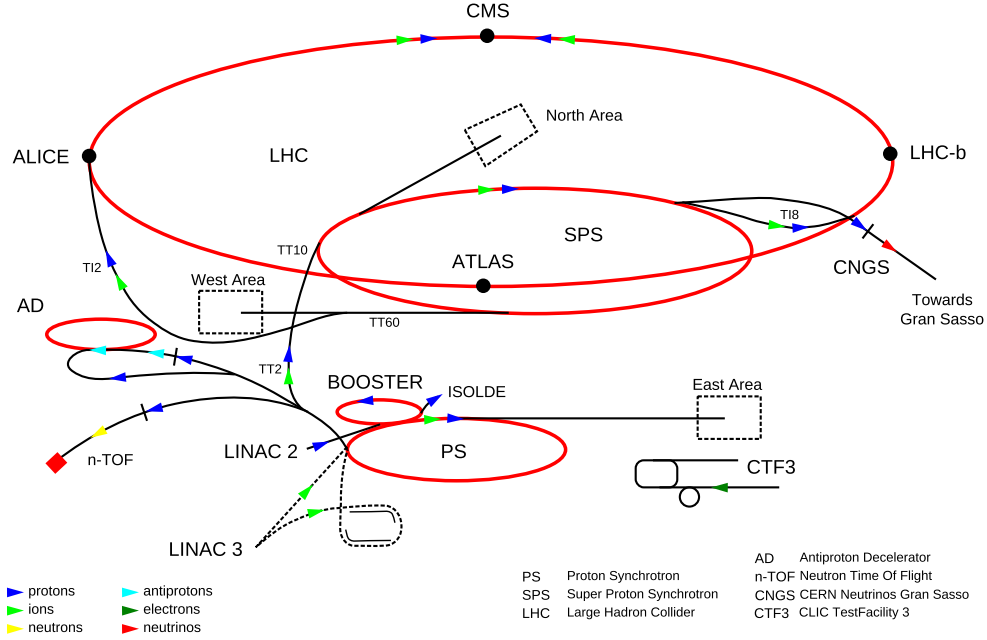


Figure 3.2.: Overview of the beamline at CERN. The COMPASS experiment is located in the north area. The picture is taken from [48].

Fig. 3.2 shows the CERN beamline system. The COMPASS experiment is located in the North Area at the Super Proton Synchrotron (SPS). Linac 2 accelerates protons to 50 MeV/c and injects them into the Booster of the Proton Synchrotron (PS). In the booster the protons are accelerated to 1.4 GeV/c and injected into the PS. The PS accelerates the protons to 25 GeV/c and injects them into the SPS, where they are accelerated up to 450 GeV/c. One SPS cycle from injection over acceleration to extraction has a duration of 16.8 s. The protons are extracted into the North Area and split among several experiments. Per SPS cycle about $1.2 \cdot 10^{12}$ protons are extracted in 4.8 s long spills into the M2 beamline leading to COMPASS. A schematic view of the M2 beamline is given in Fig. 3.3. The protons hit Beryllium target (T6) of various thickness (4, 10, 50 cm) depending on the desired intensity for the experiment. During normal operation, the target with 50 cm thickness is used, yielding a high-intensity secondary beam. In the Beryllium target a pion beam with about 4% kaon contamination is produced via $p + \text{Be} \rightarrow K^+, \pi^+ + X$. Two movable absorbers (Tax) are used to remove other

3. The COMPASS Experiment

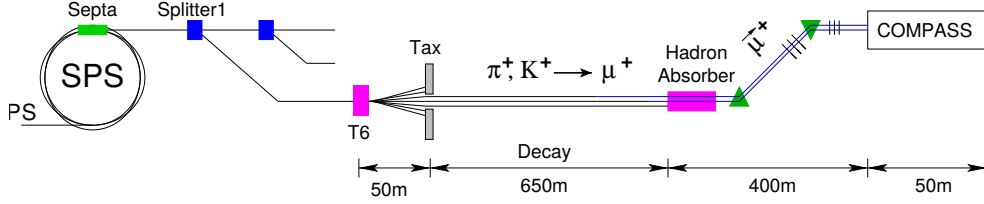


Figure 3.3.: Schematic view of the M2 beamline.

particles from the beam by momentum and direction selection. On the following 650 m long beam pipe pions and kaons decay amongst others into muons via the process $\pi^+, K^+ \rightarrow \mu^+ + \nu_\mu$. Behind the channel a hadron absorber, consisting of nine 1.1 m thick modules of Beryllium, blocks all remaining hadrons but lets muons through. Bending and focusing quadrupole magnets lead the muon beam to the experimental hall. About 100 m upstream of the experimental hall a beam momentum station (BMS) measures the muon momenta on an event-by-event basis.

3.2. The Target System

The muon and the hadron program have different requirements on the target. In 2004 the hadron program required a target with large atomic numbers for Primakoff scattering and a target with low atomic numbers for studies on diffractive meson production. For Primakoff scattering lead was chosen as the main target material. Copper and carbon targets were used for systematic studies. The carbon target was also used to perform a parallel study of diffractive meson production where a target with low atomic numbers is required. Since both measurements imply a small momentum transfer, a recoil detector barrel, acting as a veto detector, was set up around the target.

To measure cross section asymmetries, needed for the muon program, a polarized target is required. It consists of target cells surrounded by a microwave cavity, solenoid and dipole magnets and a cryostat. In 2006 deuterated Lithium (${}^6\text{LiD}$) was chosen as isoscalar target material. The target material is polarizable up to $> 50\%$ with a fraction of polarizable material of the order of 0.35.

The composition of ${}^6\text{LiD}$ is approximately that of a spin-0 ${}^4\text{He}$ nucleus and a deuteron. The isoscalar target consists of an equal number of protons and neutrons. Consequently the muons scatter off the same number of up and down valence quarks. This isoscalar composition allows for the extraction of deuteron multiplicities parallel to asymmetry measurements. Thus, the isoscalar target enables to measure the multiplicities, and from those to determine FFs, in the channel $\mu(\text{pn}) \rightarrow \mu' hX$.

3.3. Large and Small Angle Spectrometers

The target material is contained at the center of the polarized target in three cylindrical target cells of 3 cm diameter separated by 5 cm gaps. The upstream and downstream target cells have a length of 30 cm, while the center target cell is twice as long (60 cm). The target cells are surrounded by a microwave cavity, a superconducting solenoid that produces a 2.5 T longitudinal field and a dipole magnet with an 0.42 T transverse field. To exclude false asymmetries, the parallel and anti-parallel spin states are measured at the same time. Therefore the up- and downstream target cells have opposite polarization with respect to the center target cell. Furthermore the longitudinal field is rotated frequently to avoid false asymmetries caused by different acceptances of the target cells. The target material is polarized with dynamic nuclear polarization (DNP), in which the electron spin is transferred to the nuclear spins using a microwave field. To minimize the relaxation of the polarization, a $^3\text{He}/^4\text{He}$ mix is used to cool the target cavity down to 3 K.

3.3. Large and Small Angle Spectrometers

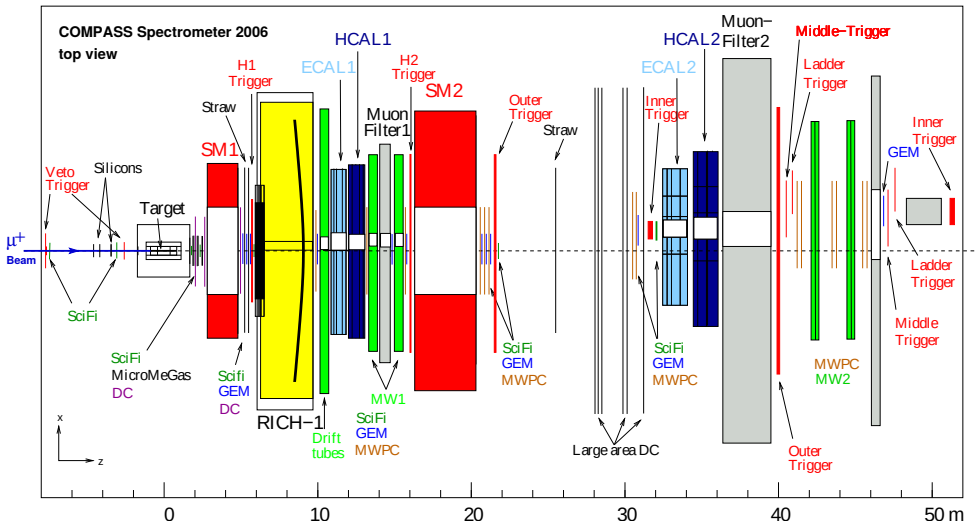


Figure 3.4.: Top view of the COMPASS experiment setup of 2006.

The COMPASS experiment contains two spectrometers. Its setup is shown in Fig. 3.4. The Large Angle Spectrometer (LAS) is located downstream of the target with a design goal of 180 mrad polar acceptance. LAS is capable to identify hadrons with momentum ranging from a few GeV/c to 43 GeV/c. The Small Angle Spectrometer (SAS) is located directly behind LAS. It is designed to detect particles with momenta greater than 5 GeV/c at small angles up to 30 mrad.

3. The COMPASS Experiment

Both spectrometers have the same basic setup but the detector specifications and dimensions are adapted to meet their design requirements. In the following detectors of LAS have the subscript 1, detectors of SAS have the subscript 2. The center of the spectrometers are dipole magnets SM1 and SM2 with field strengths of 1 Tm and 4.4 Tm, respectively. Their field is vertical so that the particles are bent in the horizontal plan. In front of and behind each magnet there are tracking detectors installed to identify charged particles. They are followed by electromagnetic calorimeters ECAL1 and ECAL2 and hadron calorimeters HCAL1 and HCAL2, respectively. Each spectrometer is completed by a muon wall system for muon identification. In addition to the basic setup, LAS has a RICH detector in between SM1 and ECAL1. The detectors of LAS have a hole in the central area that matches the acceptance of SAS where no detector material has been placed. Detectors of SAS have a hole for the primary beam only.

3.3.1. Tracking detectors

The COMPASS tracking system has several tracking stations, distributed over the entire length of the experiment. Their purpose is to track the incoming and outgoing beam particles and charged reaction products. A tracking station consists of a set of detectors of the same type, located at almost the same z position but with different spatial orientation.

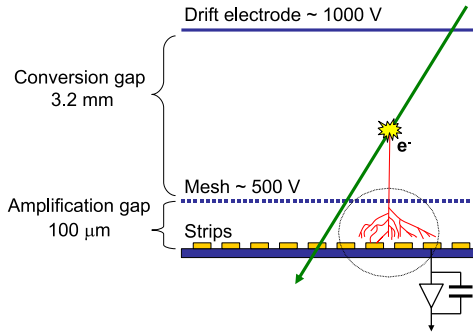
The terms X- and Y-plane are used to refer to detectors that measure horizontal and vertical coordinates, respectively. Detectors in the U- and V-plane are rotated by a few degrees clockwise and counter-clockwise, respectively, around the z -axis. The additional detector planes enable to detect multiple hits in a detector. The tracking detectors are grouped as Very Small Area Trackers (VSAT), Small Area Trackers (SAT) and Large Area Trackers (LAT). VSAT detectors cover the area in and around the beamline up to a radial distance of 3 cm. Due to the high beam intensity of up to $10^5 \text{ s}^{-1} \text{ mm}^{-2}$ in that area, very high spatial and temporal resolutions are required to distinguish between hits of different particles. Eight scintillating fiber (SciFi) detectors and three silicon microstrip detectors fulfill this task. SAT detectors cover a radial distance from 2.5 to 40 cm. In this region Gas Electron Multipliers (GEMs) and Micromegas are employed. The outer regions are covered by LAT detectors. Here drift chambers (DC), straw tube chambers and multiwire proportional counters are used.

(Very) Small Area Tracking Detectors

Scintillating Fibers (SciFi) SciFi stations are applied to identify incoming and outgoing beam particles and charged particles close to the beamline. Each station consists of two or three SciFi detectors with different X, Y, U and V orientations. A SciFi detector itself consists of up to 14 layers of scintillating fibers placed in paral-

lel, with 0.5 – 1 mm diameter, whereas stations further upstream have more layers. Their active area is from $3.9 \times 3.9 \text{ cm}^2$ in front of the target up to $12.9 \times 12.9 \text{ cm}^2$ downstream SM2. The produced light is transported via optical non-scintillating fibers to photomultipliers and pipelined leading edge discriminators and TDCs for readout. The time resolution is between 350–450 ps. SciFi stations are part of VSAT and SAT.

Silicon Microstrip Detectors As part of VSAT, three silicon microstrip detector stations are positioned upstream of the target. Their purpose is the tracking of incoming beam particles. A silicon microstrip detector consists of two $5 \times 7 \text{ cm}^2$ silicon wafers. Both wafers are bonded with $54.6 \mu\text{m}$ pitched silicon strips. One wafer is bonded with n-type silicon strips, the other with p-type silicon strips. The n-type strips are orthogonal to the p-type strips, providing two dimensional position information. Each station consists of two silicon microstrip detectors. One detector measures the X- and Y- plane while the other detector is rotated by 5° measuring the U- and V-plane. A spatial resolution of up to $14 \mu\text{m}$ is achieved.



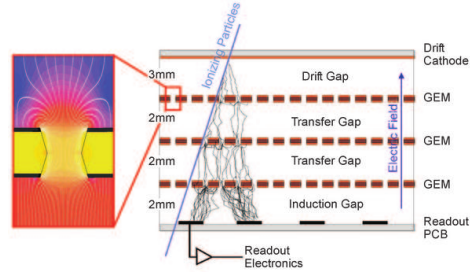
Micromegas Three stations of Micromegas, short for micromesh gas chambers, are part of SAS. Their purpose is to track charged particles between the target and SM1. Each station consists of four $40 \times 40 \text{ cm}^2$ detector planes (X, Y, U, V) where U and V are rotated by $\pm 45^\circ$ with respect to the beam axis. A detector plane consists of a parallel plate electrode structure filled with a gas mixture. A metallic

micromesh divides the structure in a 3.2 mm conversion and a $100 \mu\text{m}$ amplification gap. The ionization takes place in the conversion gap. There the primary electrons of the ionization process are accelerated with 1 kV/cm and drift towards the amplification gap. Due to the small distance of $100 \mu\text{m}$ of the amplification gap, the width of the captured signal is about 100 ns. Once inside, the electrons are accelerated with 50 kV/cm resulting in an avalanche of electron/ion pairs. The readout is done by parallel microstrips of $360 \mu\text{m}$ (center) and $420 \mu\text{m}$ (outer part) pitch, on one side of the electrode structure. A mean time resolution of 9.3 ns and a spatial resolution of $90 \mu\text{m}$ is achieved.

3. The COMPASS Experiment

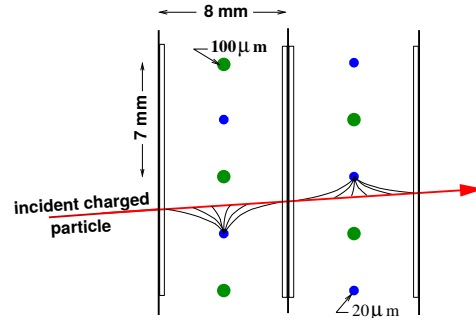
Gas Electron Multiplier (GEM)

Gas Electron Multiplier (GEM) detectors are another type of microstrip gas detectors used in the COMPASS experiment. Three GEM amplification stages are inserted between two parallel plate electrodes inside a gas (Ar/CO₂) filled chamber. A GEM amplification stage is a 50 μm thick Kapton foil with 5 μm copper cladding on both sides. About $10^4/\text{cm}^2$ holes of diameter 70 μm have been chemically etched in the copper and the foil. Suitable electric fields between the plate electrodes and the GEM stages guide the primary electrons into the holes. A potential difference of about 400 V between the two surfaces of each GEM induces very high electric fields inside the holes. The primary electrons are amplified and an avalanche multiplication occurs. The electric field is chosen such that the electric field strength on the upper foil surface is smaller than on the bottom side. Thus primary electrons are accelerated towards the next GEM stage or the readout anode while the much heavier ions stay near the hole and are collected by the upper foil surface. The readout is done by two sets of readout strips perpendicular to each other, so that two projections are measured simultaneously. A GEM station consists of two GEM detectors with one detector rotated by 45°. Thus, each GEM station measures hits in X-, Y-, U- and V-planes. A time resolution of 12 ns and a spatial resolution of 46 μm is achieved.



Large Area Tracking Detectors

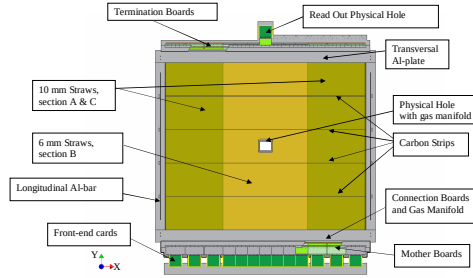
Drift Chambers (DC) Three identical drift chambers (DC) are part of LAT. One is placed upstream and two are placed downstream of SM1. Their active area of $180 \times 127 \text{ cm}^2$ covers the whole acceptance of SM1. Each DC consists of eight layers with four different wire orientations: vertical, horizontal and rotated by $\pm 20^\circ$. Thus, the X, Y, U and V projections are measured simultaneously. Layers with the same orientation are shifted by half a drift cell with respect to each other to resolve left-right ambiguities. Each layer consists of 176 sensitive wires of 20 μm diameter and 177 potential wires of 100 μm diameter, alternately arranged with a distance of 3.5 mm. The layers are enclosed with Mylar cathode foils defining a gas gap of 8 mm. The cathode foils and wire distances define small drift cells of 8×7



3.3. Large and Small Angle Spectrometers

mm^2 . Smaller the drift cells have smaller incident fluxes and electron drift times per cell. This results in shorter time windows and minimized number of correlated particles. A gas mixture of $\text{Ar}/\text{C}_2/\text{H}_6/\text{CF}_4$ was chosen. It combines a high primary electron rate with fast drift times and good spatial resolution. Parallel and orthogonal to the bending plane of SMI the spatial resolutions are $110\ \mu\text{m}$ and $170\ \mu\text{m}$, respectively.

Straw Tubes Straw tube drift chambers are located downstream of SMI. Their purpose is to track charged particles at large scattering angles. One station consists of three straw detectors with an active area of 9 m^2 each. Two detectors measure the X- and Y-plane while the third is rotated by 10° . The tubes are made of two layers of Kapton foil. The inner layer is $40\ \mu\text{m}$ thick carbon loaded Kapton foil that is glued to the outer layer of $12\ \mu\text{m}$ thick aluminium coated Kapton foil. Centered inside the tubes are anodes made of gold-plated tungsten. A gas mixture of $\text{Ar}/\text{CO}_2/\text{CF}_4$ is used as the counting gas. To resolve left-right ambiguities, each detector consists of two staggered layers of tubes. The detectors are divided into three parts with different tube sizes. The tubes in the center region have a diameter of 6 mm, while the tubes in the outer regions have a diameter of 10 mm. The tubes are read out at the bottom side. The detectors spatial resolution is up to $190\ \mu\text{m}$.



Multiwire Proportional Chambers (MWPC) Multiwire Proportional Chambers (MWPC) are the main detectors for tracking particles at large radial distances in SAS. A MWPC consists of several wire layers. The layers are made of wires of 1 m length and a diameter of $20\ \mu\text{m}$, pitched by 2 mm. Each wire layer is enclosed on both sides by Mylar foils to provide field symmetry and enclose the detector gas. The MWPCs are operated with a gas mixture of $\text{Ar}/\text{CO}_2/\text{CF}_4$. A total of 34 wire layers in three different configurations are in use. Two configurations have X-, U-, V- or X-, Y-, U-, V-planes with an active area of $178 \times 120\text{ cm}^2$. The third configuration has X-, V- or X-, U-planes with an active area of $178 \times 80\text{ cm}^2$. With MWPCs a spatial resolution of 1.6 mm is achieved.

Large Area Drift Chambers In SAS, six Large Area Drift Chambers are in use to complete the tracking of charged particles, scattered by a large angle. Each chamber has an active area of $5 \times 2.5\text{ m}^2$ and four wire layers. A wire layer consists of sensitive anode wires pitched by 4 cm and cathode wires with a pitch of 2 mm.

3. The COMPASS Experiment

Two wire layers with the same orientation form a detector plane. To resolve left-right ambiguities, the layers are shifted by half the wire pitch. Two chambers measure hits in XY-planes, the other four measure XV-, XU-, YV- and YU-planes. The Large Area Drift Chambers have a spatial resolution of 0.5 mm.

3.3.2. Particle Identification

Scattered muons are reconstructed by two muon wall systems located downstream of LAS and SAS. The hadron identification is done by a RICH detector in LAS and the hadron and electromagnetic calorimeters in LAS and SAS.

Ring Imaging Cherenkov (RICH)

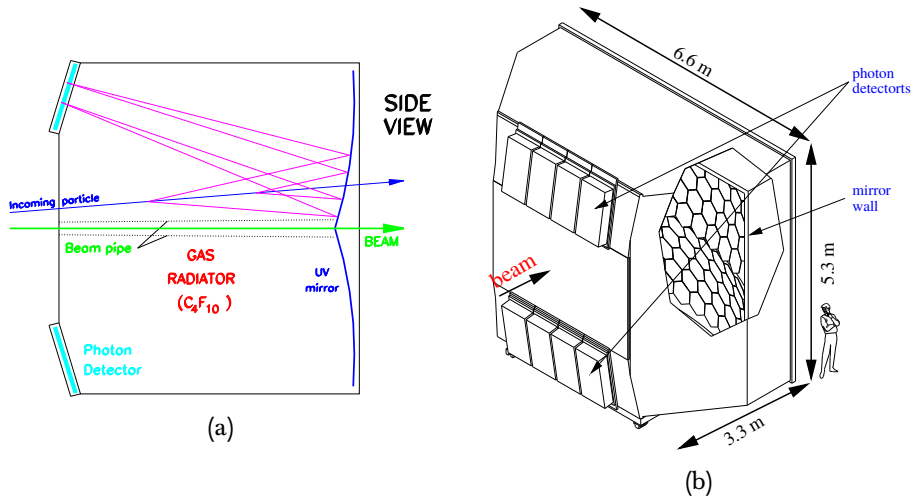


Figure 3.5.: Schematic view of the RICH detector.

The Ring Imaging Cherenkov (RICH) detector is used to identify pions, kaons and protons in the momentum range of about 10–43 GeV/c. Its dimension covers the whole acceptance of LAS. The setup of RICH is shown in Fig. 3.5. Particles enter from the left and produce Cherenkov light inside the radiator gas, a mixture of C₄F₁₀. Two mirrors at the far end of the detector reflect the photons into photon detectors. The mirrors are located outside of LAS acceptance so that they do not interfere with other produced particles. As photon detectors, eight MWPCs with CsI coated photocathodes are used. The angle of the Cherenkov light is measured with a resolution up to 0.5 mrad. Pions and kaons can be separated within 2.5σ .

Muon Wall system

The identification of scattered muons is performed by two muon wall systems, located at the end of LAS and SAS. The muon wall systems consist of an absorber, thick enough to stop incoming hadrons, preceded and followed by tracking detectors (muon walls). A muon is successfully identified, if its track can be reconstructed by both muon walls. The first muon wall system (MW1 system) consists of two stations of squared drift tubes preceding and following a 60 cm thick iron wall. The second muon wall system (MW2 system) is located downstream of SAS. Its absorber is a 2.4 m thick concrete wall. Muons upstream of the absorber are reconstructed by SAS. Downstream of the absorber are two steel drift tube systems for muon reconstruction.

Calorimetry

Both spectrometers, LAS and SAS, have a hadronic and electromagnetic calorimeter each. The hadron calorimeters measure the energy of hadrons and are part of the trigger system. The electromagnetic calorimeters are used to measure electromagnetic showers.

Hadron Calorimeter

The hadron calorimeters HCAL1 and HCAL2 are located upstream of the muon walls MW1 and MW2, respectively. They consist of modules that are arranged in a matrix. The modules are sampling calorimeters, that is they consist of several layers of absorber and scintillator plates. Incoming hadrons produce particle showers in the absorber plates. The showers are either absorbed and re-emitted in the form of light by the intermediate scintillator plates or hit the next absorber plate. The light pulses from the scintillator plates are guided to photomultiplier tubes for readout. The calorimeter's thickness is several radiation length, such that hadrons up to energies of $100 \text{ GeV}/c^2$ are fully absorbed. HCAL1 has a e/π ratio of 1.2 ± 0.1 and a spatial resolution of $\sigma_{x,y} = (14 \pm 2) \text{ mm}$.

Electromagnetic Calorimeter

The electromagnetic calorimeters ECAL1 and ECAL2 consist of lead glass modules arranged in a matrix. Inside, high-energy photons and electrons develop electromagnetic showers. The electrons and positrons from the showers emit Cherenkov light, whose amount is proportional to the energy deposited in the lead glass. Photomultiplier tubes are attached to one end of the lead glass to measure the intensity of the light. ECAL1 is located upstream of HCAL1. Its dimensions cover the $\pm 180 \text{ mrad}$ acceptance of SM1. It measures the energy of low energetic photons and neutral pions. ECAL2 is located upstream of HCAL2.

3. The COMPASS Experiment

3.3.3. Trigger System

The purpose of the trigger system is the selection of suitable events. It triggers the readout of detectors and front-end electronics and provides an event time reference. It is designed to make the write decision in less than 500 ns with a minimum dead time between triggers. The setup is versatile, depending on beam and kinematics, and usually consists of three elements: horizontal and vertical hodoscopes, energy deposits in hadron calorimeters, and veto hodoscopes.

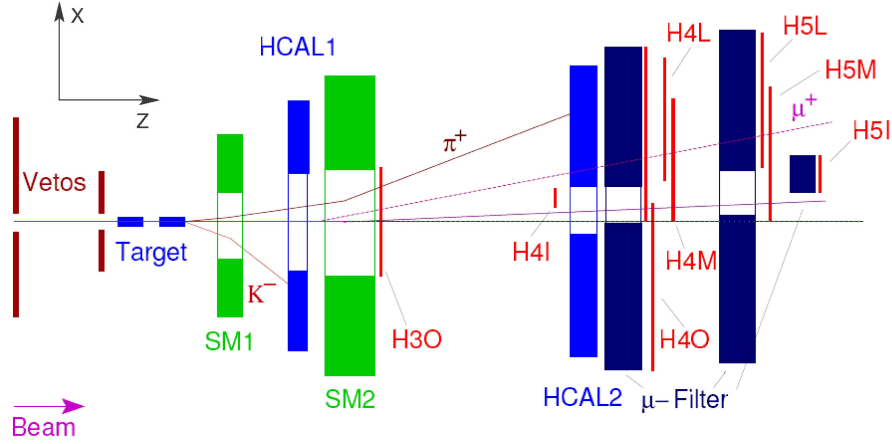


Figure 3.6.: Overview of the trigger components.

For the muon setup an overview of the trigger components is shown in Fig. 3.6. It is designed to trigger on events from $Q^2 \approx 0$ to the maximum allowed by kinematics of about 50 GeV/c and to cover a large range in ν . The hodoscopes are used to trigger on scattered muons. They are subdivided into inner (H4I, H5I), ladder (H4L, H5L), middle (H4M, H5M) and outer (H4O, H5O) trigger systems.

Events with $Q^2 > 0.5 (\text{GeV}/c)^2$ are mainly triggered using scattered muon information in the non-bending plane. Therefore two horizontal hodoscopes measure the scattering angle in θ . The track is then extrapolated to the target position and checked for compatibility.

Fig. 3.7 shows the concept for events with lower Q^2 . These events have muon scattering angles close to zero, making target pointing not feasible. Instead the energy loss is calculated from the bending of the scattered muon in the spectrometer magnets. To measure the bending, the stripes of two vertical hodoscopes are arranged as rows and columns of a coincidence matrix. The matrix holds the coincidences for all combinations of the hodoscope stripes. The coincidence matrix can be set up to only trigger on physical combinations. For example, as shown in the schematic, a virtual diagonal line can be drawn to sets a threshold to the

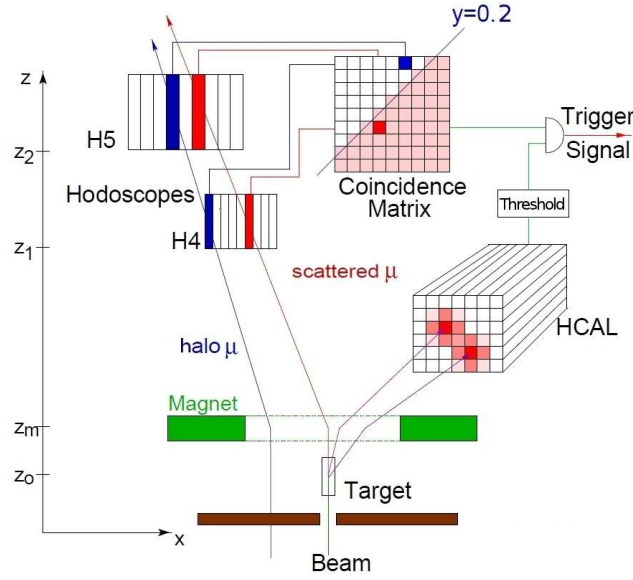


Figure 3.7.: Schematic of the trigger principle.

energy level. To suppress background events such as elastic scattering of electrons or target nuclei, additional energy clusters, corresponding to produced hadrons, are required in the hadron calorimeters.

The muon beam has a large halo that causes unintended triggers in the trigger hodoscopes. To reject triggers caused by halo muons a veto system is installed upstream of the target. Fig. 3.8 shows the side view of the veto system. It consists of veto hodoscopes with a central window for beam muons. If the veto system detects a halo muon the event is not triggered on.

In addition to the veto hodoscopes, the calorimeter trigger (CALO) is used to distinguish between halo muons and final state hadrons by demanding a certain energy deposit in the hadron calorimeters HCAL1 and HCAL2.

Furthermore the CALO trigger enables to directly trigger on produced hadrons. Thereby it covers a kinematic range of large momentum transfers that is otherwise not covered by the muon hodoscopes. Fig. 3.9 shows the coverage of kinematic regions by the different trigger systems. During data taking several combinations of triggers can be selected. The important trigger combinations for this analysis are inclMT and OT, which trigger on events with scattered muons detected in only the middle trigger or the outer trigger, respectively.

3. The COMPASS Experiment

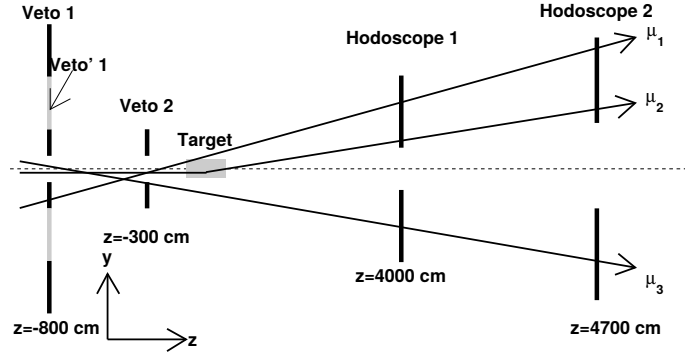


Figure 3.8.: Schematic view of the veto trigger system. Only muons that do not cross the veto hodoscopes are accepted. Track μ_2 is accepted, the tracks μ_1 and μ_3 are rejected.

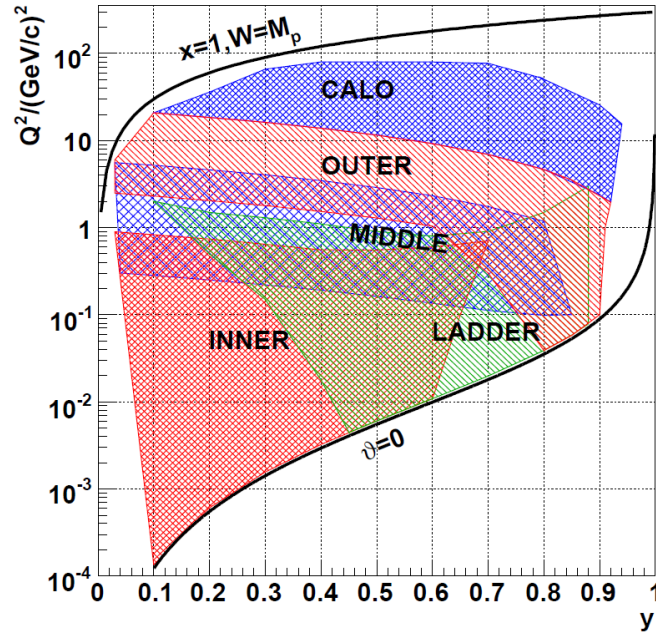


Figure 3.9.: Overview of the kinematic regions in Q^2 and y covered by the COMPASS trigger system. The figure is taken from Ref. [47].

3.4. Event Reconstruction

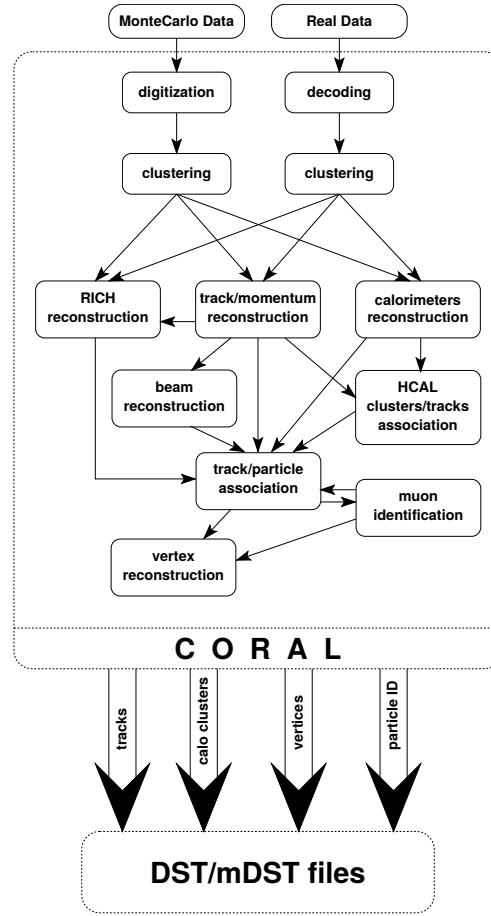


Figure 3.10.: Flow chart of CORAL, the COMPASS reconstruction software.

The event reconstruction is performed by the COMPASS event reconstruction software CORAL. It is written in C++ with an object oriented and modular architecture. Fig. 3.10 shows the flow chart of CORAL. CORAL processes either Monte Carlo (MC) data or raw data collected by COMPASS. For experimental data the first phase is to decode the different detector information from raw data and put it into a uniform data format. For MC data this phase is called digitization, where the detector response is simulated. The second phase is clustering. Signals from detectors assumed to have detected the same particle are grouped together and their geometrical position is used to reconstruct the particle's track. With this information the charge of the particle can be determined and together with the energy deposit in the calorimeters the particle identification (PID) is per-

3. The COMPASS Experiment

formed. Furthermore information of the hadron calorimeters is used to separate hadrons from muons as muons deposit nearly no energy in the calorimeters. From the data given by tracking detectors, the trajectories of charged particles are reconstructed and particle momenta are determined. The RICH is often used to separate charged hadrons such as pions, kaons, and protons. The information from the RICH photon detectors, the reconstructed tracks, and particle momenta are used to calculate the Cherenkov angles.

The reconstructed tracks are fed into a vertex finding algorithm. Its purpose is to find the location in space of primary and two-body decay (V^0) vertices. A primary vertex is the interaction point of a beam particle with the target. To find outgoing particles associated with the vertex, a fit to the vertex position is performed. For each track a χ^2 value is computed and tracks, which exceed a threshold, are rejected. It is possible to have more than one primary vertex per event. By default the vertex with the highest energetic muon is selected as best primary vertex.

V^0 vertices with the highest certainty are selected from combinations of all pairs of particles. Consequently the V^0 vertex reconstruction takes place only inside and downstream of the target. As for the primary vertices, for each V^0 a χ^2 value is computed and V^0 , for which χ^2 exceed a threshold, are rejected.

The results are stored in special ROOT trees called mini Data Summary Tapes (mDST).

4. Extraction of K_S^0 Multiplicities

The first main part of this work is the extraction of K_S^0 multiplicities from deep inelastic scattering on an isoscalar deuteron target (${}^6\text{LiD}$). To extract K_S^0 multiplicities from experimental data, the number of produced K_S^0 per DIS event is determined in bins of x (the Bjorken scaling variable), y (the relative energy transfer), and z (the fraction of the virtual photon energy carried by the final state hadron). First the DIS events are selected by tagging all events that contain an incoming and a scattered lepton. The K_S^0 are determined via their decay into pion pairs: $K_S^0 \rightarrow \pi^+\pi^-$. Therefore SIDIS events, a subsample of the DIS events, are selected, by requiring at least one secondary vertex with exactly two oppositely charged particles which are interpreted as pions. The $\pi^+\pi^-$ system is referred as K_S^0 candidates as it contains the K_S^0 as well as background particles. In the next step the K_S^0 are separated from the background and the raw multiplicities are calculated. These raw multiplicities are corrected for the limited acceptance of the detector which is determined from Monte Carlo (MC) simulation. Radiative corrections are applied and the number of measured K_S^0 is corrected for K_S^0 originating from the decay of diffractive vector mesons.

Section 4.1 describes the selection of DIS events and K_S^0 candidates. In Sect. 4.2 several methods to separate K_S^0 from the background are introduced and evaluated. The raw multiplicities are presented in Sect. 4.3 followed by the determination of the detector acceptance presented in Sect. 4.4. The correction from diffractive vector meson is done in Sect. 4.5 and a discussion of systematic uncertainties is given in section 4.6. The acceptance corrected multiplicities are presented in Sect. 4.7.

4.1. Event Selection

In this analysis the same six periods W40, W41, W42, W43, W45, and W46 from 2006 as in the charged pion analysis of Ref. [67] and the charged kaon analysis of Ref. [68] are used.

The data is ordered in runs. Each run usually consists of 100-200 spills with a few thousand events each. To ensure data quality the runs and spills must fulfill certain requirements [52]: for each spill a number of variables is monitored which include the number of beam tracks and outgoing tracks per vertex, the number of primary vertices per event, and the detector efficiency. If these values deviate

4. Extraction of K_S^0 Multiplicities

too much from the ones of the neighboring spills, the spill is considered bad and removed from further analyses. Table 4.1 shows a list of number of spills and

Week	#spills	#bad spills	% bad spills
40	24900	1618	6.5
41	17412	2546	14.6
42	15583	806	5.2
43	18841	1384	7.3
45	15543	1122	7.2
46	10559	1253	11.9

Table 4.1.: List of number of spills including bad spills for six weeks of 2006.

bad spills for the six periods. A run is completely rejected if too many bad spills occurred. In total only seven runs were rejected from all six weeks.

For the event selection the COMPASS framework PHAST [50] (PHysics Analysis Software Tools) version 7.139 is used. PHAST is an extension to ROOT [51] and provides an interface to read the stored experimental data and gives access to reconstructed events.

4.1.1. Binning

The multiplicities are extracted in nine bins of the Bjorken scaling variable x , six bins of y , the relative energy transfer, and twelve bins of z , the energy fraction carried by the final state hadrons. The binning is the same as used for the charged pion and charged kaon analyses.

$$x \{0.004, 0.010, 0.020, 0.030, 0.040, 0.060, 0.100, 0.140, 0.180, 0.400\}$$

$$y \{0.10, 0.15, 0.20, 0.30, 0.50, 0.70, 0.90\}$$

$$z \{0.20, 0.25, 0.30, 0.35, 0.40, 0.45, 0.50, 0.55, 0.60, 0.65, 0.70, 0.75, 0.85\}$$

DIS events are extracted in bins of x and y , kaon candidates are extracted in bins of x , y , and z .

4.1.2. Selection of Deep Inelastic Scattering Events

DIS events are per definition events where an incoming muon scatters off a nucleon in the target and the hadronic final state energy exceeds $W > 5 \text{ GeV}/c^2$. DIS events are selected if the vertex between the incoming and outgoing muon tracks lays inside the target region, without any requirements on the final state hadrons. Thus, a preselection of DIS events using only inclusive triggers is sufficient. A set of cuts is used to select the primary vertex. Further cuts are applied to take the geometry of the experiment into account.

The cuts for the primary vertex selection are listed in the following.

Primary Vertex Selection

1. The inclusive Middle Trigger (inclMT) or the Outer Trigger (OT) must have triggered. Both are purely inclusive triggers. The inclMT covers the low y and low Q^2 region with $y < 0.4$ and $1 (\text{GeV}/c)^2 < Q^2 < 2.5 (\text{GeV}/c)^2$. The OT covers the high y and high Q^2 region with $y > 0.4$ and $Q^2 > 2.5 (\text{GeV}/c)^2$.
2. As described in Sect. 3.4, the primary vertices are reconstructed with CORAL and defined as the interaction point of the beam particle with the target. A PHAST library function points to the best primary vertex of the triggered event, that is per default the vertex with the highest energetic muon. The CORAL function does not require an outgoing muon in the primary vertex. Thus, an additional condition is made requiring that the reconstructed scattered muon μ' is associated with the primary vertex. To avoid ambiguity events having more than one reconstructed scattered muon are rejected.
3. The primary vertex is required to be inside the target material. To ensure a homogeneously filled target, an additional cut on the z coordinate of the primary vertex position is made: $z_{pv} \in [-56\text{cm}, -35\text{cm}]$, $[-20\text{cm}, 31\text{cm}]$ or $[43\text{cm}, 66\text{cm}]$. The cut is visualized in Fig. 4.1.

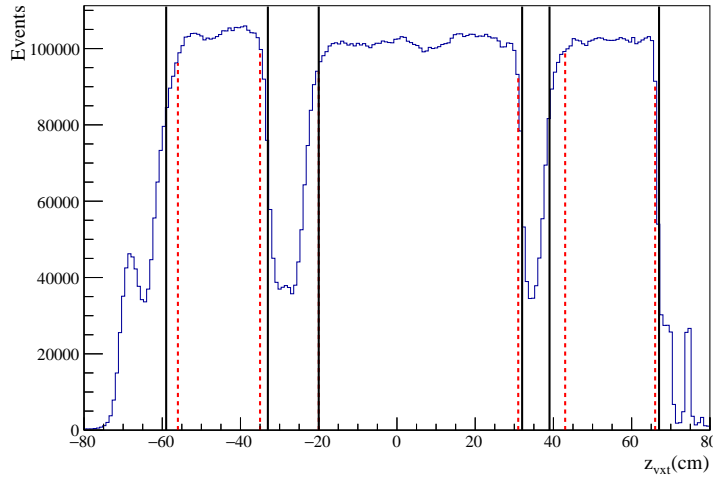


Figure 4.1.: Distribution of primary vertex positions along the z-axis. The solid black lines show the target dimension. The stricter cuts are shown as red dashed lines.

4. The muon beam is required to have crossed all three target cells. With this requirement only beam muons parallel to the dedicated beam direction are

4. Extraction of K_S^0 Multiplicities

taken into account. This is necessary to reject events from beam halo muons that were not removed by the veto trigger.

5. A geometrical compatibility between the beam particle and the beam momentum station (BMS) is required. The track of the outgoing muon is extrapolated to the position of the BMS. Then the χ^2 of the extrapolated track and the hits in BMS are compared for compatibility. As criteria the P value of χ^2 must be below $P(\chi^2) < 0.005$.

More cuts are required to select DIS events in the kinematic region that is covered by the COMPASS experiment. The selected kinematic region for this analysis is $0.004 \leq x \leq 0.4$, $0.1 \leq y \leq 0.9$, and $Q^2 > 1 \text{ (GeV/c)}^2$ following the kinematic coverage of the COMPASS experiment for DIS. The mean value of the momentum transfer for these kinematics is: $\langle Q^2 \rangle = 3 \text{ (GeV/c)}^2$. The conditions on y and Q^2 ensure that the kinematics are compatible for DIS and imply indirectly $W > 5 \text{ GeV/c}^2$. Fig. 4.2 shows the x - Q^2 distribution of selected DIS events. The

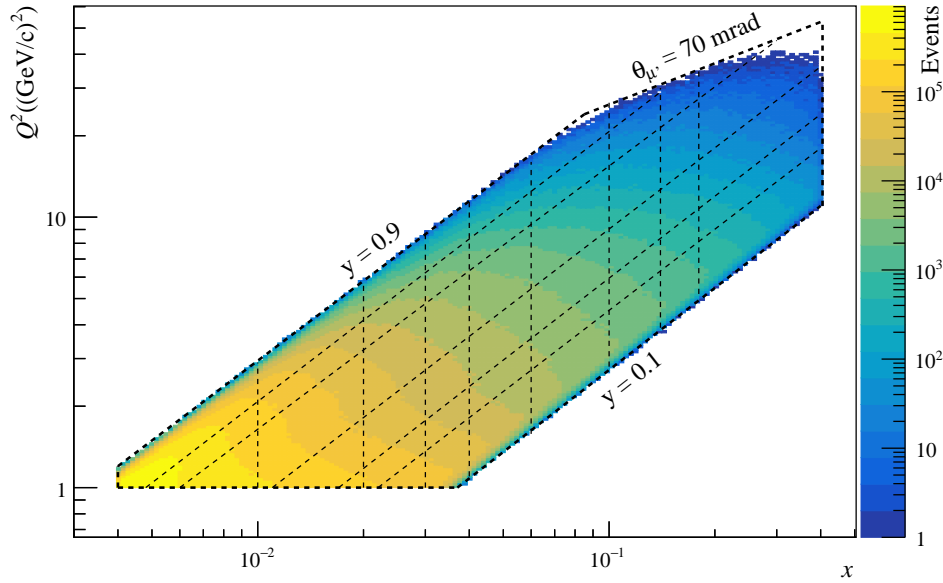


Figure 4.2.: Q^2 plotted against x . The momentum range covered by COMPASS. The dashed lines show the selection cuts of kinematic region and kinematic constraints of the COMPASS experiment.

dashed lines correspond to the bin limits of x and y bins.

The kinematic cuts are listed in the following.

Kinematic Cuts

1. The energy of the incoming muons is required to be in the range between $140 \text{ GeV}/c^2 < E_{\text{beam}} < 180 \text{ GeV}/c^2$.
2. The uncertainty of the reconstructed momentum transfer relative to the beam momentum must be smaller than $\frac{\sigma(q)}{P} < 20 \cdot 10^{-9}$.
3. The momentum transfer from the lepton to the nucleon at the primary vertex must be greater than $Q^2 > 1 (\text{GeV}/c)^2$.
4. The Bjorken scaling variable must be within the limits $0.004 \leq x \leq 0.4$.
5. The energy fraction transferred by the virtual photon must range from $0.1 \leq y \leq 0.9$. The lower limit of the y -cut excludes the region where the momentum resolution degrades. Above the upper limit large radiative corrections to inclusive cross sections are required.

To illustrate the impact of the individual cuts, the percentage of remaining events after each cut is plotted in Fig. 4.3. In addition the cuts are listed in Tab. 4.2. The

Cut No.	Description	#events	Fraction (%)
0	All events after bad spill rejection	1490263129	100.00
1	Primary vertex	1387889603	93.13
2	$140 \text{ GeV}/c^2 < E_{\text{beam}} < 180 \text{ GeV}/c^2$	766348208	51.42
3	$\sigma(q)/P < 20 \cdot 10^{-9}$	766348208	51.42
4	$Q^2 > 1 (\text{GeV}/c)^2$	61563614	4.13
5	$0.004 \leq x \leq 0.4$	57952598	3.89
6	$0.1 \leq y \leq 0.9$	41882080	2.81
7	Beam crosses cells	35012306	2.35
8	Primary vertex in target	24789292	1.66
9	BMS	20028260	1.34
10	inclMT or OT	13123640	0.88
10a	inclMT	6333332	0.42
10b	OT	6790308	0.46

Table 4.2.: The cuts for the DIS event selection.

cuts in this table appear in the order in which they are applied in this analysis.

Figure 4.4 shows the distribution of kinematic variables of DIS for real and reconstructed MC data. The plot of ν is disregarded as $\nu = y \cdot E_0$. For each variable the kinematic cuts in x , y , and Q^2 are applied. The cuts of the actual variable are not applied but shown as red dashed lines. The number of entries in

4. Extraction of K_S^0 Multiplicities

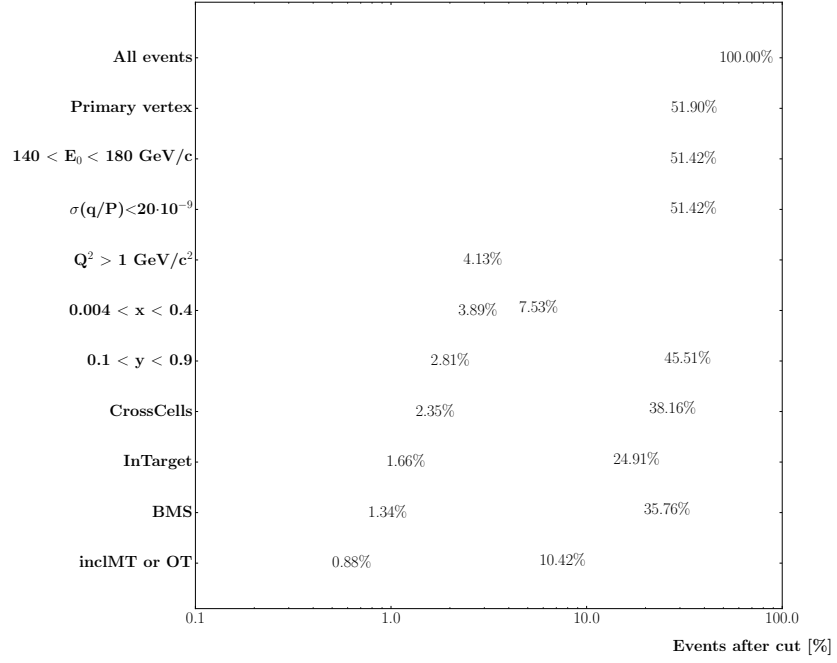


Figure 4.3.: For each cut, the light bar shows the percentage of selected events if this condition alone would be applied on the full set of events. The dark bar shows the percentage of selected events when the cuts are applied one after the other, as it is done in this analysis. The percentage values refer to the initial number of events (All trigger events).

4.1. Event Selection

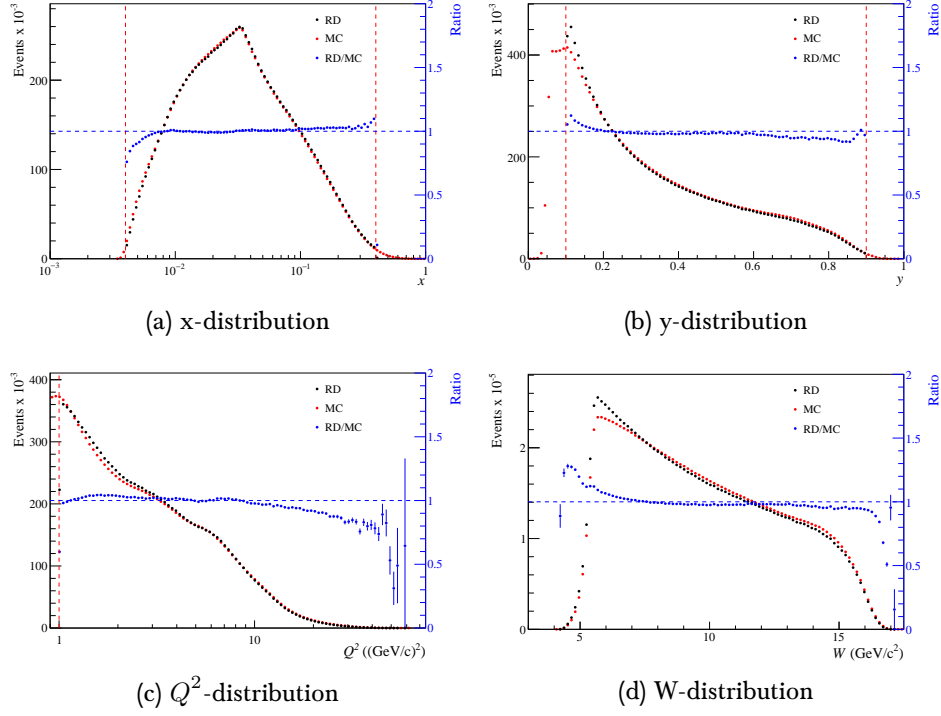


Figure 4.4.: Kinematic variables of DIS. The variables are plotted with all but its own kinematic cuts applied. The dashed red lines mark the position of the cuts to select DIS, applied on the corresponding variable.

4. Extraction of K_S^0 Multiplicities

the histograms of MC data is scaled to the number of entries in the histograms of the real data. Thereby only entries that are in the kinematic region of COMPASS, that is inside the red dashed lines, are counted and used to calculate the scaling factor. The ratio of real and reconstructed MC data shows that the MC data is able to describe the real data.

The selection of DIS events is the basis of the further analysis. From the selected DIS events the neutral kaon candidates are selected.

4.1.3. Selection of Neutral Kaon Candidates

This section describes the selection process for neutral kaon candidates from the previously selected DIS events. Neutral mesons cannot be measured directly but must be reconstructed via their decay products. In this analysis the kaons are selected in the decay channel $K_S^0 \rightarrow \pi^+ \pi^-$. Fig. 4.5 shows a schematic of the decay process. To select K_S^0 , the DIS events are filtered for events with a secondary

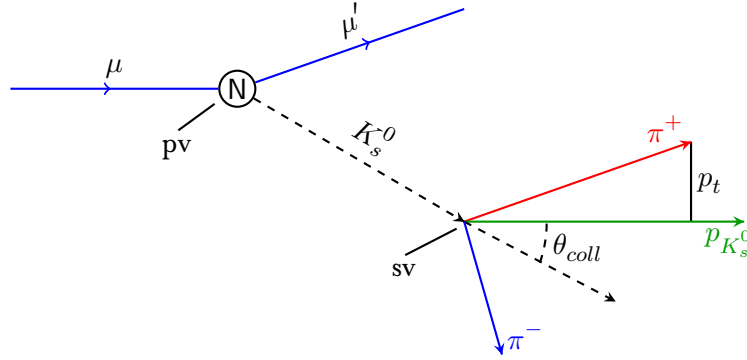


Figure 4.5.: Diagram to motivate the choice of the SIDIS event selection.

vertex that has exactly one outgoing pair of oppositely charged particles. These are then interpreted as π^+ and π^- . A secondary vertex with two outgoing particles is called V^0 . The position of V^0 is calculated in CORAL by extrapolating the tracks of the outgoing particles into the direction of the target. The χ^2 value associated with V^0 is accessed with a PHAST library function. To increase the quality of the data sample a cut on $\chi^2(V^0) < 2$ is applied.

As a further condition on the secondary vertex V^0 , it must be downstream of the primary vertex V' and they must be clearly distinguishable from each other. The distance along the beam axis of the primary and secondary vertex, normalized by their uncertainties, is given by

$$d(z_{V'}, z_{V^0}) = \frac{z_{V^0} - z_{V'}}{\sqrt{\sigma(z_{V^0})^2 + \sigma(z_{V'})^2}}. \quad (4.1)$$

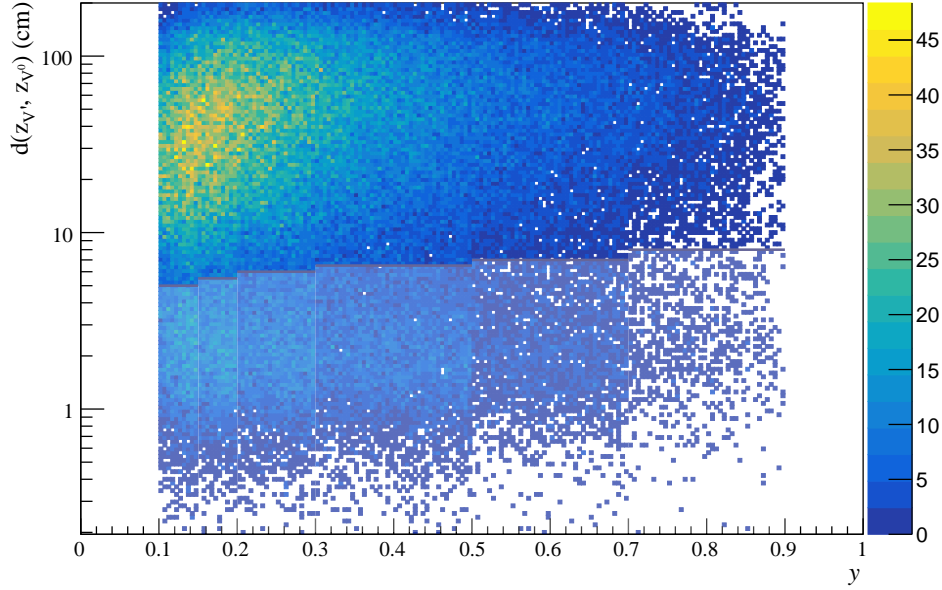


Figure 4.6.: The distances between the primary and the secondary vertices as a function of y . Events with distances in the highlighted region are rejected. To clean the plot of misidentified K_S^0 the additional cut $m_{K_S^0} \pm 15 \text{ MeV}/c^2$ on the invariant mass of the $\pi^+\pi^-$ system is applied.

Figure 4.6 shows the distance distribution as a function of y . To take the y dependence into account the minimal distance is selected with respect to the different y bins. The minimal distances are given in Tab. 4.3.

The four-momentum of the K_S^0 candidate is the sum of the four-momenta of the two pions. The angle θ_{coll} between the flight direction of the K_S^0 candidates and the direction between the reconstructed primary and secondary vertices is calculated. Events for which the two directions are not compatible are rejected. In Fig. 4.7 the angular distribution is plotted as a function of y . It shows that the angular distribution depends on y . The cut on θ_{coll} should be as low as possible without removing too many events. Therefore the cuts on θ_{coll} are applied with respect to the y bin. The maximum values for θ_{coll} are given in Tab. 4.4.

Due to low detector acceptance at low momenta, a cut on the pion momenta with $p_{\pi^\pm} > 1 \text{ GeV}/c$ is necessary. This becomes clear by looking at Fig. 4.8 where the distribution of charge times pion momentum is shown. To produce a clear plot, all SIDIS cuts except the one on the pion momentum are applied. In order to increase the quality of the distributions in Fig. 4.8, the cut $m_{K_S^0} \pm 15 \text{ MeV}/c^2$

4. Extraction of K_S^0 Multiplicities

y	$d(z_{V'}, z_{V^0})$
0.1 – 0.15	5 cm
0.15 – 0.2	5.5 cm
0.2 – 0.3	6 cm
0.3 – 0.5	6.5 cm
0.5 – 0.7	7 cm
0.7 – 0.9	8 cm

Table 4.3.: Minimal distance between the primary and secondary vertex.

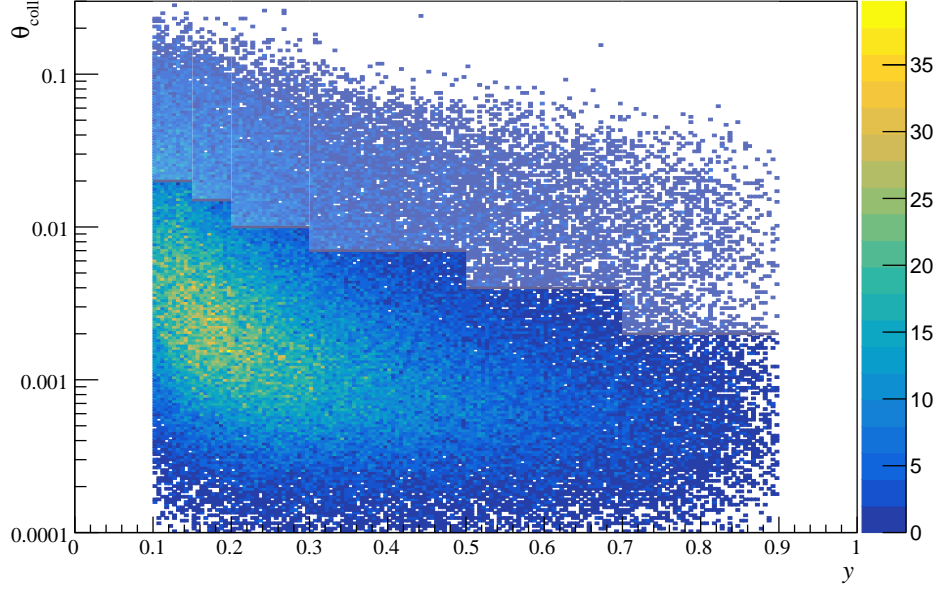


Figure 4.7.: The angle θ_{coll} between the flight direction of the K_S^0 candidates and the direction from the reconstructed primary to the secondary vertices. Events with angles in the highlighted area are rejected. To clean the plot of misidentified K_S^0 the additional cut $m_{K_S^0} \pm 15 \text{ MeV}/c^2$ on the invariant mass of the $\pi^+\pi^-$ system is applied.

y	θ_{coll}
0.1 – 0.15	0.02
0.15 – 0.2	0.015
0.2 – 0.3	0.01
0.3 – 0.5	0.007
0.5 – 0.7	0.005
0.7 – 0.9	0.002

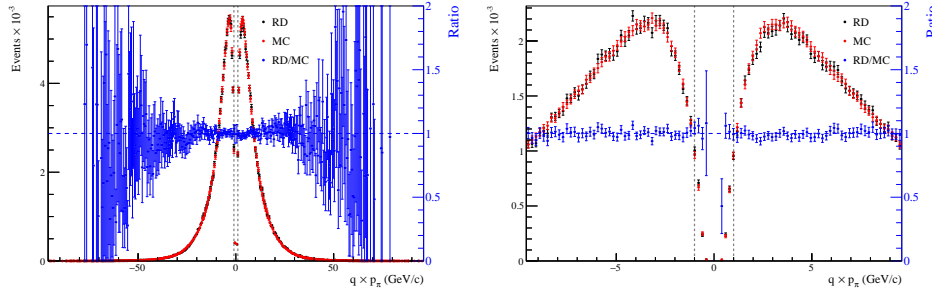
Table 4.4.: Maximum values of θ_{coll} .

Figure 4.8.: Momentum distribution of positive and negative particles originating from the second vertices. The plot on the left shows the full momentum range, while the one on the right plot is limited to $p_{\pi} < 10 \text{ GeV}/c$. The particles are interpreted as pions. All cuts but $p_{\pi\pm} > 1 \text{ GeV}/c$ are applied. To clean the plot of misidentified K_S^0 the additional cut $m_{K_S^0} \pm 15 \text{ MeV}/c^2$ on the invariant mass of the $\pi^+\pi^-$ system is applied.

4. Extraction of K_S^0 Multiplicities

is applied on the invariant mass of the $\pi^+\pi^-$ system to remove misidentified K_S^0 .

The K_S^0 candidate sample is still contaminated by events coming from other processes, for which at least one of the final state pions was misidentified. The main contamination comes from the decay of Λ and $\bar{\Lambda}$ baryons, $\Lambda \rightarrow \pi^- p$ and $\bar{\Lambda} \rightarrow \pi^+ \bar{p}$, respectively, as well as gamma decay $\gamma \rightarrow e^+e^-$. They can be distinguished by plotting a corresponding Armenteros-Podolanski plot [54], that is the transverse momentum p_t of the pions with respect to the V^0 direction of flight is plotted against the longitudinal pion momentum asymmetry $\alpha = \frac{p_t^+ - p_t^-}{p_t^+ + p_t^-}$. Fig. 4.9 shows the Armenteros-Podolanski plot for this analysis. By cutting the

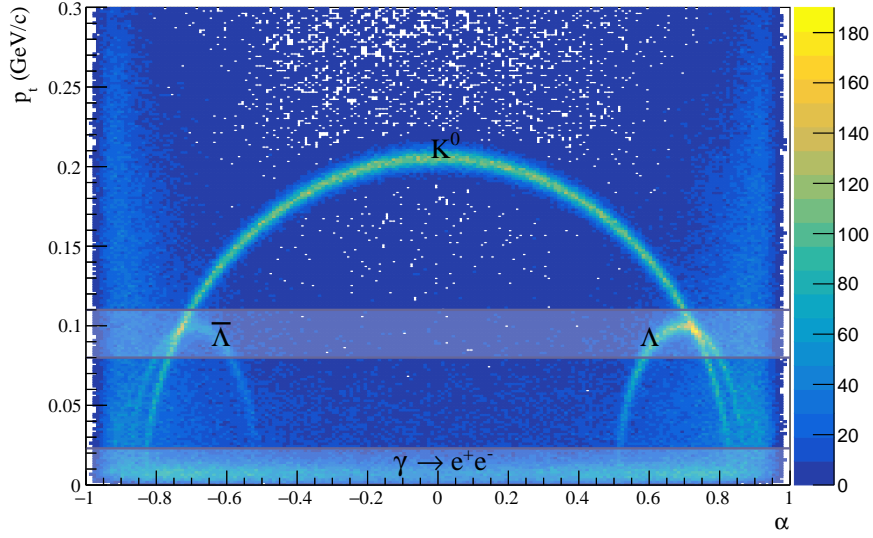


Figure 4.9.: The Armenteros-Podolanski plot. This plot visualizes the e^-e^+ and $\Lambda, \bar{\Lambda}$ contamination of the $\pi^+\pi^-$ invariant mass spectrum. The marked regions from $0 < p_t < 23$ MeV/c and $80 < p_t < 110$ MeV/c are excluded.

region below $p_t < 23$ MeV/c the main contribution of $\gamma \rightarrow e^+e^-$ is rejected. A cut in the region $80 \text{ MeV/c} < p_t < 110 \text{ MeV/c}$ removes the main contribution of γ and Λ events.

Figure 4.10 shows the p_t distribution with all cuts except the ones on p_t applied.

To summarize, a K_S^0 candidate is a particle composed of a $\pi^+\pi^-$ system selected from DIS events that fulfills the following criteria:

1. The event must have a secondary vertex (V^0) with exactly two outgoing particles of opposite charge.
2. The χ^2 value of V^0 must be smaller than $\chi^2(V^0) < 2$.

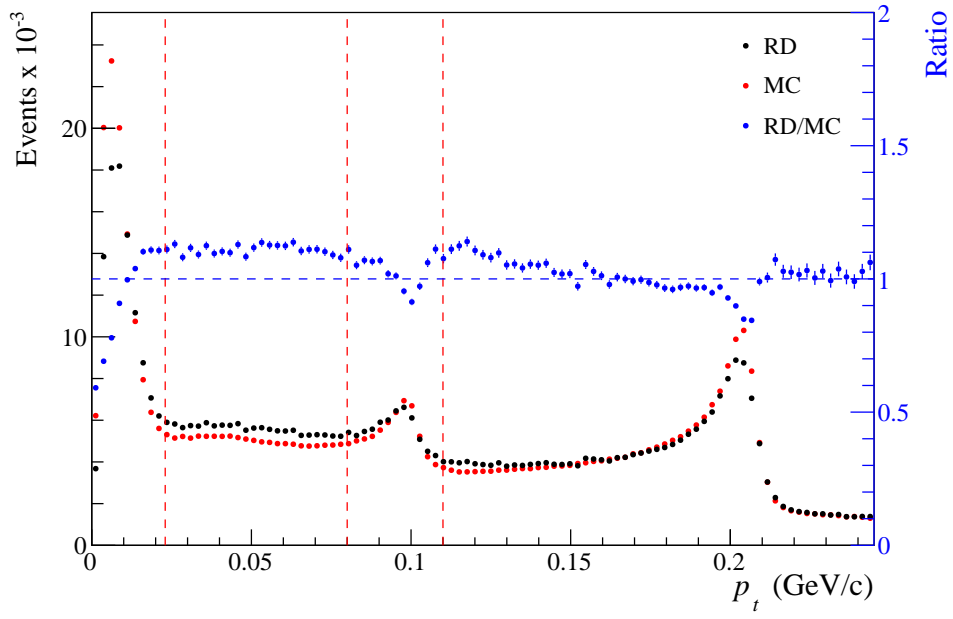


Figure 4.10.: The p_t distribution. All cuts but the cuts on p_t are applied. The red dashed lines indicate the cuts on p_t .

4. Extraction of K_S^0 Multiplicities

3. Both decay particles must cross the SM1 magnet, that is $z_{\text{first}} < z_{\text{SM1}} < z_{\text{last}}$ must hold where z_{first} and z_{last} are the z -coordinates of the first and last measurement of the decay particles.
4. The decay particles are interpreted as charged pions and they will be given the charged pion mass. The momenta of the decay particles must be $p_{\pi^\pm} > 1 \text{ GeV}/c$ due to low detector acceptance below $1 \text{ GeV}/c$.
5. The energy fraction of the virtual photon carried by the K_S^0 lies in the region $0.2 \leq z_{K_S^0} \leq 0.85$. The full z -distribution is presented in Fig. 4.11.
6. $\theta_{\text{coll}} < 0.01 \text{ rad}$ must hold for the angle between the vector from V' to V^0 and the flight direction of the reconstructed K_S^0 candidate.
7. The secondary vertex must be downstream of the primary vertex. To avoid an overlap of the vertices it must be true that $z(V^0) - z(V') < 3 \cdot \sqrt{(\sigma(z_{V^0}))^2 + (\sigma(z_{V'}))^2}$.
8. The cuts $0 < p_t < 23 \text{ MeV}/c$ and $80 < p_t < 110 \text{ MeV}/c$ are motivated by the Armenteros-Podolanski plot [54] shown in fig. 4.9. It is a two dimensional plot of the transverse momentum p_t of the oppositely charged decay particles w.r.t. the V^0 direction of light versus the longitudinal momentum asymmetry $\alpha = \frac{p_l^+ - p_l^-}{p_l^+ + p_l^-}$. It shows a contamination of Λ and $\bar{\Lambda}$ baryons around $p_t = 100 \text{ MeV}/c$ and a $\gamma \rightarrow e^+e^-$ contamination for $p_t < 23 \text{ MeV}/c$.

Figure 4.12 illustrates the impact of the cuts on the number of SIDIS events. The percentage of remaining events is shown in the order in which the cuts are applied as well as the impact of the cut on the total number of events.

The cuts are summarized in Tab. 4.5.

4.1.4. Radiative Corrections

The DIS cross section as written in Eq. (2.6) includes only contributions of one-photon-exchange terms ($\sigma_{1,\gamma}$). However, the real cross section depends also on other electromagnetic processes. The main contributions in leading order are photon emission by the initial and final state muon, vertex corrections and vacuum polarization. The radiative correction factor is defined as

$$\eta(x, y) = \frac{\sigma_{1,\gamma}(x, y)}{\sigma_{\text{measured}}(x, y)} \quad (4.2)$$

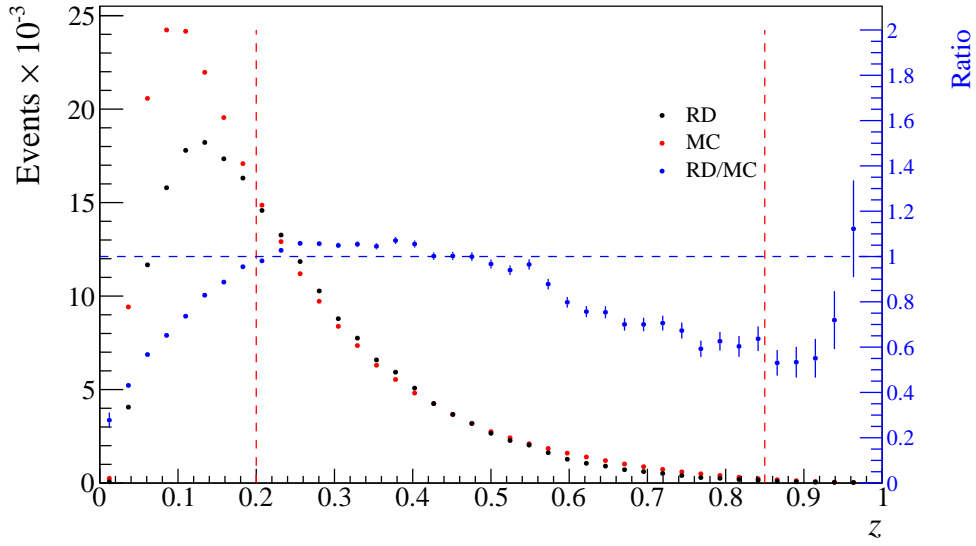


Figure 4.11.: The z -distribution of the $\pi^+\pi^-$ system. The red dashed lines indicate the applied cuts on z .

Cut No.	Description	#events	Fraction (%)
0	all secondary vertices	65383649	100.00
1	not primary vertex	51706183	81.47
2	exactly two outgoing tracks	51686216	79.05
3	χ^2 of vertex < 2	36452842	55.75
4	tracks have opposite charge	36452148	55.75
5	$z_{\text{first}} < 350$ cm	35439062	54.20
6	$z_{\text{last}} > 350$ cm	33075991	50.59
7	$p_\pi > 1$ GeV	12099903	18.51
8	$0.2 < z < 0.85$	11603612	17.75
9	$\theta_{\text{coll}} < 0.01$	1200097	1.84
10	$(z_{\text{sv}} - z_{\text{pv}}) < 3 \cdot \sqrt{(\sigma(z_{\text{sv}}))^2 + (\sigma(z_{\text{pv}}))^2}$	589581	0.90
11	$23 < p_t(V^0) < 80$ or $p_t(V^0) > 110$ MeV/c	417735	0.64

Table 4.5.: The cuts for the selection of K_S^0 candidates.

4. Extraction of K_S^0 Multiplicities

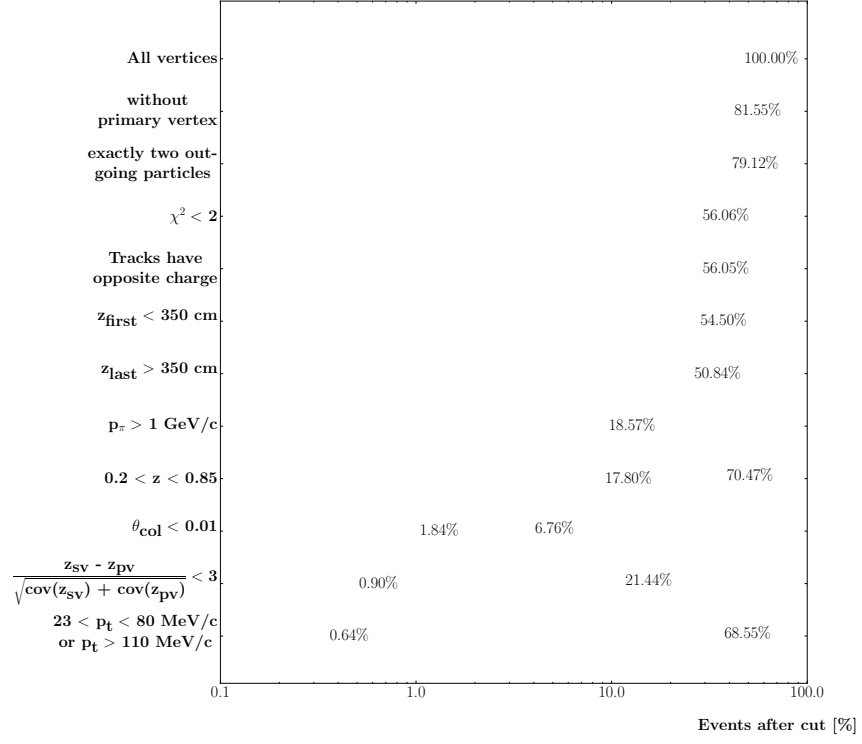


Figure 4.12.: For each cut, the light bar shows the percentage of selected events if this condition alone would be applied on the full set of all vertices of the previously selected DIS events. The dark bar shows the percentage of selected events when the cuts are applied one after the other, as it is done in this analysis. The percentage values refer to the initial number of vertices (All vertices).

where σ_{measured} denotes the measured cross section. The inclusive and semi-inclusive radiative correction factors are precalculated for different target types and stored in tables. The radiative corrections were initially calculated for the kinematical region of the EMC experiment, the predecessor of COMPASS [53]. Thus, they are valid for the kinematic range of COMPASS too. A new set of tables, which takes the different filling densities of the COMPASS target cells into account, was recently produced and made available by the author of Ref. [53]. In this analysis the radiative correction factors are applied binwise on an event-by-event basis. Both the numbers of DIS events and kaon candidates are corrected by inclusive and semi-inclusive correction factors, respectively. Table 4.6 shows the numbers for the period of six weeks, summed over all x and y bins, before and after radiative corrections. The total correction factor is, with about 90%, practically the same for both, the number of DIS events and the number of K_S^0 candidates.

	DIS	K_S^0
identified	13123640	447088
corrected	11893437	409971

Table 4.6.: Numbers of DIS events and kaon candidates before and after radiative corrections.

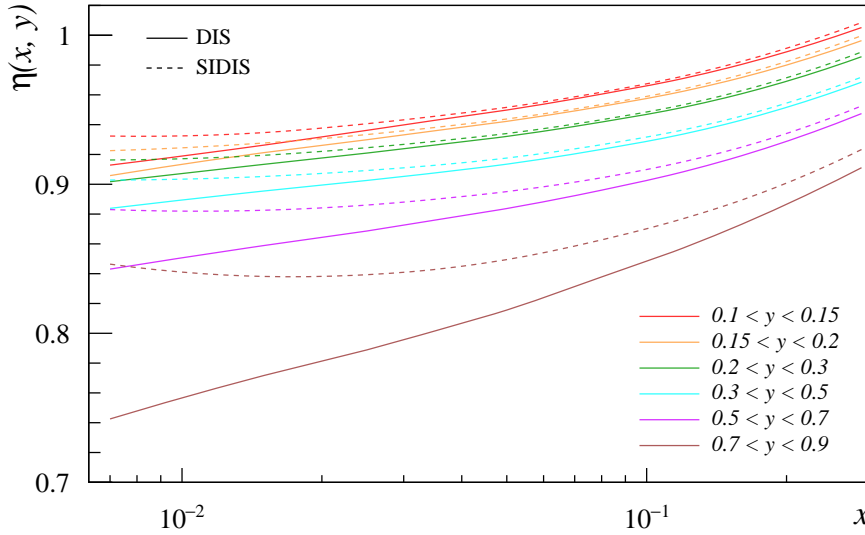


Figure 4.13.: The radiative corrections for DIS and SIDIS as a function of x are plotted for different bins of y .

4. Extraction of K_S^0 Multiplicities

This can also be seen from Fig. 4.13 where the radiative corrections for DIS and SIDIS are plotted as a function of x for different bins of y . The difference between DIS and SIDIS corrections becomes larger for decreasing x and increasing y . Due to the sparse population of bins of high y , those bins contribute less to the total correction factor.

4.2. K^0 Identification

In the next step of the analysis the $\pi^+\pi^-$ invariant mass distribution is plotted. Figure 4.14 shows the distribution for all K_S^0 candidates. It has a prominent peak

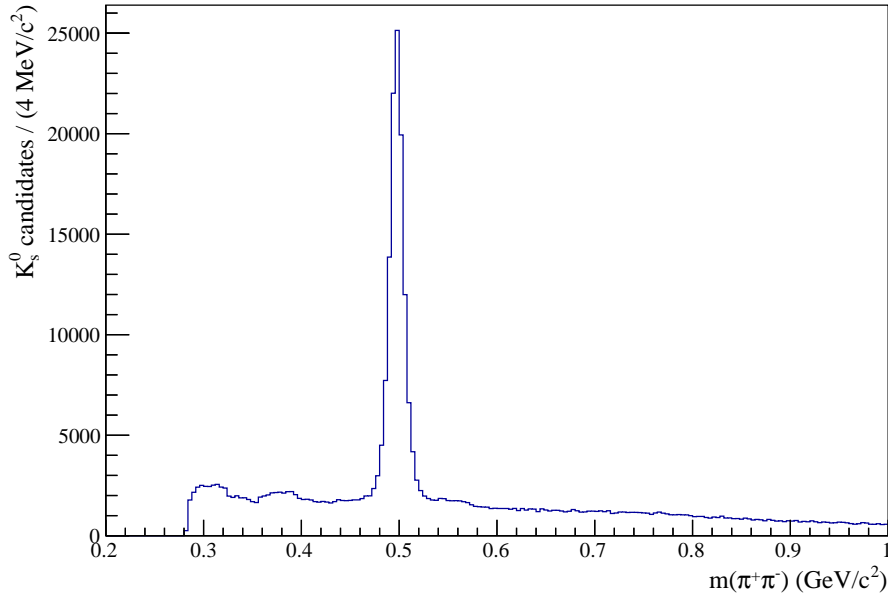


Figure 4.14.: The $\pi^+\pi^-$ invariant mass distribution for all K_S^0 candidates.

around the K_S^0 mass on top of a linear background. In general the distribution can be described as the sum of a signal and a background function where the size of the signal function is correlated to the yield of K_S^0 . Usually, particles are described by a Voigtian, that is the convolution of a Breit-Wigner, representing the natural shape of a resonance, and a Gaussian, representing the experimental resolution. The K_S^0 is a long-lived particle that decays weakly. Using the lifetime τ of the K_S^0 from Tab. 2.2 to estimate the width Γ of the Breit-Wigner function yields

$$\Gamma = \frac{\hbar}{\tau} \approx 7 \cdot 10^{-6} \text{ eV}. \quad (4.3)$$

Thus, the width of the Breit-Wigner function is small compared with the width of the Gaussian and it is sufficient to describe the signal function with a Gaussian that only reflects the detector resolution. For the background a linear polynomial is used.

The number of K_S^0 has to be determined for each of the three dimensional bins in x , y , and z . The K_S^0 identification is only performed, if the bin has at least 15 entries, otherwise the bin is discarded from further analysis. Two different methods, the integral method and the sideband subtraction method, to separate the number of K_S^0 from the background are used in this analysis. The integral method with a Gaussian as signal function and a linear polynomial as background function is used as the default method. The sideband subtraction method and the integral method with a Voigtian as signal function are used to estimate the systematic uncertainty of the K_S^0 identification.

In the following the integral and the sideband subtraction methods are described:

Integral method The sum of the signal and background functions is fitted to the $\pi^+\pi^-$ invariant mass distribution. The integral of the signal function is taken as the value and the integral's error is taken as the uncertainty of the number of K_S^0 . It was found that for most bins ($> 80\%$ for real data and $> 90\%$ for reconstructed MC data) using a Voigtian (with a width $\Gamma \gg \frac{\hbar}{\tau}$ of the order of the width of the Gaussian) as signal function results in a fit with a slightly lower χ^2 value.

Figure 4.15 shows the ratio of K_S^0 numbers extracted with a Gaussian and with a Voigtian as signal functions. Using a Voigtian as the signal function yields a higher number of K_S^0 for most bins, but generally, both signal functions agree within their uncertainties.

An example for a selected bin is given in Fig. 4.16, showing the fits with a Gaussian and a Voigtian as signal functions. It shows that the top of the peak is better described by the Voigtian. A possible explanation is that due to the different characteristics of the two spectrometers of the COMPASS experiment, the spectrometers have a different detector resolution and therefore must be described by the sum of two different Gaussian functions. Indeed a second Gaussian with a smaller amplitude and larger width than the first Gaussian could describe the peak better. However, it was technically not feasible to find a solution with two Gaussian signal functions that worked for all bins of x , y , and z in a satisfying manner. Especially bins with low statistics proved difficult to fit with two Gaussian functions.

One point against two Gaussians is that the binning in x , y , and z separates the energy region of the spectrometers. Thus, it should be possible to generally describe the signal with a single Gaussian. Also, the choice of the signal function

4. Extraction of K_S^0 Multiplicities

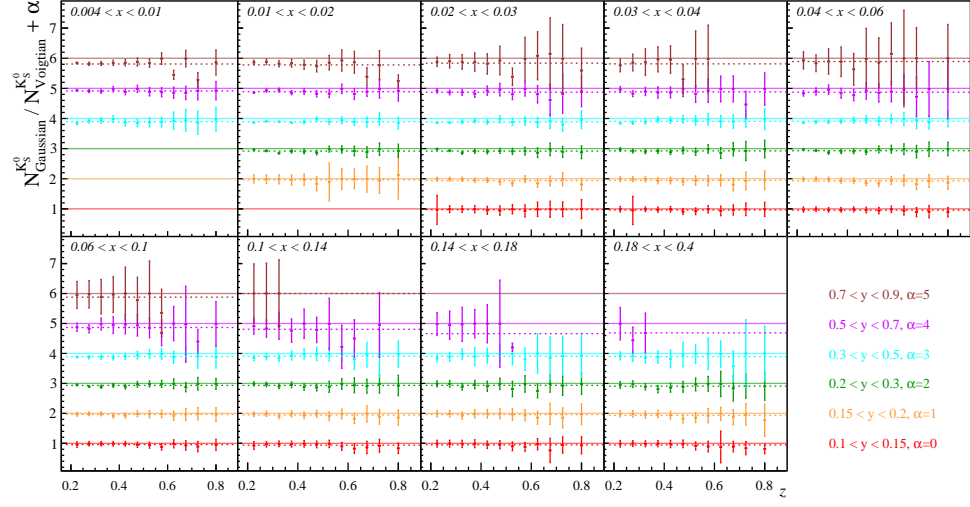


Figure 4.15.: Ratios of the K_S^0 numbers extracted with a Gaussian and Voigtian as signal function. The dashed lines are the mean values of the ratios of the corresponding y bin. The y bins are staggered for clarity.

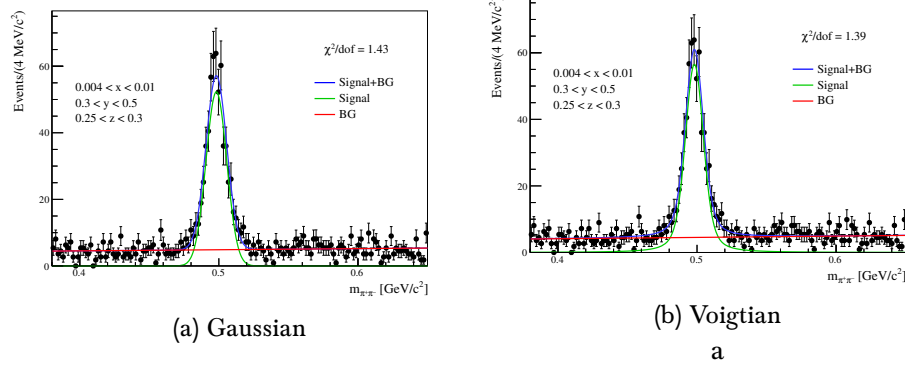


Figure 4.16.: Comparison of the Gaussian and the Voigtian signal functions for a selected bin.

is expected to affect the measured and the MC data in the same way, thus, it is safe to assume that the differences will be canceled out by the acceptance correction. Therefore, the Gaussian is selected as the default signal function.

Sideband subtraction method In the sideband subtraction method the background below the peak is determined from the background in the sidebands left and right of the peak.

First the width of the signal must be determined. Therefore the sum of the signal and background function is fitted to the invariant mass distribution of all K_S^0 candidates. A Gaussian and a linear polynomial are used as signal and background functions, respectively. The number of K_S^0 is determined by first determining the width σ of the signal function and then counting the events in $[-2\sigma, 2\sigma]$ and subtracting the number of events in the sidebands $[-5\sigma, -3\sigma]$ and $[3\sigma, 5\sigma]$. The number of K_S^0 taken from $[-2\sigma, 2\sigma]$ corresponds only to 95.45% of the total number of K_S^0 and it must be multiplied by $1/0.9545$. Disadvantages of this method are that it only works for linear backgrounds and that the width σ is only determined once for all K_S^0 candidates.

4.3. Raw Multiplicities

With the number of K_S^0 known, the raw multiplicities can be calculated according to Eq. (2.25). Fig. 4.17 presents the raw multiplicities as a function of z in bins of x and y .

4.4. Acceptance

The COMPASS spectrometer has a limited geometrical coverage and detector efficiency. For the COMPASS multiplicities to be a physically relevant result and to allow the comparison with other analyses, the multiplicities must be corrected for the geometric and kinematic detector acceptance. The acceptance is determined from MC simulation. It is defined as:

$$A^h(x, y, z) = \frac{M_r^h(x, y, z)}{M_g^h(x, y, z)} \quad (4.4)$$

where M_r^h and M_g^h denote the reconstructed and generated multiplicities from MC data.

A set of MC events was produced with a LEPTO [55] generator tuned for COMPASS, using PDFs of the MSTW2008 parametrization. The hadronization process of quarks into final state hadrons is described by JETSET [56] and a simulation of the experimental setup of COMPASS is performed with COMGEANT.

4. Extraction of K_S^0 Multiplicities

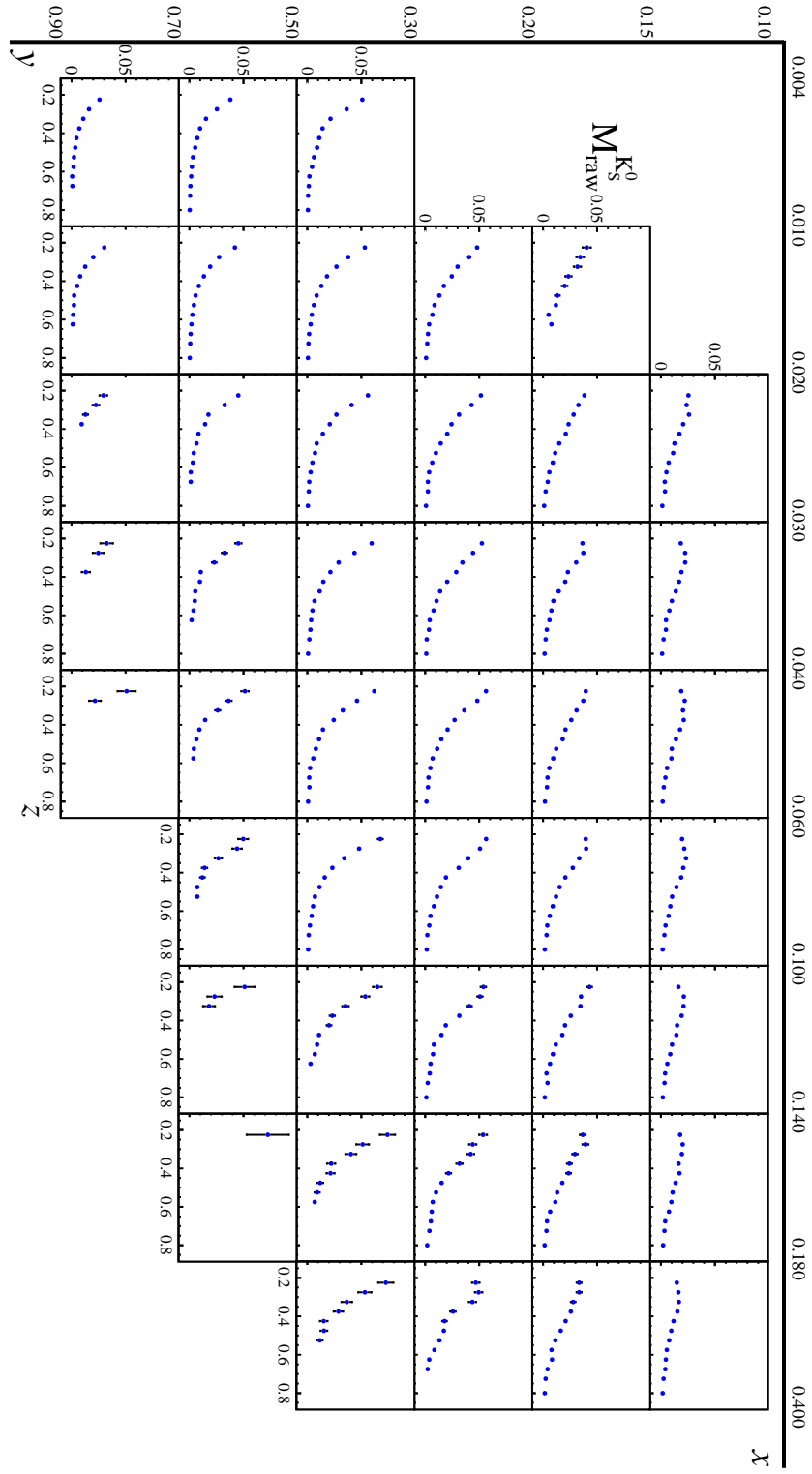


Figure 4.17.: K_S^0 raw multiplicities data plotted against z in bins of x and y .

COMGEANT is derived from the simulation tool Geant 3.21 [57]. It describes materials and geometries, such as position and dimension, for the target and detectors of COMPASS components as well as the magnetic field strengths. The output of COMGEANT is fed into CORAL as described in Sect. 3.4.

The total number of about 4×10^8 MC events were generated in the kinematical region: $Q^2 > 0.8 \text{ GeV}/c^2$, $x \in [10^{-4}, 0.99]$, $y \in [0.05, 0.95]$ and $\nu \in [0, 250]$. The data is generated in an enlarged kinematic region to take smearing effects, that is bin migration due to detector uncertainties, into account.

The reconstructed multiplicities are determined by applying the same analysis chain to the MC data as for the experimental data in Sect. 4.1.

The generated multiplicities on the other hand, which correspond to the number of generated K_S^0 in terms of generated DIS events, are determined from MC data applying the following cuts:

DIS

1. The primary vertex must be inside the target with the stricter cuts on the z coordinate $z_{pv} \in [-56\text{cm}, -35\text{cm}], [-20\text{cm}, 31\text{cm}]$ or $[43\text{cm}, 66\text{cm}]$.
2. The muon beam must cross all three target cells.
3. The energy of the incoming muon is required to be in the range $140 < E < 180 \text{ GeV}/c^2$.
4. The momentum transfer must be greater than $Q^2 > 1 (\text{GeV}/c)^2$.
5. The Bjorken scaling variable lies in the region $0.004 \leq x \leq 0.180$.
6. The fraction of the energy transferred by the virtual photon is between $0.1 \leq y \leq 0.9$.

K_S^0 selection

1. The particle id in Geant3 notation of the final state hadron must be PID = 16 for K_S^0 .
2. The K_S^0 was produced in the primary vertex.
3. The energy fraction of the virtual photon that is carried by the K_S^0 lies between $0.2 < z_{K_S^0} < 0.85$.

The measured and reconstructed MC multiplicities are only determined in the charged decay channel $K_S^0 \rightarrow \pi^+ \pi^-$. By selecting the number of generated K_S^0 produced in the primary vertex, the neutral decay channel, $K_S^0 \rightarrow \pi^0 \pi^0$, is taken into account as well. Thus, the acceptance correction includes the correction for the branching ratio of the investigated decay mode.

4. Extraction of K_S^0 Multiplicities

4.4.1. Uncertainty Estimation

Putting Eq. (2.25) into Eq. (4.4) yields

$$A^h(x, y, z) = \frac{N_r^h(x, y, z)/N_r^{\text{DIS}}(x, y)}{N_g^h(x, y, z)/N_g^{\text{DIS}}(x, y)}. \quad (4.5)$$

The numbers of DIS events and the numbers of K_S^0 are not independent which complicates the calculation of the uncertainty. To estimate the uncertainty nonetheless it is assumed that the numbers are independent. Rewriting Eq. (4.5) as:

$$A^h(x, y, z) = \frac{N_r^h(x, y, z)}{N_g^h(x, y, z)} \cdot \frac{1}{\frac{N_r^{\text{DIS}}(x, y)}{N_g^{\text{DIS}}(x, y)}} \quad (4.6)$$

and applying Gaussian error propagation yields the standard deviation:

$$\sigma_A(x, y, z) = A^h \cdot \sqrt{\left(\frac{N_r^h}{N_g^h}\right)^2 \cdot V(N_r^h, N_g^h) + \left(\frac{N_g^{\text{DIS}}}{N_h^{\text{DIS}}}\right)^2 \cdot V(N_h^{\text{DIS}}, N_g^{\text{DIS}})}. \quad (4.7)$$

The variances are estimated following the Bayesian approach as described in Ref. [24]. In Bayesian statistics the probability associated with a parameter is treated as the degree of belief about where the true value of the parameter lies.

The reconstructed DIS events and K_S^0 originate mostly from their generated counterpart, following a binomial distribution.

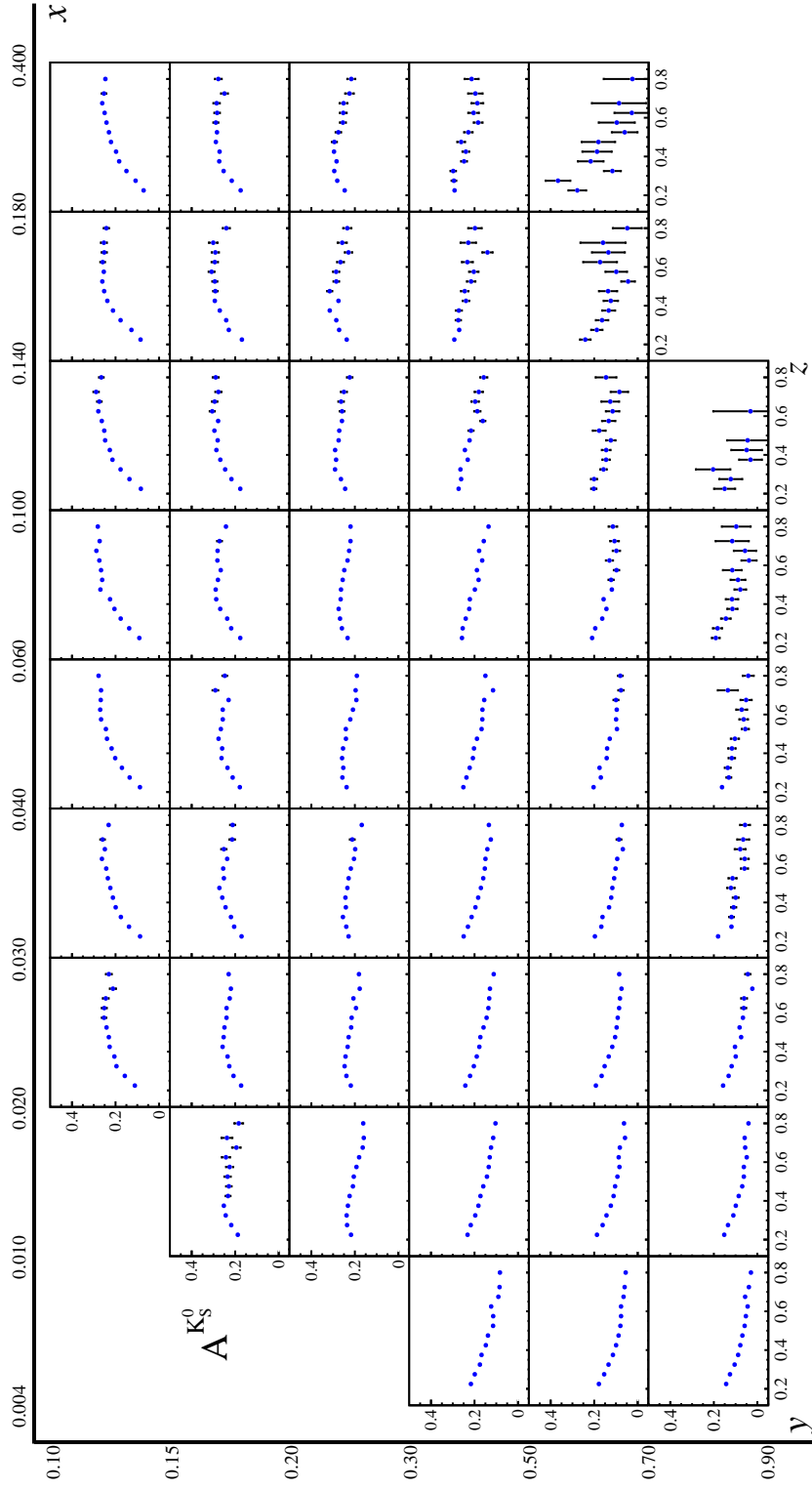
Following the Bayesian approach in Ref. [24] yields for the variance $V(R, G)$ with $R \subset G$:

$$V(R, G) = \frac{(R+1)(G-R+1)}{(G+2)^2(G+3)} \quad (4.8)$$

Fig. 4.18 shows the calculated acceptance for K_S^0 multiplicities plotted in the same format as the raw multiplicities. For low values of z the acceptance drops below 20% for the three lowest y bins.

4.5. Vector Meson Correction

A fraction of the detected K_S^0 originates from the decay of diffractive 1γ produced vector mesons. This process is not described by the fragmentation mechanism of quarks fragmenting into K_S^0 . The production of diffractive vector mesons is process dependent, thus violating the universality of FFs. Therefore, the contribution of vector mesons decaying into K_S^0 has to be estimated and corrected for. Only


 Figure 4.18.: Acceptance of K_S^0 plotted against z in bins of x and y .

4. Extraction of K_S^0 Multiplicities

the channel $\phi \longrightarrow K_S^0 K_L^0$ is taken into account as it is the channel with the largest cross section. Other channels have smaller cross sections and do not contribute significantly to the number of produced K_S^0 .

Since the decay $\phi \longrightarrow K_S^0 K_L^0$ is not included in the currently available MC data, the determination of the contamination from ϕ events is performed by making use of results on the reaction $\phi \longrightarrow K^+ K^-$ from Ref. [58]. The SIDIS events without diffractive contributions are simulated using the LEPTO event generator as in Sect. 4.4. The diffractive ϕ production is simulated using the HEPGEN [59] event generator. The fractions of kaons resulting from diffractive ϕ are calculated for different bins of x , y , and z using the usual binning of the analysis:

$$f_{\phi}^{K^{\pm}}(x, y, z) = \frac{N_{\text{HEPGEN}}^{K^{\pm}}(x, y, z)}{N_{\text{LEPTO}}^{K^{\pm}}(x, y, z) + N_{\text{HEPGEN}}^{K^{\pm}}(x, y, z)} \quad (4.9)$$

The number of DIS events generated with LEPTO already includes diffractive ϕ . Thus, the DIS correction factor reads:

$$f_{\text{DIS}}^{\phi}(x, y) = \frac{N_{\phi}^{\text{DIS}}(x, y)}{N_{\text{LEPTO}}^{\text{DIS}}(x, y)} \quad (4.10)$$

Then, the final correction is:

$$B^{K^{\pm}}(x, y, z) = \frac{1 - f_{\phi}^{K^{\pm}}(x, y, z)}{1 - f_{\text{DIS}}^{\phi}(x, y)} \quad (4.11)$$

The K^+ and K^- have a different acceptance and consequently different vector meson corrections. The correction factors for K_S^0 are determined from the averaged K^+ and K^- correction factors adjusted for the different branching ratios of K_S^0 and K^{\pm} :

$$B^{K_S^0}(x, y, z) = \left(\frac{B^{K^+}(x, y, z) + B^{K^-}(x, y, z)}{2} - 1 \right) \cdot \frac{\text{br}(K_S^0)}{\text{br}(K^{\pm})} + 1 \quad (4.12)$$

Since $B^{K^{\pm}}$ are multiplicative factors centered around one, they are subtracted by one to achieve the correction factors in percent, before they are corrected by the branching ratios. After the correction by the branching ratios, the result is added by one to achieve again multiplicative factors centered around one.

One caveat is that the vector meson correction was produced for a different binning with only eight x bins with the last bin ranging from 0.15–0.7. This last bin covers the last two x bins of this analysis (0.14–0.18 and 0.18–0.4) almost

completely. The corrections in this region of x are less than $< 1\%$. Hence the small difference in the binning is negligible. The results for the diffractive ϕ corrections to the number of K_S^0 are presented in Fig. 4.19.

In general, the corrections are small but can reach up to nearly 18% for certain bins in the medium z region at low x and y .

4.6. Systematic Uncertainties

Systematic uncertainties arise from the K_S^0 identification, the acceptance calculation, and the estimation of the vector meson contribution to the number of K_S^0 .

4.6.1. From K_S^0 identification

The systematic uncertainties arising from the K_S^0 identification are evaluated by comparing different methods used to separate the K_S^0 from the background. The standard method to determine the number of K_S^0 is per definition the integral method using a Gaussian as the signal function ($N_{\text{Gaussian}}^{K_S^0}$). It is compared with the K_S^0 numbers yielded by the integral method using a Voigtian as the signal function ($N_{\text{Voigtian}}^{K_S^0}$) and by the sideband subtraction method ($N_{\text{ss}}^{K_S^0}$). At first the relative deviation from the standard method is calculated as follows:

$$\sigma_{\text{sys}}^i = \frac{N_i^{K_S^0} - N_{\text{Gaussian}}^{K_S^0}}{N_{\text{Gaussian}}^{K_S^0}} \quad (4.13)$$

where i is either Voigtian or ss.

The deviations are shown in Fig.4.20. To reduce statistical variations three bins are combined by averaging their values weighted by their statistical uncertainties. Except for a few bins the systematic uncertainty is below 5 %. Larger uncertainties at bins of high x or high y as well as the trend to larger uncertainties towards higher z , are explained by the smaller statistics in that bins. Smaller statistics means the data has larger variations, consequently leading to larger deviations in the determination of the number of K_S^0 between the different methods.

4.6.2. From Acceptance

The estimation of systematic uncertainty due to the underlying physics model used for the acceptance correction has been investigated for charged hadron multiplicities [60]. Thereby, the acceptance has been evaluated using different MC samples with different quark fragmentation function parameters in JETSET and different PDFs in LEPTO. A systematic uncertainty of about 5% has been estimated and is provisionally adopted for this work but could be adjusted in further research.

4. Extraction of K_S^0 Multiplicities

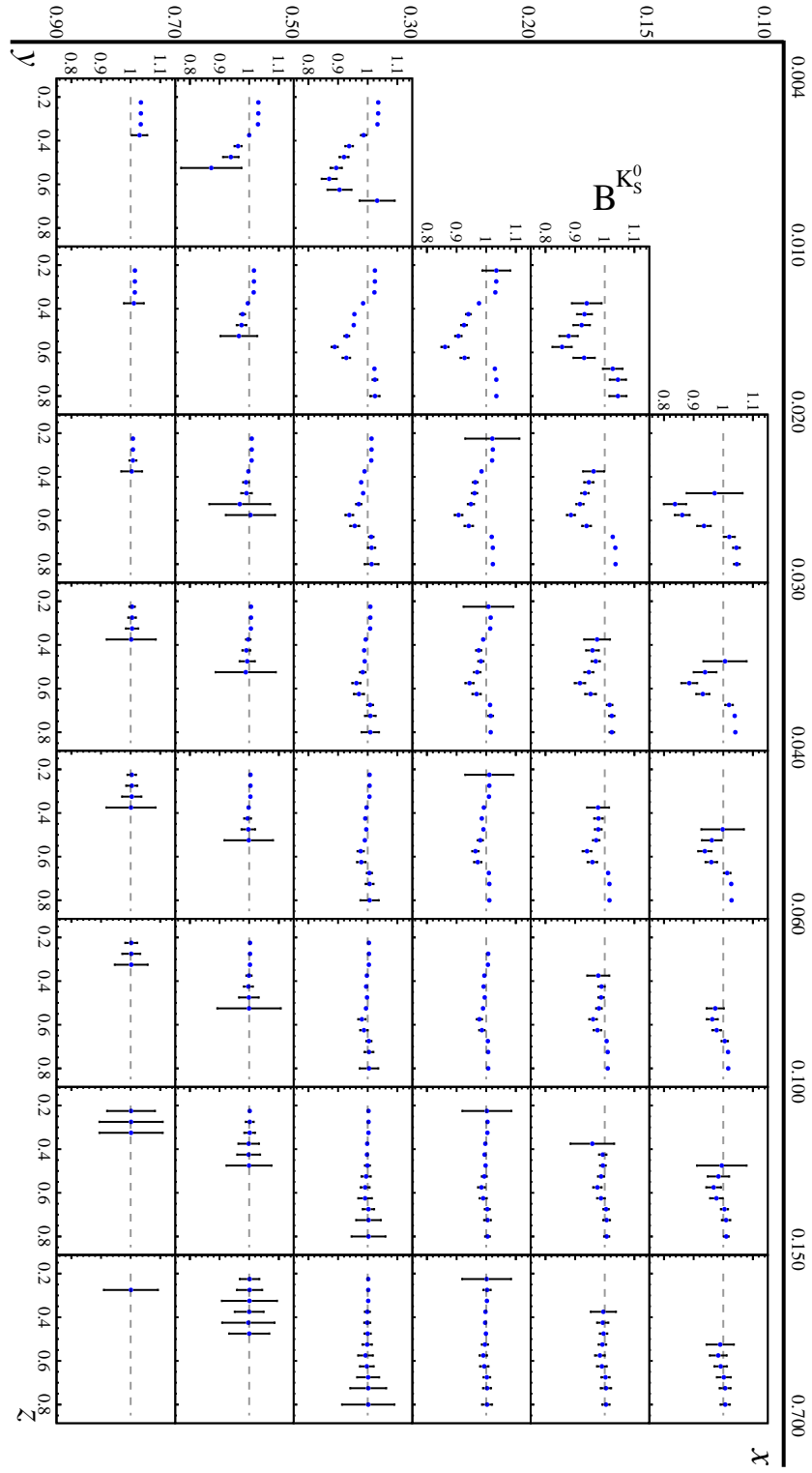
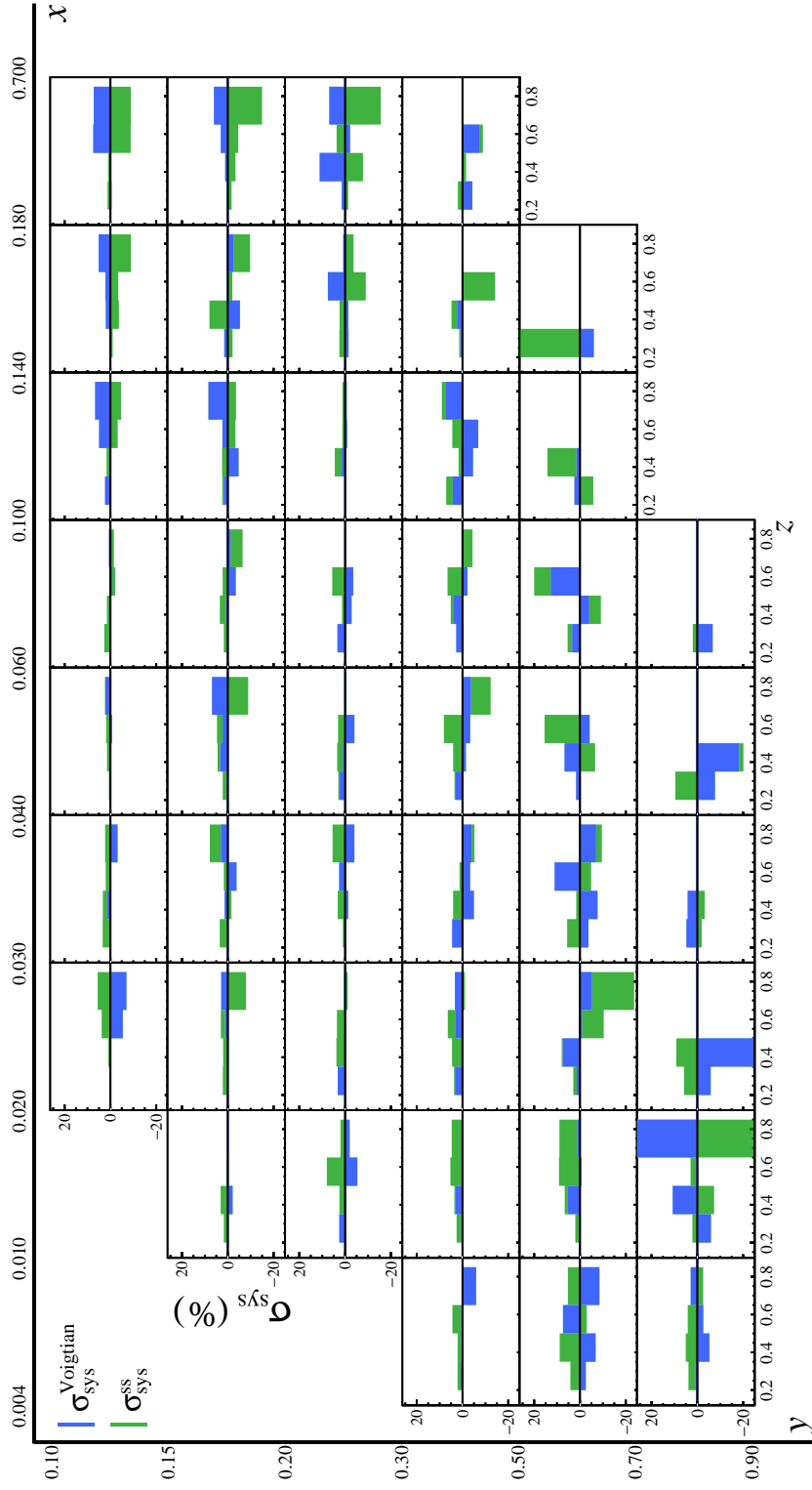


Figure 4.19.: Correction factor resulting from the diffractive ϕ contribution to the raw multiplicities.


 Figure 4.20.: The systematic uncertainties arising from the K_S^0 identification.

4. Extraction of K_S^0 Multiplicities

It requires the evaluation of the acceptance with different MC models which lies beyond the scope of this work.

A measure of the quality of the acceptance correction is the ratio of multiplicities of K_S^0 produced in different target cells. Figure 4.21 shows the ratio of multiplicities from the upstream target cell ($-56 \text{ cm} < z_{\text{vxt}} < -35 \text{ cm}$) and the downstream target cell ($43 \text{ cm} < z_{\text{vxt}} < 66 \text{ cm}$). For intermediate y bins with sufficiently large statistics the compatibility between the two samples is in the range of 10–15%. For low y bins a systematic shift appears towards higher multiplicities originating from the downstream target cell.

The multiplicity should of course be independent of the position of the primary vertex in the target. Therefore, it is worth to take a closer look into the region with the largest deviations, that is the region with $x > 0.1$ and $y < 0.2$.

Figure 4.22 compares RD and MC events of the said region with the total number of MC events is normalized to the total number of RD events. The plots show the primary vertex position of DIS events and the primary vertex position of events of possible K_S^0 , that is events with a final state hadron of mass $m = m_{K_S^0} \pm 15 \text{ MeV}/c^2$ that decayed into two oppositely charged particles. While there is no significant difference between MC and RD for the primary vertex position of DIS events, the ratio of RD and MC events of the primary vertex position of possible K_S^0 deviates from one and has a positive slope towards higher values of z_{pv} . The same difference can be seen in Fig. 4.23 for the secondary vertex position of the final state hadron.

Finding the source of this discrepancy is beyond the scope of this thesis, instead the systematic uncertainties that arise from the primary vertex position are estimated. The multiplicities that originate from the downstream, center, and upstream target cells are determined separately and the systematic uncertainties are calculated in the same manner as for the systematic uncertainties of the K_S^0 identification in 4.6.1. In this case the standard method are the multiplicities integrated over all target cells, that is the multiplicities presented in Sect. 4.7. Three z bins are combined to reduce variations due to low statistics.

The results are presented in Fig. 4.24. To give a better overview, the uncertainties in this view are cropped at $\pm 60\%$. As expected, the lowest y bin has large uncertainties in nearly all z bins which rise towards higher x . The systematic shifts of the downstream target cell are mainly positive while the ones from the upstream target cell are mainly negative. The large uncertainties in the highest y bin and those in the other bins at high z can be explained by the low statistics in these bins.

4.6.3. From Diffractive Vector Mesons

The cross section for exclusive vector meson production including the estimation of systematic uncertainties is evaluated in Ref. [58]. For charged kaons the sys-

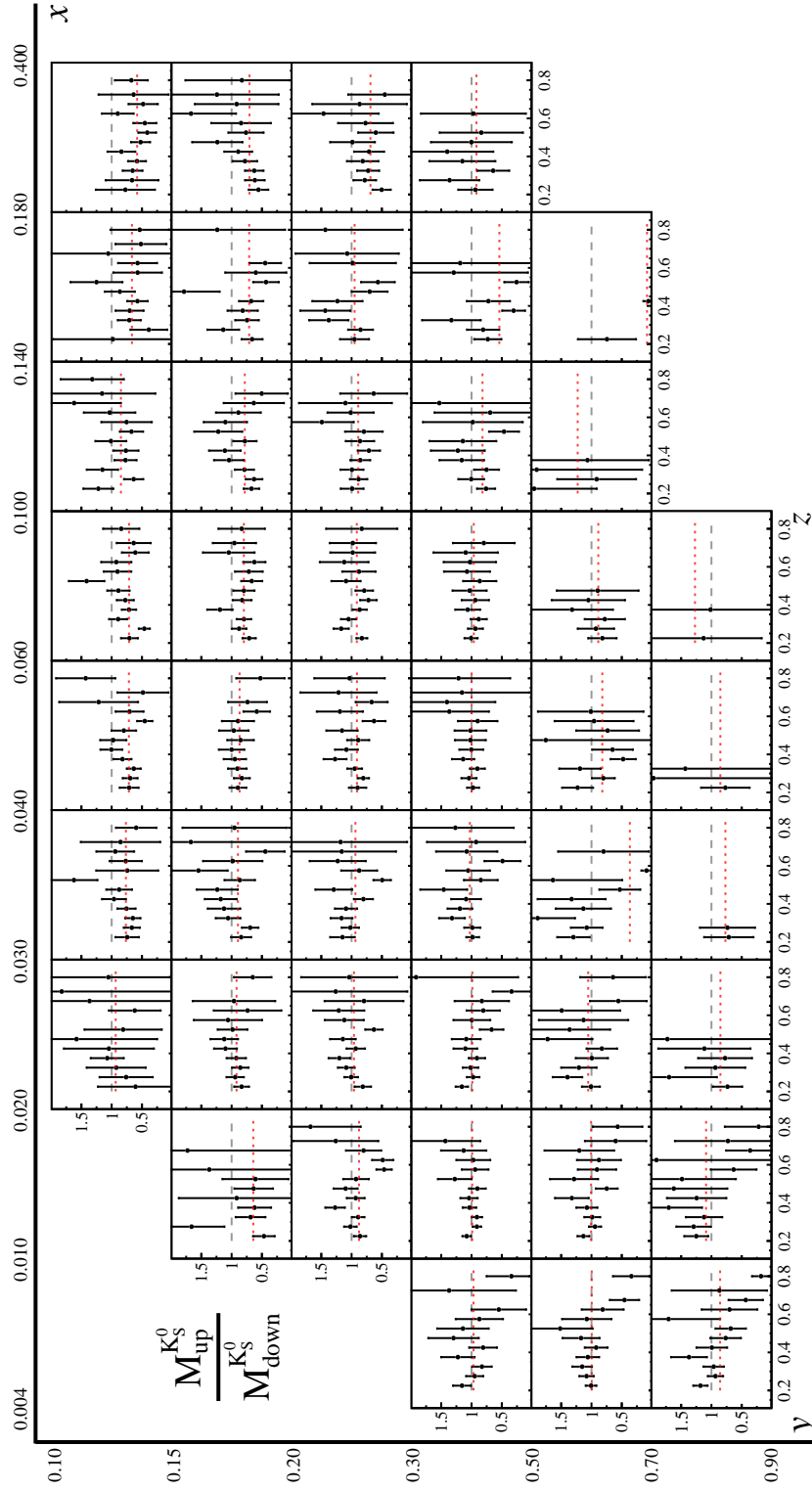


Figure 4.21.: The ratio of the acceptance corrected multiplicities extracted from the upstream and the downstream target cells. The red dashed line matches the weighted mean value of the corresponding x - y bin.

4. Extraction of K_S^0 Multiplicities

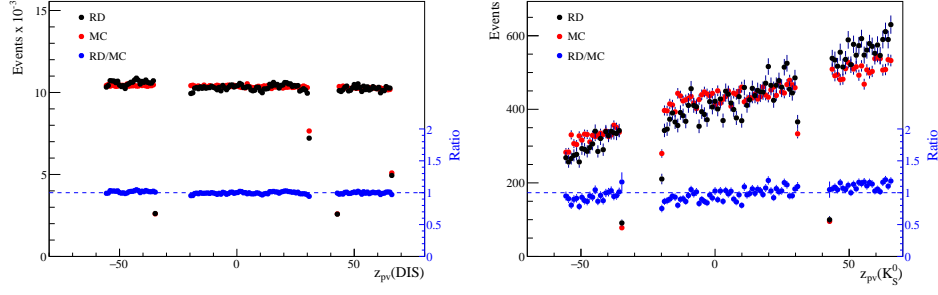


Figure 4.22.: Primary vertex position of all DIS events (left) and primary vertex position of events with a final state hadron of mass $m = m_{K_S^0} \pm 15 \text{ MeV}/c^2$ (right) for RD, MC, and the ratio RD/MC in the region $x > 0.1$ and $y < 0.2$.

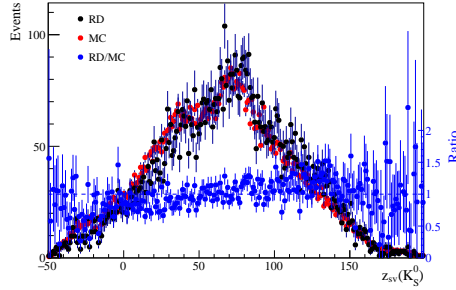


Figure 4.23.: Secondary vertex position of events with a final state hadron of mass $m = m_{K_S^0} \pm 15 \text{ MeV}/c^2$ for RD, MC, and the ratio RD/MC in the region $x > 0.1$ and $y < 0.2$.

tematic uncertainty following from diffractive vector mesons is smaller than 6%. Propagating this uncertainty using the Gaussian error propagation on Eq. (4.12) yields uncertainties for neutral kaons of less than 4% as shown in Fig. 4.25.

The charged kaons are analyzed only up to $y < 0.7$. Thus, no systematic uncertainties were produced for the highest y bin. It follows from Fig. 4.19 that the systematic uncertainties decrease with rising y and it should be save to neglect them for $0.7 < y < 0.9$.

4.6.4. Stability over Time

The data sample used in this analysis is taken over a period of six weeks. Table 4.7 shows the number of DIS events, kaon candidates and multiplicities for the six different weeks. The standard deviation between the six weeks is found to be less

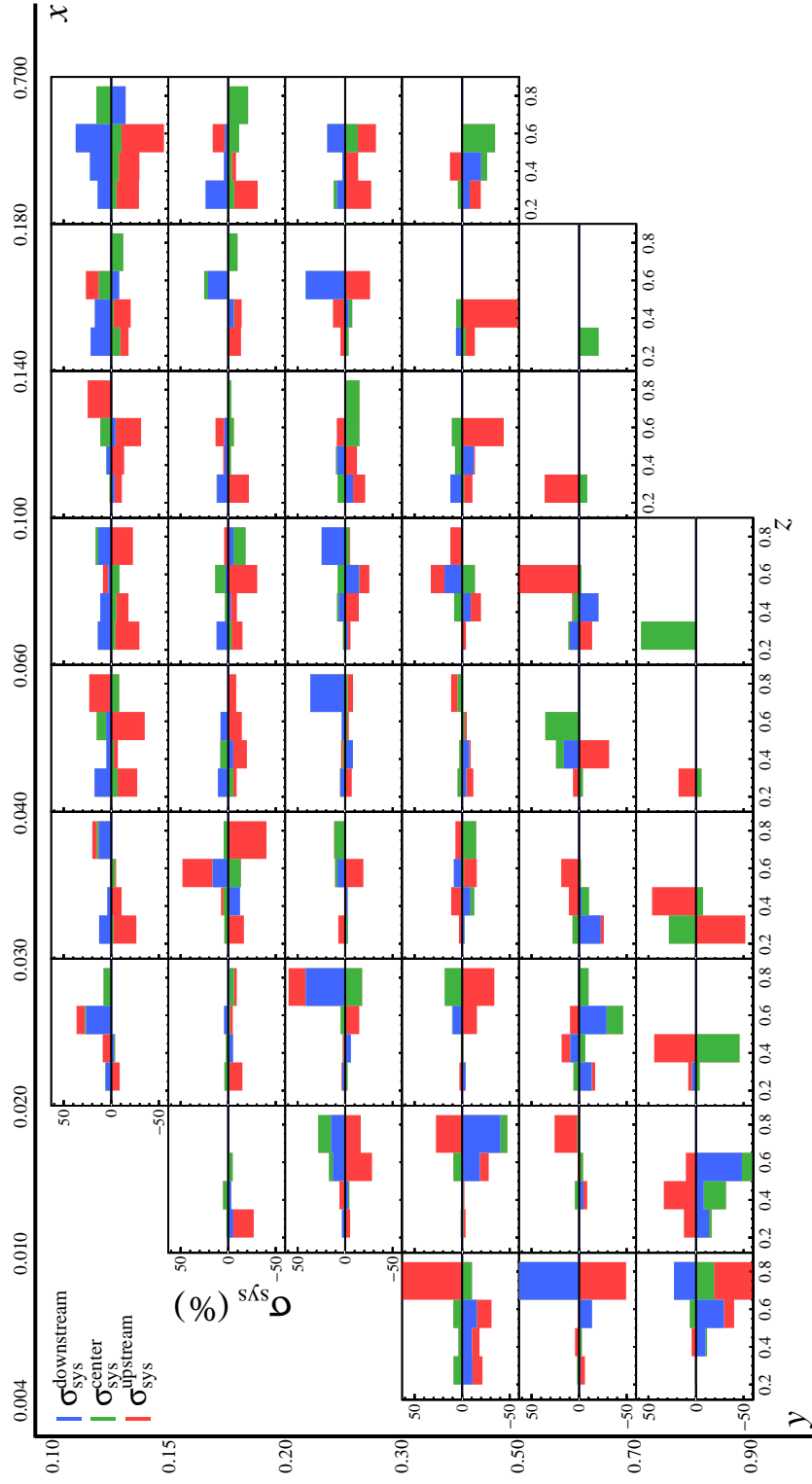


Figure 4.24.: The systematic uncertainties arising from variations of the multiplicities originating from different target cells.

4. Extraction of K_S^0 Multiplicities

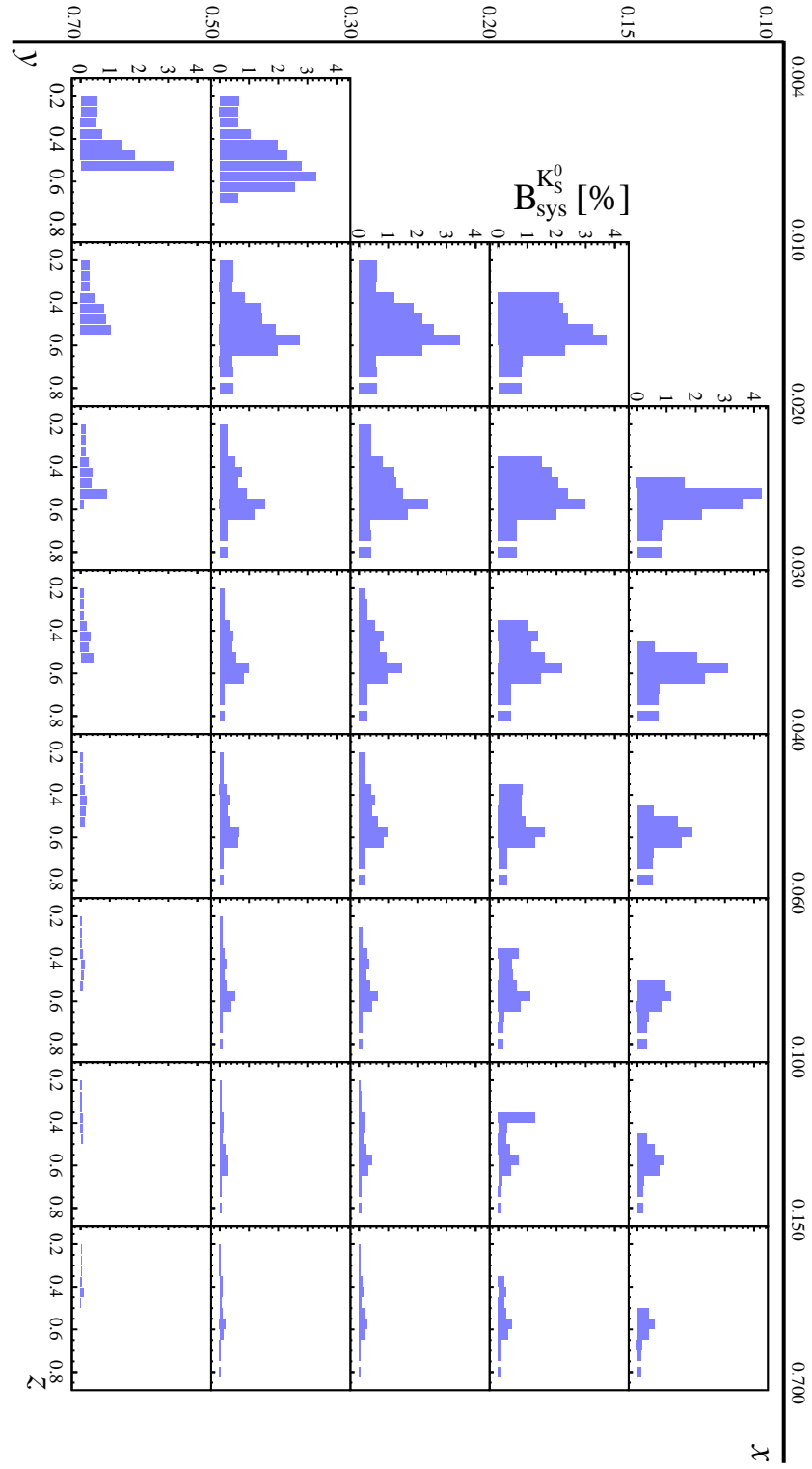


Figure 4.25.: Correction factor resulting from the diffractive ϕ contribution to the raw multiplicities.

Week	N^{DIS}	$N_{\text{corr}}^{\text{DIS}}$	N^{KS}_0	$N_{\text{corr}}^{\text{KS}}_0$	$N^{\text{KS}}_0/N^{\text{DIS}}$	$N^{\text{KS}}_0/N_{\text{corr}}^{\text{DIS}}$
W40	3172032	2873092.2	106884	98077.5	0.0337 ± 0.0001	0.0341 ± 0.0001
W41	2179180	1975198.7	74726	68719.4	0.0343 ± 0.0001	0.0348 ± 0.0001
W42	2197447	1992044.1	75080	69050.1	0.0342 ± 0.0001	0.0347 ± 0.0001
W43	2354547	2134139.2	80197	73756.0	0.0341 ± 0.0001	0.0345 ± 0.0001
W45	1964305	1780338.2	68122	61621.3	0.0347 ± 0.0001	0.0345 ± 0.0001
W46	1256129	1138624.2	42079	38746.7	0.0335 ± 0.0002	0.0340 ± 0.0002
total	13123640	11893436.6	447088	409971.0	0.0341 ± 0.0001	0.0345 ± 0.0001

Table 4.7.: Numbers of DIS events and kaon candidates as well as their ratios before and after radiative corrections for the six periods.

4. Extraction of K_S^0 Multiplicities

than 1%.

Next, the z -dependence of the ratio of the multiplicities measured in different weeks is studied. To obtain sufficiently enough statistics, the ratio is build over the combined weeks W40, W41, W45 and the combined weeks W42, W43, W46. For each x - y bin the weighted means and their corresponding standard deviations is calculated and plotted in Tab. 4.8. 83% of the ratio are compatible with 1 within the 1σ uncertainty and all of the ratio is compatible with 1 within 2σ . Deviations from 1 with more than 1σ are highlighted in the table. Since the deviations are very small, in this analysis the systematic uncertainties from the stability over time will not be taken into account.

4.6.5. Total Systematic Uncertainties

The systematic uncertainties of the K_S^0 identification $\sigma_{\text{sys}}^{\text{K}_S^0\text{Id}}$, the acceptance $\sigma_{\text{sys}}^{\text{tc}}$ and the diffractive vector meson contribution $\sigma_{\text{sys}}^{\text{B}}$ are combined to a total systematic uncertainty according to:

$$\sigma_{\text{sys}}^2 = \left(\sigma_{\text{sys}}^{\text{K}_S^0\text{Id}}\right)^2 + \left(\sigma_{\text{sys}}^{\text{tc}}\right)^2 + \left(\sigma_{\text{sys}}^{\text{B}}\right)^2. \quad (4.14)$$

Here $\sigma_{\text{sys}}^{\text{K}_S^0\text{Id}}$ and $\sigma_{\text{sys}}^{\text{tc}}$ are the sum over the absolute values of their individual contributions ($\sigma_{\text{sys}}^{\text{ss}}$, $\sigma_{\text{sys}}^{\text{Voigtian}}$) and ($\sigma_{\text{sys}}^{\text{downstream}}$, $\sigma_{\text{sys}}^{\text{center}}$, $\sigma_{\text{sys}}^{\text{upstream}}$), respectively, weighted by their statistical uncertainties:

$$\sigma_{\text{sys}}^i = \frac{\sum_i |\sigma_{\text{sys}}^i| / (\sigma_{\text{stat}}^i)^2}{1 / (\sigma_{\text{stat}}^i)^2}, \quad i = \text{K}_S^0\text{Id}, \text{tc} \quad (4.15)$$

Figure 4.26 shows the total systematic uncertainties with the contributions of $\sigma_{\text{sys}}^{\text{K}_S^0\text{Id}}$, $\sigma_{\text{sys}}^{\text{tc}}$, and $\sigma_{\text{sys}}^{\text{B}}$. They are dominated by the contribution of $\sigma_{\text{sys}}^{\text{tc}}$.

The total systematic uncertainties still vary a lot and show a randomly distributed amplitude, which contradicts the expectations. To smooth the systematic uncertainties, they are averaged over y , again weighted by their statistical uncertainties. The y averaged systematic uncertainties are presented in Fig. 4.27 as a function of z for bins of x . In general the uncertainties lie between 5%–10% with exceptions for the highest x bin, where they lie between 10%–20% and for the three lowest x bins, in which the uncertainties of the largest z bin rise up to 30%.

4.7. Final K_S^0 Multiplicities

To obtain the final K_S^0 multiplicities, the raw multiplicities are corrected by the acceptance (Sect. 4.4) and the diffractive vector meson contribution (Sect. 4.5):

x	0.004-0.01	0.01-0.02	0.02-0.03	0.03-0.04	0.04-0.06
y	$\bar{R} \pm \sigma_R$	$\bar{R} \pm \sigma_R$	$\bar{R} \pm \sigma_R$	$\bar{R} \pm \sigma_R$	$\bar{R} \pm \sigma_R$
0.10-0.15	—	—	0.94 ± 0.21	0.91 ± 0.15	0.92 ± 0.17
0.15-0.20	—	0.78 ± 0.23	0.93 ± 0.10	0.88 ± 0.15	0.96 ± 0.16
0.20-0.30	—	0.97 ± 0.09	0.94 ± 0.10	0.99 ± 0.09	0.90 ± 0.18
0.30-0.50	0.95 ± 0.12	0.98 ± 0.09	0.98 ± 0.11	0.97 ± 0.11	0.99 ± 0.14
0.50-0.70	1.02 ± 0.09	0.99 ± 0.08	0.90 ± 0.18	0.83 ± 0.23	0.62 ± 0.37
0.70-0.90	0.94 ± 0.15	0.90 ± 0.16	0.84 ± 0.37	0.59 ± 0.31	0.48 ± 0.37

x	0.06-0.1	0.1-0.14	0.14-0.18	0.18-0.4
y	$\bar{R} \pm \sigma_R$	$\bar{R} \pm \sigma_R$	$\bar{R} \pm \sigma_R$	$\bar{R} \pm \sigma_R$
0.10-0.15	0.88 ± 0.10	0.92 ± 0.21	0.87 ± 0.21	0.85 ± 0.14
0.15-0.20	0.91 ± 0.07	0.85 ± 0.15	0.87 ± 0.18	0.86 ± 0.14
0.20-0.30	0.92 ± 0.06	0.98 ± 0.12	0.98 ± 0.20	0.95 ± 0.15
0.30-0.50	0.96 ± 0.17	1.00 ± 0.34	0.99 ± 0.19	0.74 ± 0.25
0.50-0.70	0.86 ± 0.18	0.90 ± 0.25	0.48 ± 0.32	—
0.70-0.90	1.20 ± 0.42	—	—	—

Table 4.8.: The weighted mean values and corresponding standard deviation for the ratio of the multiplicities extracted from the combined weeks W40, W41, W45 and the combined weeks W42, W43, W46. Bins deviating from 1 with more than 1σ , are highlighted.

4. Extraction of K_S^0 Multiplicities

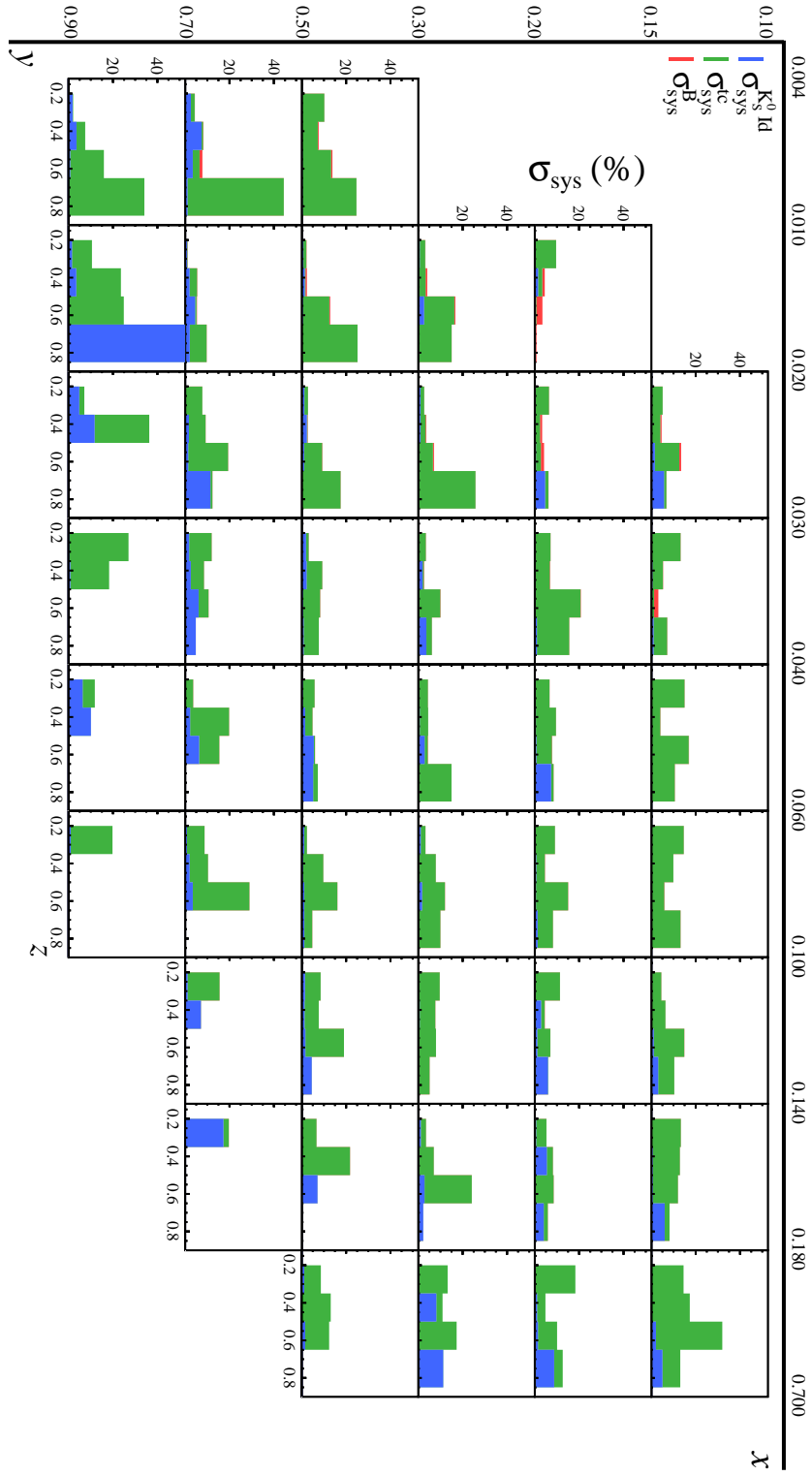
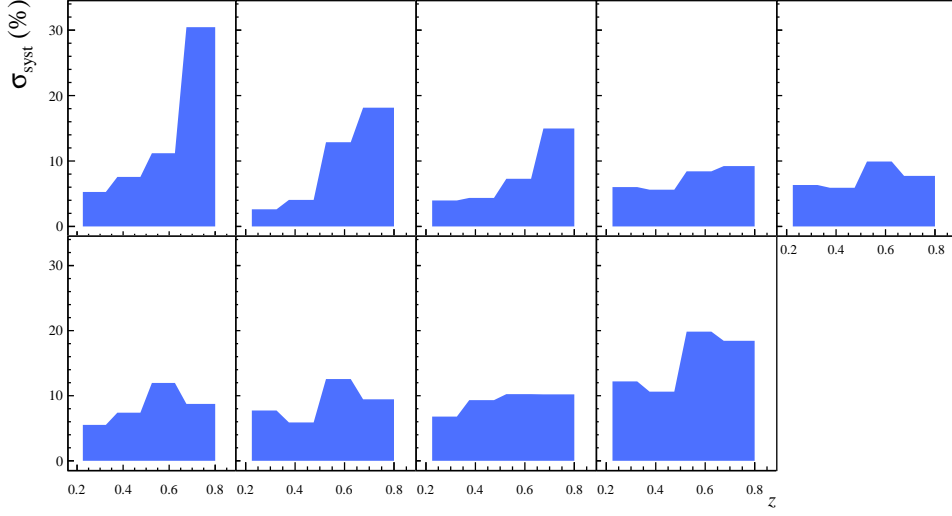


Figure 4.26: Total systematic uncertainties. The individual contributions of the K_S^0 identification (blue), the different target cells (green), and the vector meson contribution (red) are shown proportionally.


 Figure 4.27.: Final y averaged systematic uncertainties as a function of z for bins of x .

$$M_{\text{final}}^{\text{KS}^0}(x, y, z) = \frac{M_{\text{raw}}^{\text{KS}^0}(x, y, z)}{A(x, y, z)} B^{\text{KS}^0}(x, y, z) \quad (4.16)$$

The statistical uncertainties are composed as follows:

$$\sigma_{\text{final}}^{\text{KS}^0}(x, y, z) = M_{\text{final}}^{\text{KS}^0}(x, y, z) \cdot \sqrt{\left(\frac{\sigma_{\text{raw}}^{\text{KS}^0}(x, y, z)}{M_{\text{raw}}^{\text{KS}^0}(x, y, z)} \right)^2 + \left(\frac{\sigma_A(x, y, z)}{A(x, y, z)} \right)^2 + \left(\frac{\sigma_B(x, y, z)}{B^{\text{KS}^0}(x, y, z)} \right)^2} \quad (4.17)$$

The final KS^0 multiplicities are presented in Fig. 4.28. Only statistical uncertainties are plotted together with the multiplicity points. The bands on the bottom of each plot corresponds to the y averaged systematic uncertainties. They are achieved by multiplying the y averaged total systematic uncertainties with the corresponding y averaged multiplicity of that bin.

The KS^0 multiplicities are the final result of the of this analysis. They are used to extract the kaon FFs as described in the following chapter.

4. Extraction of K_S^0 Multiplicities

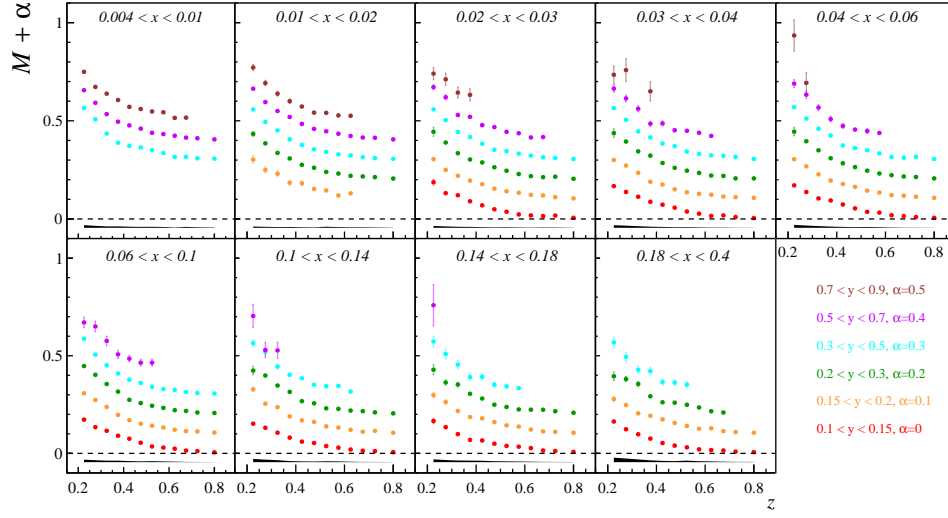


Figure 4.28.: Acceptance corrected K_S^0 multiplicities plotted versus z for bins in x and bins in y (staggered for clarity). Only statistical uncertainties are plotted with the multiplicity points. The bands on the bottom of each plot corresponds to the y averaged systematic uncertainties.

5. Extraction of Fragmentation Functions

The second main part of this analysis consists in the extraction of a parametrization of kaon FFs from the multiplicities measured at COMPASS. In general, to extract a parametrization of FFs a LO pQCD fit is performed on the multiplicities. The fit procedure is described in detail in Sect. 5.1.

To show the functionality of the fit, at first the extraction of pion FFs from present π^+ and π^- multiplicities measured at COMPASS is described and presented in Sect. 5.2.

In the next section, Sect. 5.3, the extraction of kaon FFs from measured COMPASS kaon multiplicities is performed. First, in Sect. 5.3.1 the FFs are extracted from K^+ and K^- multiplicities only. In Sect. 5.3.2 the K_S^0 multiplicities of this analysis are included and used to extract the parametrization of kaon FFs with a combined fit on K^+ , K^- , and K_S^0 multiplicities. In the final part, Sect. 5.3.3, the extracted kaon FFs are used to estimate the multiplicities at the kinematics of measured multiplicities of HERMES.

5.1. General Fit Method

The parametrizations of FFs are extracted from measured multiplicities in (x, y, z) by performing a LO pQCD fit. Therefore a χ^2 minimization procedure is performed on the measured multiplicities. For each data point $M^{\text{exp}}(x_j, Q_j^2, z_j)$ of the measured multiplicities, the theoretical multiplicity

$$T(x_j, Q_j^2, z_j) = \frac{\sum_q e_q^2 \left[q(x, Q^2) D_q^h(z, Q^2) + \bar{q}(x, Q^2) D_{\bar{q}}^h(z, Q^2) \right]}{\sum_q e_q^2 \left[q(x, Q^2) + \bar{q}(x, Q^2) \right]}, \quad (5.1)$$

according to Eq. (2.25), is evaluated. The values of $q(x, Q^2)$ of a selected PDF set are taken from LHAPDF where the PDFs are available as functions of x and Q^2 . The parametrization of the FFs $D_q^h(z, Q_0^2)$ is evaluated at the initial scale $Q_0^2 = 1 \text{ GeV}/c^2$ and evolved to the Q_j^2 value of the given data point, using a DGLAP Q^2 evolution code provided by M.Hirai and S. Kumano [62]. The parametrization has the general form:

5. Extraction of Fragmentation Functions

$$zD_q^h(z, Q_0^2) = N_q f_q(z, Q_0^2), \quad (5.2)$$

where N_q is the contribution of D_q^h to the sum rule in Eq. (2.22) and $f_q(z, Q_0^2)$ is the shape function of D_q^h at the initial scale $Q_0^2 = 1 \text{ GeV}/c^2$. The shape function is normalized within the kinematic limits of $z \in [0.2, 0.85]$:

$$\int_{0.2}^{0.85} f(z) dz = 1. \quad (5.3)$$

The shape function is expected to be a smooth function that vanishes at the kinematical limit $z = 1$. Typically a functional form like

$$f_q(z, Q_0^2) = z^{\alpha_q} (1 - z)^{\beta_q} \quad (5.4)$$

is selected, where z^{α_q} defines the shape at low z and $(1 - z)^{\beta_q}$ defines the shape at large z . In recent global fits the shape function is extended by two additional parameters to

$$f_q(z, Q_0^2) = z^{\alpha_q} (1 - z)^{\beta_q} (1 + \gamma_q (1 - z)^{\delta_q}). \quad (5.5)$$

The additional part is introduced to accommodate the experimental information of lepton-nucleon and hadron-hadron scattering data and to avoid artificial correlations between the behavior of FFs in different regions of z [28]. For this particular analysis it turned out that the simple form is sufficient because the final values of γ_q were set to zero as a result of the fit.

The minimization procedure is performed with the minimization framework Minuit2 of the ROOT package. The parameters of $zD_q^h(z, Q_0^2)$ are fit to minimize the difference of experimental and theoretical multiplicities weighted by the statistical uncertainties σ_j :

$$\chi^2 = \sum_{j=1}^N \left[\left(T(x_j, Q_j^2, z_j) - M^{\text{exp}}(x_j, Q_j^2, z_j) \right) / \sigma_j \right]^2, \quad (5.6)$$

where N denotes the number of data points.

5.1.1. FF Uncertainties

The statistical and systematic uncertainties of the extracted FFs are determined by using a bootstrap method [63]. Therefore a number of resamples of the original multiplicity data are constructed. For each resample, the data points are fluctuated proportional to their uncertainty, resulting in a set of data points:

$$M'_j = M_j + R \cdot \sigma_j \quad (5.7)$$

where M_j and σ_j are the original value and the corresponding uncertainty of data point j , respectively. The factor R is a Gaussian randomly distributed value in the range $[-\infty, \infty]$. Its determination is differently treated for statistical and systematic uncertainties.

The statistical uncertainties are uncorrelated and the deviation of each data point j is calculated with an individual random value R_j . Thus, for statistical uncertainties, Eq. (5.7) can be written as:

$$M'_{j,stat} = M_j + R_j \cdot \sigma_{j,stat}. \quad (5.8)$$

Therefore for each resample only one random value R' of the standard Gaussian distribution is generated. Then, Eq. (5.7) can be written as:

$$M'_{j,sys} = M_j + R' \cdot \sigma_{j,sys}. \quad (5.9)$$

For both, the statistical and the systematic uncertainties, a set of 100 resamples is created. Then for each resample, the fit is performed, as it is done for the original data. To calculate the uncertainty bands, for each z bin, the mean and RMS values are calculated from the resulting FFs. The uncertainties are centered around the mean value and have the width of the corresponding RMS value.

5.2. Pion Fragmentation Functions

To this date, FFs of charged pions are the best determined FFs. The pion is the lightest meson and the meson with the largest cross section. Due to its valence quark configuration:

$$\begin{aligned} \pi^+ &= u\bar{d} \\ \pi^- &= \bar{u}d, \end{aligned} \quad (5.10)$$

it is the simplest to produce. If an u or d quark is struck, to produce a pion only a $d\bar{d}$ or $u\bar{u}$ quark pair has to be created from the vacuum. The detection of charged pions is similar to the detection of charged kaons. Usually, groups that work on the extraction of charged kaon FFs already have parametrizations for charged pions, see for example Refs. [65] and [66]. Thus, to prove the effectiveness of the fit method, determining the pion FFs with good accuracy should be accomplished before the extraction of kaon or other particle's FFs is performed.

The COMPASS π^+ and π^- multiplicities of 2006 data are presented in Ref. [67, 69]. The data covers the same kinematic region as the data of the current analysis and the same binning in x , y , and z is applied. In Figs. 5.1 and 5.2, multiplicities of π^+ and π^- are presented in bins of x and y .

5. Extraction of Fragmentation Functions

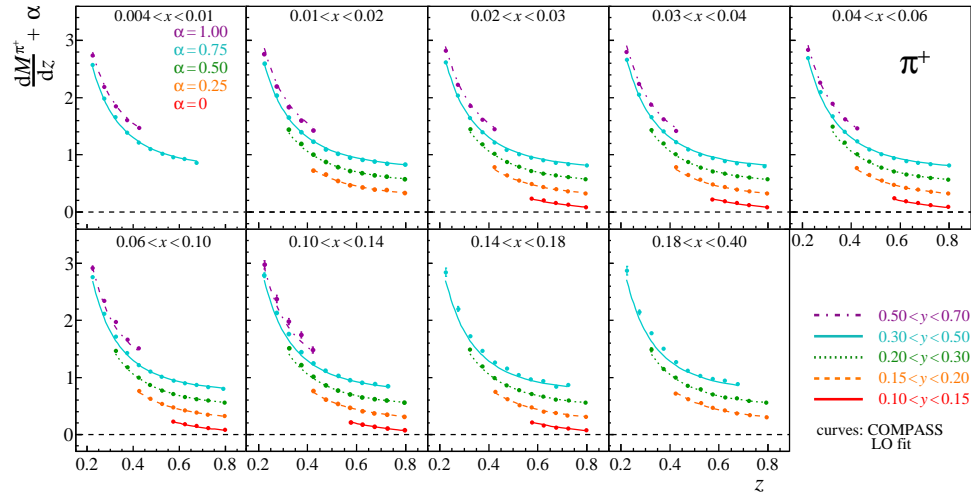


Figure 5.1.: π^+ multiplicities versus z for nine x bins and five y bins (staggered for clarity by α). Only statistical uncertainties are shown. The curves correspond to the LO fit. The plot is taken from Ref. [67].

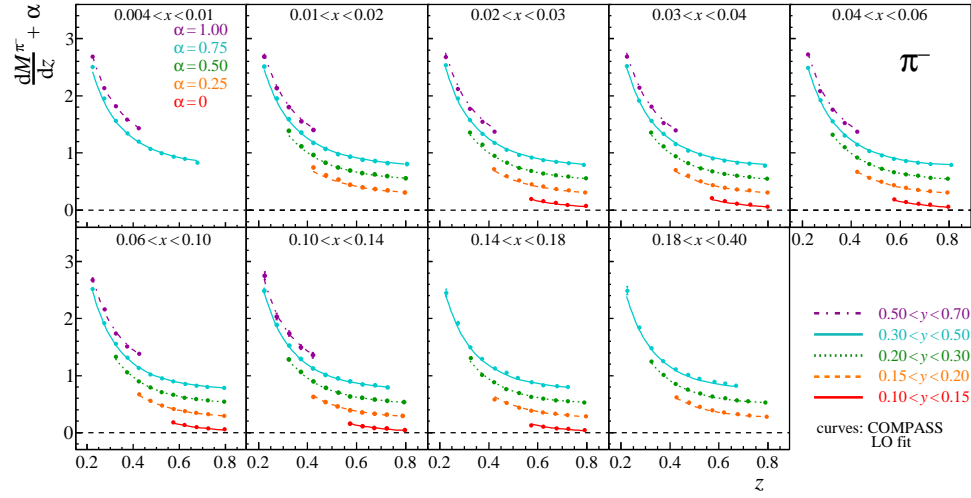


Figure 5.2.: Same as Fig. 5.1 but for π^- multiplicities.

Only statistical uncertainties are shown, which are in most cases smaller than the size of the markers. The multiplicities are corrected for diffractive ρ^0 production. The main contributions to the systematic uncertainties are acceptance and RICH uncertainties, and the misidentification of pions from diffractive ρ^0 production.

The unpolarized COMPASS final state hadrons carry no information about the struck quark in the nucleon. By exploiting isospin and charge symmetry the number of different π^\pm FFs is reduced to three independent FFs (including the gluon FF):

$$\begin{aligned} D_{\text{fav}} &= D_u^{\pi^+} = D_d^{\pi^+} = D_d^{\pi^-} = D_u^{\pi^-} \\ D_{\text{unf}} &= D_d^{\pi^+} = D_u^{\pi^+} = D_u^{\pi^-} = D_d^{\pi^-} = D_s^{\pi^\pm} = D_{\bar{s}}^{\pi^\pm} \\ D_g &= D_g^{\pi^\pm}. \end{aligned} \quad (5.11)$$

The simple parametrization

$$zD_q(z, Q^2) = N_q z^{\alpha_q} (1-z)^{\beta_q} \quad (5.12)$$

is used to parameterize the FFs ($q = \text{fav}, \text{unf}, g$). Thus, the number of free parameters is $n_f = 9$.

The multiplicities are given by:

$$M^{\pi^+}(x, Q^2, z) = \frac{(4(u+d) + \bar{u} + \bar{d})D_{\text{fav}}^{\pi} + (u+d + 4(\bar{u} + \bar{d}) + 2(s + \bar{s}))D_{\text{unf}}^{\pi}}{5(u+d + \bar{u} + \bar{d}) + 2(s + \bar{s})} \quad (5.13)$$

and

$$M^{\pi^-}(x, Q^2, z) = \frac{(u+d + 4(\bar{u} + \bar{d}))D_{\text{fav}}^{\pi} + (4(u+d) + \bar{u} + \bar{d} + 2(s + \bar{s}))D_{\text{unf}}^{\pi}}{5(u+d + \bar{u} + \bar{d}) + 2(s + \bar{s})}. \quad (5.14)$$

Detailed derivations of 5.11, 5.13, and 5.14 can be found in A.1.

Table 5.1 shows the final parameters. For the fit a reduced χ^2 value of $\chi^2/n_d = 1.69$ is achieved.

The pion FFs are shown in Fig. 5.3. The small statistical uncertainties result in a narrow uncertainty band, only slightly larger than the line width of the drawn FF. For comparison they are plotted together with NLO FFs from DSEHS [66], LSS [65], and HKNS [29]. The choice to compare the COMPASS FFs of LO with NLO FFs is because there are no LO FFs from LSS available. The large difference

5. Extraction of Fragmentation Functions

	N	α	β
D_{fav}^π	0.160 ± 0.004	-0.92 ± 0.05	0.26 ± 0.04
D_{unf}^π	0.065 ± 0.001	-0.7 ± 0.1	1.3 ± 0.2
D_g^π	0.35 ± 0.01	5.1 ± 1.1	4.0 ± 0.9

Table 5.1.: Final fit parameters for $Q_0^2 = 1 \text{ GeV}/c^2$

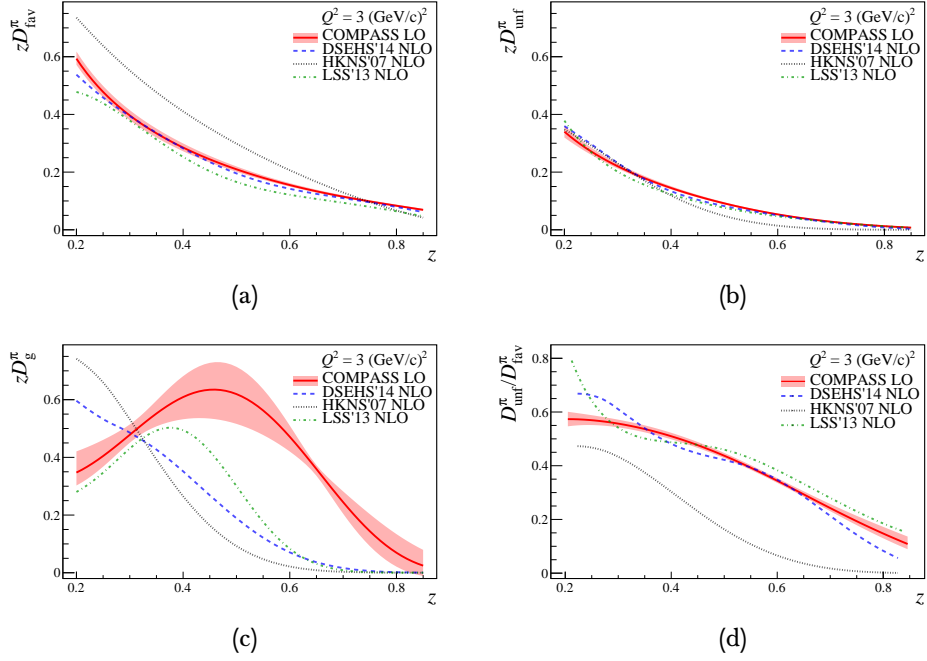


Figure 5.3.: The favored (a), unfavored (b), and gluon (c) pion FFs and the ratio $D_{\text{unf}}^\pi/D_{\text{fav}}^\pi$, as obtained from COMPASS LO fit compared to the DSEHS, HKNS, and LSS fits at NLO. The bands represent the total uncertainties for the FFs and the statistical uncertainty for the ratio.

to HKNS is expected since HKNS FFs are based on e^-e^+ -annihilation data only. Although the universality principle of FFs predicts that FFs are independent of the underlying processes, to extract with them precision large data sets, including different kinds of data, are necessary.

Fig. 5.3 also shows the ratio of unfavored and favored FFs. Here, the uncertainty band is from statistical uncertainty only, since it is assumed that the systematic uncertainties are canceled out when building the ratio.

5.3. Kaon Fragmentation Functions

This section presents the extraction of kaon FFs from kaon multiplicities of COMPASS 2006 data. The charged kaon multiplicities from COMPASS 2006 data [68, 70, 71] are presented in Fig. 5.4 plotted against z in bins of x and y . It is the same binning as introduced in Sect. 4.1.1 with the exception that only the lowest five y bins from $0.1 < y < 0.7$ are used. This is due to kinematic reasons as the highest bin $0.7 < y < 0.9$ is too sparsely populated with charged kaon multiplicities.

Just as in the case of charged pions the analysis of charged kaons depends on the RICH detector for particle identification. Therefore the momenta of K^+ and K^- are limited to the range of 12–40 GeV/c. This has a direct effect on the z range covered by the charged kaon multiplicities, as the y bin $0.3 < y < 0.5$ alone covers the full z range. Here, the neutral kaon multiplicities are complementary to the charged kaon multiplicities because they do not depend on the RICH detector for particle identification and cover the full z range for all y bins, except the two highest ones ($0.5 < y < 0.7$ and $0.7 < y < 0.9$).

The positive and negative kaon multiplicities have 310 data points each, the neutral kaons 543 data points. This sums up to 620 data points for charged multiplicities and 1163 data points for charged and neutral multiplicities combined.

As already shown in Sect. 2.5.1, using isospin symmetry, charge invariance, and the additional assumption that all unfavored FFs are equal, the kaon FFs are reduced to three independent FFs plus the gluon FF:

$$\begin{aligned}
 D_{\text{fav}}^K &= D_{\text{fav}}^{K^0} = D_{\text{fav}}^{K^+} \\
 D_s^K &= D_s^{K^0} = D_s^{K^+} \\
 D_{\text{unf}}^K &= D_{\text{unf}}^{K^0} = D_{\text{unf}}^{K^+} \\
 D_g^K &= D_g^{K^0} = D_g^{K^+}
 \end{aligned} \tag{5.15}$$

As for the case with charged pions, in LO the gluon FF is only determined indirectly during the Q^2 evolution.

5. Extraction of Fragmentation Functions

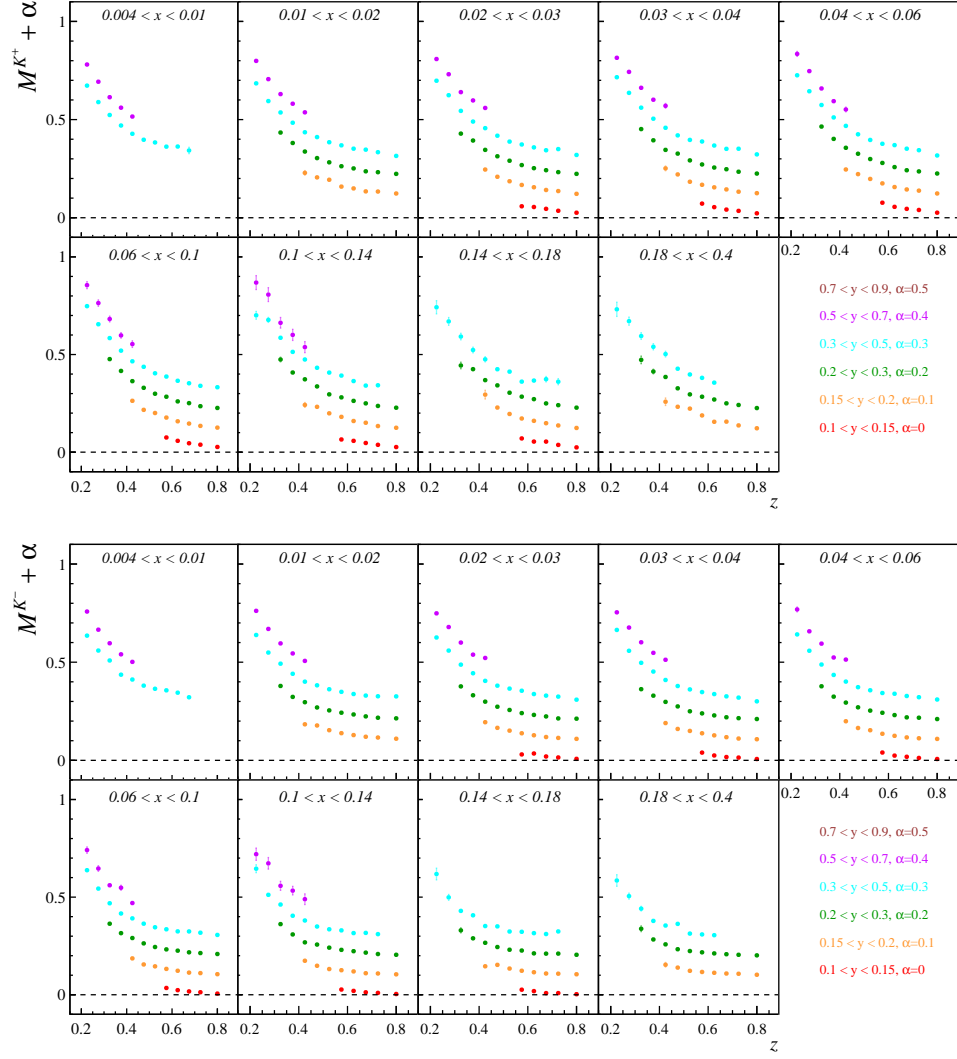


Figure 5.4.: K^+ (top) and K^- (bottom) multiplicities versus z for nine x bins and five y bins (staggered for clarity by α).

The LO multiplicities of K^+ , K^- , and K_S^0 for the three independent FFs are:

$$M^{K^+} = \frac{4(u+d)D_{\text{fav}}^K + 2\bar{s}D_s^K + (5(\bar{u}+\bar{d})+u+d+2s)D_{\text{unf}}^K}{5(u+\bar{u}+d+\bar{d})+2(s+\bar{s})} \quad (5.16)$$

$$M^{K^-} = \frac{4(\bar{u}+\bar{d})D_{\text{fav}}^K + 2sD_s^K + (5(u+d)+\bar{u}+\bar{d}+2\bar{s})D_{\text{unf}}^K}{5(u+\bar{u}+d+\bar{d})+2(s+\bar{s})} \quad (5.17)$$

$$M^{K_S^0} = \frac{\left(\frac{1}{2}D_{\text{fav}}^K + \frac{9}{2}D_{\text{unf}}^K\right)(u+\bar{u}+d+\bar{d}) + \left(D_{\text{unf}}^K + D_s^K\right)(s+\bar{s})}{5(u+\bar{u}+d+\bar{d})+2(s+\bar{s})} \quad (5.18)$$

A detailed derivation is given in A.2.

Due to D_s^K the extraction of kaon FFs is sensitive to the strange quark distribution in the nucleon. The strange PDF has especially large uncertainties compared to the other PDFs and the different PDF sets do not agree among each other, see Sect. 2.3. To study the influence of the selected PDF set on the FFs, the fit is performed with the following PDF sets:

- MSTW08
- MMHT14 (successor of MSTW08)
- NNPDF2.3
- NNPDF3.0 (successor of NNPDF2.3)
- CT10

For clarity only selected results of MMHT14, NNPDF3.0, and CT10 are shown in this chapter. A complete set of plots, including the results of MSTW08 and NNPDF2.3, can be found in B.

All FFs are parameterized using the simple functional form introduced in Sect. 5.1,

$$zD_q(z, Q^2) = N_q z^{\alpha_q} (1-z)^{\beta_q}, \quad (5.19)$$

where $q = \text{fav}, \text{unf}, s, g$. This means that the number of free parameters for the fit is $n_f = 12$. The start parameters that were used for all fits are presented in table 5.2. The starting values for N_q are estimated by the relation $N_q = \int_{0.2}^{0.85} zD_q(z, Q^2) dz$ which is the average number of final state kaons produced from a struck parton of type q .

Compared with the parameter value, the initial step size is relatively large which will make Minuit2 cover a large value range but makes it less observant for local

5. Extraction of Fragmentation Functions

FF	parameter	start value	step size
$D_{\text{fav}}^{\text{K}}$	N	0.055	0.05
	α	0.2	2
	β	1.2	4
D_{s}^{K}	N	0.235	0.03
	α	0.2	2
	β	2.67	4
$D_{\text{unf}}^{\text{K}}$	N	0.002	0.001
	α	0.2	2
	β	8	4
D_{g}^{K}	N	0.09	0.02
	α	10	10
	β	4	10

Table 5.2.: Start values and initial step size for the parameters of the kaon FFs for the fit at $Q^2 = 1 \text{ (GeV/c)}^2$.

minima. However, the initial step size is not fixed as it is adjusted during the fitting process by Minuit2.

For the extracted FFs the statistical and systematic uncertainties of the multiplicities as well as systematic uncertainties arising from the parametrization of the PDF, given by the PDF set, are determined using the procedure described in Sect. 5.1.1.

In Sect. 5.3.1 the FFs extracted from a fit of charged kaon multiplicities are studied. In the following Sect. 5.3.2 the FFs are extracted from a simultaneous fit of charged and neutral kaon multiplicities. Thereafter, in section 5.3.3 the charged kaon multiplicities from HERMES are compared to the charged kaon multiplicities from COMPASS and the HERMES multiplicities are estimated from the extracted COMPASS FFs.

5.3.1. Kaon Fragmentation Functions from K^\pm Multiplicities

In this section the kaon FFs extracted only from charged kaon multiplicities are presented. The resulting χ^2/n_d values and fit parameters for $Q_0^2 = 1 \text{ (GeV/c)}^2$ are given in Tab. 5.3.

Figure 5.5 shows the measured K^+ and K^- multiplicities together with the estimations from the LO fit with PDFs from MMHT14. The result of the fit with MMHT14 PDFs is representative for the other fits with different PDF sets as the plots do not change significantly.

In general the measured multiplicities are well described by the fit. The χ^2/n_d

5.3. Kaon Fragmentation Functions

PDF	χ^2/n_d	FF	N	α	β
MSTW08	2.48	fav	0.05381 ± 0.0007	0.09 ± 0.07	0.85 ± 0.05
		s	0.094 ± 0.02	10.0 ± 2.0	20.0 ± 3.0
		unf	0.005627 ± 0.0006	9.0 ± 2.0	30.0 ± 5.0
		g	0.0925 ± 0.003	20.0 ± 4.0	9.0 ± 2.0
MMHT14	2.47	fav	0.0541 ± 0.001	0.16 ± 0.09	0.9 ± 0.06
		s	0.073 ± 0.02	8.0 ± 2.0	10.0 ± 3.0
		unf	0.005497 ± 0.0008	7.0 ± 2.0	20.0 ± 5.0
		g	0.0972 ± 0.004	20.0 ± 3.0	8.0 ± 2.0
NNPDF2.3	1.79	fav	0.04799 ± 0.0006	-0.11 ± 0.07	0.7 ± 0.05
		s	0.25 ± 0.03	9.0 ± 1.0	10.0 ± 1.0
		unf	0.006676 ± 0.0004	8.0 ± 1.0	20.0 ± 3.0
		g	0.0842 ± 0.003	10.0 ± 2.0	3.0 ± 0.7
NNPDF3.0	2.59	fav	0.05456 ± 0.0008	0.15 ± 0.08	0.97 ± 0.06
		s	0.092 ± 0.02	6.0 ± 3.0	10.0 ± 3.0
		unf	0.004625 ± 0.0008	5.0 ± 1.0	20.0 ± 3.0
		g	0.101 ± 0.005	10.0 ± 2.0	5.0 ± 1.0
CT10	1.93	fav	0.05057 ± 0.0009	0.2 ± 0.1	0.84 ± 0.06
		s	0.093 ± 0.01	5.0 ± 1.0	10.0 ± 1.0
		unf	0.004385 ± 0.0008	7.0 ± 2.0	20.0 ± 6.0
		g	0.107 ± 0.005	10.0 ± 2.0	5.0 ± 0.9

Table 5.3.: Parameters and χ^2/n_d values of fits of charged kaon multiplicities with different PDF sets for $Q_0^2 = 1 \text{ (GeV/c)}^2$.

5. Extraction of Fragmentation Functions

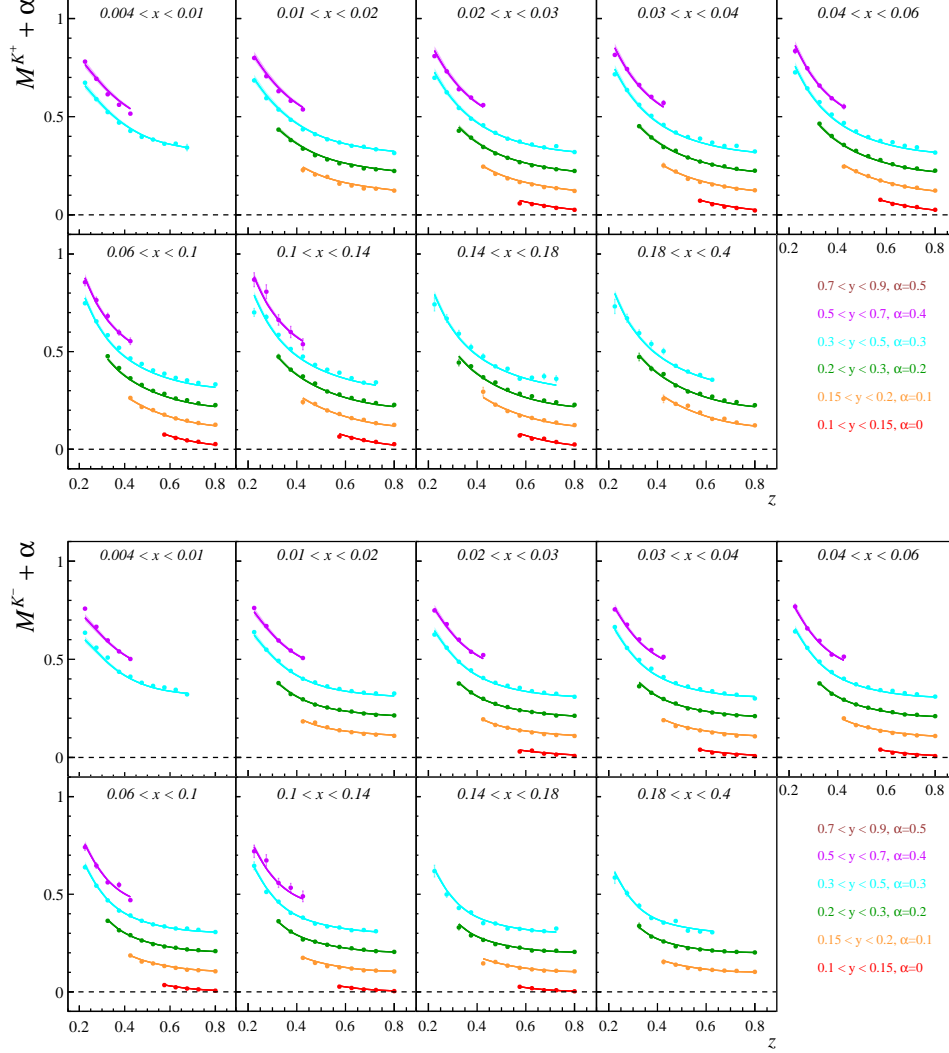


Figure 5.5.: Fit of K^+ (top) and K^- (bottom) multiplicities from COMPASS 2006 data. The points are the measured multiplicities with their statistical uncertainties. The curves correspond to the LO fit performed with MMHT14 as PDF set. The other PDF sets yield a similar good description.

values are in the range of 1.93–2.59 depending on the selected PDF set. The number of degrees of freedom n_d is the number of data points n minus the number of free parameters n_f , that is for the case of charged and neutral kaons of this analysis $n_d = n - n_f = 620 - 12 = 608$.

The χ^2/n_d value can be used as a measure of the goodness-of-fit [64]. If the fit is able to describe the data its value should be close to one. A value much smaller than one usually indicates overestimated uncertainties. If on the other hand the value is much larger, as it is the case in this analysis, two possible reasons have to be considered. Either the uncertainties are underestimated or the underlying LO model to describe the measured multiplicities is insufficient.

To give a number one can quote the significance level (P-value) for a given χ^2 value. The P-value describes the probability that another measurement yields a worse χ^2 than the actual one. It is obtained by

$$P = \int_{\chi^2}^{\infty} f(z; n_d) dz, \quad (5.20)$$

where $f(z; n_d)$ is the χ^2 distribution for n_d degrees of freedom. Figure 5.6 shows

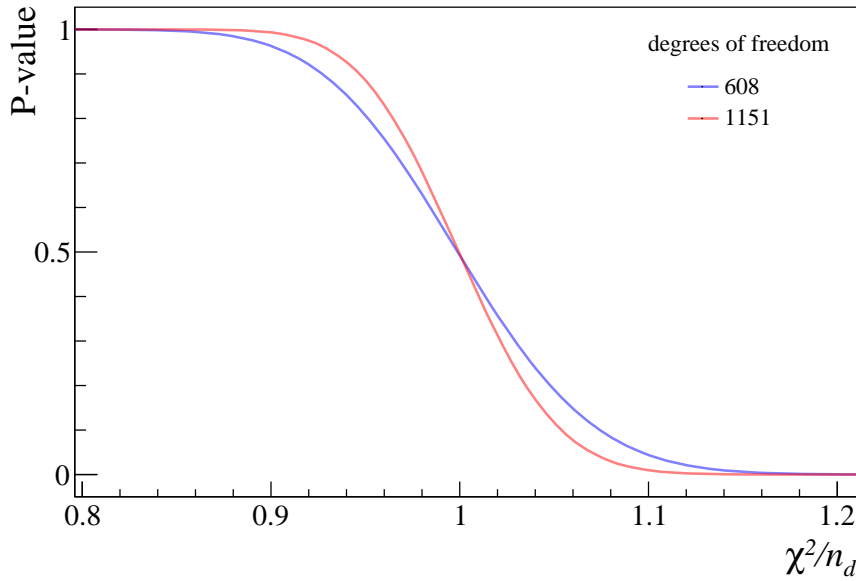


Figure 5.6.: The P-value plotted against χ^2/n_d for different degrees of freedom. The degrees of freedom are selected according to the current analysis.

the P-values for different degrees of freedom used in this analysis. It is obvious that all χ^2 values in this analysis are much larger than one, indicating either underestimated uncertainties or an insufficient model.

5. Extraction of Fragmentation Functions

To find out where the large χ^2 values originate from, the residuals, that is the non-squared contributions to the χ^2 sum:

$$\text{res}_j(x_j, Q_j^2, z_j) = \frac{T(x_j, Q_j^2, z_j) - M^{\text{exp}}(x_j, Q_j^2, z_j)}{\sigma_j}, \quad (5.21)$$

are plotted.

In Fig. 5.7 the residuals of the fit of K^+ and K^- multiplicities are presented in bins of x , y , and z for the analysis with the MMHT14 PDF set. The gray area visualizes the region of data points which if they alone were contributing to the χ^2 sum would yield to a total $\chi^2/n_d \approx 1$. The graphics show that in general only a few bins are responsible for the large total χ^2 value. The largest contribution comes from the low x and low y bins. Here, the high z bins of the K^- multiplicities are systematically underestimated by the fit. The opposite is observed for K^+ multiplicities, which are systematically overestimated for high z at high x and medium y .

The extracted FFs, evolved to the COMPASS mean $Q^2 = 3 (\text{GeV}/c)^2$ and plotted against z , are presented in Fig. 5.9. The uncertainty bands correspond to statistical (dark) and systematic (light) uncertainties, which are determined with the method presented in Sect. 5.1.1. The FFs are compared with NLO parametrizations from DSS, HKNS, and AKK. The NLO parametrizations are chosen because AKK does not provide any in LO. The favored and unfavored FFs are stable with respect to the choice of the PDF set and the favored FF is larger than the unfavored FF for all values of z as expected. However, with the currently available charged kaon data alone, it is not possible to constrain the strange FF. The integral and the shape of the strange FF differ significantly for the different PDF sets. This is emphasized by the large uncertainty bands corresponding to the systematic uncertainties of the PDF which basically allows any value from zero up to above the result of the DSS fit.

Using the equality of kaon FFs from Eq. (5.15), the extracted kaon FFs can be used to estimate the K_S^0 multiplicities. To make the FFs available at the kinematics of the measured K_S^0 multiplicities, the FFs are calculated and stored in a grid of different z and Q^2 values. The z and Q^2 values are stored with step sizes of 0.1 and $1 (\text{GeV}/c)^2$, respectively. To get the FF value at the exact z, Q^2 position, the FFs are interpolated between the neighboring z and Q^2 values. The PDFs are taken from LHAPDF as usual.

Fig. 5.10 presents the estimated and measured K_S^0 multiplicities for fits based on PDF sets of MMHT14 and NNPDF3.0. They show an agreement for bins of z covered by data points of K^\pm multiplicities. The extrapolation to z ranges not covered by the K^\pm multiplicities is not compatible with the K_S^0 multiplicities.

The reason for this discrepancy becomes clear by studying the individual contributions of the quarks to the multiplicities, as shown in Figs. 5.11 and 5.12 for

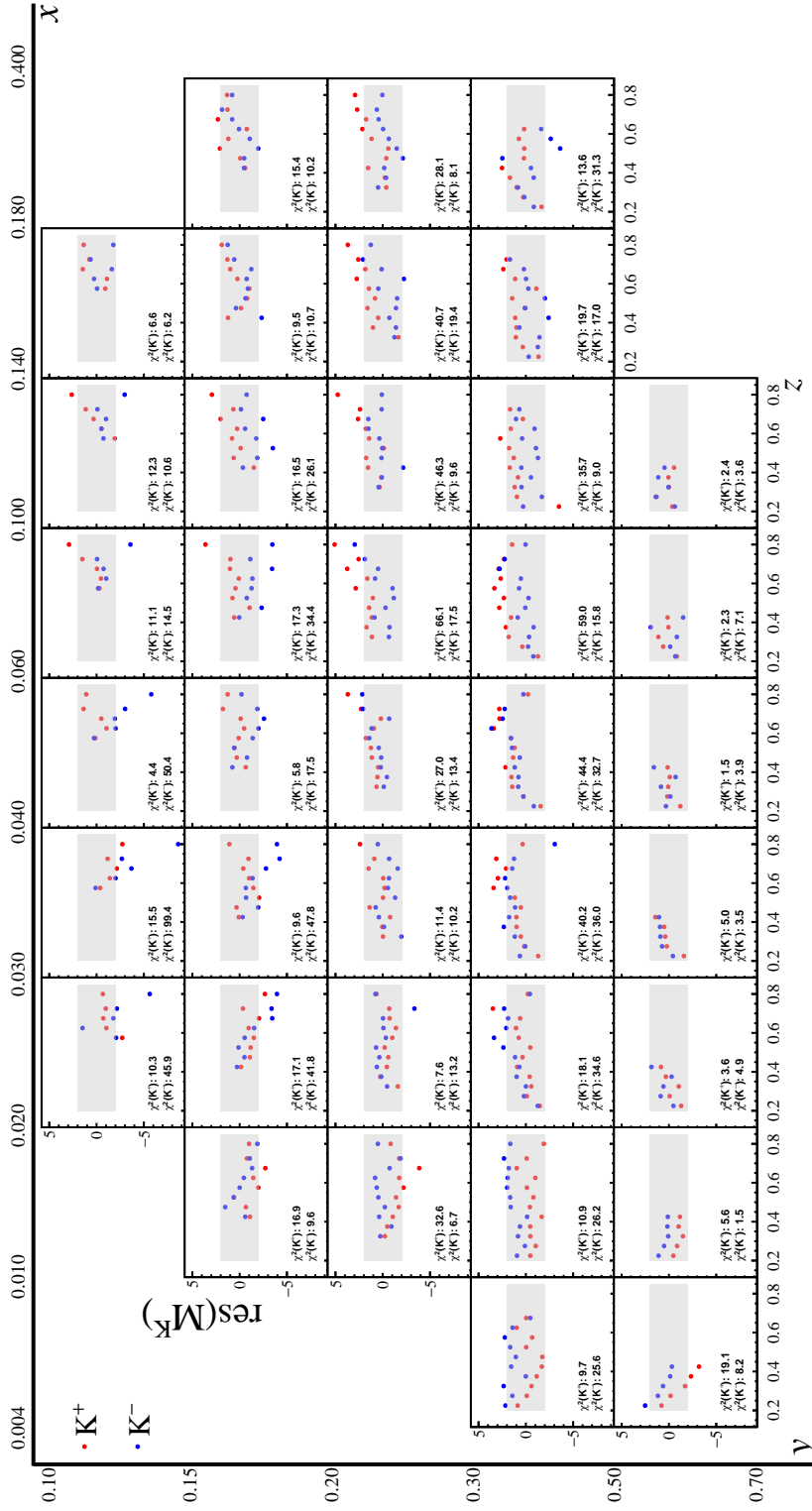


Figure 5.7.: The difference between fitted and measured multiplicities weighted by $1/\sigma_{stat}$ for bins of x , y , and z . The fitted multiplicities are calculated with the PDF parametrization from MMHT14. In the lower left corner of each bin the bin's contribution to the positive and negative χ^2/n_d values is shown. The gray area visualizes the region of data points which alone included yield a total $\chi^2/n_d \approx 1$.

5. Extraction of Fragmentation Functions

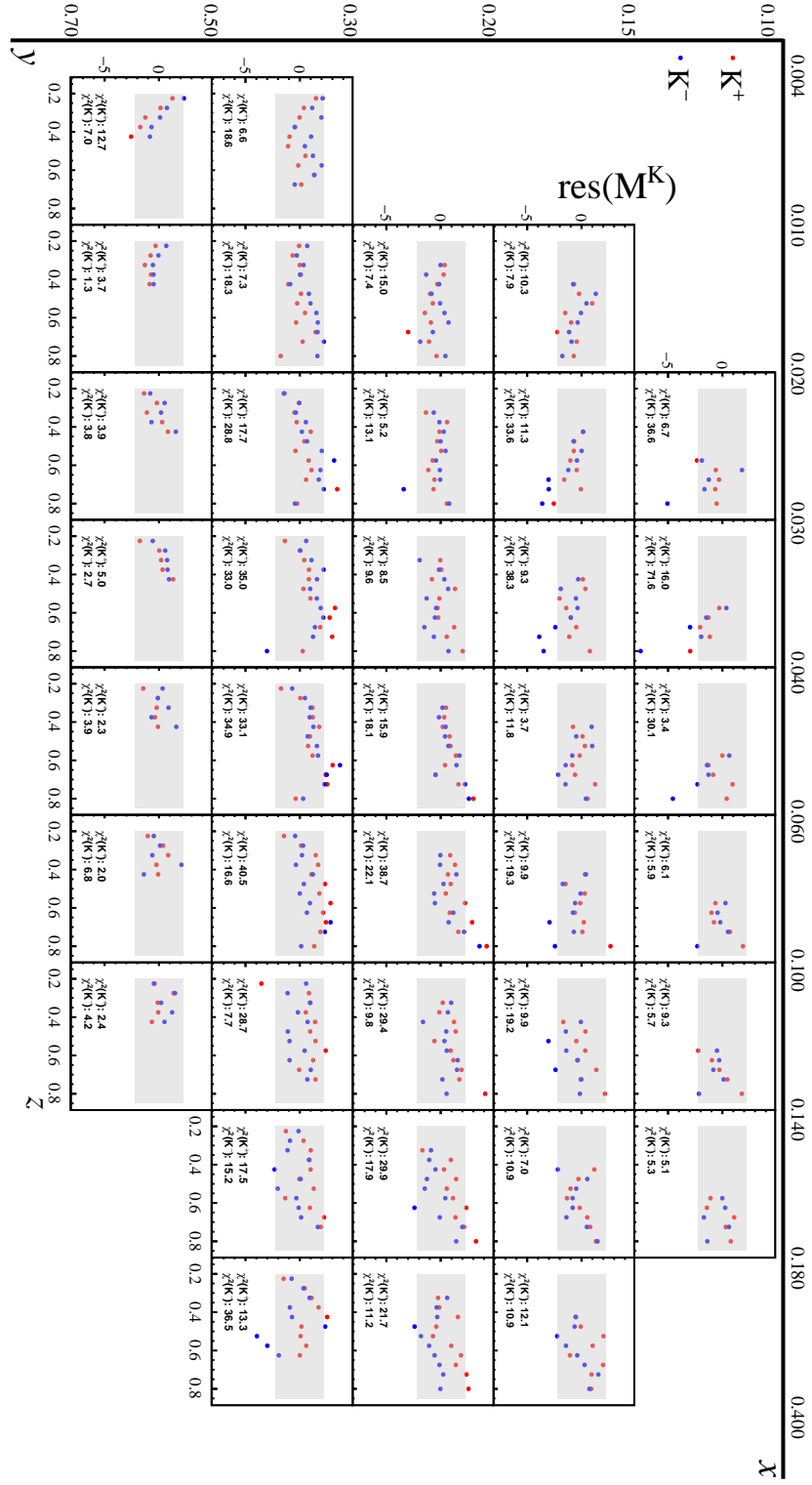


Figure 5.8.: Same as Fig. 5.7 but for the PDF parametrization from CT10.

5.3. Kaon Fragmentation Functions

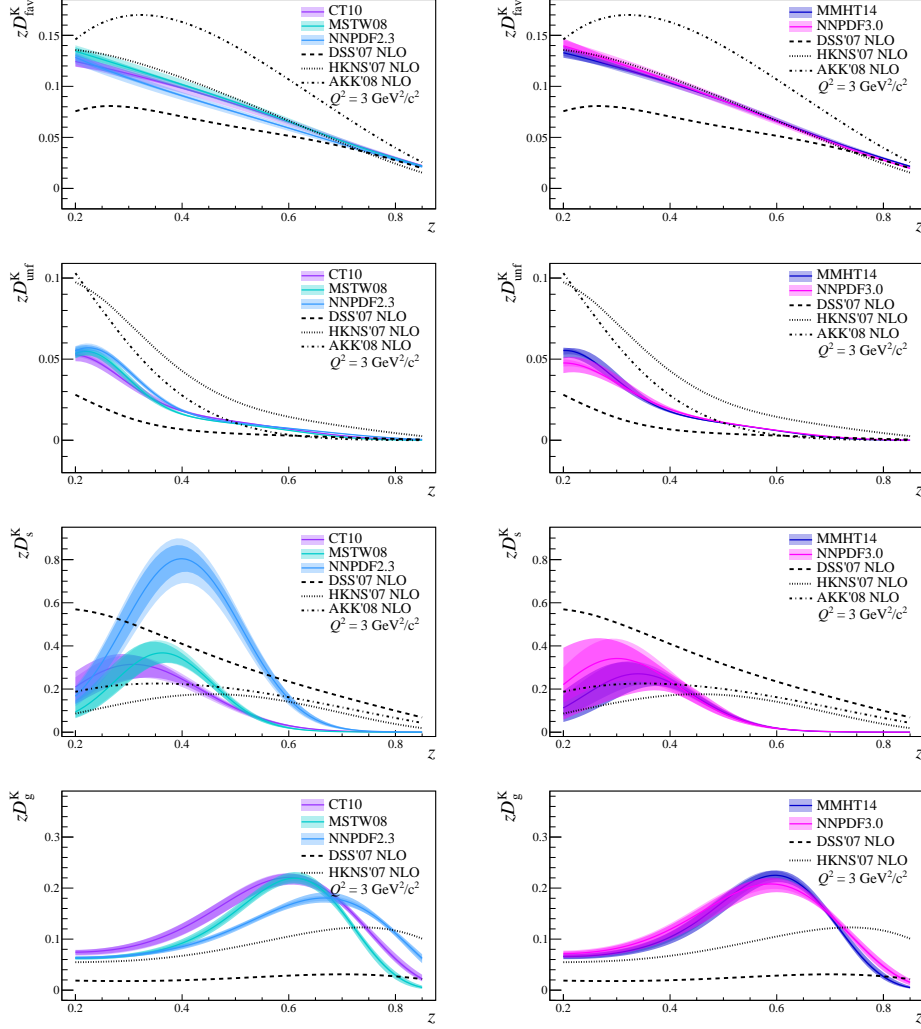


Figure 5.9.: The kaon FFs extracted from K^+ and K^- multiplicities, compared with parametrizations from DSS, HKNS, and AKK. The left column shows the FFs extracted with PDFs from MSTW08 and NNPDF2.3. The right column shows the FFs extracted with PDFs from CT10, MMHT14, and NNPDF3.0. The uncertainty bands correspond to statistical (dark) and systematic (light) uncertainties.

5. Extraction of Fragmentation Functions

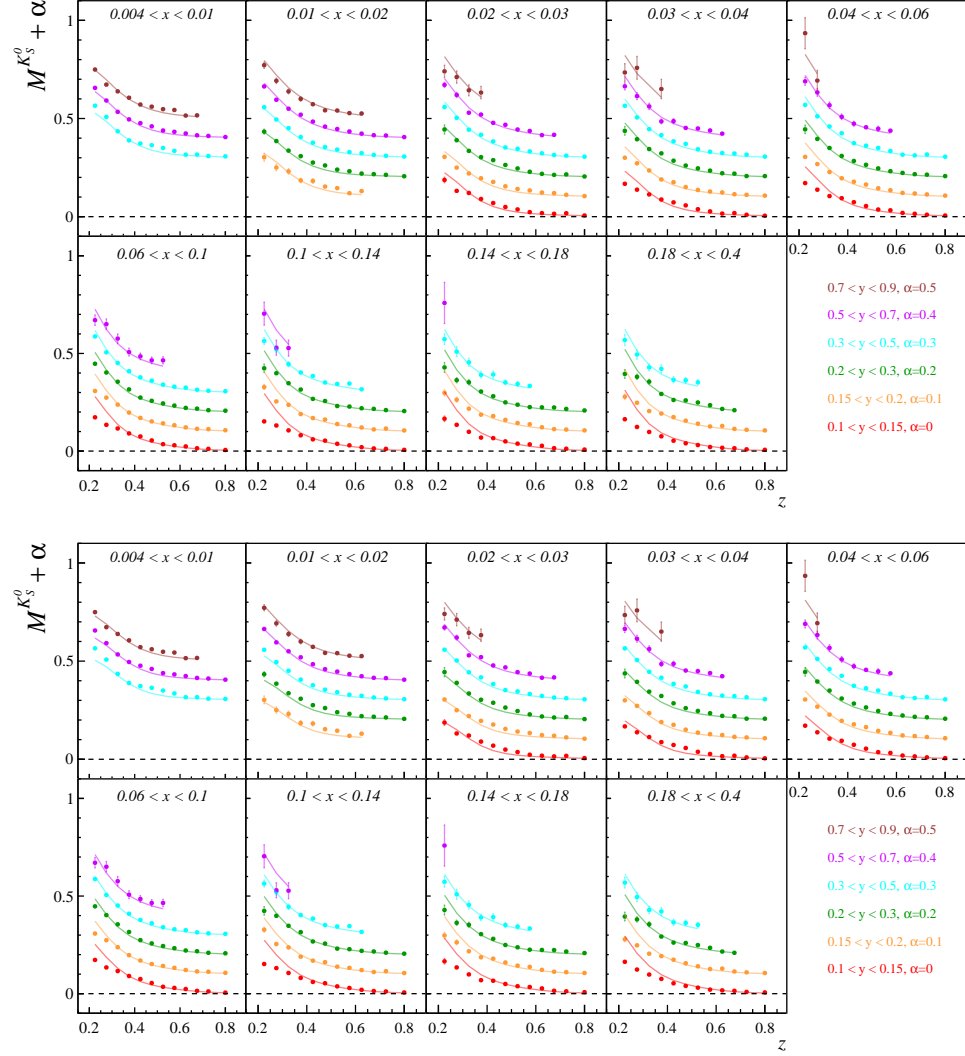


Figure 5.10.: The measured K_S^0 multiplicities (dots) plotted together with the estimations (lines) from kaon parametrization of FFs extracted from charged multiplicities only. The PDF sets that were used for the extraction are MMHT14 (top) and NNPDF3.0 (bottom).

5.3. Kaon Fragmentation Functions

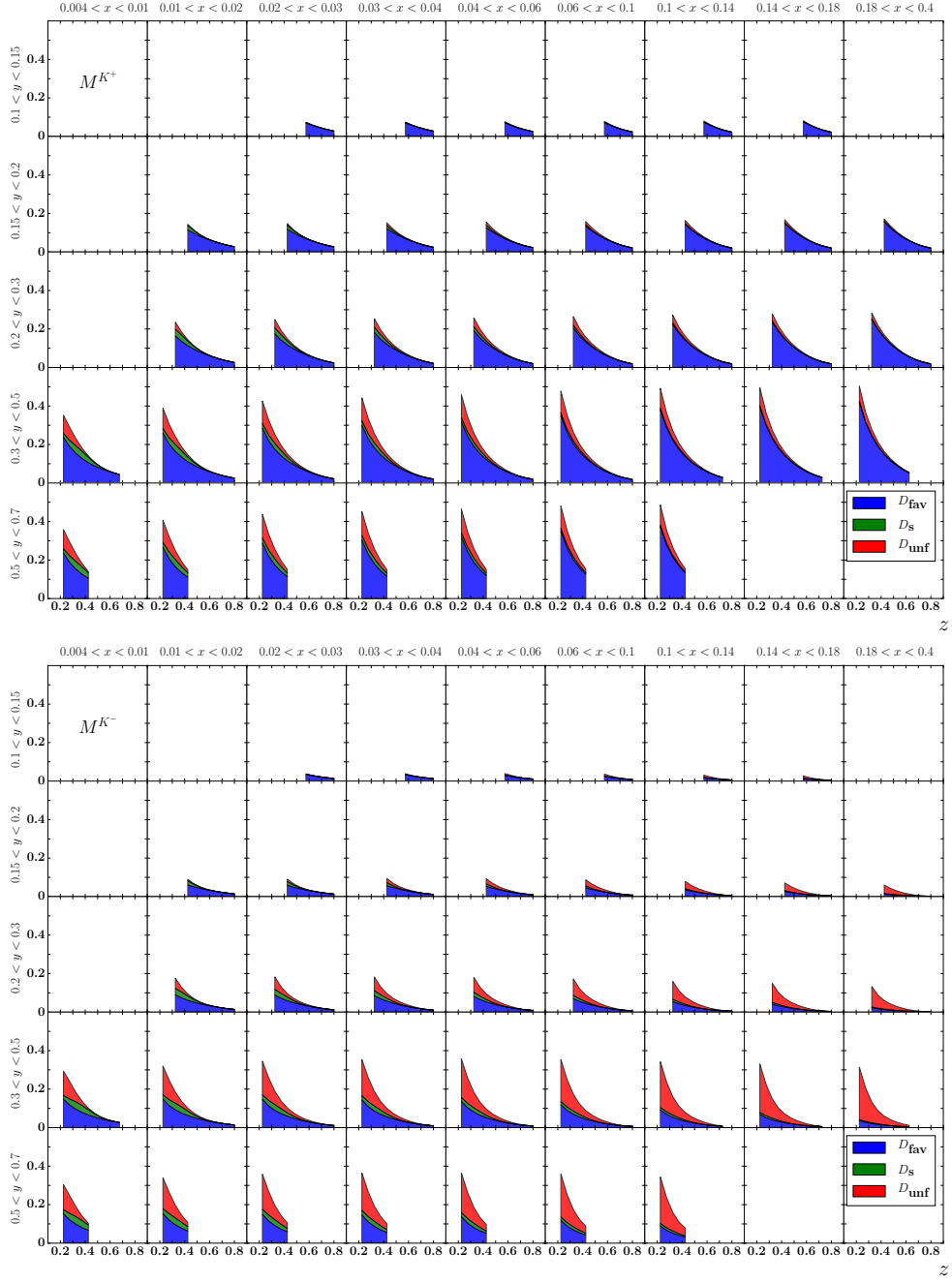


Figure 5.11.: Contribution of FFs to K^+ (top) and K^- (bottom) multiplicities resulting from a fit on only charged kaon multiplicities using the MMHT14 PDF set.

5. Extraction of Fragmentation Functions

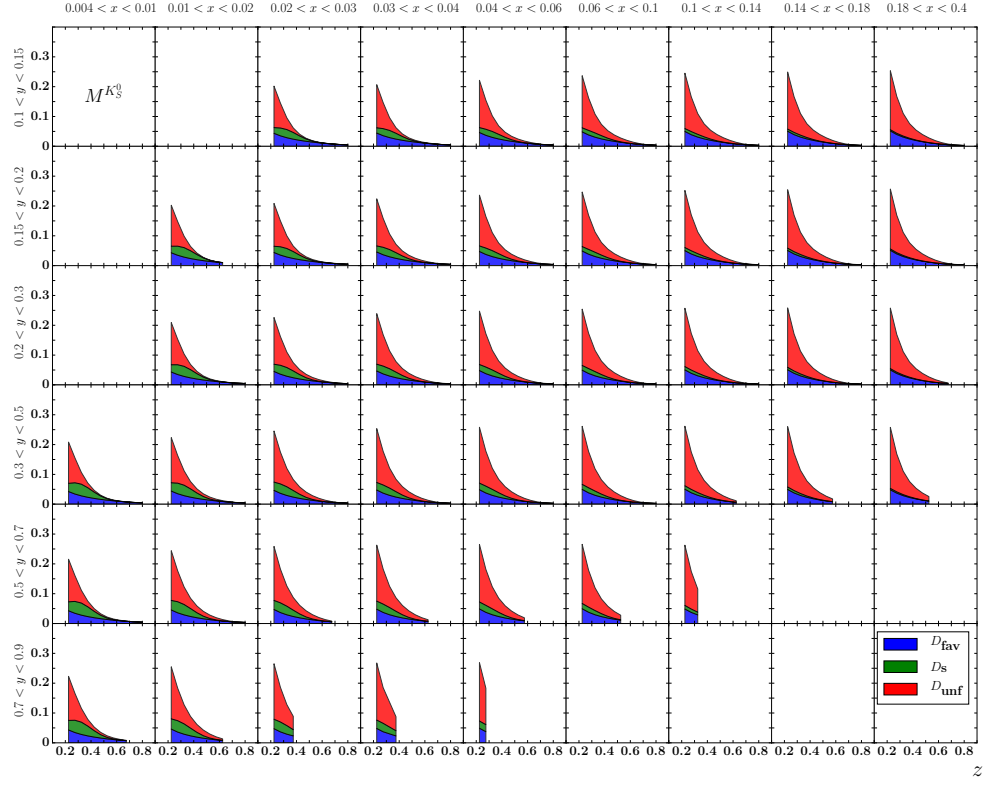


Figure 5.12.: Same as Fig. 5.11 but for K_S^0 multiplicities.

parametrizations extracted with PDF sets from MMHT14. The parametrization with the MMHT14 PDF set is representative for all PDF sets as they all have a small contribution from D_s^K and yield a similar result. The small contribution of the strange quark PDF with respect to those of the up and down quarks, combined with the unexpected small strange FF yields an almost negligible contribution of the strange quark to the K^+ and K^- multiplicities in the kinematic region covered by the COMPASS experiment. It is compensated by a larger contribution of the unfavored FF which can be seen by the rise of D_{unf}^K towards lower values of z . According to Eq. (5.18) the contribution of D_{unf}^K to the K_S^0 multiplicity is nine times larger than those of D_{fav}^K . Thus, the large unfavored FF at low z yields to the overestimated K_S^0 multiplicities.

To constrain the strange FF it is necessary to include additional data to the fit. In this case it suggests itself to use the newly determined K_S^0 multiplicities.

5.3.2. Kaon Fragmentation Functions from K^\pm and K_S^0 Multiplicities

This section presents the resulting FFs from simultaneous fits of K^+ , K^- , and K_S^0 multiplicities. Again the fit is performed for the different PDF sets using the same start parameters as in the previous chapter. The resulting χ^2/n_d values and fit parameters are summarized in Tab. 5.4. The comparison of fitted and measured multiplicities is presented in Figs. 5.13 and 5.14 for the fit with the MMHT14 PDF set which is representative for all PDF sets. The fit is able to describe the measured data for most bins, with χ^2/n_d values ranging from 2.23–3.18, depending on the PDF set.

At low y and low z deviations larger than 1σ between the measured multiplicities and the estimations from the fit are clearly visible. The deviations increase for bins towards higher x values. If similar deviations exist for K^\pm multiplicities they cannot be seen because of the limited z coverage of K^\pm multiplicities.

The residuals for the parametrization with PDFs from MMHT14 are shown in Fig. 5.15. Those of K^+ and K^- show a similar behavior as in the previous section. Again the largest contribution is from K^- at bins of low y and low x . The residuals of the K_S^0 are in general small. Exceptions are of course in bins of high x and small y which show visible deviations between the measured and estimated K_S^0 multiplicities.

The extracted FFs are shown in Fig. 5.16. The most striking difference to the previous fit without the K_S^0 multiplicities can be found at the strange and unfavored FFs. The strange FF does not drop at low z and for all fits, regardless of the choice of the PDF set, its integral is about two times larger than before. Consequently, the unfavored FF rises less strongly towards low z .

The effect of this change can be seen best in Figs. 5.17 and 5.18 where the

5. Extraction of Fragmentation Functions

PDF	χ^2/n_d	FF	N	α	β
MSTW08	2.77	fav	0.04747 ± 0.0005	0.19 ± 0.06	0.83 ± 0.05
		s	0.289 ± 0.009	2.0 ± 0.2	6.0 ± 0.4
		unf	0.001035 ± 0.0003	9.0 ± 2.0	10.0 ± 3.0
		g	0.0854 ± 0.002	10.0 ± 1.0	4.0 ± 0.6
MMHT14	2.75	fav	0.04786 ± 0.0005	0.17 ± 0.06	0.82 ± 0.05
		s	0.2 ± 0.006	1.0 ± 0.2	5.0 ± 0.4
		unf	0.001152 ± 0.0003	9.0 ± 2.0	20.0 ± 4.0
		g	0.0996 ± 0.002	8.0 ± 1.0	3.0 ± 0.6
NNPDF2.3	2.27	fav	0.04644 ± 0.0004	0.099 ± 0.06	0.84 ± 0.05
		s	0.49 ± 0.02	0.9 ± 0.2	4.0 ± 0.4
		unf	0.003492 ± 0.0002	4.0 ± 0.6	9.0 ± 0.8
		g	0.0612 ± 0.002	10.0 ± 2.0	3.0 ± 0.5
NNPDF3.0	3.18	fav	0.05218 ± 0.0004	0.079 ± 0.06	0.93 ± 0.05
		s	0.174 ± 0.008	0.05 ± 0.3	4.0 ± 0.7
		unf	0.005196 ± 0.0002	4.0 ± 0.4	9.0 ± 0.6
		g	0.073 ± 0.002	7.0 ± 1.0	2.0 ± 0.5
CT10	2.23	fav	0.04678 ± 0.0005	0.12 ± 0.06	0.75 ± 0.05
		s	0.172 ± 0.004	1.0 ± 0.2	5.0 ± 0.3
		unf	0.0004635 ± 0.0002	10.0 ± 7.0	24.0 ± 10.0
		g	0.105 ± 0.002	8.0 ± 1.0	3.0 ± 0.4

Table 5.4.: Parameters and χ^2 values of fits of charged and neutral kaon multiplicities with different PDF sets.

5.3. Kaon Fragmentation Functions

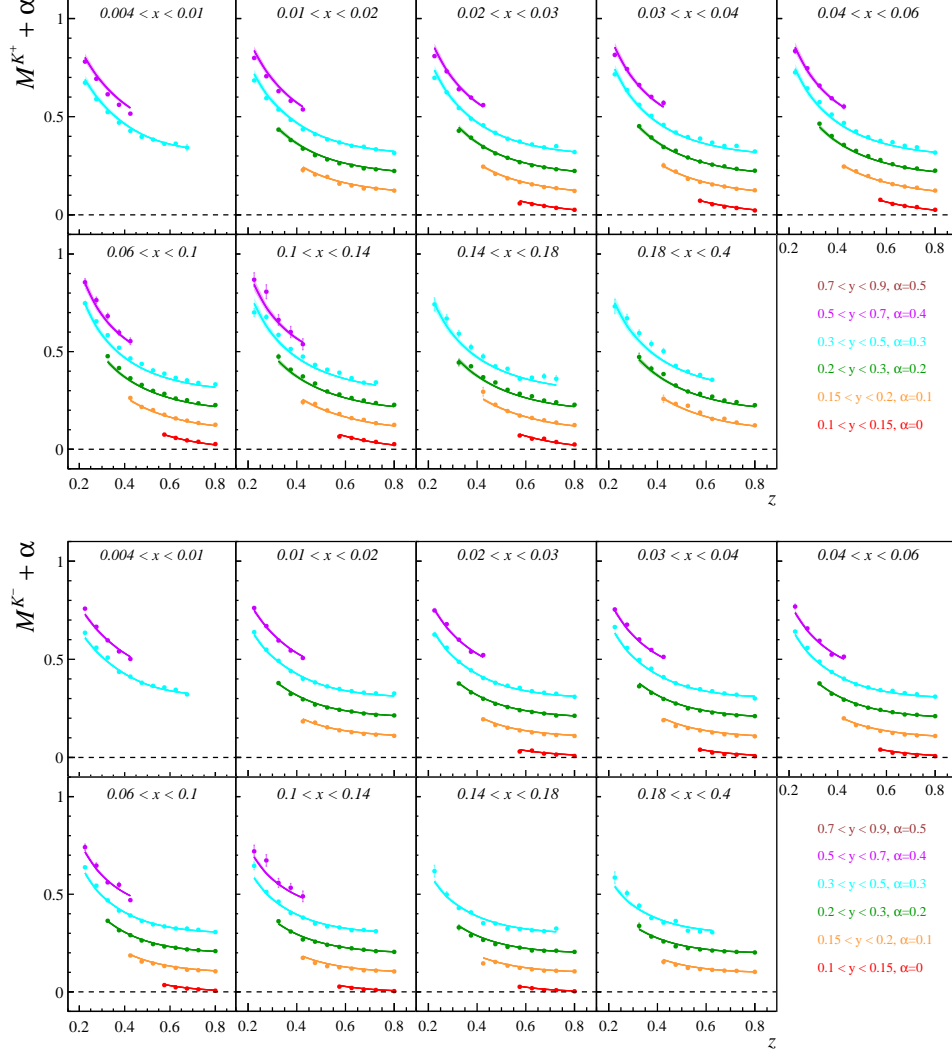


Figure 5.13.: Fit of K^+ and K^- multiplicities from COMPASS 2006 data. The points are the measured multiplicities with their statistical uncertainties. The curves correspond to the fitted multiplicities. The MMHT14 PDF set was used for the extraction of the FFs.

5. Extraction of Fragmentation Functions

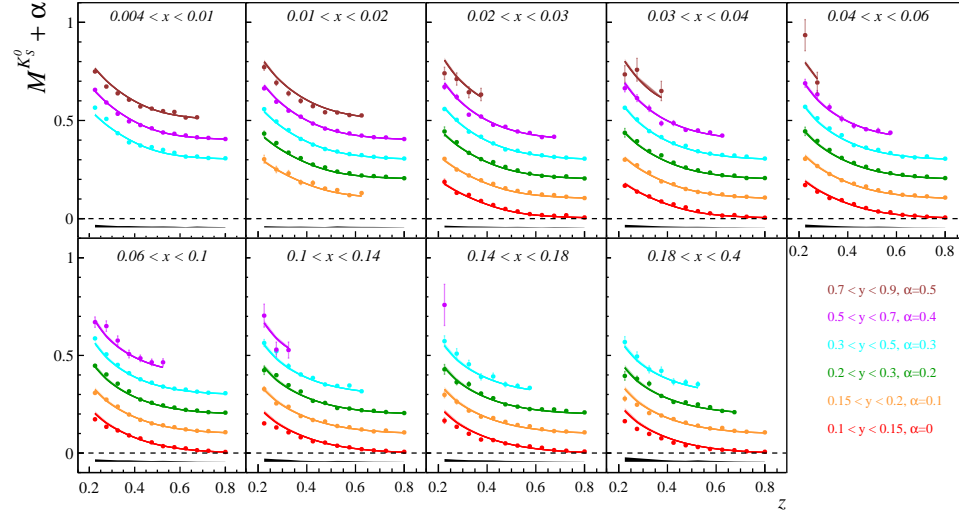


Figure 5.14.: Same as Fig. 5.13 but showing K_S^0 multiplicities.

individual contributions of the quarks to the multiplicities are shown. In contrast to the case where the FFs were determined by fits of only K^+ and K^- multiplicities (Fig. 5.11), now the strange quark contributes significantly to all kaons.

One way to quantify the difference between fits with and without K_S^0 multiplicities is to integrate the resulting FFs over the analyzed z range (0.2–0.85):

$$N_q(Q^2) = \int_{0.2}^{0.85} D_q^K(z, Q^2) dz, \quad (5.22)$$

and additionally build the ratios

$$R_{q_1 q_2}(Q^2) = \frac{N_{q_1}(Q^2)}{N_{q_2}(Q^2)}, \quad (5.23)$$

where q , q_1 , and q_2 denote the selected quark flavors fav, s, and unf.

To calculate the uncertainties of the ratio

$$\sigma_R = \frac{N_{q_1}}{N_{q_2}} \left[\left(\frac{\sigma_{q_1}}{N_{q_1}} \right)^2 + \left(\frac{\sigma_{q_2}}{N_{q_2}} \right)^2 - 2 \frac{\text{cov}(N_{q_1}, N_{q_2})}{N_{q_1} \cdot N_{q_2}} \right]^{\frac{1}{2}}, \quad (5.24)$$

the covariance between N_{q_1} and N_{q_2} is needed.

The covariance between N_{q_1} and N_{q_2} can be visualized best by plotting the correlation

$$\text{corr} = \frac{\text{cov}(N_{q_1}, N_{q_2})}{\sigma_{q_1} \cdot \sigma_{q_2}}. \quad (5.25)$$

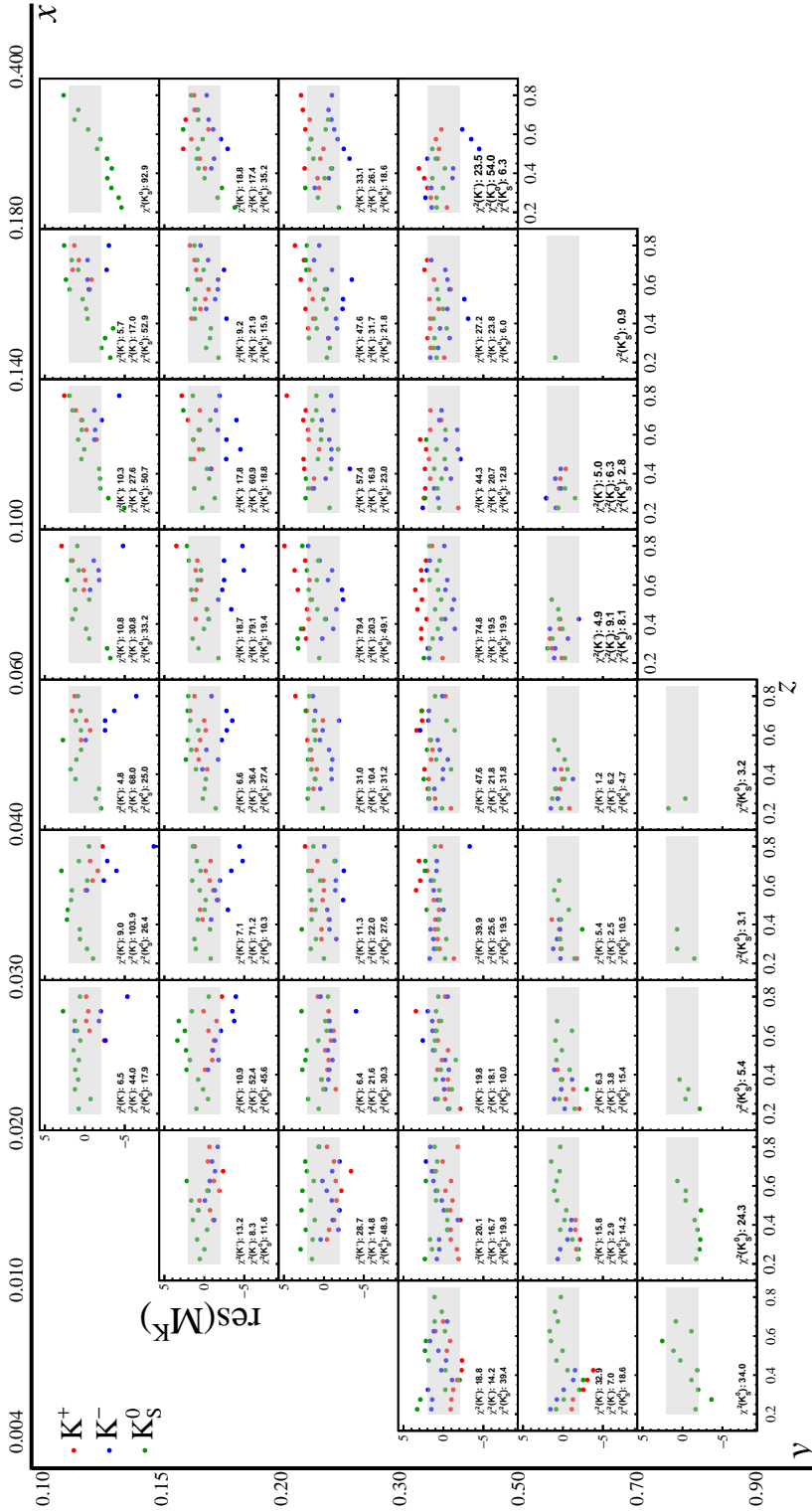


Figure 5.15.: The difference between fitted and measured multiplicities weighted by $1/\sigma_{stat}$ for bins of x , y , and z . The fitted multiplicities are calculated with MMHT14 and the extracted FFs from K^+ , K^- , and K_S^0 multiplicities. The dashed line shows the mean value of the x - y bin. The gray area visualizes the region which the difference of the values should not exceed to achieve a total $\chi^2/n_d < 2$.

5. Extraction of Fragmentation Functions

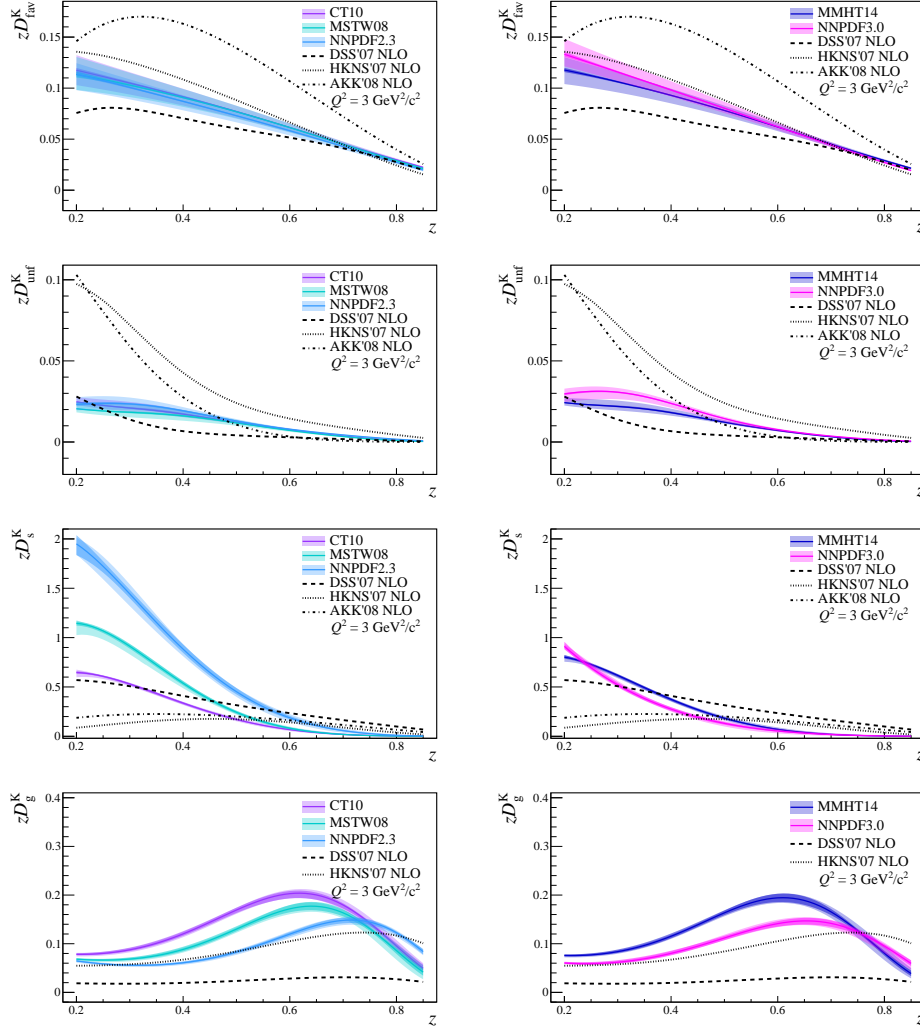


Figure 5.16.: The kaon FFs extracted from combined K^+ , K^- , and K_S^0 multiplicities, compared with parametrizations from DSS, HKNS, and AKK. The left column shows the FFs extracted with PDFs from MSTW08 and NNPDF2.3. The right column shows the FFs extracted with PDFs from CT10, MMHT14, and NNPDF3.0. The uncertainty bands correspond to statistical (dark) and systematic (light) uncertainties.

5.3. Kaon Fragmentation Functions

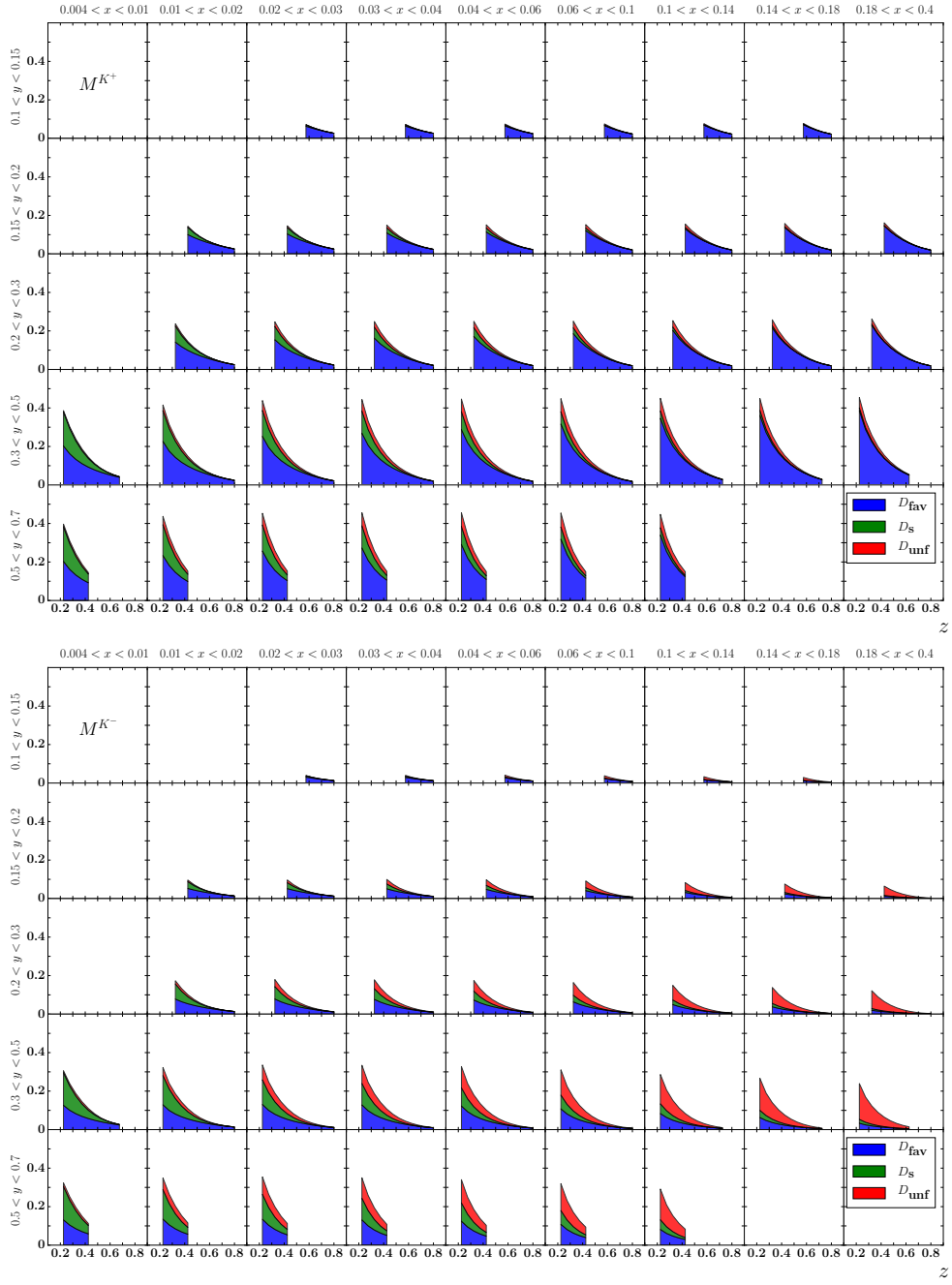


Figure 5.17.: Contribution of FFs to K^+ (top) and K^- (bottom) multiplicities resulting from a fit on K^+ , K^- , and K_S^0 multiplicities using the MMHT14 PDF set.

5. Extraction of Fragmentation Functions

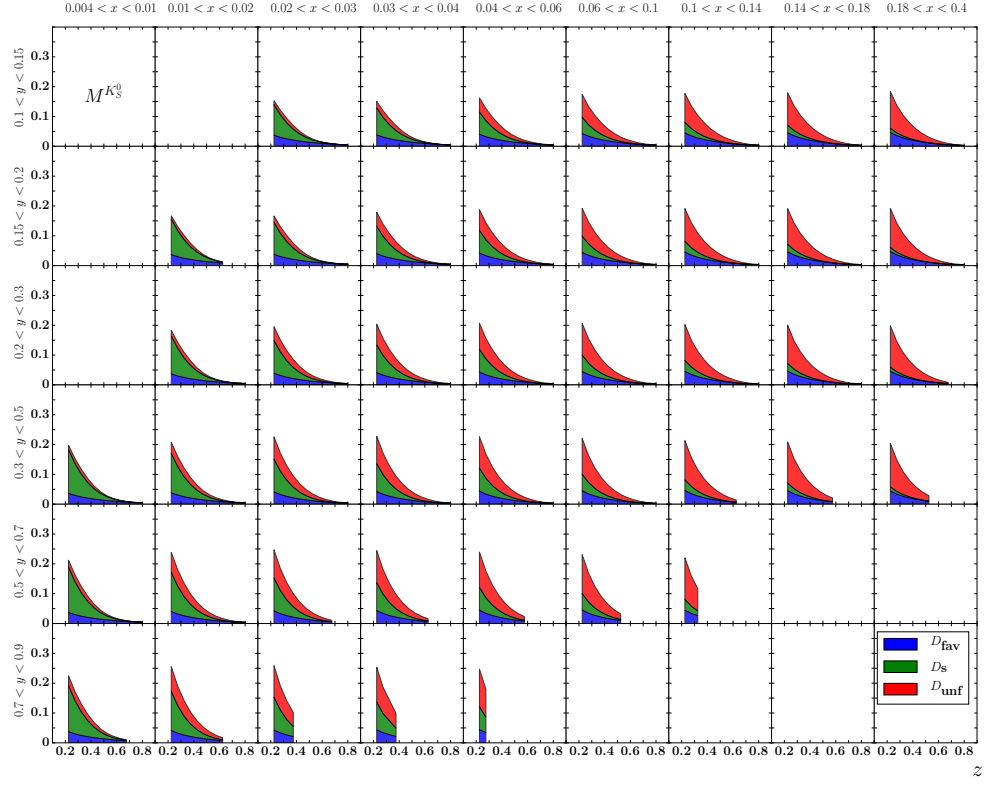


Figure 5.18.: Same as Fig. 5.17 but showing K_S^0 multiplicities.

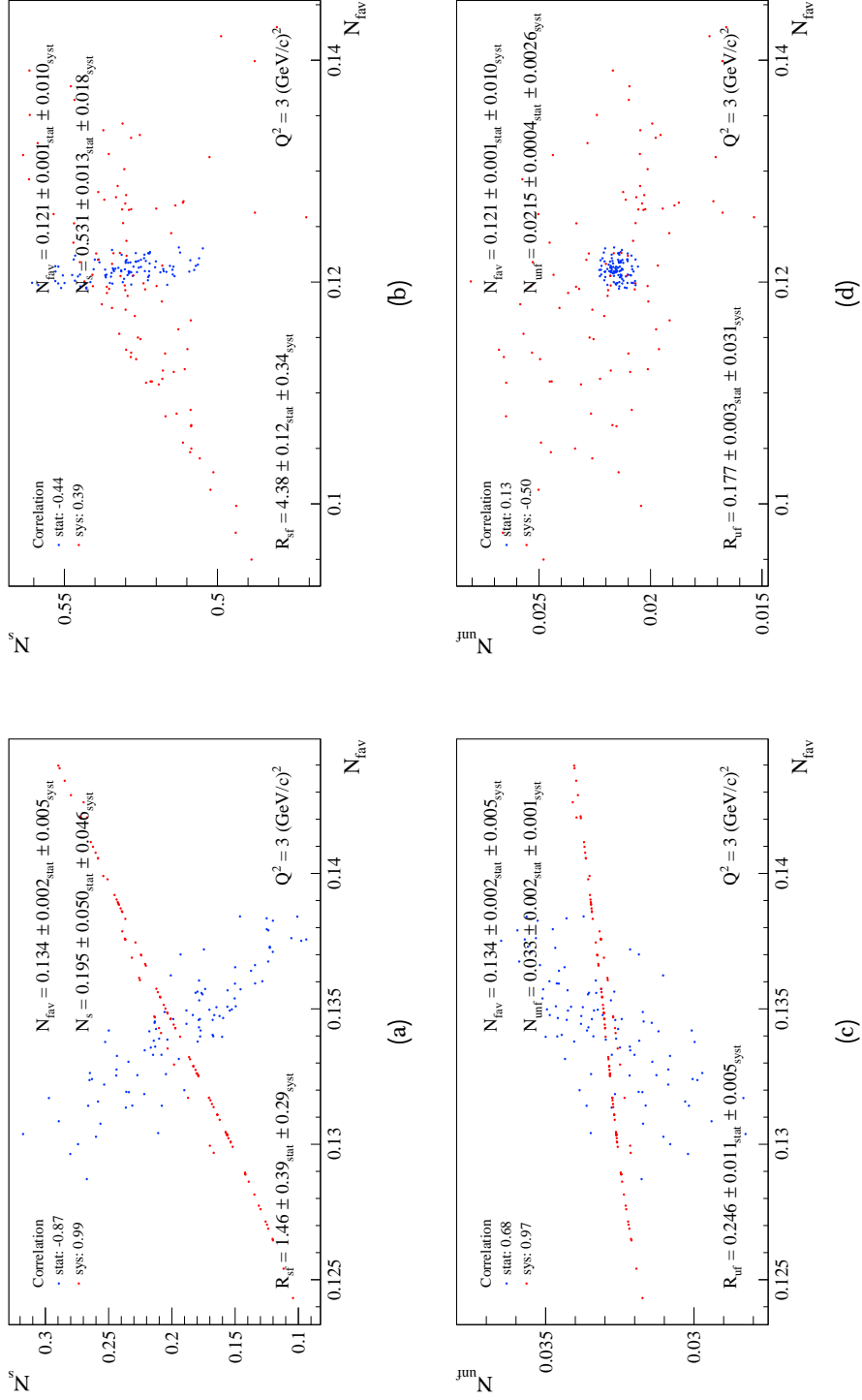


Figure 5.19.: Integrated FFs for each resample of the statistical (blue) and systematical (red) uncertainty estimation of the fits for K^+ and K^- excluding K_S^0 (left) and including K_S^0 (right). Both fits are performed with the MMHT14 PDF set.

5. Extraction of Fragmentation Functions

Therefore, N_{q_1} is plotted versus N_{q_2} for each resample of the statistical and systematic uncertainty estimation for $Q^2 = 3 \text{ (GeV/c)}^2$. Figure 5.19 shows plots for combinations of N_s and N_{fav} (top) as well as N_{unf} and N_{fav} (bottom) for fits with K^+ and K^- only (left) and K^+ , K^- , and K_S^0 (right) multiplicities. The most striking difference between the fits with and without K_S^0 multiplicities is the correlation of the systematic resamples. For the fit with the K^+ and K^- multiplicities only, it has a positive correlation of one. That is because the systematic uncertainties of K^+ and K^- are fully correlated, that is all multiplicities of a resample are shifted by the same relative amount.

However, no direct correlation between the charged kaons and the neutral kaon exists. The only correlation is due to the vector meson correction (Sect. 4.6.3) but it is negligibly small compared to the other uncertainties. The missing correlation between the charged and neutral kaons means in detail that two independent randomly distributed numbers are generated for each resample, one for the K^+ and K^- multiplicities and another one for the K_S^0 multiplicities. Thus, it comes by no surprise that a correlation of less than one is found for the fits with K^+ , K^- , and K_S^0 multiplicities.

Table 5.5 presents the z-integrated FFs for both fit types (fits with K^+ and K^- only and fits with K^+ , K^- , and K_S^0) for different PDF sets. The integrals of D_{fav} and D_{unf} itself agree within their uncertainties for fits with different PDF sets. However, they are significantly larger for fits with K^+ and K^- multiplicities only than for fits with the K_S^0 multiplicities included, especially N_{unf} is about 50% larger. The integral of the strange FF, on the other hand, is about two to three times larger for the simultaneous fit of K^+ , K^- , and K_S^0 multiplicities. This has a direct impact on the ratio R_{sf} which itself is about two to three times larger for the fit with the K_S^0 multiplicities included.

The statistical uncertainties are smaller for fits with the K_S^0 included, while the systematic uncertainties are larger. An exception is the integrated D_s where both the statistical and systematic uncertainties are smaller. This shows once again that the strange FF can be determined with higher accuracy with the additional K_S^0 multiplicity data. It can be expected that the systematic uncertainties will be reduced once the target cell discrepancy of the K_S^0 multiplicities is resolved.

5.3.3. Comparison with HERMES Multiplicities

From the principle of universality of FFs it follows that the FFs extracted from COMPASS data can be used to estimate the multiplicities in other kinematics, covered for example by other experiments. In this section the K^+ and K^- multiplicities are estimated for the most recent results from HERMES [44]. HERMES was a fixed target experiment at DESY with electron or positron beams at an energy of 27.6 GeV/c^2 on a hydrogen or deuterium target. The HERMES kinematics are close to those of COMPASS. Their four-momentum transfer is in the range of

5.3. Kaon Fragmentation Functions

PDF set	FF	$K^+ + K^-$	$K^+ + K^- + K_S^0$
MSTW08	fav	0.133 $\pm 0.002 \pm 0.006$	0.118 $\pm 0.001 \pm 0.012$
	s	0.240 $\pm 0.042 \pm 0.045$	0.764 $\pm 0.018 \pm 0.035$
	unf	0.033 $\pm 0.001 \pm 0.001$	0.0188 $\pm 0.0004 \pm 0.0035$
	N_s/N_{fav}	1.81 $\pm 0.34 \pm 0.26$	6.47 $\pm 0.20 \pm 0.64$
MMHT14	fav	0.134 $\pm 0.002 \pm 0.005$	0.121 $\pm 0.001 \pm 0.010$
	s	0.195 $\pm 0.050 \pm 0.046$	0.531 $\pm 0.013 \pm 0.018$
	unf	0.033 $\pm 0.001 \pm 0.001$	0.0215 $\pm 0.0004 \pm 0.0026$
	N_s/N_{fav}	1.46 $\pm 0.39 \pm 0.29$	4.38 $\pm 0.12 \pm 0.34$
NNPDF2.3	fav	0.122 $\pm 0.002 \pm 0.005$	0.115 $\pm 0.001 \pm 0.010$
	s	0.563 $\pm 0.055 \pm 0.094$	1.265 $\pm 0.036 \pm 0.068$
	unf	0.036 $\pm 0.001 \pm 0.002$	0.0228 $\pm 0.0005 \pm 0.0032$
	N_s/N_{fav}	4.63 $\pm 0.49 \pm 0.57$	11.03 $\pm 0.39 \pm 0.43$
NNPDF3.0	fav	0.137 $\pm 0.002 \pm 0.006$	0.129 $\pm 0.001 \pm 0.010$
	s	0.253 $\pm 0.083 \pm 0.070$	0.471 $\pm 0.018 \pm 0.021$
	unf	0.031 $\pm 0.003 \pm 0.001$	0.0280 $\pm 0.0004 \pm 0.0032$
	N_s/N_{fav}	1.85 $\pm 0.63 \pm 0.43$	3.65 $\pm 0.15 \pm 0.16$
CT10	fav	0.128 $\pm 0.002 \pm 0.006$	0.120 $\pm 0.001 \pm 0.011$
	s	0.246 $\pm 0.035 \pm 0.046$	0.456 $\pm 0.010 \pm 0.019$
	unf	0.032 $\pm 0.002 \pm 0.001$	0.0211 $\pm 0.0004 \pm 0.0025$
	N_s/N_{fav}	1.92 $\pm 0.30 \pm 0.27$	3.80 $\pm 0.10 \pm 0.42$

Table 5.5.: Results for $N_q = \int_{0.2}^{0.85} D_q(z, Q^2 = 3 \text{ (GeV/c)}^2) dz$, with $q = \text{fav, s, unf}$, and the ratio $R_{sf} = N_s/N_{\text{fav}}$ for fits with K^+ and K^- only and K^+ , K^- , and K_S^0 multiplicities performed for different PDF sets.

5. Extraction of Fragmentation Functions

$1 (\text{GeV}/c)^2 < Q^2 < 15 (\text{GeV}/c)^2$ with an average $\langle Q^2 \rangle = 2.5 (\text{GeV}/c)^2$ and $W^2 \approx 10^2 (\text{GeV}/c^2)^2$. Apart from x which has a slightly smaller range $0.023 < x < 0.6$, the other kinematic variables $0.1 < y < 0.85$ and $0.2 < z < 0.8$ are similar to those of COMPASS. HERMES used a RICH detector for the identification of charged hadrons, too. Its momentum acceptance ($2 \text{ GeV}/c < p_h < 15 \text{ GeV}/c$) is almost completely below the one of COMPASS ($12 \text{ GeV}/c < p_h < 43 \text{ GeV}/c$).

The HERMES collaboration presents their released multiplicities as a function of the kinematic quantities x , Q^2 , z , and p_t in four different binnings. Each binning has a different focus on the kinematic quantities. The first one has a fine grain in p_t . For the comparison it is excluded naturally since the COMPASS multiplicities used in this analysis are integrated over p_t . The second binning with focus on z has only two x bins and is therefore insufficient for a comparison with COMPASS data. The third binning is in z - Q^2 . Each bin covers a large range in x but gives only an average x value. Since the multiplicities have a strong x dependence, using this binning would result in falsely estimated multiplicities. Thus, the best binning to compare COMPASS and HERMES data is the z - x binning from HERMES integrated over p_t . After the integration, the binning has nine bins in x and six bins in z , within the limits:

$$\begin{aligned} x & \{0.023, 0.040, 0.055, 0.075, 0.100, 0.140, 0.200, 0.300, 0.400, 0.600\} \\ z & \{0.10, 0.20, 0.30, 0.40, 0.60, 0.80, 1.10\} \end{aligned}$$

The first and last bins in z should not be used. The last bin $z > 0.8$ is excluded because of large contributions from exclusive vector meson production. The lowest bin with $z < 0.2$ is excluded due to increased contribution from target fragmentation.

Since this binning is only two dimensional, the only way to directly compare COMPASS with HERMES is to use y -averaged COMPASS multiplicities. The y averaged multiplicities are computed as follows:

$$M(x, z) = \frac{\sum_y M(x, y, z) / \sigma^2(x, y, z)}{\sum_y 1 / \sigma^2(x, y, z)}. \quad (5.26)$$

The COMPASS and HERMES multiplicities have different kinematics. Table 5.6 compares the Q^2 values for similar x values of the HERMES and the y -averaged COMPASS multiplicities. While the Q^2 values of COMPASS are almost constant for all z bins of a given y bin, the Q^2 values of the y -averaged multiplicities differ for different z . One reason is that the y -averaged multiplicities are the weighted mean of all y bins. The y bins have different weights and not all of them cover the full z range. The HERMES multiplicities are presented with an average Q^2 value, constant for all z bins of a given x bin.

COMPASS			HERMES	
\bar{x}	Q_{\min}^2	Q_{\max}^2	\bar{x}	$\overline{Q^2}$
0.0072	1.02	1.27	–	–
0.015	1.19	2.13	–	–
0.025	1.45	3.65	–	–
0.035	1.74	5.13	0.033	1.19
0.049	2.58	7.06	0.047	1.38
–	–	–	0.065	1.56
0.076	4.05	10.88	–	–
–	–	–	0.087	1.73
0.12	6.13	16.44	0.12	2.17
0.16	8.11	20.41	0.165	3.17
0.25	15.06	32.25	0.24	4.88
–	–	–	0.34	7.48
–	–	–	0.45	10.24

Table 5.6.: Overview of the COMPASS and HERMES Q^2 values for similar \bar{x} . For COMPASS the range from Q_{\min}^2 – Q_{\max}^2 is given. For HERMES the mean value of Q^2 the corresponding x bin is shown.

The Figs. 5.20 and 5.21 show the K^+ and K^- multiplicities measured by HERMES in the z - x binning (blue points). They are compared with the multiplicities estimated from the extracted COMPASS FFs with the MMHT14 PDF set (green points). In addition the ratio of HERMES over COMPASS multiplicities (red points) is shown. The estimations and the multiplicities measured by HERMES agree within 25% although the difference between estimated and measured multiplicities shows a systematic trend. From low to high z the ratio increases for K^+ while it decreases for K^- . There is also a systematic deviation visible for x bins. Towards higher x the ratio becomes lower. This could point again to a not yet understood y - or Q^2 -dependence of the multiplicities since for the same value of x COMPASS and HERMES have different values of Q^2 .

To have a compact view on the data, the sum and the ratio of the y -averaged and z -integrated K^+ and K^- multiplicities ($\int \langle M^{K^\pm}(x, y, z) \rangle_y dz$) are plotted in Fig. 5.22 for COMPASS (red points) and HERMES (blue points). The z range covered by COMPASS and HERMES is 0.2–0.85 and 0.2–0.8, respectively. The difference in the z range, $\Delta z = 0.05$, is negligible because at large z the multiplicity is small and only contributes little to the integral.

The sum and ratio of the experimental data are compared with estimations (solid line with uncertainty band) calculated from the extracted COMPASS FFs with the MMHT14 PDF set. The estimations in the top row plots are calculated

5. Extraction of Fragmentation Functions

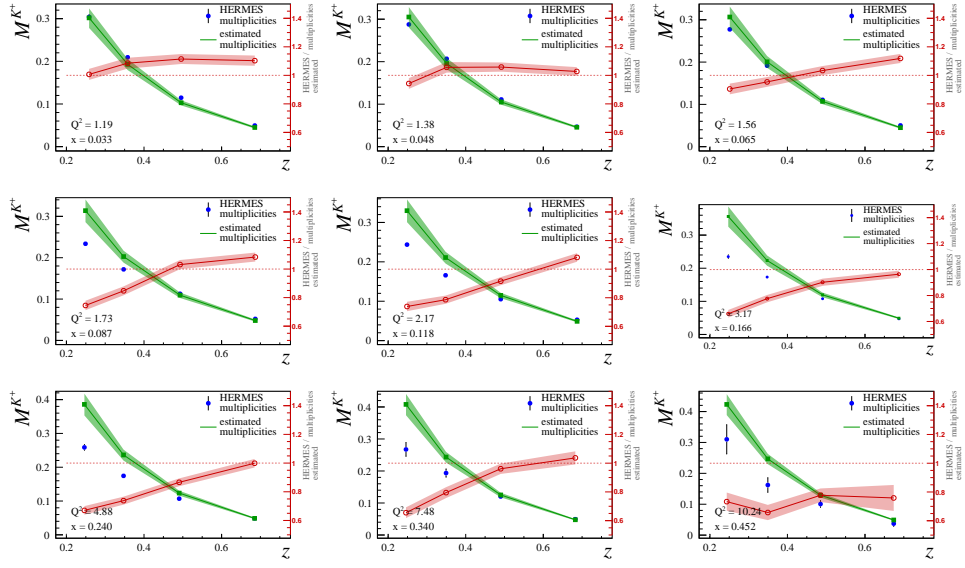


Figure 5.20.: The K^+ multiplicities measured at the HERMES (blue points) compared with multiplicities estimated from the extracted FFs of the fit of K^+ , K^- , and K_S^0 multiplicities from COMPASS (green points). In addition the ratio of HERMES over COMPASS multiplicities (red points) is shown. The PDF set used for the FF extraction and the estimation is MSTW14.

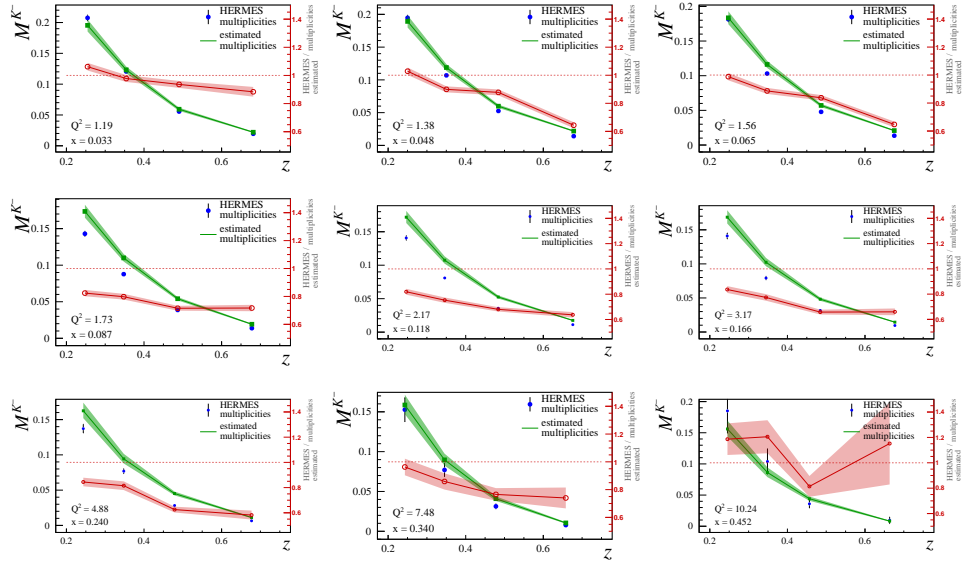


Figure 5.21.: Same as Fig. 5.20 but for K^- .

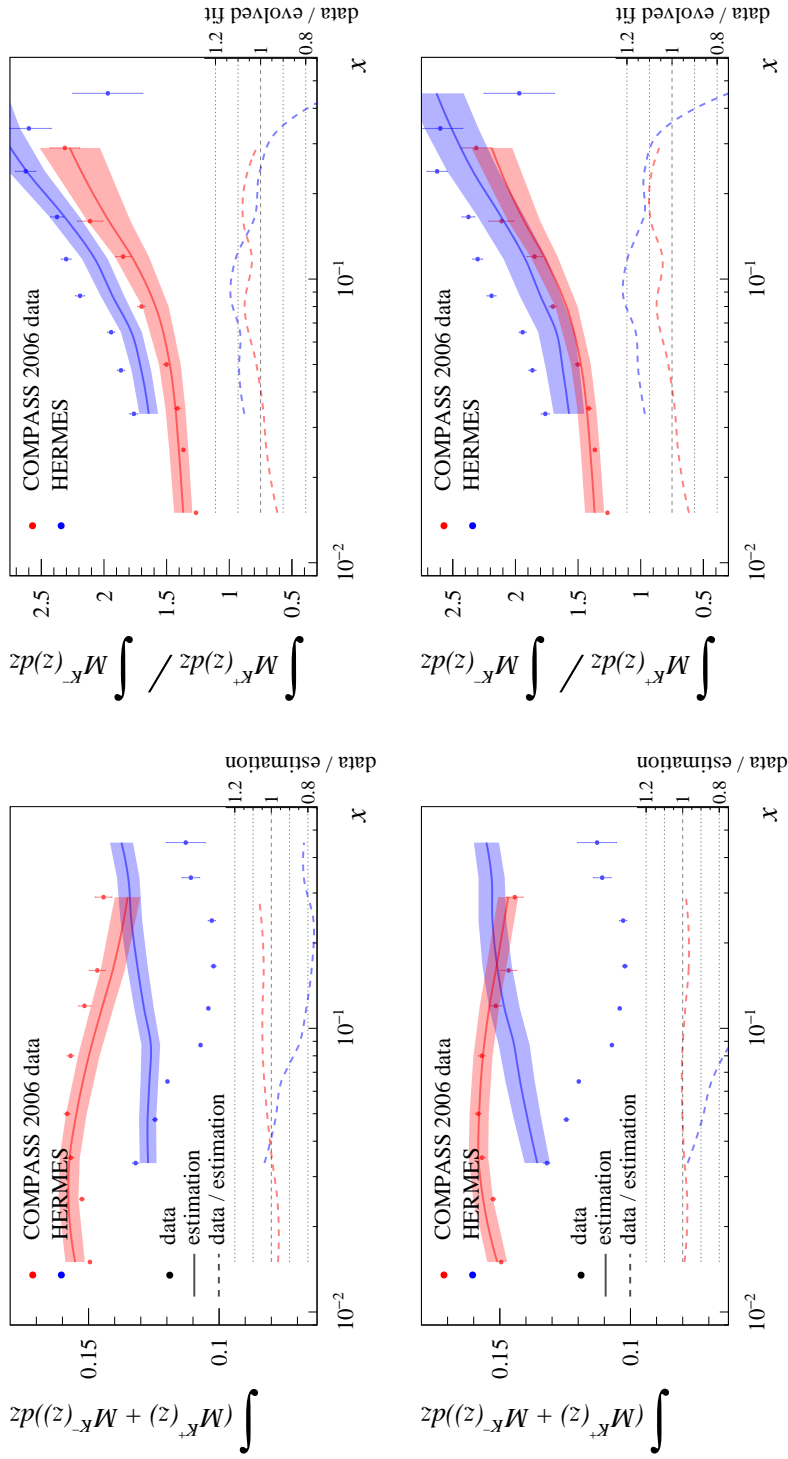


Figure 5.22.: Comparison between kaon multiplicities measured at COMPASS and HERMES. The plots on the left show the sum, the plots on the right show the ratio of the z -integrated K^+ and K^- multiplicities. In addition to the measured multiplicities, estimations from extracted COMPASS FFs are shown. The estimations in the top row are calculated with FFs extracted from K^+ , K^- , and K_S^0 multiplicities, while the bottom row is for FFs extracted from K^+ and K^- only. Both FFs are determined with the MMHT14 PDF set.

5. Extraction of Fragmentation Functions

from FFs extracted from K^+ , K^- , and K_S^0 multiplicities, while the estimations in the bottom row plots are from FFs extracted from K^+ and K^- multiplicities only. In addition, each plot shows the ratio of the measured and the estimated data (dashed line).

The sum of the COMPASS multiplicities shows no strong x dependence and the difference between the measured data and the estimations with FFs extracted from K^+ , K^- , and K_S^0 multiplicities is less than 10% and less than 5% for the ones with K^+ and K^- multiplicities only. The difference is smaller for the latter because the fit on K^+ and K^- multiplicities only is not influenced by the K_S^0 multiplicities. In contrast, the sum of the multiplicities from HERMES shows a strong x dependence and neither its shape nor its magnitude can be described by the estimations. The estimations, especially those from K^+ , K^- , and K_S^0 multiplicities, show a kink at around $x = 0.09$ that correlates with a jump in the HERMES data.

The ratios of K^+ and K^- have a similar shape for COMPASS and HERMES data but the HERMES ratios lie systematically above those of COMPASS. Note that for the case of pions the ratio results of COMPASS and HERMES are in good agreement [67]. The estimated kaon ratio of HERMES is also shifted but by a lesser amount than the one of the data. That means the difference between the ratio results of COMPASS and HERMES can be partially explained by the Q^2 evolution, as COMPASS and HERMES have different values of Q^2 for the same value of x . For COMPASS the difference between the measured and estimated ratio is below 10% regardless of the fit.

For HERMES the difference for the estimation from only K^+ and K^- multiplicities lies between 10 and 25% for the first x bins and beyond 25% for the largest x bin. The estimations with FFs extracted from K^+ , K^- , and K_S^0 multiplicities differ for less than 15% from the data for all except the highest x bins.

In general, the estimations for HERMES multiplicities are better with FFs extracted from K^+ , K^- , and K_S^0 multiplicities

The origin of the difference between COMPASS and HERMES data is unknown and currently suspect of investigation by several theorists [].

5.3.4. Summary

In this chapter the method to extract the FFs with a LO pQCD fit on hadron multiplicities is described. Its effectiveness is demonstrated by extracting the well known pion FFs from COMPASS pion multiplicities [67]. A good agreement between the COMPASS FFs and the predictions from DSEHS [66] and LSS [65] is achieved.

Next, the extraction of kaon FFs from COMPASS kaon multiplicities is tackled. Two sets of kaon multiplicities are available, the K^+ and K^- multiplicities [68, 70, 71], and the K_S^0 multiplicities of this analysis. The influence of different PDF sets on the extraction of FFs is studied. Therefore, the extraction of the FFs is performed

with different PDF sets, namely MSTW08, MMHT14, NNPDF2.3, NNPDF3.0, and CT10.

In a first attempt the FFs are extracted from K^+ and K^- multiplicities only. The favored and unfavored FFs are relatively stable with respect to the choice of the PDF set and they have moderate uncertainties. On the other hand, the shape and the integral of the strange FF depend on the choice of the PDF set which is underlined by its large uncertainties. The integral of the strange FF is surprisingly low, implying that only few K^+ and K^- would originate from strange quarks.

By exploiting the universality of the FFs, the K_S^0 multiplicities are estimated from the previously extracted kaon FFs and compared with the measured K_S^0 multiplicities. The K_S^0 multiplicities in the kinematical region, covered by the charged multiplicities, are well described but the estimated and measured K_S^0 multiplicities diverge for the uncovered kinematics region especially at low z . The K_S^0 multiplicities are largely overestimated due to the different weight of the FFs on the multiplicity equations for charged and neutral kaons. The unfavored FF has a much larger impact on the K_S^0 multiplicities than on the K^+ and K^- multiplicities.

The extraction of the FFs with a simultaneous fit of the K^+ , K^- , and K_S^0 multiplicities yields a better constraint and larger strange FF, while the favored and the unfavored FFs remain stable. The unfavored FF is smaller to compensate for the larger strange FF.

The estimated and measured multiplicities of K^+ , K^- , and K_S^0 are in much better agreement, although some differences, smaller but still significant, remain between the estimated and measured K_S^0 multiplicities for large x and low y . The source of the differences is most likely the discrepancy between the K_S^0 multiplicities of the different target cells.

The universality of the FFs is exploited one more time to compare the K^+ and K^- multiplicities from COMPASS with measurements from HERMES. A significant difference in shape and size is observed, which is only partially explained by the Q^2 evolution.

6. Summary and Conclusions

The goal of this thesis is the extraction of kaon fragmentation functions (FFs) from kaon multiplicities of COMPASS 2006 data. In the first part of the analysis the extraction of the K_S^0 multiplicities is achieved. Together with the K^+ and K^- multiplicities from previous analyses [68, 70, 71], now a complete set of kaon multiplicities is available. In the second part of the analysis kaon FFs are extracted and the results are discussed.

The analyzed data covers six weeks of muon deep inelastic scattering (DIS) on an isoscalar ^6LiD target. The K_S^0 multiplicities are extracted in bins of x , the momentum fraction carried by the struck parton, y , the relative energy transfer of the virtual photon, and z , the fraction of the virtual photon energy carried by the final state hadron. The kinematic domain covered is: $Q^2 > 1 (\text{GeV}/c)^2$, $0.004 < x < 0.4$, $0.1 < y < 0.9$, and $0.2 < z < 0.85$. The K_S^0 are identified by their decay into $\pi^+\pi^-$ pairs. To separate the K_S^0 from background the sum of a Gaussian function and a linear polynomial is fitted to the $\pi^+\pi^-$ invariant mass distribution. The number of K_S^0 is obtained by the integral of the Gaussian function.

This method to identify the K_S^0 is complementary to K^+ and K^- , which depend on the RICH detector for particle identification. The two methods for particle identification result in different systematic uncertainties and a different kinematic coverage of the charged and neutral kaon multiplicities. The RICH detector limits the analyzed momentum range to $12 \text{ GeV}/c$ – $43 \text{ GeV}/c$, which results in a limited z coverage for most bins of x and y .

During the analysis of the K_S^0 multiplicities an unresolved dependency of the target cells was observed. After the acceptance correction the K_S^0 multiplicity yield is found to linearly rise with the longitudinal primary vertex position in the target cell. To clarify this issue, further analysis is required which is beyond the scope of this thesis.

The FFs are extracted by performing a LO pQCD fit on the multiplicities. The FFs are grouped into favored (D_{fav}^K), strange (D_s^K), unfavored (D_{unf}^K), and gluon (D_g^K). Two kinds of fits were performed, the first one fitting only K^+ and K^- multiplicities, the second one including the K_S^0 multiplicities determined in this analysis, thus, fitting simultaneously K^+ , K^- , and K_S^0 multiplicities.

To study the impact of the PDF sets on the fit, both kinds of fits are performed with the following PDF sets: MSTW08 [14], MMHT14 [15], NNPDF2.3 [16],

6. Summary and Conclusions

NNPDF3.0 [17], and CT10 [18]. The resulting FFs are compared with NLO predictions from AKK [27], DSS [28], and HKNS [29].

The FFs D_{fav}^K and D_{unf}^K of fits with only K^+ and K^- multiplicities are stable with respect to the choice of the PDF set, while D_s^K has large uncertainties and varies for fits with different PDF sets.

The universality of the FFs is exploited to estimate the K_S^0 multiplicities from kaon FFs extracted from K^+ and K^- multiplicities only. The estimation and the measured K_S^0 multiplicities agree for those kinematic bins covered by the K^+ and K^- multiplicities. However, an extrapolation into the uncovered z region fails as the K_S^0 multiplicities are largely overestimated. It is shown that this is due to the large impact of D_{unf}^K to the K_S^0 multiplicity.

For the extraction of FFs, the K_S^0 multiplicities are again complementary to the K^+ and K^- multiplicities. The FFs extracted with fits on K^+ , K^- , and K_S^0 multiplicities differ significantly from the results of the fits with the K_S^0 multiplicities excluded. The most visible difference is observed for the strange FF, which comes out significantly larger, if the K_S^0 multiplicities are included and, at the same time, has significantly smaller uncertainty bands. However, differences between the fits with different PDF sets still exist. The variations of the fit's center bands are comparable to those fits with the K_S^0 excluded. To quantitatively compare the FFs from fits with and without the K_S^0 included, the FFs are integrated over the analyzed z range $0.2 < z < 0.85$. The center values for fits with different PDF sets range between:

fit type	$\int_{0.2}^{0.85} D_{\text{fav}}^K dz$	$\int_{0.2}^{0.85} D_s^K dz$	$\int_{0.2}^{0.85} D_{\text{unf}}^K dz$
$K^+ + K^-$	0.122–0.137	0.195–0.563	0.031–0.036
$K^+ + K^- + K_S^0$	0.115–0.129	0.456–1.265	0.0188–0.0280

While the integral of D_{fav}^K with the K_S^0 included is only slightly smaller, the one of D_{unf}^K is reduced by about 33% which then consequently is compensated by a intuitively more natural D_s^K . A comparison of the ratio R_{sf} of the z -integrated D_s^K and D_{fav}^K yields values ranging from 1.46–4.63 from fits with K^+ and K^- multiplicities only and 3.65–11.03 from fits with K^+ , K^- , and K_S^0 multiplicities. This would make kaons the expected good tag for strange quarks, as it is required to separate the flavor contributions to the nucleon spin mentioned in the introduction.

By exploiting the universality of the FFs one more time, the FFs are used to estimate the kaon multiplicities at the kinematics of the HERMES experiment. It turns out that neither do the measured multiplicities of COMPASS and HERMES agree nor are the estimations from the extracted FFs able to describe the deviations.

To conclude, the essence of this thesis is the extraction of the K_S^0 multiplicities from COMPASS 2006 data and the extraction of kaon FFs. The multiplicities

of K_S^0 are of special interest because they are in two ways complementary to the already determined K^+ and K^- multiplicities. First, they are identified by their decay into $\pi^+\pi^-$ pairs, in contrast to the charged kaons which rely on the RICH detector for particle identification. This yields a different coverage of z and different systematic uncertainties. Second, the FFs have a different weight on the multiplicities of charged and neutral kaons. Thus, fits with the K_S^0 multiplicities included are able to constrain the FFs with more accuracy. This has a large impact on the extraction of the FFs, especially the extracted strange FF is larger and more stable. A comparison of kaon multiplicities from COMPASS and HERMES shows large differences between the two, which, in LO, cannot be explained by their different kinematics. This clearly shows that more experimental data and research is needed. The K^+ and K^- multiplicities, together with the K_S^0 multiplicities of this thesis, present a full set of kaon multiplicities for further analyses especially for the extraction of FFs.

Appendices

A. Multiplicity Equations

The LO multiplicities for π^\pm , K^\pm and K_S^0 for a deuteron target are calculated from the LO multiplicity equation:

$$\frac{1}{N^{DIS}(x, Q^2)} \frac{dN^h}{dx dz dQ^2} = \frac{N^h}{N^{DIS}} = \frac{\sum_q e_q^2 q(x, Q^2) D_q^h(z, Q^2)}{\sum_q e_q^2 q(x, Q^2)}, \quad (\text{A.1})$$

where q denotes the quark flavors $u, d, s, \bar{u}, \bar{d}, \bar{s}$. The PDFs are denoted by $q(x, Q^2)$, and the FFs by $D_q^h(z, Q^2)$. The general approach is the same for all particles: At first the equation is expanded for the quark distribution of the proton. Applying isospin invariance yields the equation for the quark distribution of the neutron. The sum of both equations yields the multiplicity for the deuteron.

The denominator of Eq. (A.1) is the number of DIS events N^{DIS} . It is the same for all final state hadrons. Expanding N^{DIS} for the proton yields:

$$N_p^{DIS} = \sum_q e_q^2 q(x, Q^2) = \frac{1}{9} [4u + 4\bar{u} + d + \bar{d} + s + \bar{s}]. \quad (\text{A.2})$$

Applying isospin invariance yields the neutron share:

$$N_n^{DIS} = \sum_q e_q^2 q(x, Q^2) = \frac{1}{9} [4d + 4\bar{d} + u + \bar{u} + s + \bar{s}]. \quad (\text{A.3})$$

The sum

$$N_d^{DIS} = N_p^{DIS} + N_n^{DIS} = \frac{1}{9} [5(u + \bar{u} + d + \bar{d}) + 2(s + \bar{s})] \quad (\text{A.4})$$

yields the number of DIS events for deuterons.

A.1. Pions

A.1.1. Pion Fragmentation Functions

The valence quark configurations of the charged pions are:

$$\begin{aligned} \pi^+ &= u\bar{d} \\ \pi^- &= \bar{u}d \end{aligned}$$

A. Multiplicity Equations

For the π^+ the favored FFs are $D_u^{\pi^+}$ and $D_d^{\pi^+}$; the unfavored FFs are $D_{\bar{u}}^{\pi^+}$, $D_{\bar{d}}^{\pi^+}$, $D_s^{\pi^+}$, and $D_{\bar{s}}^{\pi^+}$. Applying isospin and charge invariance, relates the favored FFs for π^+ and π^- :

$$D_{\text{fav}}^{\pi} \equiv D_u^{\pi^+} = D_d^{\pi^-} = D_{\bar{d}}^{\pi^+} = D_{\bar{u}}^{\pi^-}. \quad (\text{A.5})$$

The same is true for the unfavored FFs. Here the additional assumption is made that the strange unfavored FFs are equal to the other unfavored FFs:

$$D_{\text{unf}}^{\pi} \equiv D_u^{\pi^-} = D_{\bar{u}}^{\pi^+} = D_d^{\pi^+} = D_{\bar{d}}^{\pi^-} = D_s^{\pi^{\pm}} = D_{\bar{s}}^{\pi^{\pm}}. \quad (\text{A.6})$$

Thus, there exist two independent FFs for the charged pions.

A.1.2. Pion Multiplicities

Expanding the nominator of A.1 for the proton yields:

$$\begin{aligned} N_p^{\pi^+} &= (4u + \bar{d})D_{\text{fav}}^{\pi} + (4\bar{u} + d + s + \bar{s})D_{\text{unf}}^{\pi} \\ N_p^{\pi^-} &= (4\bar{u} + d)D_{\text{fav}}^{\pi} + (4u + \bar{d} + s + \bar{s})D_{\text{unf}}^{\pi} \end{aligned} \quad (\text{A.7})$$

Applying isospin invariance yields the nominator for the neutron:

$$\begin{aligned} N_n^{\pi^+} &= (4d + \bar{u})D_{\text{fav}}^{\pi} + (4\bar{d} + u + s + \bar{s})D_{\text{unf}}^{\pi} \\ N_n^{\pi^-} &= (4\bar{d} + u)D_{\text{fav}}^{\pi} + (4d + \bar{u} + s + \bar{s})D_{\text{unf}}^{\pi} \end{aligned} \quad (\text{A.8})$$

Combining Eq. A.7 and A.8 to get the nominator for the deuteron yields:

$$M^{\pi^+}(x, Q^2, z) = \frac{(4(u + d) + \bar{u} + \bar{d})D_{\text{fav}}^{\pi} + (u + d + 4(\bar{u} + \bar{d}) + 2(s + \bar{s}))D_{\text{unf}}^{\pi}}{5(u + d + \bar{u} + \bar{d}) + 2(s + \bar{s})} \quad (\text{A.9})$$

$$M^{\pi^-}(x, Q^2, z) = \frac{(u + d + 4(\bar{u} + \bar{d}))D_{\text{fav}}^{\pi} + (4(u + d) + \bar{u} + \bar{d} + 2(s + \bar{s}))D_{\text{unf}}^{\pi}}{5(u + d + \bar{u} + \bar{d}) + 2(s + \bar{s})} \quad (\text{A.10})$$

A.2. Kaons

A.2.1. Relation between Charged and Neutral Kaon Fragmentation Functions

The valence quark configurations for K^0 , \bar{K}^0 , and K^\pm are:

$$\begin{aligned}
 K^+ &= u\bar{s} \\
 K^- &= \bar{u}s \\
 K^0 &= d\bar{s} \\
 \bar{K}^0 &= \bar{d}s
 \end{aligned} \tag{A.11}$$

Applying charge invariance yields two favored FFs for both the charged and neutral kaons. For historic reasons the favored FF of u , d , \bar{u} , and \bar{d} quarks is denoted as D_{fav} and the favored FF of s and \bar{s} quarks as D_s :

$$\begin{aligned}
 D_{\text{fav}}^{K^+} &\equiv D_u^{K^+} = D_{\bar{u}}^{K^-} \\
 D_s^{K^+} &\equiv D_{\bar{s}}^{K^+} = D_s^{K^-} \\
 D_{\text{fav}}^{K^0} &\equiv D_d^{K^0} = D_{\bar{d}}^{\bar{K}^0} \\
 D_s^{K^0} &\equiv D_{\bar{s}}^{K^0} = D_s^{\bar{K}^0}
 \end{aligned} \tag{A.12}$$

Applying SU(2) and the assumption that the unfavored strange FF is equal to the other unfavored FFs, reduces the unfavored FFs to one each:

$$\begin{aligned}
 D_{\text{unf}}^{K^+} &\equiv D_d^{K^\pm} = D_{\bar{d}}^{K^\pm} = D_{\bar{u}}^{K^+} = D_u^{K^-} = D_s^{K^+} = D_{\bar{s}}^{K^-} \\
 D_{\text{unf}}^{K^0} &\equiv D_u^{K^0, \bar{K}^0} = D_{\bar{u}}^{K^0, \bar{K}^0} = D_{\bar{d}}^{K^0} = D_d^{\bar{K}^0} = D_s^{K^0} = D_{\bar{s}}^{\bar{K}^0}
 \end{aligned} \tag{A.13}$$

Isospin symmetry and charge symmetry also relates K^0 , \bar{K}^0 , and K^\pm fragmentation functions:

A. Multiplicity Equations

$$\begin{aligned}
D_{\text{fav}}^{\text{K}} &\equiv D_{\text{fav}}^{\text{K}^0} \stackrel{\text{isospin}}{=} D_{\text{fav}}^{\text{K}^+} \\
D_{\text{s}}^{\text{K}} &\equiv D_{\text{s}}^{\text{K}^0} \stackrel{\text{isospin}}{=} D_{\text{s}}^{\text{K}^+} \\
D_{\text{unf}}^{\text{K}} &\equiv D_{\text{unf}}^{\text{K}^0} \stackrel{\text{isospin}}{=} D_{\text{unf}}^{\text{K}^+}
\end{aligned} \tag{A.14}$$

A.2.2. Charged Kaon Multiplicities

Expanding the nominator of A.1 for the proton yields:

$$\begin{aligned}
N_{\text{p}}^{\text{K}^+} &= 4uD_{\text{fav}}^{\text{K}} + \bar{s}D_{\text{s}}^{\text{K}} + (4u + d + \bar{d} + s)D_{\text{unf}}^{\text{K}} \\
N_{\text{p}}^{\text{K}^-} &= 4\bar{u}D_{\text{fav}}^{\text{K}} + sD_{\text{s}}^{\text{K}} + (4u + d + \bar{d} + \bar{s})D_{\text{unf}}^{\text{K}}
\end{aligned} \tag{A.15}$$

Applying isospin invariance ($u \rightarrow d$, $d \rightarrow u$) yields the nominator for the neutron:

$$\begin{aligned}
N_{\text{n}}^{\text{K}^+} &= 4dD_{\text{fav}}^{\text{K}} + \bar{s}D_{\text{s}}^{\text{K}} + (4\bar{d} + u + \bar{u} + s)D_{\text{unf}}^{\text{K}} \\
N_{\text{n}}^{\text{K}^-} &= 4\bar{d}D_{\text{fav}}^{\text{K}} + sD_{\text{s}}^{\text{K}} + (4d + u + \bar{u} + \bar{s})D_{\text{unf}}^{\text{K}}
\end{aligned} \tag{A.16}$$

Combining Eq. A.15 and A.16 to get the nominator for the deuteron yields:

$$\begin{aligned}
N_{\text{d}}^{\text{K}^+} &= 4(u + d)D_{\text{fav}}^{\text{K}} + 2\bar{s}D_{\text{s}}^{\text{K}} + (5(\bar{u} + \bar{d}) + u + d + 2s)D_{\text{unf}}^{\text{K}} \\
N_{\text{d}}^{\text{K}^-} &= 4(\bar{u} + \bar{d})D_{\text{fav}}^{\text{K}} + 2sD_{\text{s}}^{\text{K}} + (5(u + d) + \bar{u} + \bar{d} + 2\bar{s})D_{\text{unf}}^{\text{K}}
\end{aligned} \tag{A.17}$$

Putting Eq. A.17 and A.4 together yields the multiplicity for K^+ and K^- :

$$M^{\text{K}^+} = \frac{4(u + d)D_{\text{fav}}^{\text{K}} + 2\bar{s}D_{\text{s}}^{\text{K}} + (5(\bar{u} + \bar{d}) + u + d + 2s)D_{\text{unf}}^{\text{K}}}{5(u + \bar{u} + d + \bar{d}) + 2(s + \bar{s})} \tag{A.18}$$

$$M^{\text{K}^-} = \frac{4(\bar{u} + \bar{d})D_{\text{fav}}^{\text{K}} + 2sD_{\text{s}}^{\text{K}} + (5(u + d) + \bar{u} + \bar{d} + 2\bar{s})D_{\text{unf}}^{\text{K}}}{5(u + \bar{u} + d + \bar{d}) + 2(s + \bar{s})} \tag{A.19}$$

A.2.3. Neutral Kaon Multiplicities

Expanding the nominator of A.1 for the proton yields:

$$\begin{aligned}
N_{\text{p}}^{\text{K}^0} &= dD_{\text{fav}}^{\text{K}} + \bar{s}D_{\text{s}}^{\text{K}} + (4u + 4\bar{u} + \bar{d} + s)D_{\text{unf}}^{\text{K}} \\
N_{\text{p}}^{\bar{\text{K}}^0} &= \bar{d}D_{\text{fav}}^{\text{K}} + sD_{\text{s}}^{\text{K}} + (4u + 4\bar{u} + d + \bar{s})D_{\text{unf}}^{\text{K}}
\end{aligned} \tag{A.20}$$

Applying isospin invariance yields the nominator for the neutron:

$$\begin{aligned} N_n^{K^0} &= uD_{\text{fav}}^K + \bar{s}D_s^K + (4d + 4\bar{d} + \bar{u} + s)D_{\text{unf}}^K \\ N_n^{\bar{K}^0} &= \bar{u}D_{\text{fav}}^K + sD_s^K + (4d + 4\bar{d} + u + \bar{s})D_{\text{unf}}^K \end{aligned} \quad (\text{A.21})$$

At COMPASS only K_S^0 are measured, hence

$$N_p^{K_S^0} = \frac{1}{2}(K^0 + \bar{K}^0) = \frac{1}{2} \left[(d + \bar{d})D_{\text{fav}}^K + (s + \bar{s})D_s^K + (8u + 8\bar{u} + d + \bar{d} + s + \bar{s})D_{\text{unf}}^K \right] \quad (\text{A.22})$$

$$N_n^{K_S^0} = \frac{1}{2}(K^0 + \bar{K}^0) = \frac{1}{2} \left[(u + \bar{u})D_{\text{fav}}^K + (s + \bar{s})D_s^K + (8d + 8\bar{d} + u + \bar{u} + s + \bar{s})D_{\text{unf}}^K \right] \quad (\text{A.23})$$

Combining Eq. A.22 and A.23 to get the nominator for the deuteron yields:

$$N_d^{K_S^0} = \frac{1}{2} \left[(D_{\text{fav}}^K + 9D_{\text{unf}}^K)(u + \bar{u} + d + \bar{d}) + 2(D_{\text{unf}}^K + D_s^K)(s + \bar{s}) \right] \quad (\text{A.24})$$

Putting Eq. A.24 and A.4 together yields the multiplicity for K_S^0 :

$$2 \cdot M^{K_S^0} = \frac{(D_{\text{fav}}^K + 9D_{\text{unf}}^K)(u + \bar{u} + d + \bar{d}) + 2(D_{\text{unf}}^K + D_s^K)(s + \bar{s})}{5(u + \bar{u} + d + \bar{d}) + 2(s + \bar{s})} \quad (\text{A.25})$$

B. Fragmentation Functions

B.1. Kaon FFs from Fits to K^+ and K^- Multiplicities

B.1.1. Residuals

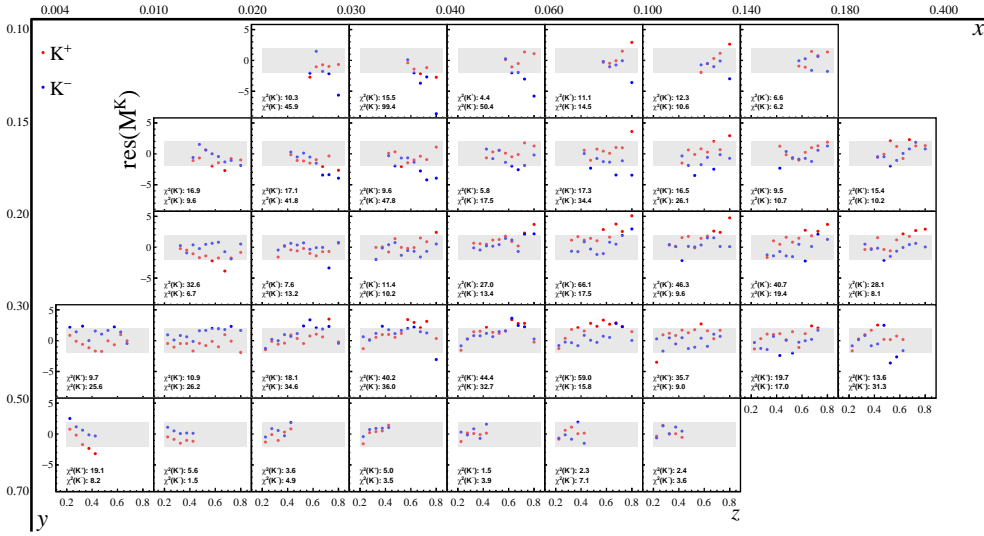


Figure B.1.: Residuals for the parametrization with the MMHT14 PDF set.

B. Fragmentation Functions

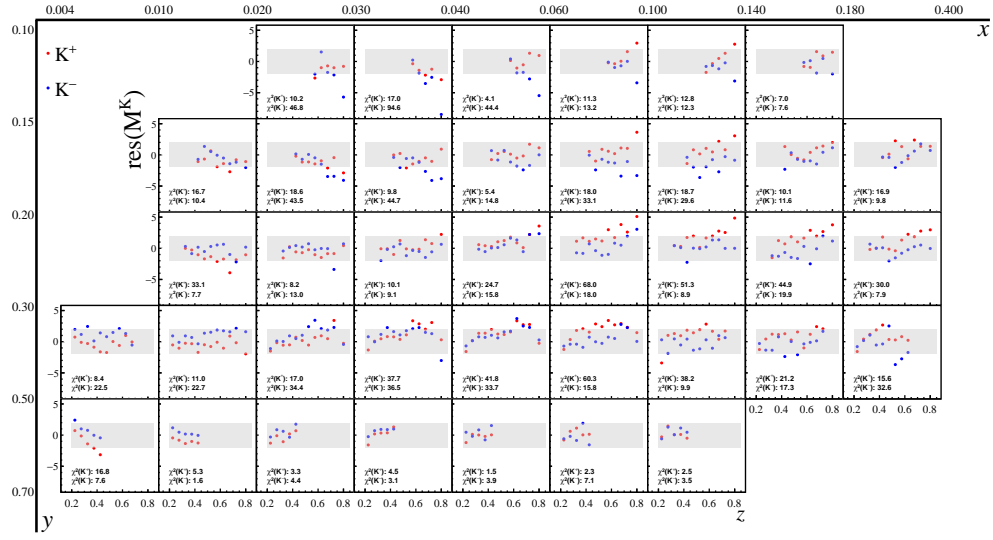


Figure B.2.: Residuals for the parametrization with the MSTW08 PDF set.

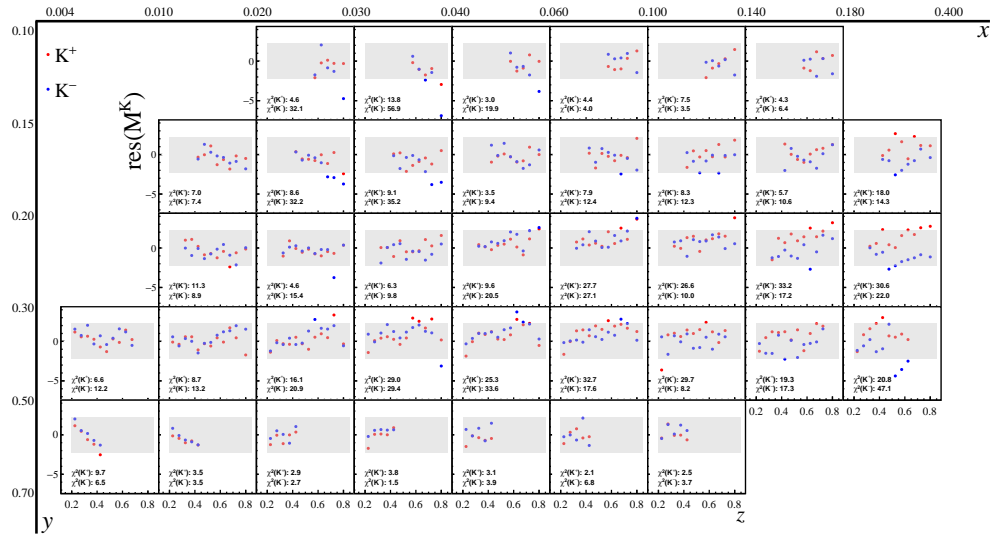


Figure B.3.: Residuals for the parametrization with the NNPDF2.3 PDF set.

B.1. Kaon FFs from Fits to K^+ and K^- Multiplicities

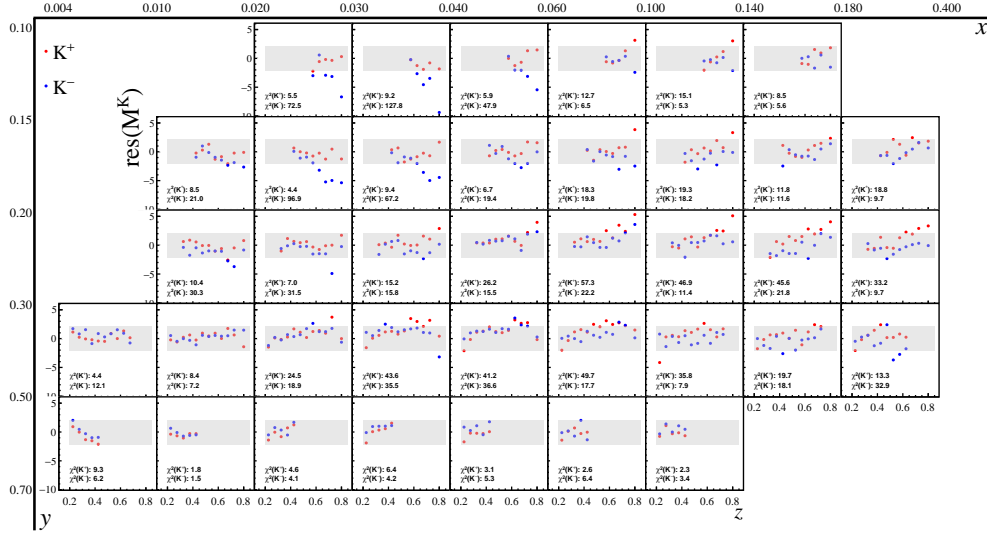


Figure B.4.: Residuals for the parametrization with the NNPDF3.0 PDF set.

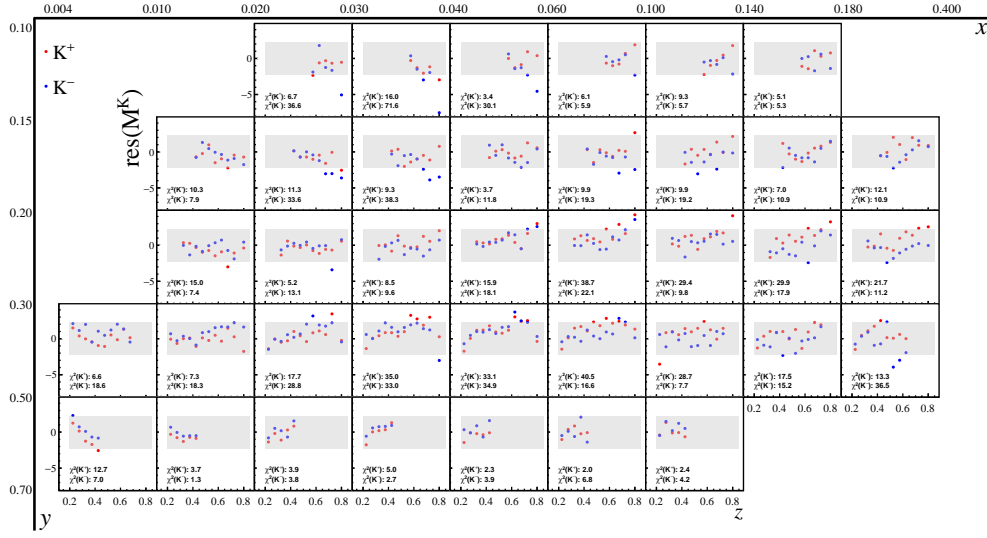


Figure B.5.: Residuals for the parametrization with the CT10 PDF set.

B. Fragmentation Functions

B.1.2. Individual Quark Contributions to the Multiplicities

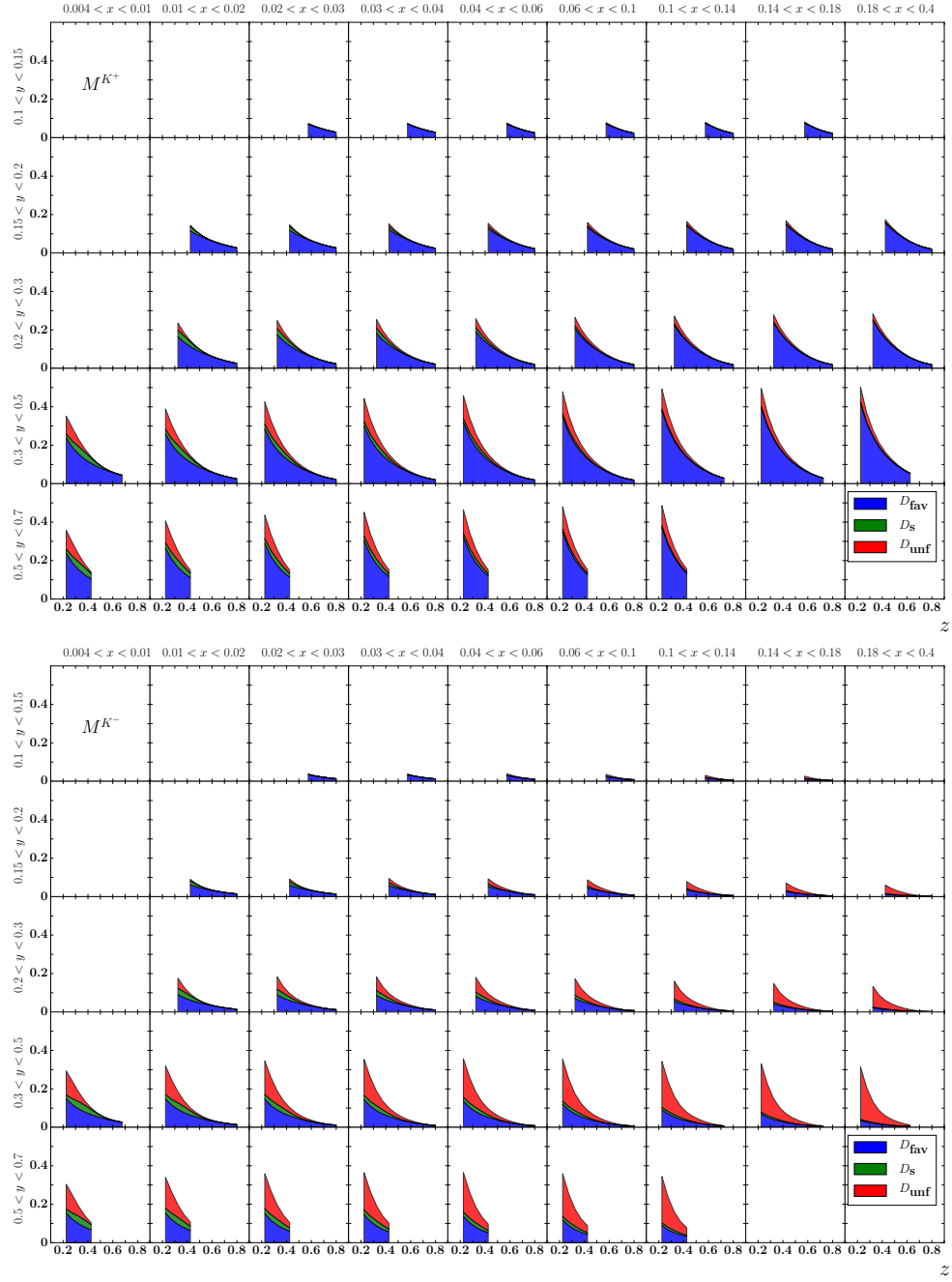


Figure B.6.: Contribution of FFs to K^+ (top) and K^- (bottom) multiplicities resulting from a fit on only charged kaon multiplicities using the MMHT14 PDF set.

B.1. Kaon FFs from Fits to K^+ and K^- Multiplicities

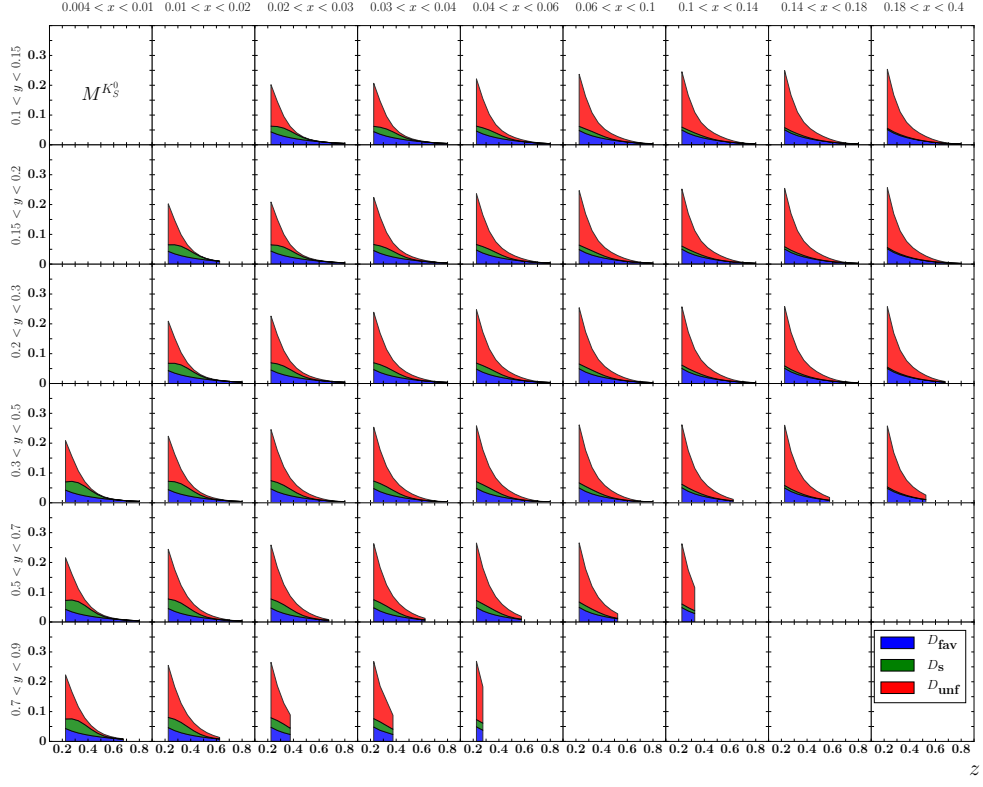


Figure B.7.: Same as Fig. B.6 but for K_S^0 .

B. Fragmentation Functions

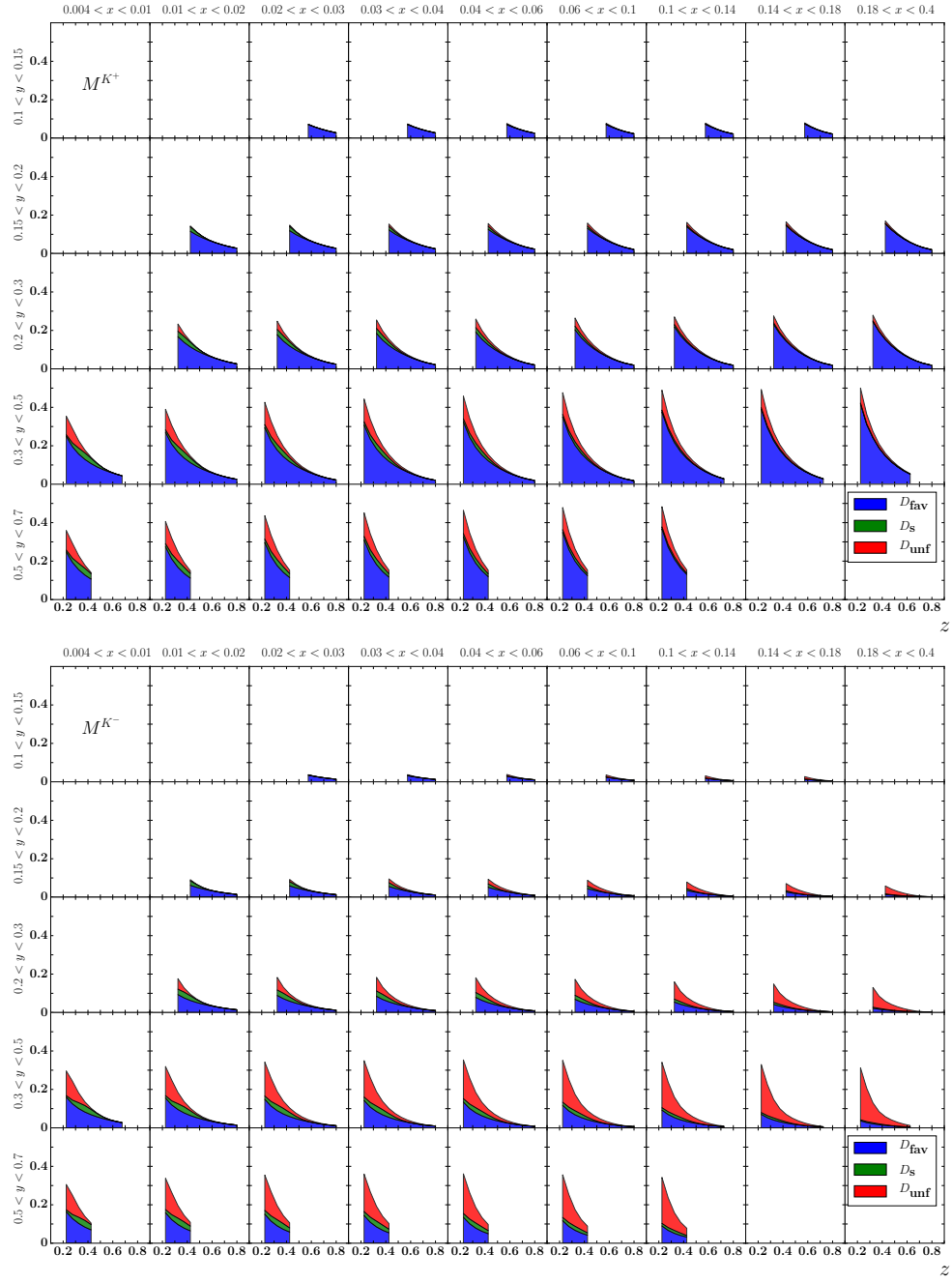


Figure B.8.: Contribution of FFs to K^+ (top) and K^- (bottom) multiplicities resulting from a fit on only charged kaon multiplicities using the MSTW08 PDF set.

B.1. Kaon FFs from Fits to K^+ and K^- Multiplicities

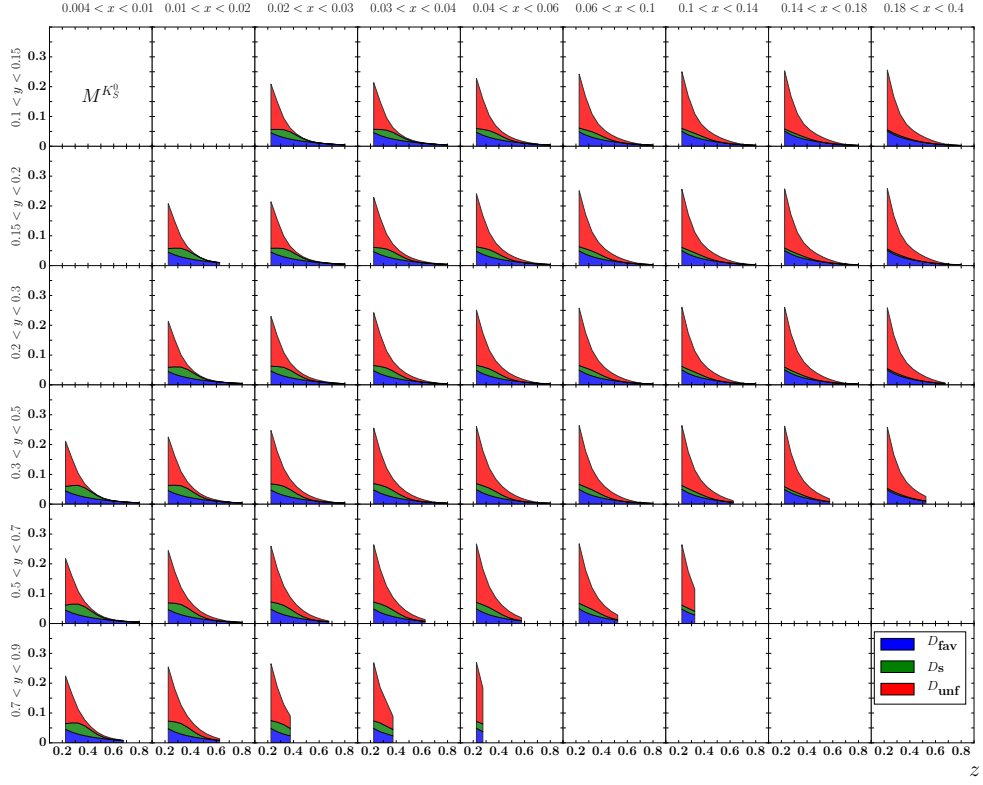


Figure B.9.: Same as Fig. B.8 but for K_S^0 .

B. Fragmentation Functions

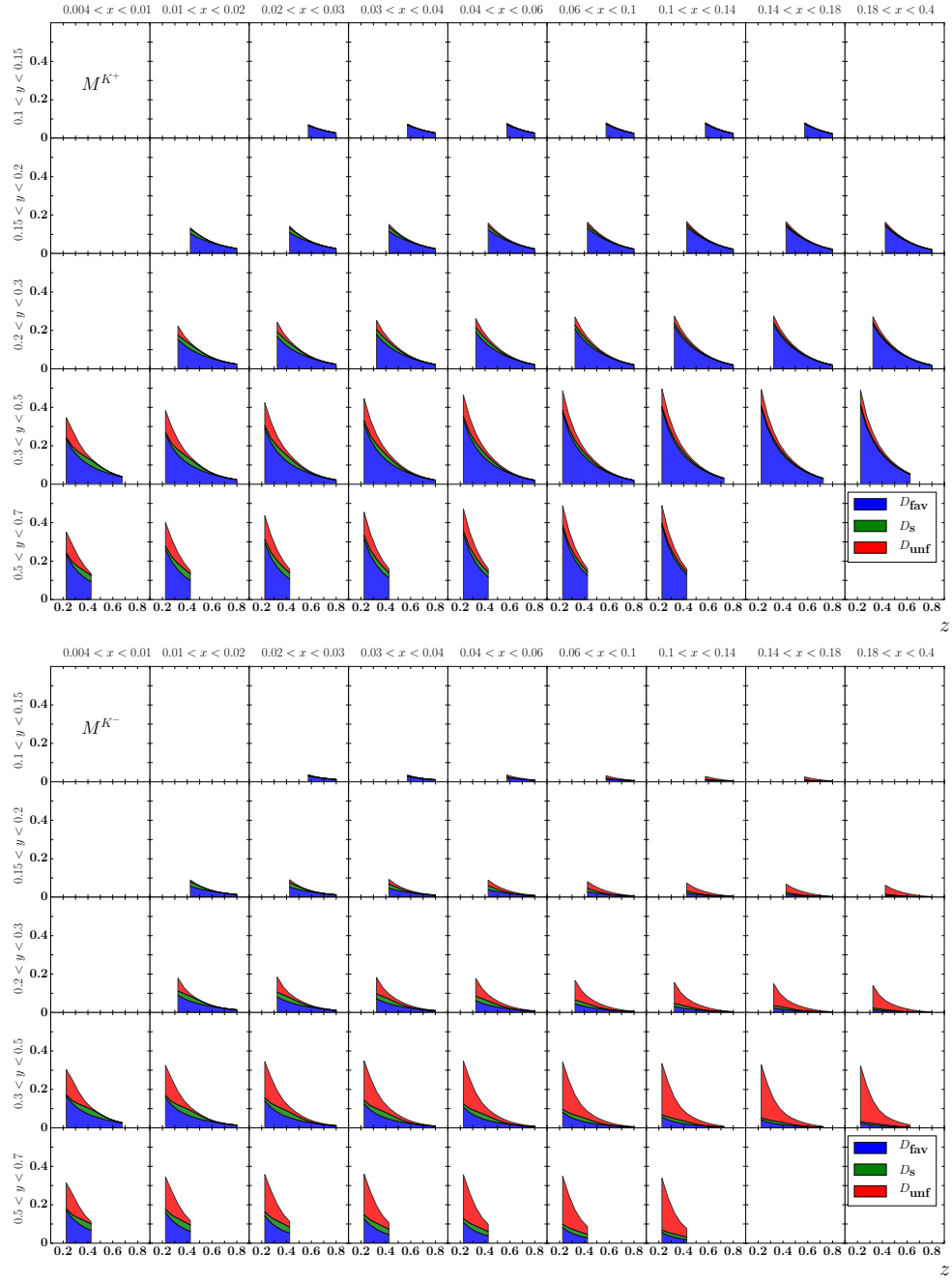


Figure B.10.: Contribution of FFs to K^+ (top) and K^- (bottom) multiplicities resulting from a fit on only charged kaon multiplicities using the NNPDF2.3 PDF set.

B.1. Kaon FFs from Fits to K^+ and K^- Multiplicities

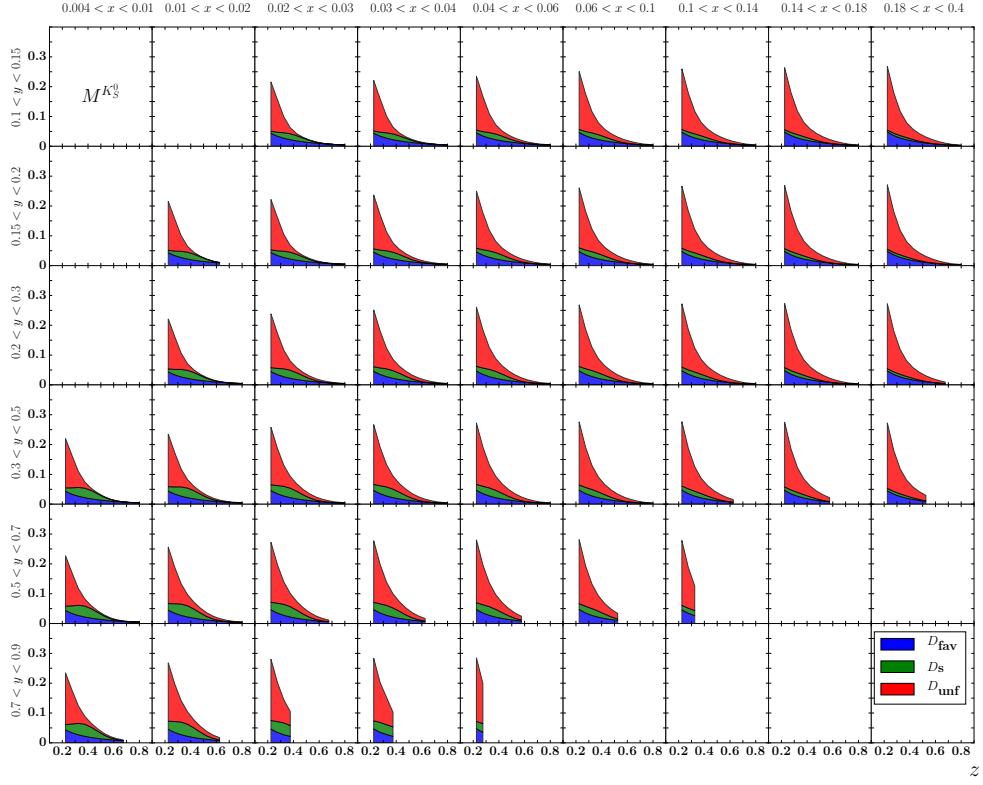


Figure B.11.: Same as Fig. B.10 but for K_S^0 .

B. Fragmentation Functions

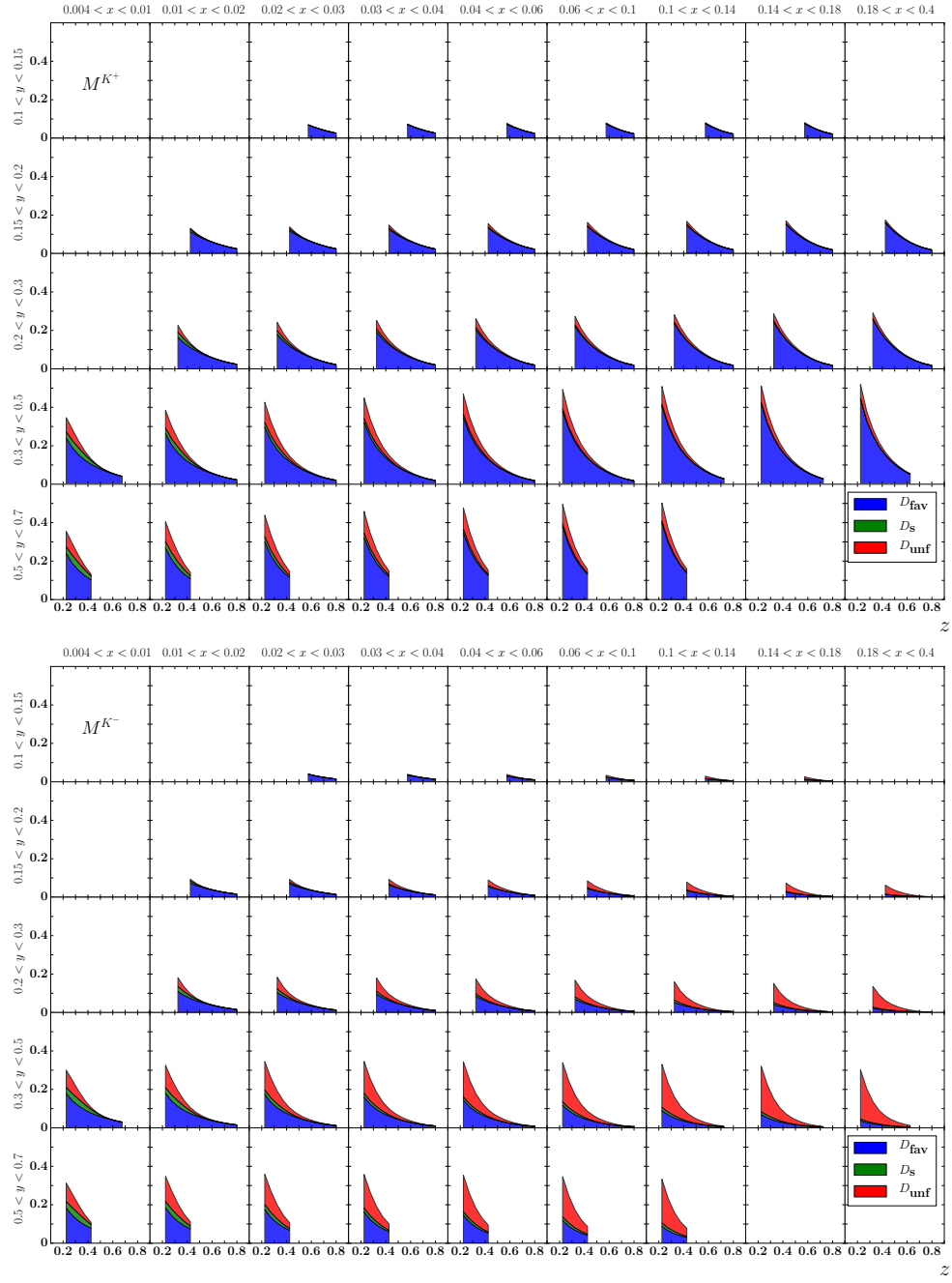


Figure B.12.: Contribution of FFs to K^+ (top) and K^- (bottom) multiplicities resulting from a fit on only charged kaon multiplicities using the NNPDF3.0 PDF set.

B.1. Kaon FFs from Fits to K^+ and K^- Multiplicities

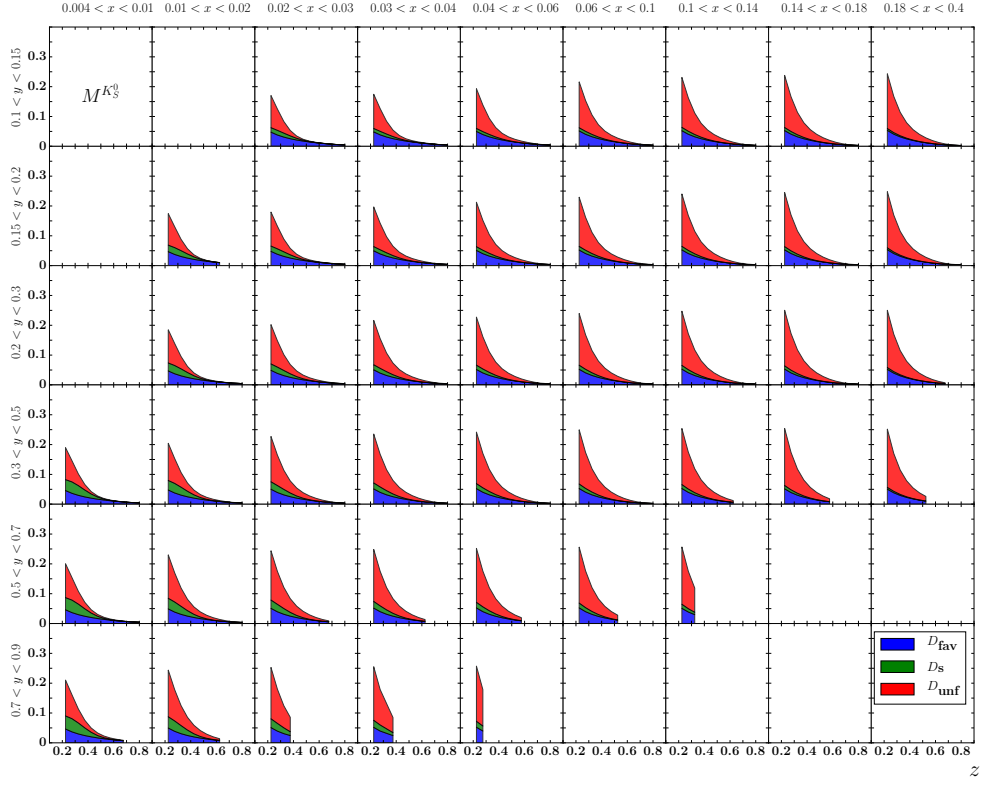


Figure B.13.: Same as Fig. B.12 but for K_S^0 .

B. Fragmentation Functions

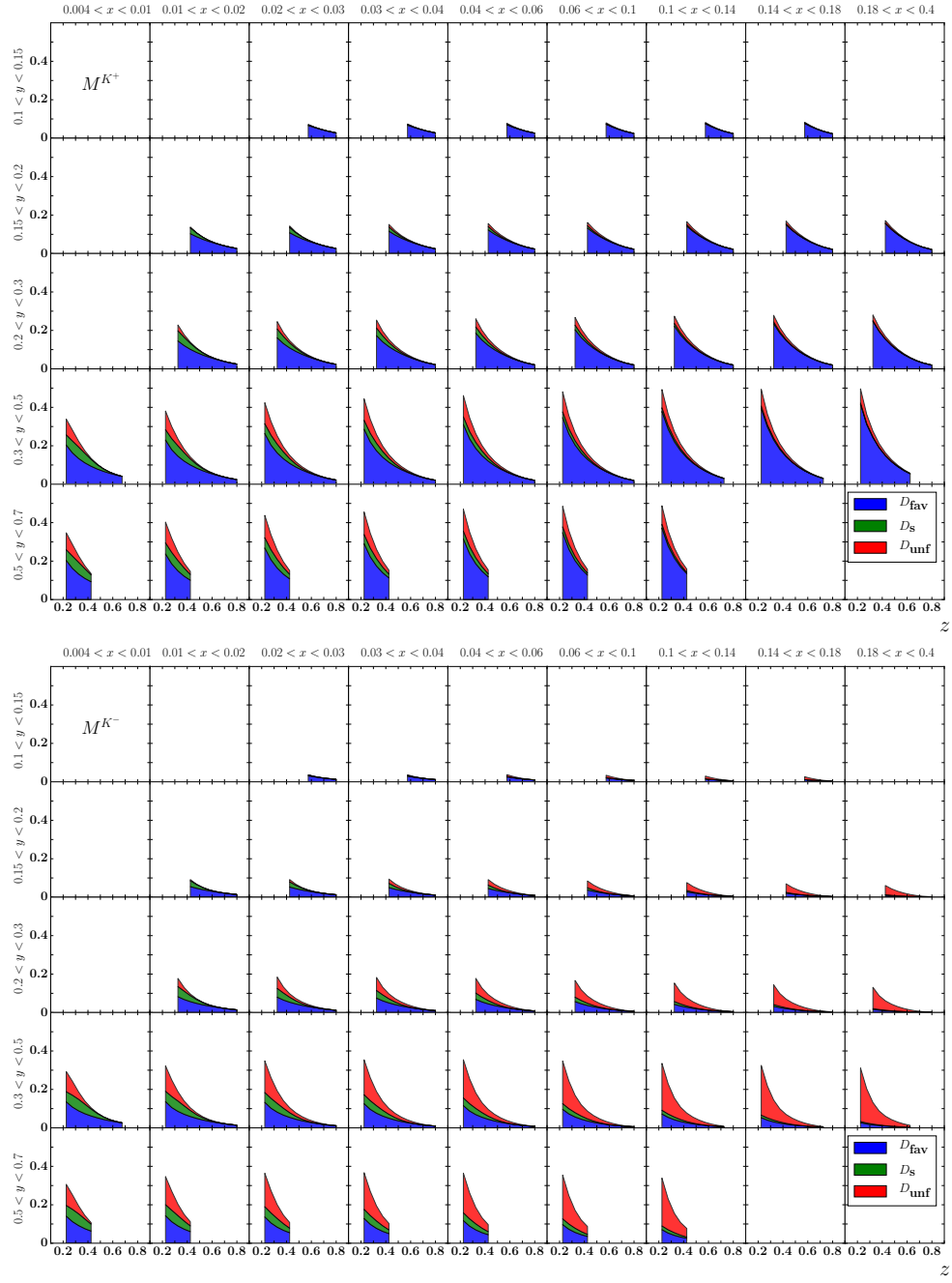


Figure B.14.: Contribution of FFs to K^+ (top) and K^- (bottom) multiplicities resulting from a fit on only charged kaon multiplicities using the CT10 PDF set.

B.1. Kaon FFs from Fits to K^+ and K^- Multiplicities

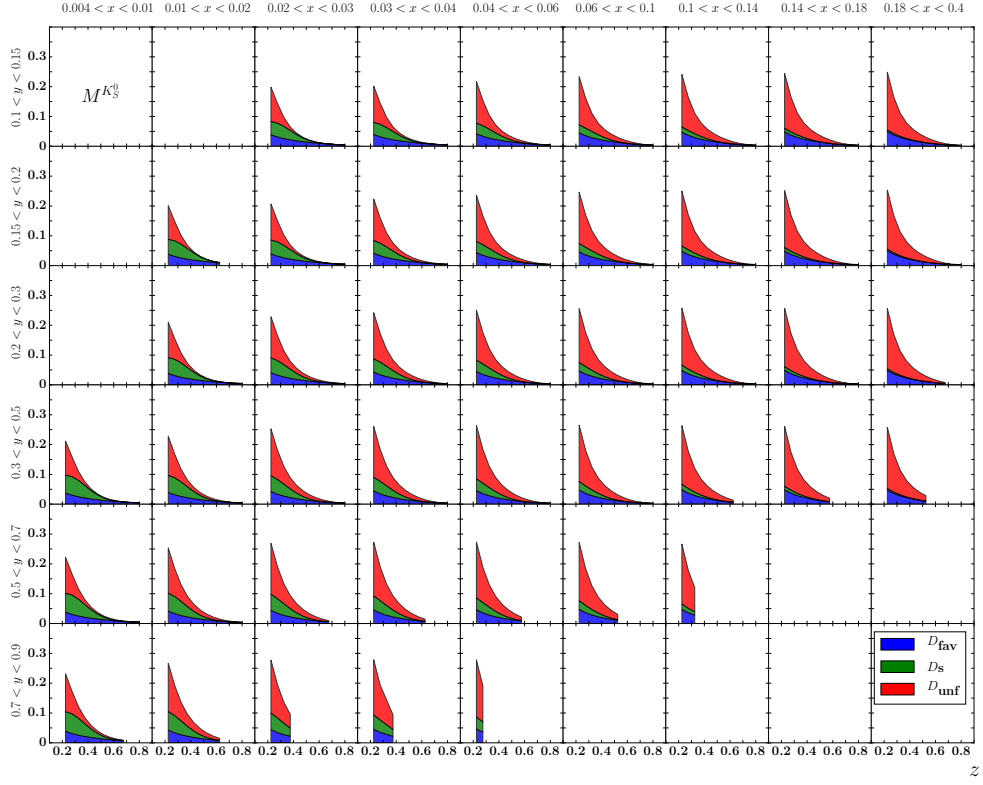


Figure B.15.: Same as Fig. B.14 but for K_S^0 .

B. Fragmentation Functions

B.2. Kaon FFs from Fits to K^+ , K^- , and K_S^0 Multiplicities

B.2.1. Residuals

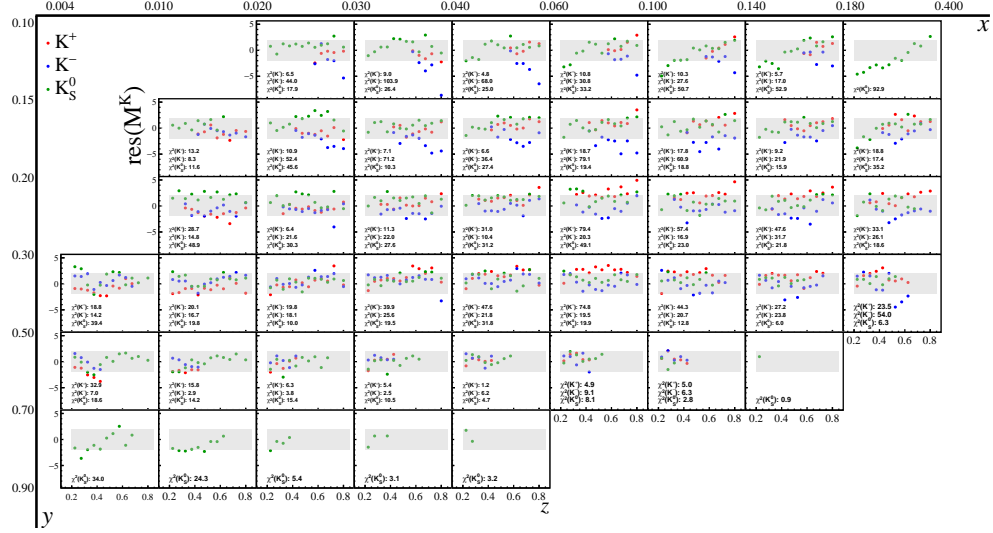


Figure B.16.: Residuals for the parametrization with the MMHT14 PDF set.

B.2. Kaon FFs from Fits to K^+ , K^- , and K_S^0 Multiplicities

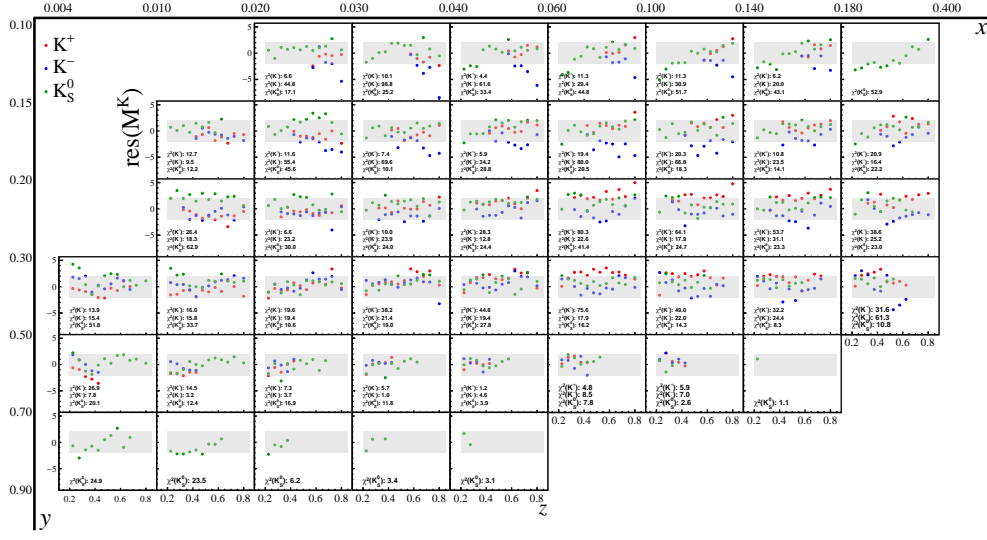


Figure B.17.: Residuals for the parametrization with the MSTW08 PDF set.

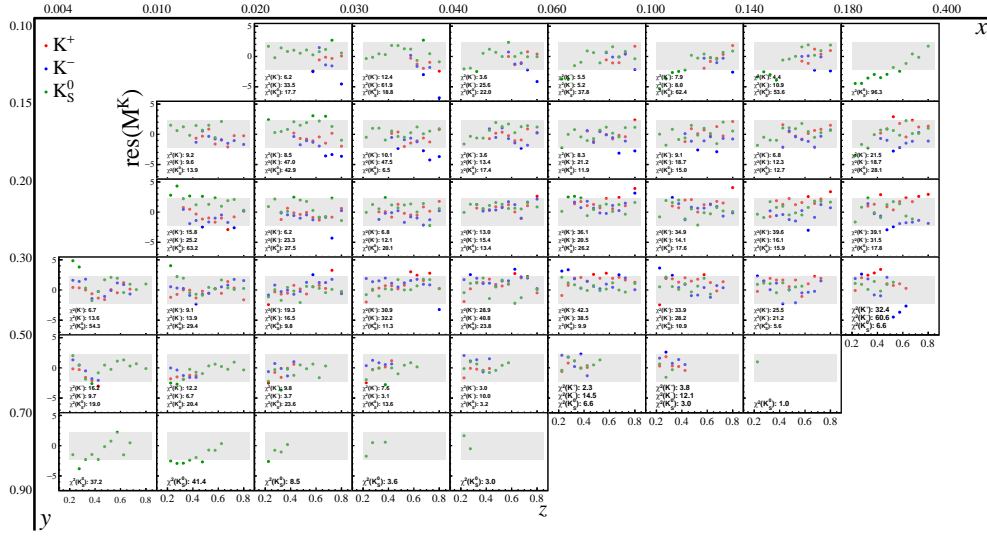


Figure B.18.: Residuals for the parametrization with the NNPDF2.3 PDF set.

B. Fragmentation Functions

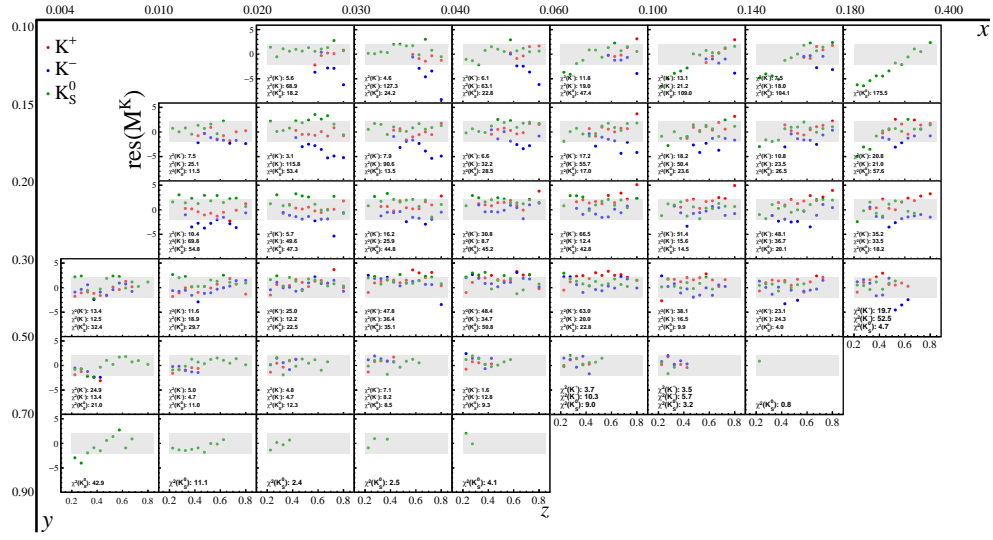


Figure B.19.: Residuals for the parametrization with the NNPDF3.0 PDF set.

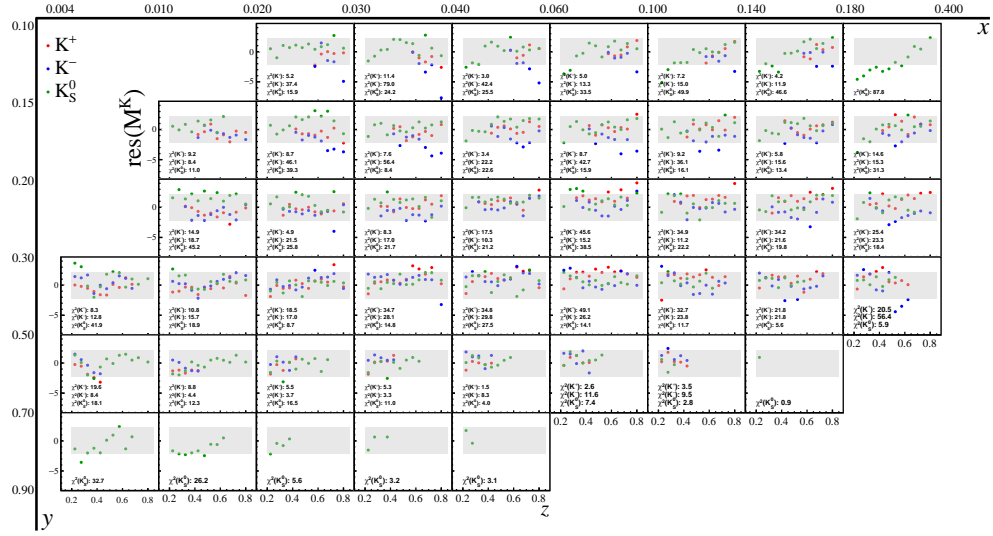


Figure B.20.: Residuals for the parametrization with the CT10 PDF set.

B.2. Kaon FFs from Fits to K^+ , K^- , and K_S^0 Multiplicities

B.2.2. Individual Quark Contributions to the Multiplicities

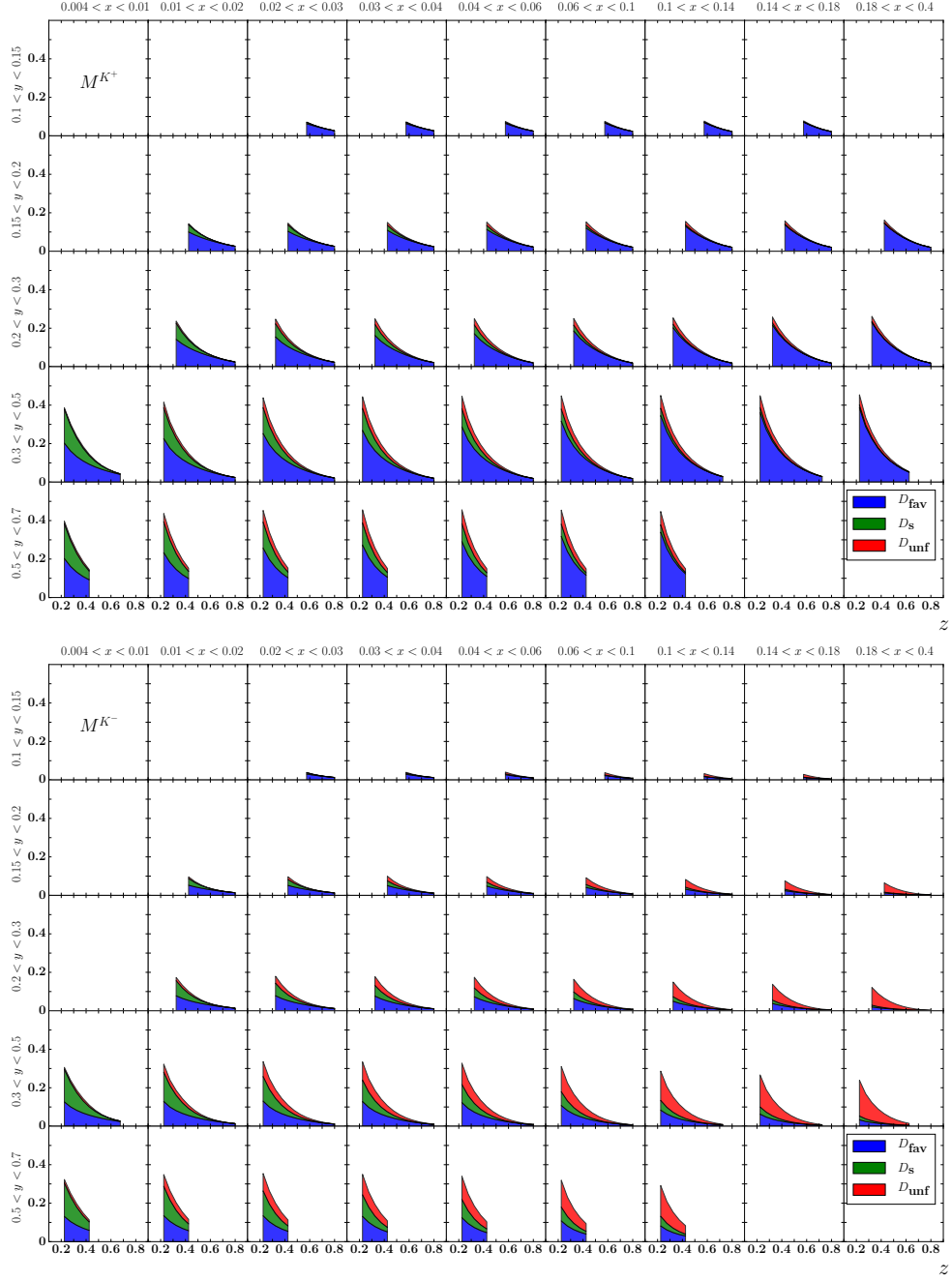


Figure B.21.: Contribution of FFs to K^+ (top) and K^- (bottom) multiplicities resulting from a fit on only combined kaon multiplicities using the MMHT14 PDF set.

B. Fragmentation Functions

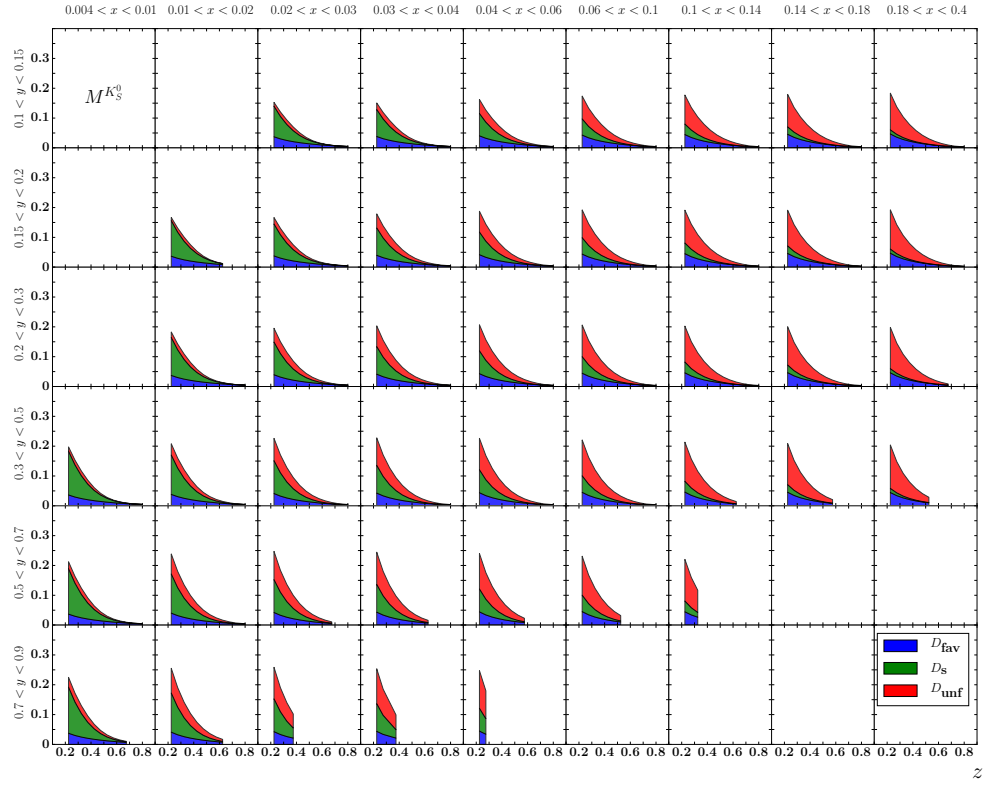


Figure B.22.: Same as Fig. B.21 but for K_S^0 .

B.2. Kaon FFs from Fits to K^+ , K^- , and K_S^0 Multiplicities

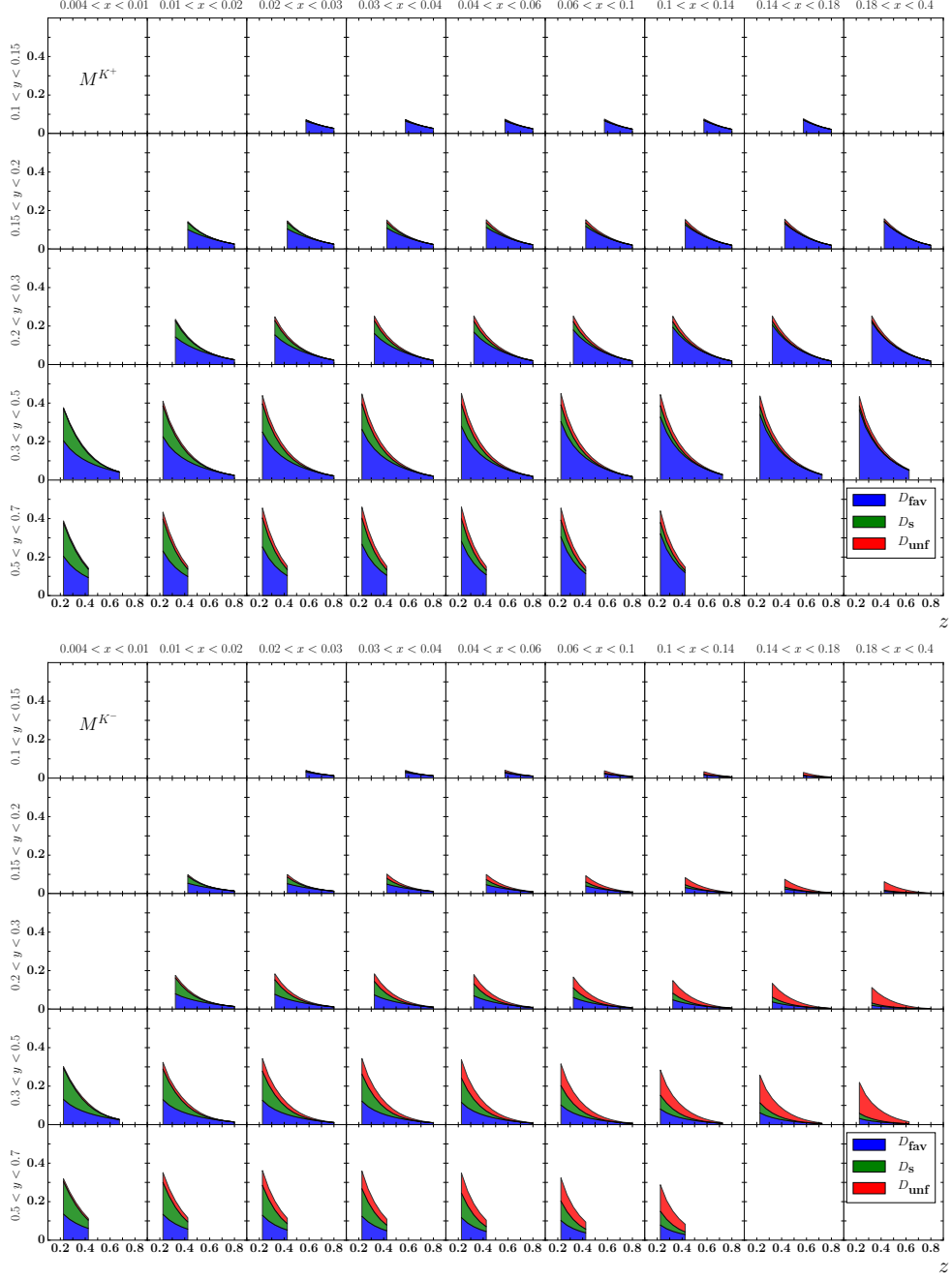


Figure B.23.: Contribution of FFs to K^+ (top) and K^- (bottom) multiplicities resulting from a fit on only combined kaon multiplicities using the MSTW08 PDF set.

B. Fragmentation Functions

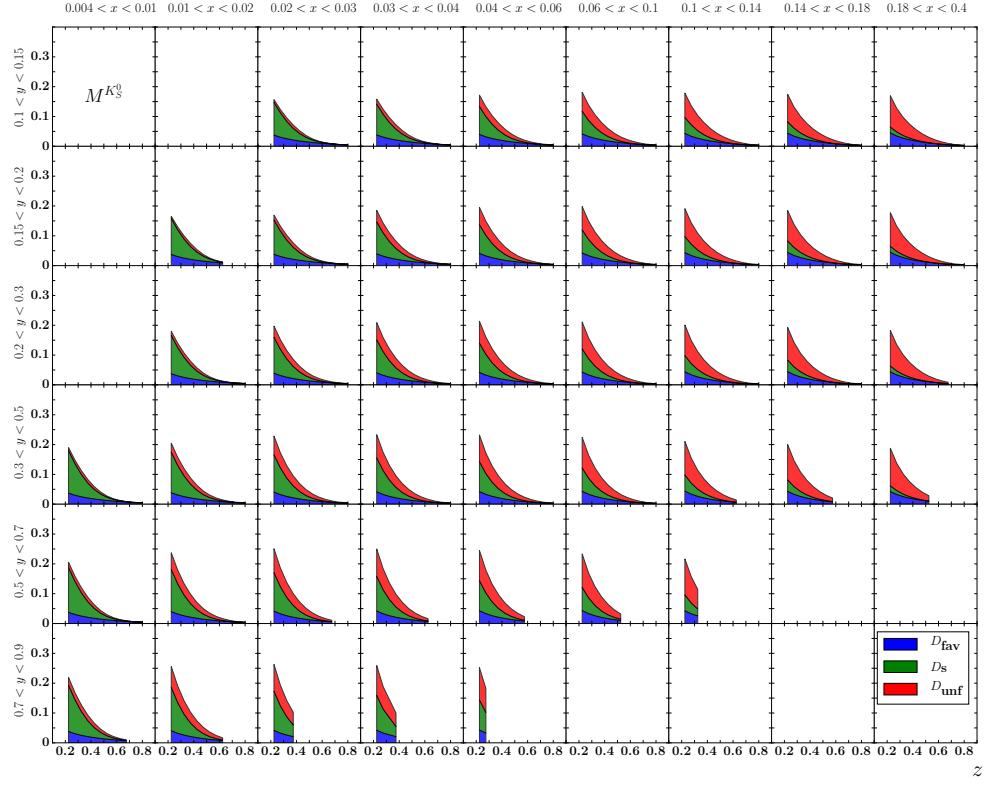


Figure B.24.: Same as Fig. B.23 but for K_S^0 .

B.2. Kaon FFs from Fits to K^+ , K^- , and K_S^0 Multiplicities

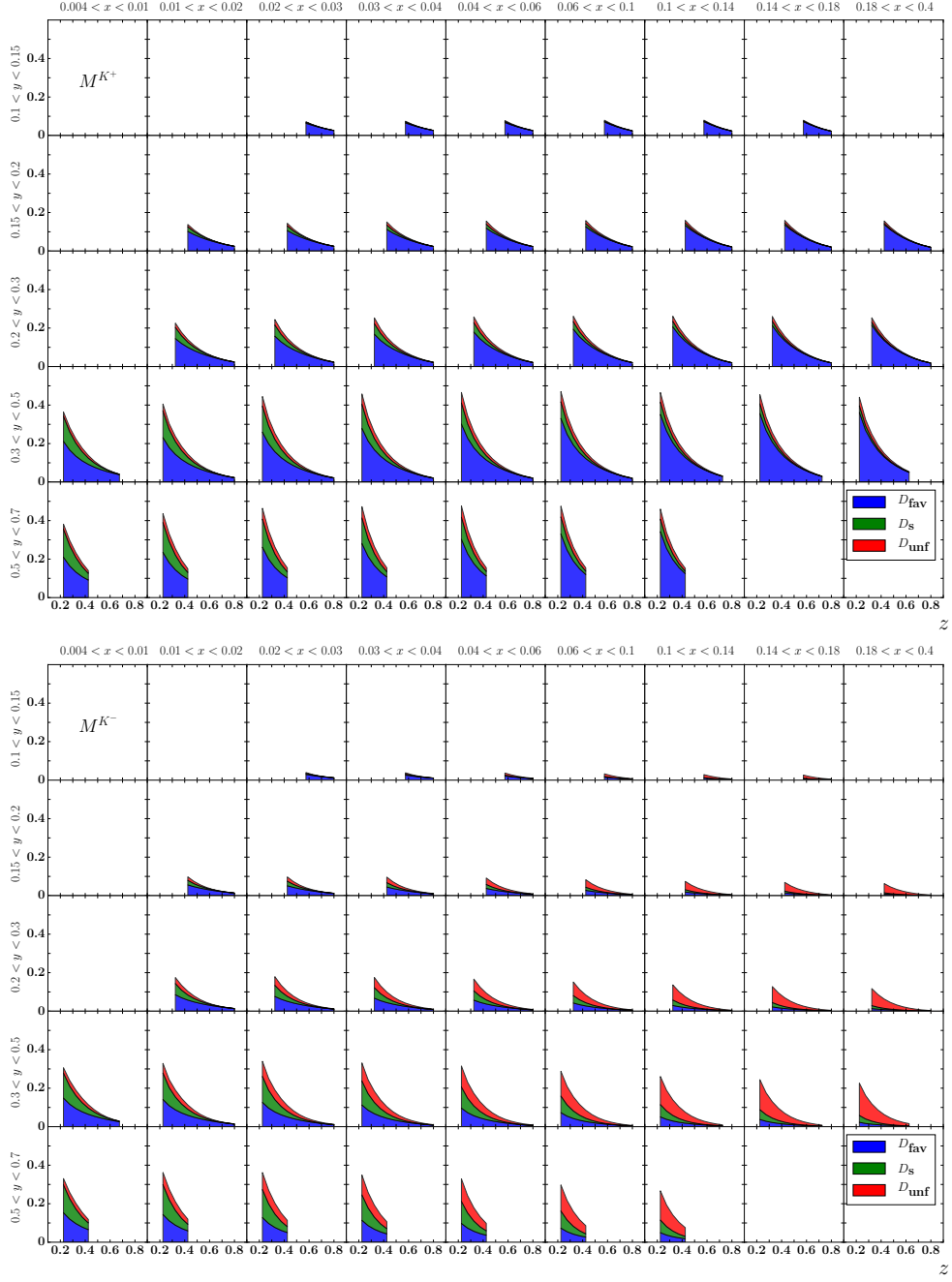


Figure B.25.: Contribution of FFs to K^+ (top) and K^- (bottom) multiplicities resulting from a fit on only combined kaon multiplicities using the NNPDF2.3 PDF set.

B. Fragmentation Functions

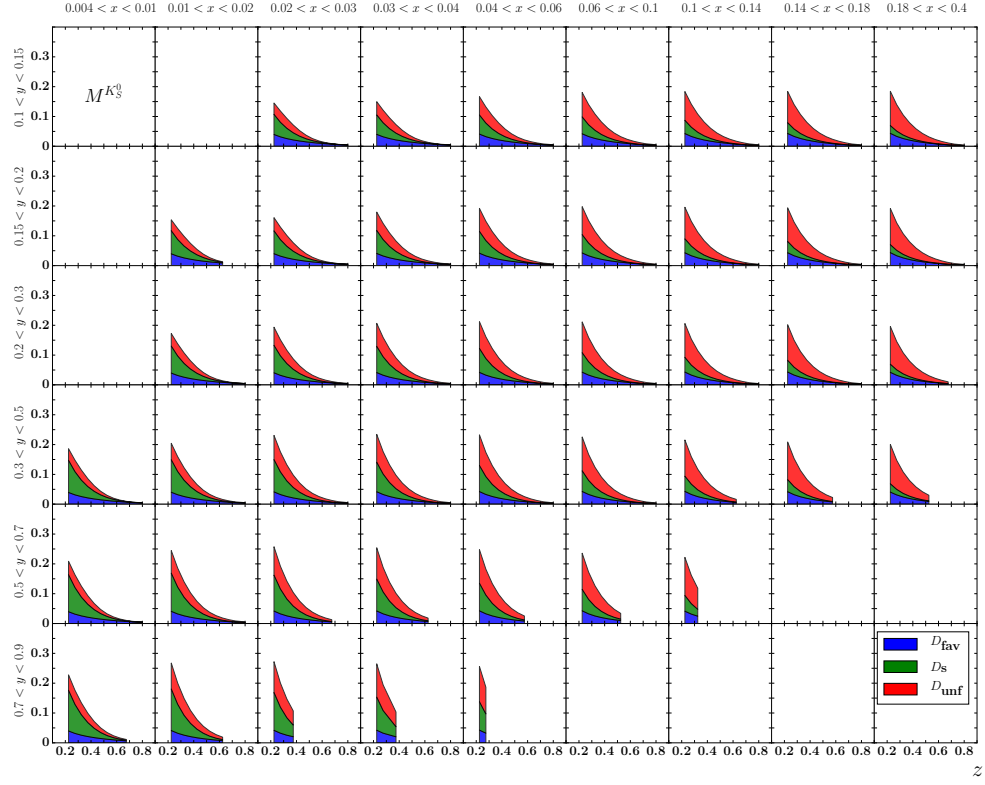


Figure B.26.: Same as Fig. B.25 but for K_S^0 .

B.2. Kaon FFs from Fits to K^+ , K^- , and K_S^0 Multiplicities

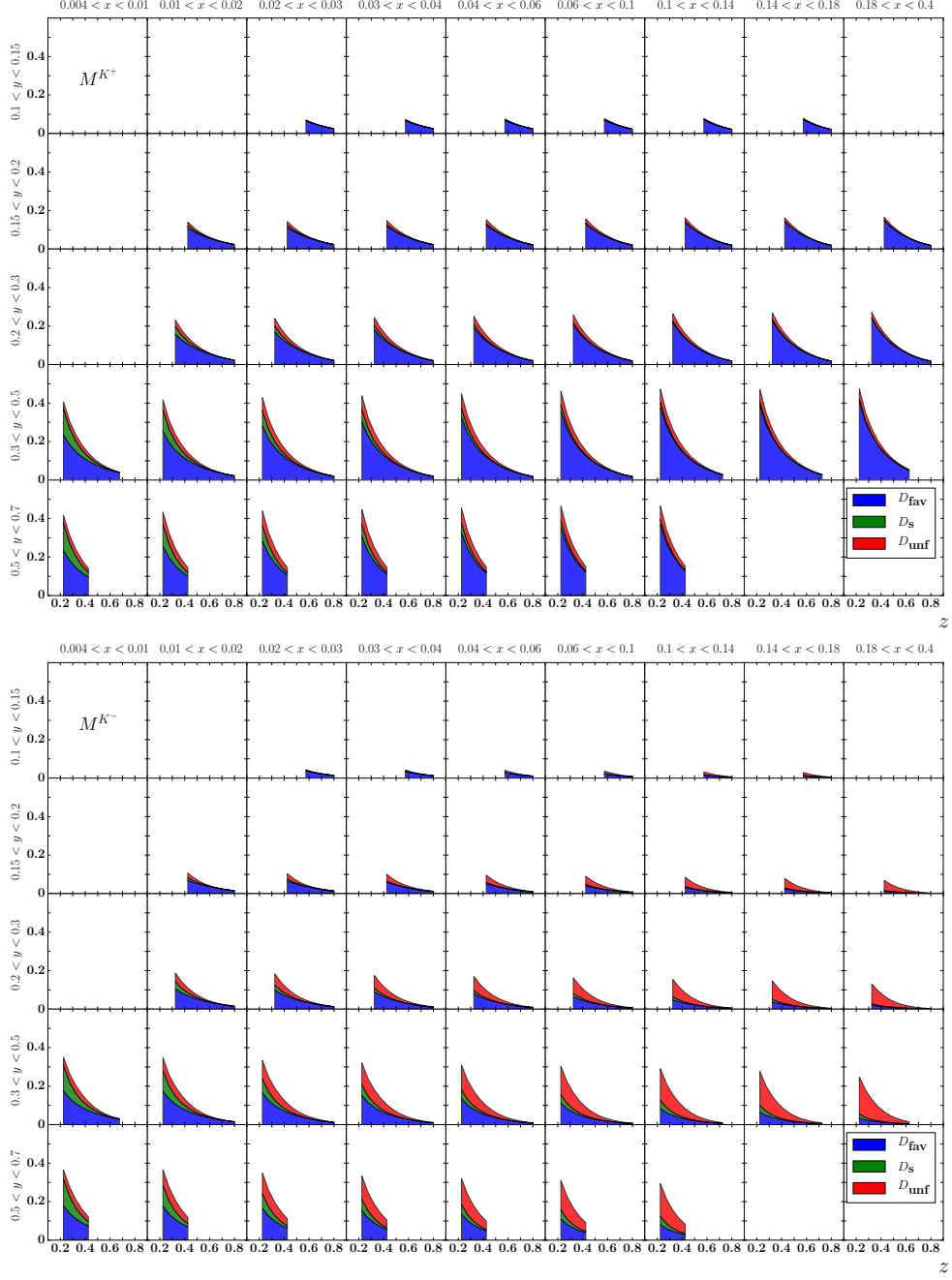


Figure B.27.: Contribution of FFs to K^+ (top) and K^- (bottom) multiplicities resulting from a fit on only combined kaon multiplicities using the NNPDF3.0 PDF set.

B. Fragmentation Functions

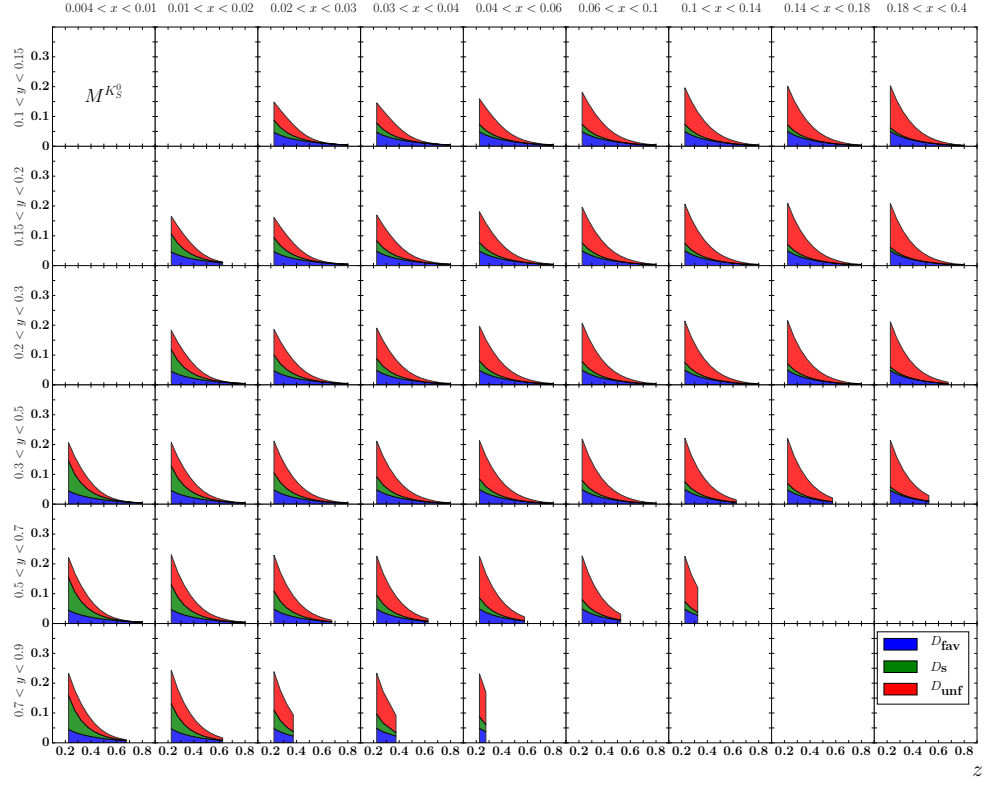


Figure B.28.: Same as Fig. B.27 but for K_S^0 .

B.2. Kaon FFs from Fits to K^+ , K^- , and K_S^0 Multiplicities

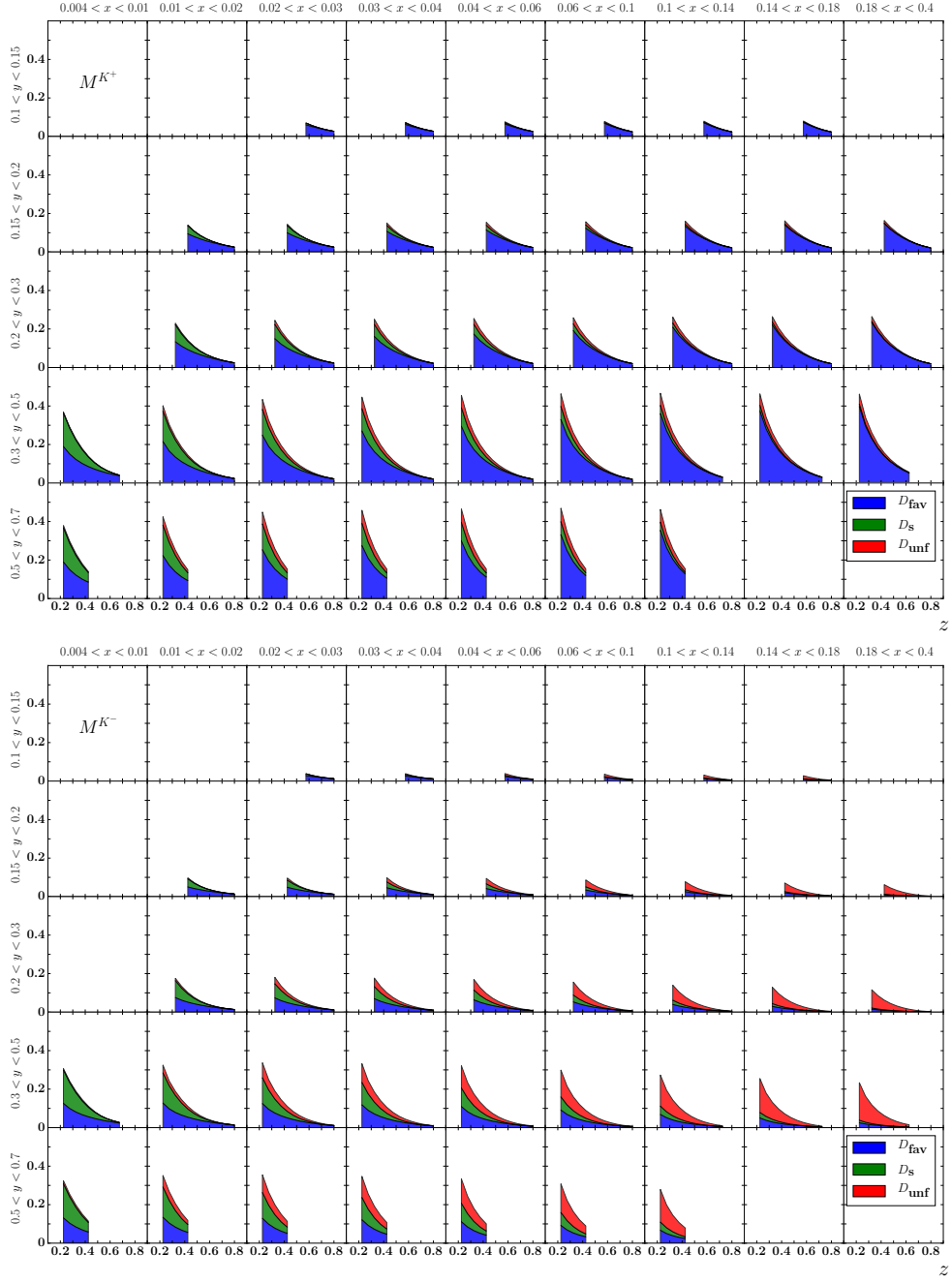


Figure B.29.: Contribution of FFs to K^+ (top) and K^- (bottom) multiplicities resulting from a fit on only combined kaon multiplicities using the CT10 PDF set.

B. Fragmentation Functions

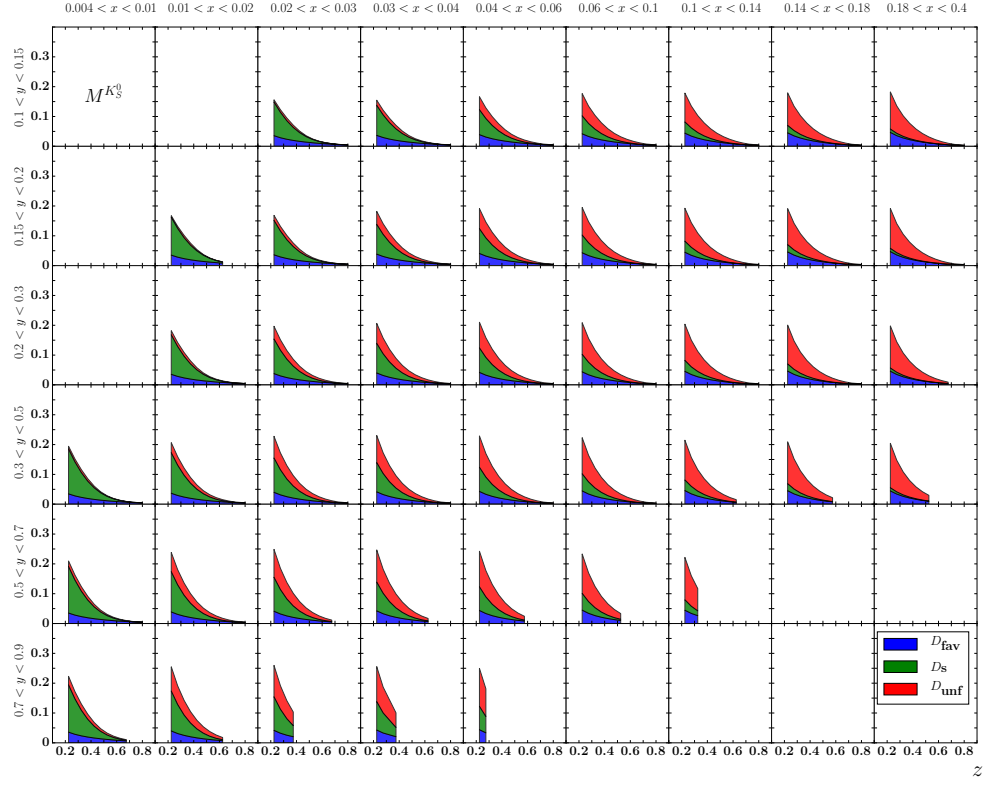


Figure B.30.: Same as Fig. B.29 but for K_S^0 .

Bibliography

- [1] Povh, B. and Rith, K. and Scholz, C. and Zetsche, F. *Particles and Nuclei: An Introduction to the Physical Concepts*, Springer, 2015.
- [2] Francis Halzen, Alan D. Martin, *Quarks and Lepton: An Introductory Course in Modern Particle Physics*, Addison Wesley, Massachusetts, John Wiley& Sons, Inc, 1984.
- [3] C. G. Callan and D. J. Gross, Phys. Rev. Lett. **22**, 156 (1969)
- [4] J. D. Bjorken, *Asymptotic Sum Rules at Infinite Momentum*, Phys. Rev. 179, 1547-1553 (1969).
- [5] S. L. Adler and W.-K. Tung, *Breakdown of Asymptotic Sum Rules in Perturbation Theory*, Phys. Rev. Lett. 22, 978-981 (1969).
- [6] R. Jackiw and G. Preparata, *Probes for the Constituents of the Electromagnetic Current and Anomalous Commutators*, Phys. Rev. Lett. 22, 975-977 (1969).
- [7] Yu.L. Dokshitzer. Sov.Phys. JETP 46:641 (1977).
- [8] V.N. Gribov, L.N. Lipatov. Sov.J.Nucl.Phys. 15:438 (1972).
- [9] G. Altarelli and G. Parisi. Nucl.Phys. B126:298 (1977).
- [10] K. A. Olive *et al.* [Particle Data Group Collaboration], *Review of Particle Physics*, Chin. Phys. C **38** (2014) 090001.
URL <http://pdg.lbl.gov>
- [11] J. C. Collins, D. E. Soper and G. F. Sterman, *Factorization of Hard Processes in QCD*, Adv. Ser. Direct. High Energy Phys. **5** (1989) 1, doi:10.1142/9789814503266_0001, [hep-ph/0409313].
- [12] S. Alekhin, J. Blumlein and S. Moch, Phys. Rev. D **89** (2014) 5, 054028 doi:10.1103/PhysRevD.89.054028, arxiv:1310.3059.
- [13] A. M. Cooper-Sarkar [ZEUS and H1 Collaborations], PoS EPS -**HEP2011** (2011) 320, arXiv:1112.2107.

Bibliography

- [14] A. D. Martin, W. J. Stirling, R. S. Thorne and G. Watt, *Parton distributions for the LHC*, Eur. Phys. J. C **63** (2009) 189 doi:10.1140/epjc/s10052-009-1072-5, arXiv:0901.0002.
- [15] L. A. Harland-Lang, A. D. Martin, P. Motylinski and R. S. Thorne, *Parton distributions in the LHC era: MMHT 2014 PDFs*, Eur. Phys. J. C **75** (2015) 5, 204 doi:10.1140/epjc/s10052-015-3397-6, arXiv:1412.3989.
- [16] R. D. Ball *et al.* [NNPDF Collaboration], *Parton distributions with QED corrections*, Nucl. Phys. B **877** (2013) 290 doi:10.1016/j.nuclphysb.2013.10.010, arXiv:1308.0598.
- [17] R. D. Ball *et al.* [NNPDF Collaboration], JHEP **1504** (2015) 040 doi:10.1007/JHEP04(2015)040, arXiv:1410.8849.
- [18] H. L. Lai, M. Guzzi, J. Huston, Z. Li, P. M. Nadolsky, J. Pumplin and C.-P. Yuan, Phys. Rev. D **82** (2010) 074024 doi:10.1103/PhysRevD.82.074024, arXiv:1007.2241.
- [19] A. Buckley, J. Ferrando, S. Lloyd, K. Nordström, B. Page, M. Rüfenacht, M. Schönherr and G. Watt, *LHAPDF6: parton density access in the LHC precision era*, Eur. Phys. J. C **75** (2015) 132 doi:10.1140/epjc/s10052-015-3318-8, arXiv:1412.7420.
- [20] E. Berger, *Proceedings of the NPAS Workshop on Electron Nuclear Physics with Internal Targets (SIAC, 1987)*, SLAC report 316, eds R. G. Arnold and R. C. Mmehart, p82; Preprint ANL-HEP-CP-87-45, April 30, 1987.
- [21] P. J. Mulders, *Current fragmentation in semiinclusive lepton production*, AIP Conf. Proc. **588** (2001) 75 doi:10.1063/1.1413147, hep-ph/0010199.
- [22] L. Trentadue and G. Veneziano, *Fracture functions. An improved description of inclusive hard processes in QCD*, Phys. Lett. B **323**, 201 (1994).
- [23] T. Sloan, G. Smadja and R. Voss, Phys. Rep. **162** (1988) 45.
- [24] Glen Cowan, *Error analysis for efficiency*, RHUL Physics, 2008; note available from <https://www.pp.rhul.ac.uk/cowan/stat/notes/efferr.pdf>.
- [25] M. Gell-Mann, A. Pais: Phys. Rev. **97** (1955) 1387.
- [26] Andersson, Bo and Gustafson, G. and Ingelman, G. and Sjostrand, T., *Parton Fragmentation and String Dynamics*, Phys. Rept. **97**(2-3):31-145, 1983
- [27] S. Albino, B. A. Kniehl and G. Kramer, *AKK Update: Improvements from New Theoretical Input and Experimental Data*, Nucl. Phys. B **803** (2008) 42 doi:10.1016/j.nuclphysb.2008.05.017, arXiv:0803.2768.

- [28] D. de Florian, R. Sassot and M. Stratmann, *Global analysis of fragmentation functions for pions and kaons and their uncertainties*, Phys. Rev. D **75** (2007) 114010 doi:10.1103/PhysRevD.75.114010, hep-ph/0703242.
- [29] M. Hirai, S. Kumano, T.-H. Nagai and K. Sudoh, *Determination of fragmentation functions and their uncertainties*, Phys. Rev. D **75** (2007) 094009 doi:10.1103/PhysRevD.75.094009, hep-ph/0702250
- [30] ALEPH Collaboration, D. Buskulic et al., Z. Phys. C66, 355 (1995).
- [31] OPAL Collaboration, R. Akers et al., Zeit. Phys. C63, 181 (1994).
- [32] DELPHI Collaboration, P. Abreu et al., Eur. Phys. J. C5, 585 (1998).
- [33] TP Collaboration, H. Aihara et al., Phys. Rev. Lett. 61, 1263 (1998); Phys. Lett. B184, 299 (1987); X.-Q. Lu, Ph.D. thesis, John Hopkins University, UMI-87-07273, 1986.
- [34] LD Collaboration, K. Abe et al., Phys. Rev. D59, 052001 (1999).
- [35] M. Derrick et al. (HRS collaboration), Phys. Rev. D35, 2639 (1987).
- [36] R. Itoh et al. (TOPAZ collaboration), Phys. Lett. B345, 335 (1995).
- [37] TASSO Collaboration, W. Braunschweig et al., Zeit. Phys. C42, 189 (1989).
- [38] R. Brandelik et al. (TASSO collaboration), Phys. Lett. B94, 444 (1980).
- [39] M. Althoff et al. (TASSO collaboration), Z. Phys. C17, 5 (1983).
- [40] PHENIX Collaboration, S.S. Adler et al., Phys. Rev. Lett. 91, 241803 (2003); K. Barish (PHENIX Collaboration), *The PHENIX Spin Program: Recent Results and Future Prospects*, talk presented at SPIN 2006, Kyoto, Japan.
- [41] STAR Collaboration, J. Adams et al., Phys. Rev. Lett. 97, 152302 (2006).
- [42] BRAHMS Collaboration, I. Arsene et al., hep-ex/0701041.
- [43] M. Hartig [HERMES Collaboration], *Hadron multiplicities at HERMES*, hep-ex/0505086.
- [44] A. Airapetian *et al.* [HERMES Collaboration], *Multiplicities of charged pions and kaons from semi-inclusive deep-inelastic scattering by the proton and the deuteron*, Phys. Rev. D **87** (2013) 074029 doi:10.1103/PhysRevD.87.074029, arXiv:1212.5407.
- [45] F. Arleo and J. Guillet, *FF generator*, <http://lapth.cnrs.fr/ffgenerator/>.

Bibliography

- [46] Sidney D. Drell and Tung-Mow Yan, *Massive Lepton-Pair Production in Hadron-Hadron Collisions at High Energies*, Phys. Rev. Lett. **25**(5): 316–320 (1970).
- [47] The COMPASS Collaboration, *The COMPASS experiment at CERN*, 2007, hep-ex:0703049v1.
- [48] Wikipedia user:Forthommel, License: CC BY-SA 3.0, <https://en.wikipedia.org/wiki/File:Cern-accelerator-complex.svg>.
- [49] The COMPASS Collaboration, *The deuteron spin-dependent structure function g_1^d and its first moment*, Physics Letters B 647, 8-17, 2007.
- [50] The **PH**ysics **A**nalysis **S**oftware **T**ools. PHAST homepage: <https://ges.web.cern.ch/ges/phast/index.html>.
- [51] Rene Brun and Fons Rademakers, *ROOT - An Object Oriented Data Analysis Framework*, Proceedings AIHENP'96 Workshop, Lausanne, Sep. 1996, Nucl. Inst. & Meth. in Phys. Res. A 389 (1997) 81-86, ROOT homepage: <https://root.cern.ch/>.
- [52] Q.M. Curiel Garcia, *Measurement of hadron multiplicities in deep inelastic scattering and extraction of quark fragmentation functions*, 2014 COMPASS publications: <https://wwwcompass.cern.ch/compass/publications>.
- [53] B. Badelek, D. Bardin, K. Kurek and K. Scholz. *Radiative correction schemes in deep inelastic muon scattering*, Z. Phys. C **66** (1995) 591.
- [54] J. Podolanski & R. Armenteros (1954) III. *Analysis of V-events*, Philosophical Magazine Series 7, 45:360, 13-30.
- [55] G. Ingelman, A. Edin and J. Rathsman, *LEPTO 6.5: A Monte Carlo generator for deep inelastic lepton - nucleon scattering*, Comput. Phys. Commun. **101** (1997) 108 doi:10.1016/S0010-4655(96)00157-9, hep-ph/9605286.
- [56] T. Sjostrand, *PYTHIA 5.7 and JETSET 7.4: Physics and manual*, hep-ph/9508391.
- [57] R. Brun et al. *Geant: Simulation Program for Particle Physics Experiments. User Guide and Reference Manual*, CERN-DD-78-2-REV, 2014
- [58] Florian Thibaud. *Développement de détecteurs Micromegas pixellisés pour les hauts flux de particules et évaluation de la contribution diffractive à la lepto-production de hadrons à COMPASS*. Instrumentation and Detectors [physics.ins-det]. Université Paris Sud - Paris XI, 2014. French. <NNT : 2014PA112239>. <tel-01084556>, <https://tel.archives-ouvertes.fr/tel-01084556>.

- [59] A. Sandacz and P. Sznajder, *HEPGEN - generator for hard exclusive leptoproduction*, arXiv:1207.0333.
- [60] N. Makke, J.F. Rajotte, F. Kunne, Y. Bedfer, R. Windmolders, *Kaon and Pion multiplicities from muon Deep Inelastic Scattering on ^6LiD* , Internal COMPASS Release Note June 2011. <http://wwwcompass.cern.ch/results/2011/>.
- [61] Minuit2 homepage: <https://seal.web.cern.ch/seal/MathLibs/Minuit2/html/>.
- [62] M. Hirai and S. Kumano, *Numerical solution of Q^2 evolution equations for fragmentation functions*, Comput. Phys. Commun. **183** (2012) 1002 doi:10.1016/j.cpc.2011.12.022, arXiv:1106.1553.
- [63] W.H. Press, S.A. Teukolsky, W.T. Vetterling and B.P. Flannery, Numerical Recipes in C (2nd Ed.): The Art of Scientific Computing 1992.
- [64] Glen Cowan, *Statistical Data Analysis*, Oxford Science Publications, 1998.
- [65] E. Leader, A. V. Sidorov and D. Stamenov, *Importance of Semi Inclusive DIS Processes in Determining Fragmentation Functions*, arXiv:1312.5200 [hep-ph].
- [66] D. de Florian, R. Sassot, M. Epele, R.J. Hernandez-Pinto, and M. Stratmann, *Parton-to-pion fragmentation reloaded*, Phys. Rev. D 91 (2015) 014035.
- [67] C. Adolph *et al.* [COMPASS Collaboration], *Multiplicities of charged pions and unidentified charged hadrons from deep-inelastic scattering of muons off an isoscalar target*, arXiv:1604.02695, 2016.
- [68] The COMPASS collaboration, *Multiplicities of charged kaons from semi-inclusive deep-inelastic scattering of muons off an isoscalar target*, in preparation.
- [69] E. Seder, D. Hahne *et al.* *Publication update for charged pion and unidentified hadron multiplicities from muon deep inelastic scattering on ^6LiD (2006 COMPASS data)*, COMPASS release note of November 2015, http://wwwcompass.cern.ch/compass/results/2015/november_pi_mult_2006
- [70] Y. Bedfer, N. du Fresne, D. Hahne, N. Pierre, E. Seder, M. Stolarski *et al.*, *Charged kaon multiplicities from muon deep inelastic scattering on ^6LiD (2006 COMPASS data)*, COMPASS release note (April 2015), http://wwwcompass.cern.ch/compass/results/2015/april_kaon_mult
- [71] E.Seder *et al.*, *Charged kaon multiplicities in semi-inclusive deep-inelastic scattering from COMPASS*, Proceedings of the 23rd Int. Workshop on Deep-Inelastic Scattering and Related Subjects (DIS2015), Dallas TX, USA (2015), PoS DIS2015 (2015) 214 http://pos.sissa.it/archive/conferences/247/214/DIS2015_214.pdf

List of Figures

2.1.	DIS process $lN \rightarrow l'X$ of a lepton off a nucleon.	6
2.2.	The F_2 structure function for the proton. $F_2(x, Q^2)$ is plotted against Q^2 for different values of x . The F_2 for different x are staggered. The plot is taken from [10].	10
2.3.	Illustration of scale breaking due to resolution. At small values of $Q^2 = Q_0^2$ (left) the photon cannot resolve the quark-gluon structure and measures the compound as one unit. At Q^2 values larger than Q_0^2 (right) the resolution increases and the individual momenta of q and g are resolved. The quark is measured without the gluon.	11
2.4.	The splitting functions describe the probability that (a) a quark radiates a gluon, (b) a gluon splits into two quarks, (c) a gluon originates from a quark, and (d) a gluon radiates a gluon.	12
2.5.	Comparison of LO PDF parametrizations from MMHT14, MSTW08, and NNPDF2.3, NNPDF3.0, and CT10 for $Q^2 = 3 (\text{GeV}/c)^2$. The solid line represents the distribution of quarks and the dashed line the ones for antiquarks. The plots on the left and on the right side show the same PDFs but the ones on the left highlight NNPDF3.0 and MMHT14, while the ones on the right highlight MSTW08, NNPDF2.3, and CT10. The PDF values are taken from [19].	15
2.6.	Schematic representation of the SIDIS scattering process.	16
2.7.	Comparison of NLO (left) and LO (right) FFs extracted from DSS, AKK, and HKNS at $Q^2 = 3 \text{ GeV}^2/c^2$. The FF values are generated with [45].	23
3.1.	Setup of the COMPASS experiment.	26
3.2.	Overview of the beamline at CERN. The COMPASS experiment is located in the north area. The picture is taken from [48].	27
3.3.	Schematic view of the M2 beamline.	28
3.4.	Top view of the COMPASS experiment setup of 2006.	29
3.5.	Schematic view of the RICH detector.	34
3.6.	Overview of the trigger components.	36
3.7.	Schematic of the trigger principle.	37
3.8.	Schematic view of the veto trigger system. Only muons that do not cross the veto hodoscopes are accepted. Track μ_2 is accepted, the tracks μ_1 and μ_3 are rejected.	38

List of Figures

3.9.	Overview of the kinematic regions in Q^2 and y covered by the COMPASS trigger system. The figure is taken from Ref. [47]. . . .	38
3.10.	Flow chart of CORAL, the COMPASS reconstruction software. . . .	39
4.1.	Distribution of primary vertex positions along the z-axis. The solid black lines show the target dimension. The stricter cuts are shown as red dashed lines.	43
4.2.	Q^2 plotted against x . The momentum range covered by COMPASS. The dashed lines show the selection cuts of kinematic region and kinematic constraints of the COMPASS experiment.	44
4.3.	For each cut, the light bar shows the percentage of selected events if this condition alone would be applied on the full set of events. The dark bar shows the percentage of selected events when the cuts are applied one after the other, as it is done in this analysis. The percentage values refer to the initial number of events (All trigger events).	46
4.4.	Kinematic variables of DIS. The variables are plotted with all but its own kinematic cuts applied. The dashed red lines mark the position of the cuts to select DIS, applied on the corresponding variable.	47
4.5.	Diagram to motivate the choice of the SIDIS event selection. . . .	48
4.6.	The distances between the primary and the secondary vertices as a function of y . Events with distances in the highlighted region are rejected. To clean the plot of misidentified K_S^0 the additional cut $m_{K_S^0} \pm 15 \text{ MeV}/c^2$ on the invariant mass of the $\pi^+\pi^-$ system is applied.	49
4.7.	The angle θ_{coll} between the flight direction of the K_S^0 candidates and the direction from the reconstructed primary to the secondary vertices. Events with angles in the highlighted area are rejected. To clean the plot of misidentified K_S^0 the additional cut $m_{K_S^0} \pm 15 \text{ MeV}/c^2$ on the invariant mass of the $\pi^+\pi^-$ system is applied.	50
4.8.	Momentum distribution of positive and negative particles originating from the second vertices. The plot on the left shows the full momentum range, while the one on the right plot is limited to $p_\pi < 10 \text{ GeV}/c$. The particles are interpreted as pions. All cuts but $p_{\pi^\pm} > 1 \text{ GeV}/c$ are applied. To clean the plot of misidentified K_S^0 the additional cut $m_{K_S^0} \pm 15 \text{ MeV}/c^2$ on the invariant mass of the $\pi^+\pi^-$ system is applied.	51

4.9.	The Armenteros-Podolanski plot. This plot visualizes the e^-e^+ and $\Lambda, \bar{\Lambda}$ contamination of the $\pi^+\pi^-$ invariant mass spectrum. The marked regions from $0 < p_t < 23$ MeV/c and $80 < p_t < 110$ MeV/c are excluded.	52
4.10.	The p_t distribution. All cuts but the cuts on p_t are applied. The red dashed lines indicate the cuts on p_t	53
4.11.	The z -distribution of the $\pi^+\pi^-$ system. The red dashed lines indicate the applied cuts on z	55
4.12.	For each cut, the light bar shows the percentage of selected events if this condition alone would be applied on the full set of all vertices of the previously selected DIS events. The dark bar shows the percentage of selected events when the cuts are applied one after the other, as it is done in this analysis. The percentage values refer to the initial number of vertices (All vertices).	56
4.13.	The radiative corrections for DIS and SIDIS as a function of x are plotted for different bins of y	57
4.14.	The $\pi^+\pi^-$ invariant mass distribution for all K_S^0 candidates.	58
4.15.	Ratios of the K_S^0 numbers extracted with a Gaussian and Voigtian as signal function. The dashed lines are the mean values of the ratios of the corresponding y bin. The y bins are staggered for clarity.	60
4.16.	Comparison of the Gaussian and the Voigtian signal functions for a selected bin.	60
4.17.	K_S^0 raw multiplicities data plotted against z in bins of x and y	62
4.18.	Acceptance of K_S^0 plotted against z in bins of x and y	65
4.19.	Correction factor resulting from the diffractive ϕ contribution to the raw multiplicities.	68
4.20.	The systematic uncertainties arising from the K_S^0 identification.	69
4.21.	The ratio of the acceptance corrected multiplicities extracted from the upstream and the downstream target cells. The red dashed line matches the weighted mean value of the corresponding x - y bin.	71
4.22.	Primary vertex position of all DIS events (left) and primary vertex position of events with a final state hadron of mass $m = m_{K_S^0} \pm 15$ MeV/c ² (right) for RD, MC, and the ratio RD/MC in the region $x > 0.1$ and $y < 0.2$	72
4.23.	Secondary vertex position of events with a final state hadron of mass $m = m_{K_S^0} \pm 15$ MeV/c ² for RD, MC, and the ratio RD/MC in the region $x > 0.1$ and $y < 0.2$	72
4.24.	The systematic uncertainties arising from variations of the multiplicities originating from different target cells.	73

List of Figures

4.25.	Correction factor resulting from the diffractive ϕ contribution to the raw multiplicities.	74
4.26.	Total systematic uncertainties. The individual contributions of the K_S^0 identification (blue), the different target cells (green), and the vector meson contribution (red) are shown proportionally.	78
4.27.	Final y averaged systematic uncertainties as a function of z for bins of x	79
4.28.	Acceptance corrected K_S^0 multiplicities plotted versus z for bins in x and bins in y (staggered for clarity). Only statistical uncertainties are plotted with the multiplicity points. The bands on the bottom of each plot corresponds to the y averaged systematic uncertainties.	80
5.1.	π^+ multiplicities versus z for nine x bins and five y bins (staggered for clarity by α). Only statistical uncertainties are shown. The curves correspond to the LO fit. The plot is taken from Ref. [67].	84
5.2.	Same as Fig. 5.1 but for π^- multiplicities.	84
5.3.	The favored (a), unfavored (b), and gluon (c) pion FFs and the ratio $D_{\text{unf}}^\pi/D_{\text{fav}}^\pi$, as obtained from COMPASS LO fit compared to the DSEHS, HKNS, and LSS fits at NLO. The bands represent the total uncertainties for the FFs and the statistical uncertainty for the ratio.	86
5.4.	K^+ (top) and K^- (bottom) multiplicities versus z for nine x bins and five y bins (staggered for clarity by α).	88
5.5.	Fit of K^+ (top) and K^- (bottom) multiplicities from COMPASS 2006 data. The points are the measured multiplicities with their statistical uncertainties. The curves correspond to the LO fit performed with MMHT14 as PDF set. The other PDF sets yield a similar good description.	92
5.6.	The P-value plotted against χ^2/n_d for different degrees of freedom. The degrees of freedom are selected according to the current analysis.	93
5.7.	The difference between fitted and measured multiplicities weighted by $1/\sigma_{\text{stat}}$ for bins of x , y , and z . The fitted multiplicities are calculated with the PDF parametrization from MMHT14. In the lower left corner of each bin the bin's contribution to the positive and negative χ^2/n_d values is shown. The gray area visualizes the region of data points which alone included yield a total $\chi^2/n_d \approx 1$	95
5.8.	Same as Fig. 5.7 but for the PDF parametrization from CT10.	96

5.9.	The kaon FFs extracted from K^+ and K^- multiplicities, compared with parametrizations from DSS, HKNS, and AKK. The left column shows the FFs extracted with PDFs from MSTW08 and NNPDF2.3. The right column shows the FFs extracted with PDFs from CT10, MMHT14, and NNPDF3.0. The uncertainty bands correspond to statistical (dark) and systematic (light) uncertainties.	97
5.10.	The measured K_S^0 multiplicities (dots) plotted together with the estimations (lines) from kaon parametrization of FFs extracted from charged multiplicities only. The PDF sets that were used for the extraction are MMHT14 (top) and NNPDF3.0 (bottom).	98
5.11.	Contribution of FFs to K^+ (top) and K^- (bottom) multiplicities resulting from a fit on only charged kaon multiplicities using the MMHT14 PDF set.	99
5.12.	Same as Fig. 5.11 but for K_S^0 multiplicities.	100
5.13.	Fit of K^+ and K^- multiplicities from COMPASS 2006 data. The points are the measured multiplicities with their statistical uncertainties. The curves correspond to the fitted multiplicities. The MMHT14 PDF set was used for the extraction of the FFs.	103
5.14.	Same as Fig. 5.13 but showing K_S^0 multiplicities.	104
5.15.	The difference between fitted and measured multiplicities weighted by $1/\sigma_{stat}$ for bins of x , y , and z . The fitted multiplicities are calculated with MMHT14 and the extracted FFs from K^+ , K^- , and K_S^0 multiplicities. The dashed line shows the mean value of the x - y bin. The gray area visualizes the region which the difference of the values should not exceed to achieve a total $\chi^2/n_d < 2$	105
5.16.	The kaon FFs extracted from combined K^+ , K^- , and K_S^0 multiplicities, compared with parametrizations from DSS, HKNS, and AKK. The left column shows the FFs extracted with PDFs from MSTW08 and NNPDF2.3. The right column shows the FFs extracted with PDFs from CT10, MMHT14, and NNPDF3.0. The uncertainty bands correspond to statistical (dark) and systematic (light) uncertainties.	106
5.17.	Contribution of FFs to K^+ (top) and K^- (bottom) multiplicities resulting from a fit on K^+ , K^- , and K_S^0 multiplicities using the MMHT14 PDF set.	107
5.18.	Same as Fig. 5.17 but showing K_S^0 multiplicities.	108
5.19.	Integrated FFs for each resample of the statistical (blue) and systematical (red) uncertainty estimation of the fits for K^+ and K^- excluding K_S^0 (left) and including K_S^0 (right). Both fits are performed with the MMHT14 PDF set.	109

List of Figures

5.20.	The K^+ multiplicities measured at the HERMES (blue points) compared with multiplicities estimated from the extracted FFs of the fit of K^+ , K^- , and K_S^0 multiplicities from COMPASS (green points). In addition the ratio of HERMES over COMPASS multiplicities (red points) is shown. The PDF set used for the FF extraction and the estimation is MSTW14.	114
5.21.	Same as Fig. 5.20 but for K^-	114
5.22.	Comparison between kaon multiplicities measured at COMPASS and HERMES. The plots on the left show the sum, the plots on the right show the ratio of the z -integrated K^+ and K^- multiplicities. In addition to the measured multiplicities, estimations from extracted COMPASS FFs are shown. The estimations in the top row are calculated with FFs extracted from K^+ , K^- , and K_S^0 multiplicities, while the bottom row is for FFs extracted from K^+ and K^- only. Both FFs are determined with the MMHT14 PDF set.	115
B.1.	Residuals for the parametrization with the MMHT14 PDF set.	131
B.2.	Residuals for the parametrization with the MSTW08 PDF set.	132
B.3.	Residuals for the parametrization with the NNPDF2.3 PDF set.	132
B.4.	Residuals for the parametrization with the NNPDF3.0 PDF set.	133
B.5.	Residuals for the parametrization with the CT10 PDF set.	133
B.6.	Contribution of FFs to K^+ (top) and K^- (bottom) multiplicities resulting from a fit on only charged kaon multiplicities using the MMHT14 PDF set.	134
B.7.	Same as Fig. B.6 but for K_S^0	135
B.8.	Contribution of FFs to K^+ (top) and K^- (bottom) multiplicities resulting from a fit on only charged kaon multiplicities using the MSTW08 PDF set.	136
B.9.	Same as Fig. B.8 but for K_S^0	137
B.10.	Contribution of FFs to K^+ (top) and K^- (bottom) multiplicities resulting from a fit on only charged kaon multiplicities using the NNPDF2.3 PDF set.	138
B.11.	Same as Fig. B.10 but for K_S^0	139
B.12.	Contribution of FFs to K^+ (top) and K^- (bottom) multiplicities resulting from a fit on only charged kaon multiplicities using the NNPDF3.0 PDF set.	140
B.13.	Same as Fig. B.12 but for K_S^0	141
B.14.	Contribution of FFs to K^+ (top) and K^- (bottom) multiplicities resulting from a fit on only charged kaon multiplicities using the CT10 PDF set.	142
B.15.	Same as Fig. B.14 but for K_S^0	143
B.16.	Residuals for the parametrization with the MMHT14 PDF set.	144

B.17. Residuals for the parametrization with the MSTW08 PDF set. . . .	145
B.18. Residuals for the parametrization with the NNPDF2.3 PDF set. . .	145
B.19. Residuals for the parametrization with the NNPDF3.0 PDF set. . .	146
B.20. Residuals for the parametrization with the CT10 PDF set.	146
B.21. Contribution of FFs to K^+ (top) and K^- (bottom) multiplicities resulting from a fit on only combined kaon multiplicities using the MMHT14 PDF set.	147
B.22. Same as Fig. B.21 but for K_S^0	148
B.23. Contribution of FFs to K^+ (top) and K^- (bottom) multiplicities resulting from a fit on only combined kaon multiplicities using the MSTW08 PDF set.	149
B.24. Same as Fig. B.23 but for K_S^0	150
B.25. Contribution of FFs to K^+ (top) and K^- (bottom) multiplicities resulting from a fit on only combined kaon multiplicities using the NNPDF2.3 PDF set.	151
B.26. Same as Fig. B.25 but for K_S^0	152
B.27. Contribution of FFs to K^+ (top) and K^- (bottom) multiplicities resulting from a fit on only combined kaon multiplicities using the NNPDF3.0 PDF set.	153
B.28. Same as Fig. B.27 but for K_S^0	154
B.29. Contribution of FFs to K^+ (top) and K^- (bottom) multiplicities resulting from a fit on only combined kaon multiplicities using the CT10 PDF set.	155
B.30. Same as Fig. B.29 but for K_S^0	156

List of Tables

2.1.	List of inclusive and semi-inclusive DIS variables.	6
2.2.	List of kaon properties and their most common decay channels taken from [10].	20
4.1.	List of number of spills including bad spills for six weeks of 2006. . .	42
4.2.	The cuts for the DIS event selection.	45
4.3.	Minimal distance between the primary and secondary vertex. . . .	50
4.4.	Maximum values of θ_{coll}	51
4.5.	The cuts for the selection of K_S^0 candidates.	55
4.6.	Numbers of DIS events and kaon candidates before and after ra- diative corrections.	57
4.7.	Numbers of DIS events and kaon candidates as well as their ratios before and after radiative corrections for the six periods.	75
4.8.	The weighted mean values and corresponding standard deviation for the ratio of the multiplicities extracted from the combined weeks W40, W41, W45 and the combined weeks W42, W43, W46. Bins deviating from 1 with more than 1σ , are highlighted.	77
5.1.	Final fit parameters for $Q_0^2 = 1 \text{ GeV}/c^2$	86
5.2.	Start values and initial step size for the parameters of the kaon FFs for the fit at $Q^2 = 1 (\text{GeV}/c)^2$	90
5.3.	Parameters and χ^2/n_d values of fits of charged kaon multiplicities with different PDF sets for $Q_0^2 = 1 (\text{GeV}/c)^2$	91
5.4.	Parameters and χ^2 values of fits of charged and neutral kaon mul- tiplicities with different PDF sets.	102
5.5.	Results for $N_q = \int_{0.2}^{0.85} D_q(z, Q^2 = 3 (\text{GeV}/c)^2) dz$, with $q =$ fav, s, unf, and the ratio $R_{sf} = N_s/N_{\text{fav}}$ for fits with K^+ and K^- only and K^+ , K^- , and K_S^0 multiplicities performed for different PDF sets.	111
5.6.	Overview of the COMPASS and HERMES Q^2 values for similar \bar{x} . For COMPASS the range from $Q_{\text{min}}^2 - Q_{\text{max}}^2$ is given. For HERMES the mean value of Q^2 the corresponding x bin is shown.	113